



UCL

UNIVERSITY COLLEGE LONDON

Faculty of Mathematics and Physical Sciences

Department of Physics & Astronomy

CHEMICAL-MHD MODELLING OF COLLAPSING PRE-STELLAR CORES

Thesis submitted for the degree of Doctor of
Philosophy, University College London

by

Hugh Anthony Walter Stace

Supervisors:

Jonathan Rawlings

David Williams

Examiners:

Julian Pittard

Jeremy Yates

October 5, 2015

*To Robin and Ursula, simply for being such wonderful parents and
grandparents.*

I, Hugh Stace, confirm that the work presented in this thesis is my own. Where information has been derived from other sources, I confirm that this has been indicated in the thesis.

Abstract

A multi-point magnetohydrodynamic (MHD) model of the early stages of collapsing pre-stellar cores is presented that takes into account the effects of ambipolar diffusion by deriving ionization levels from a network of chemical and grain-surface reactions. The contribution from both ions and charged grains is taken into account when determining the magnetic retardation effect on the flow of neutral particles. The resulting radial chemical profiles are used to determine molecular line profiles with the objective of identifying features in the case where ambipolar diffusion plays an important role in the dynamics of collapsing pre-stellar cores. It is found that a steep ionization drop at $A_V \sim 3$ in the core is coincident with a rise in the dust-gas ratio: the drop in ionization acts as a barrier to ambipolar diffusion of charged grains; dust moves out from the centre of the core to supply the build-up of dust at the ambipolar diffusion barrier. The model predicts a broad velocity field with infall speeds increasing towards the centre; the associated spectral signature for optically thick lines is that of asymmetric line profiles with a *dip velocity* that is offset from the local standard of rest. The parameters that affect the model are analysed and their effect on collapse timescales, radial gas density distribution, synthetic line profiles and dust continuum emission determined. By varying parameters such as the cosmic ray ionization rate, initial atomic abundance fractions and grain chemistry, a picture of the sensitivity of collapsing pre-stellar cores to their environment is obtained.

Acknowledgements

I would like to thank the Charlie Lada, Sebastien Maret, Derek Ward-Thompson and Huabai Li for allowing me to reproduce their stunning figures in Chapter 1. A big thank you must go to my supervisor, Jonathan Rawlings, for enduring my long (if not record-breaking) postgraduate studentship: without his words of encouragement I would probably have abandoned my research long ago. I am indebted to Jeremy Yates for donating the code used to calculate molecular line profiles and for his tutorial on its use. I thank David Williams for his continued interest in my research despite the infrequency of my visits to UCL and our even rarer opportunities to talk. A part-time studentship does have some advantages over a full-time studentship in that I had the luxury of a long time to think and refine the models. The downside is that you are necessarily part-time in other areas of your life – in my case this felt like being a part-time husband to my wife Tracey and part-time father to my sons, Thomas and Samuel: to you I say the biggest thank you of all for putting up with my decade-long obsession. A special thank you goes to Thomas for continually referring to my research as a game to be played out on a computer. Over time I have come to realise how correct this comparison is – seeing these virtual nascent protostars take shape is fun and continues to surprise me. In gaming terminology: level 1 is complete, let level 2 begin!

I know full well that the total amount of the things I know is a tiny little pinprick of light compared with the vast unlimited darkness that surrounds it – which is all the things I don't know. I don't know more than a tiny fragment of what it's possible to know about this world. As for what goes on outside it in the rest of the universe, it's a vast darkness full of things that I don't know.

Philip Pullman

Contents

Table of Contents	11
List of Figures	15
List of Tables	21
1 Introduction	27
1.1 Molecular clouds, clumps and pre-stellar cores	27
1.1.1 The classification of dense cores	28
1.1.2 B335 – an isolated Class 0 protostellar core	30
1.1.3 Pre-stellar cores	32
1.1.4 General properties of starless cores	32
1.1.5 Barnard 68 – a gravitationally stable pre-stellar core	33
1.1.6 Lynds 1544 – a pre-stellar core undergoing collapse?	35
1.1.7 Are there other pre-stellar cores like Lynds 1544?	37
1.1.8 Giant molecular clouds and filamentary structure	39
1.1.9 The core mass function	40
1.2 Star formation theories and the role of ambipolar diffusion	41
1.2.1 High-mass and low-mass stars	41
1.2.2 The Larson-Penston flow	41
1.2.3 The Shu inside-out collapse model	43
1.2.4 Including magnetic fields in star formation theories	46
1.2.5 The magnetic field strength problem	46
1.2.6 The angular momentum problem	49
1.2.7 Support from Alfvén waves	50

1.2.8	Turbulence and core rotation	53
1.3	Observations of star forming regions	53
1.3.1	Spectroscopic studies of dense cores	53
1.3.2	The equation of radiative transfer	56
1.3.3	Measurements of core excitation temperatures and opacities	58
1.3.4	Using Ammonia line profiles to probe the temperature structure	60
1.3.5	Modelling the gas density structure	61
1.3.6	Using line profiles to probe the velocity structure	62
1.3.7	Strength of magnetic fields	64
1.3.8	Geometry of magnetic field lines	64
1.3.9	Do magnetic fields dominate the later stages of star formation?	68
1.4	Interstellar chemistry and the ionization fraction in molecular clouds	68
1.4.1	Molecular synthesis	68
1.4.2	Diffuse clouds	70
1.4.3	Dense clouds	70
1.4.4	Translucent clouds	71
1.4.5	The role of dust grains in molecule formation	71
1.4.6	Ionization fraction	72
1.4.7	Freeze-out and desorption processes	73
1.4.8	Desorption processes	74
1.4.9	An analytic model for the ionization fraction at the centre of dark clouds	76
1.5	Thesis motivation and purpose	77
2	Model	81
2.1	Core morphology	82
2.2	Drag on neutral particles due to collisions with ions and grains	84
2.3	Force equation on neutral gas	86
2.4	Electric and magnetic field forces on ions, electrons and charged grains	86
2.5	Flux freezing	88
2.6	Visual extinction	88
2.7	Temperature profile	91
2.8	Chemical model	91

2.9	Grain reactions	93
2.10	Model solution	94
2.11	Code validation	95
2.11.1	Freefall time	96
2.11.2	Sound speed	96
2.11.3	Magnetosonic speed	97
2.11.4	Magnetic flux conservation	98
2.11.5	Dust conservation	98
2.11.6	Modelling a Bonnor-Ebert sphere	100
3	Model Parameters	103
3.1	Chemistry	104
3.1.1	Standard model	104
3.1.2	Model variations	104
3.2	Grain chemistry	105
3.3	Dust grain sizes and distribution	106
3.3.1	Standard model	106
3.3.2	Model variations	109
3.4	Physical parameters	110
3.4.1	Standard model	110
3.4.2	Model variations	111
3.5	Model summary	112
4	Results for the standard model	115
4.1	Core dynamics over time	115
4.2	Chemical and dynamical radial profiles	118
4.2.1	The expansion phase	121
4.2.2	The collapse phase	122
4.3	Synthetic line profiles	124
4.3.1	Synthetic HCO ⁺ line profiles	124
4.3.2	Synthetic HCO ⁺ line profiles in a protostellar core	133
4.3.3	Synthetic line profiles using a beam size consistent with observations from ALMA	134
4.3.4	Alternative explanation for asymmetric line profiles	135

4.3.5	Synthetic CS line profiles	135
4.3.6	Synthetic line profiles for optically thin lines	136
4.4	Summary	136
5	Modelling the linewidth – drift velocity relationship	141
5.1	Linewidths of optically thin lines	141
5.2	Observations of linewidth differences	149
5.3	Summary	152
6	Results for model variations	155
6.1	Core dynamics over time	155
6.1.1	Comparing collapse times to the free-fall time	160
6.2	Chemical and dynamical radial profiles	164
6.2.1	Dynamical radial profiles	168
6.2.2	Radial profile of $n(\text{H})$	168
6.2.3	Dependence of B on $n(\text{H})$	170
6.2.4	Radial variation in visual extinction, temperature and dust-gas ratio	176
6.2.5	Chemical radial profiles	176
6.3	Synthetic line profiles	178
6.3.1	Radial line profiles	178
6.3.2	Comparing radial synthetic line profiles with observations	184
6.4	Summary	185
7	Modelling the dust continuum emission	191
7.1	Dust model	192
7.2	Model Solution	195
7.2.1	Code validation	195
7.3	Results for the standard model – dust emission	198
7.4	Results for model variations – dust emission	202
7.5	Summary	208
8	Modelling the collapse of a cloud	211
8.1	Model parameters	212
8.2	Results	212
8.2.1	Chemical and dynamical radial profiles	212

8.2.2	Oscillations at the edge of the cloud	215
8.2.3	Improving the resolution of cloud models with additional shells . . .	219
8.2.4	Radial profile of $n(\text{H})$	224
8.2.5	Comparing collapse times to the free-fall time	226
8.2.6	Consistency between cloud and core models	226
8.2.7	Synthetic line profiles	227
8.2.8	Radial line profiles	227
8.2.9	Line profiles for higher rotational transition lines	230
8.2.10	Line profiles and excitation temperature for CO (1-0)	233
8.2.11	Dust continuum emission	236
8.3	Summary	238
9	Discussion and conclusion	243
9.1	Comparison with other collapse models	243
9.2	Model limitations and future direction	249
9.2.1	Testing updated chemical reaction rate data files	249
9.2.2	Desorption processes	250
9.2.3	Modelling the effects of grain growth during core collapse	250
9.2.4	Modelling the effects of a changing ion-neutral collision cross-section	252
9.2.5	Modelling the collapse of non-spherical cores	253
9.2.6	The unexplained CO line profile in L1544	254
9.2.7	Changing the initial conditions prior to the onset of gravitational collapse	255
9.3	Conclusion	255
A	Finite difference method for the solution of ambipolar diffusion equa- tions	261
B	Spherical collapse of a uniform sphere	265
C	Chemical and dynamical radial profiles	267
D	Core temperature and dust continuum radial profiles	273
	Bibliography	280

List of Figures

1.1	Integrated C ¹⁸ O intensity contour map of the Barnard 5 core complex (image from Goldsmith et al. 1986).	28
1.2	Classification of protostellar cores by their spectral energy distributions (image from André 1994).	30
1.3	Number distribution of $\langle \delta V_{\text{CS}} \rangle$, the mean normalised velocity difference between lines of CS (2-1) and N ₂ H ⁺ (1-0) in a sample of starless cores (image from Lee et al. 2001).	36
1.4	Column density map and stability map from Herschel observations in the Aquila cloud complex (image from André et al. 2010).	38
1.5	Differential mass function (dN/dlogM) of the pre-stellar core population in the main sub-field of Aquila.	40
1.6	Examples of stable and unstable Bonnor-Ebert (BE) spheres.	43
1.7	Log-log plot of the quantity $\Delta V_{NT}/R^{0.5}$ against the magnetic flux density B	51
1.8	Half-maximum intensity contour plots for eight dense cores.	57
1.9	Near-infrared extinction of Barnard 68 (image from Alves et al. 2001 <i>a</i>). Image courtesy of ESO.	61
1.10	Spectral signature of collapse in a protostellar core (image from Rawlings 1996 <i>b</i>).	62
1.11	Molecular line profiles at the centre of Barnard 68 (image from Maret et al. 2007).	65
1.12	Magnetic field orientation in L1544 using submillimetre polarimetry (image from Ward-Thompson et al. 2000).	66
1.13	Magnetic fields in the Orion molecular cloud (image from Li et al. 2009).	67

2.1	Core Morphology.	83
2.2	Geometry for extinction due to a single ray of radiation	90
2.3	Modelling a Bonnor-Ebert sphere with a central density to external density contrast of $n_0/n_{ext} = 6.0$	102
4.1	Dynamical evolution of the model core.	116
4.2	Chemical and dynamical radial profile at $t = 1.4$ Myr.	119
4.3	Chemical and dynamical radial profile at $t = 3.75$ Myr.	120
4.4	HCO ⁺ line profiles. Left hand side plots line profiles at $t = 1.4$ Myr – corresponding to an expansion phase; right hand side plots line profiles at $t = 3.75$ Myr – corresponding to a collapse phase.	125
4.5	Observed HCO ⁺ line profiles (solid black lines) at the centre of B335 (image from Evans et al. 2005).	126
4.6	HCO ⁺ line profiles using a gas temperature that rises linearly with radial distance from 5000 AU to the core centre. The temperature at the core centre is ~ 20 K.	127
4.7	As Figure 4.6 but using angular resolutions consistent with ALMA.	128
4.8	CS line profiles. Left hand side plots line profiles at $t = 1.4$ Myr – cor- responding to an expansion phase; right hand side plots line profiles at $t = 3.75$ Myr – corresponding to a collapse phase.	129
4.9	C ¹⁸ O, HC ¹⁸ O ⁺ , NH ₃ and N ₂ H ⁺ line profiles. Left hand side plots line profiles at $t = 1.4$ Myr – corresponding to an expansion phase; right hand side plots line profiles at $t = 3.75$ Myr – corresponding to a collapse phase.	130
4.10	Schematic diagram of the ambipolar diffusion process.	138
5.1	Schematic diagram showing how the maximum ion-neutral drift velocity, V_{drift} , differs from V_{diff} , the difference between the maximum ion and neutral infall velocities.	143
5.2	Linewidth differences between NH ₃ (1,1) and HC ¹⁸ O ⁺ (1-0) during the expansion phase ($1.0 \text{ Myr} \leq t \leq 1.8 \text{ Myr}$).	144
5.3	Linewidth differences between NH ₃ (1,1) and N ₂ H ⁺ (1-0) during the expan- sion phase ($1.0 \text{ Myr} \leq t \leq 1.8 \text{ Myr}$).	145
5.4	Linewidth differences between NH ₃ (1,1) and HC ¹⁸ O ⁺ (1-0) during the collapse phase ($3.0 \text{ Myr} \leq t \leq 3.76 \text{ Myr}$).	145

5.5	Linewidth differences between NH_3 (1,1) and N_2H^+ (1-0) during the collapse phase ($3.0 \text{ Myr} \leq t \leq 3.76 \text{ Myr}$).	146
5.6	Linewidth differences between NH_3 (1,1) and N_2H^+ (1-0) during the collapse phase ($3.0 \text{ Myr} \leq t \leq 3.76 \text{ Myr}$) at a beam offset of 100 arcsec.	146
5.7	Linewidth differences between NH_3 (1,1) and N_2H^+ (1-0) during the collapse phase ($3.0 \text{ Myr} \leq t \leq 3.76 \text{ Myr}$) using a beam resolution consistent with ALMA.	149
6.1	Core dynamics overs time for the model variation <i>b4</i>	157
6.2	Core dynamics overs time for a subcritical run for model variation <i>grainchem1</i>	158
6.3	Chemical and dynamical radial profile for model <i>graindist2</i>	165
6.4	Chemical and dynamical radial profile for model <i>stick2</i>	166
6.5	Radial line profiles for the <i>standard</i> model.	179
6.6	Radial line profiles for an example of a class B model, <i>stick1</i> (neutral-grain sticking coefficient increased to 1.0).	180
6.7	Radial line profiles for an example of a class C model, <i>b4</i> (magnetic flux density reduced to $5.6 \mu\text{G}$).	181
6.8	Line profiles at the core centre for a class B model, <i>stick1</i> (neutral-grain sticking coefficient increased to 1.0).	182
6.9	Line profiles at the core centre for a class C model, <i>b4</i> (magnetic flux density reduced to $5.6 \mu\text{G}$).	183
7.1	Comparing the dust continuum radial profiles from the standard model with output from LIME/MIRIAD.	197
7.2	Core temperature and dust continuum radial profiles for the standard model.	199
7.3	Core temperature and dust continuum radial profiles for the model <i>graindist2</i>	200
8.1	Chemical and dynamical radial profile for the standard cloud model using 100 shells.	213
8.2	Chemical and dynamical radial profile for the standard cloud model at $t = 5.9 \text{ Myr}$, the epoch just prior to the onset of oscillations in the velocity profile.	216
8.3	Dynamical evolution of 10 shells near the source of cloud oscillations.	217

8.4	Chemical and dynamical radial profile for the standard cloud model, increasing the number of shells from 100 to 400.	220
8.5	Chemical and dynamical radial profile for the cloud model <i>graindist2</i> using 400 shells.	221
8.6	Radial line profiles for the <i>standard</i> cloud model.	228
8.7	Radial line profiles for cloud model <i>graindist2</i>	229
8.8	Line profiles at the cloud centre for the standard cloud model	231
8.9	Line at the cloud centre for cloud model <i>graindist2</i>	232
8.10	CO (1-0) line profiles at the cloud centre for the standard (left-hand plot) and <i>graindist2</i> (right-hand plot) cloud models.	233
8.11	CO (1-0) line profiles at the cloud centre, excluding the contribution from the outer 25% of the cloud mass for cloud model <i>graindist2</i>	234
8.12	Excitation temperature for CO (1-0) for cloud model <i>graindist2</i>	235
8.13	Temperature and dust continuum radial profiles for the standard (left-hand plot) and <i>graindist2</i> (right-hand plot) cloud models.	237
9.1	Chemical and dynamical radial profile at $t = 3.67$ Myr using the RATE12 version of the UMIST Database for Astrochemistry (McElroy et al. 2013). .	251
9.2	Ratio of shell radii between models <i>b1</i> and <i>b4</i>	253
A.1	Grid layout for solution by the finite difference method	262
C.1	Chemical and dynamical radial profiles for models <i>b1</i> , <i>b2</i> and <i>b3</i>	268
C.2	Chemical and dynamical radial profiles for models <i>b4</i> , <i>grainchem1</i> and <i>grainchem2</i>	269
C.3	Chemical and dynamical radial profiles for models <i>graindist1</i> , <i>stick1</i> and <i>temp1</i>	270
C.4	Chemical and dynamical radial profiles for models <i>xna1</i> , <i>xs1</i> and <i>zeta1</i> . . .	271
C.5	Chemical and dynamical radial profiles for model <i>zeta2</i> , <i>avcrit1</i> and <i>avcrit2</i> . .	272
D.1	Core temperature and dust continuum radial profiles for models <i>b1</i> , <i>b2</i> and <i>b3</i>	274
D.2	Core temperature and dust continuum radial profiles for models <i>b4</i> , <i>grainchem1</i> and <i>grainchem2</i>	275

D.3	Core temperature and dust continuum radial profiles for models <i>graindist1</i> , <i>graindist2</i> and <i>stick1</i>	276
D.4	Core temperature and dust continuum radial profiles for models <i>stick2</i> , <i>temp1</i> and <i>xna1</i>	277
D.5	Core temperature and dust continuum radial profiles for models <i>xs1</i> , <i>zeta1</i> and <i>zeta2</i>	278
D.6	Core temperature and dust continuum radial profiles for models <i>avcrit1</i> and <i>avcrit2</i>	279

List of Tables

2.1	Temperature T as a function of A_V	91
3.1	Elemental abundances relative to hydrogen	104
3.2	Variations on the standard chemical model	105
3.3	Variations on the standard grain chemistry	107
3.4	Variations on the dust grain sizes and distribution	110
3.5	Physical parameters of the standard model	111
3.6	Variations on the magnetic flux density	111
3.7	Model variations	113
4.1	Comparison between HCO^+ rest frequencies between Evans et al. (2005) and Cazzoli et al. (2012) and the calculated adjusted dip velocities, v_{dip} , taking into account the newer rest frequencies.	124
5.1	Central optical depths	142
5.2	Mean and standard deviation of ion-neutral velocity differences as derived from linewidths of simulated line profiles of NH_3 , HC^{18}O^+ and N_2H^+	150
5.3	Mean and standard deviation of the difference between linewidths of C_3H_2 and N_2H^+	150
5.4	Mean and standard deviation of the difference between linewidths of NH_3 and N_2H^+	150
6.1	Model variations – core dynamics over time.	159
6.2	Collapse time $t_c - t_1$ compared with free-fall time Δt_{ff} ; t_1 is the time at which the central density reaches $n_1(\text{H}) \simeq 3 \times 10^3 \text{ cm}^{-3}$	161

6.3	Collapse time $t_c - t_2$ compared with free-fall time Δt_{ff} ; t_2 is the time at which the central density reaches $n_2(\text{H}) \simeq 5 \times 10^4 \text{ cm}^{-3}$	162
6.4	Collapse time $t_c - t_3$ compared with free-fall time Δt_{ff} ; t_3 is the time at which the central density reaches $n_3(\text{H}) \simeq 2 \times 10^5 \text{ cm}^{-3}$	163
6.5	Model variations – dynamical radial profiles when $n_c(\text{H}) \sim 3 \times 10^6 \text{ cm}^{-3}$	167
6.6	Fits of $n(\text{H}) \propto R^{-\alpha}$ and $B \propto n(\text{H})^\beta$	171
6.7	Model variations – radial variation in the dust-gas ratio, visual extinction and temperature.	172
6.8	Model variations – radial profiles for fractional abundances of CO, HCO^+ and CS.	173
6.9	Model variations – radial profiles for fractional abundances of NH_3 , N_2H^+ and e^-	174
6.10	Model variations – maximum abundances for molecular species.	175
6.11	Model summary – comparing models against observational constraints.	189
7.1	Parameters of the standard model at the end of the model run.	193
7.2	Central temperature T , visual extinction A_V and least-squares fits to the density distribution of the form $n(\text{H}) \propto R^{-\alpha}$ for the inner (α_i), middle (α_m) and outer (α_o) core.	205
7.3	Fits to the intensity profiles of the form $I \propto R^{-m}$ for the inner (m_i), middle (m_m) and outer (m_o) core.	206
7.4	Fits to the constant temperature intensity profiles of the form $I \propto R^{-m}$ for the inner (m_i), middle (m_m) and outer (m_o) core.	207
8.1	Cloud dynamical radial profiles when $n_c(\text{H}) \sim 3 \times 10^6 \text{ cm}^{-3}$	223
8.2	Fits of $n(\text{H}) \propto R^{-\alpha}$ for the inner (α_i), middle (α_m) and outer (α_o) regions of the cloud and core models.	224
8.3	Collapse time compared with free-fall time for a starting central density of $n_1(\text{H}) \sim 3 \times 10^3 \text{ cm}^{-3}$ at time t_1	225
8.4	Collapse time compared with free-fall time for a starting central density of $n_2(\text{H}) \sim 5 \times 10^4 \text{ cm}^{-3}$ at time t_2	225
8.5	Collapse time compared with free-fall time for a starting central density of $n_3(\text{H}) \sim 2 \times 10^5 \text{ cm}^{-3}$ at time t_3	225

8.6	Fits to the intensity profiles of the form $I \propto R^{-m}$ for the inner (m_i) and middle (m_m) regions of the core/cloud.	238
8.7	Model summary – comparing cloud and core models against observational constraints.	241

Chapter 1

Introduction

Somewhere, something incredible is waiting to be known.

Carl Sagan

In this chapter some key terms are defined and some theoretical and observational results are described that are important in understanding the remainder of the thesis. In section 1.1, the term *pre-stellar core* is defined and the relationships between molecular clouds, clumps and pre-stellar cores are described. Section 1.2 gives some background on star formation theory in general and the role that ambipolar diffusion plays in current theories of star formation. Section 1.3 gives an overview of the types of observations that are used to test star formation theories. Section 1.4 outlines the important role that modelling the chemistry in pre-stellar cores has in determining the ionization fraction in the core, which in turn affects the dynamics of the core through ambipolar diffusion. Section 1.5 discusses the purpose and motivation behind the thesis and describes the content of the remaining chapters.

1.1 Molecular clouds, clumps and pre-stellar cores

Star forming regions in our galaxy consist of compact cores of dense molecular gas embedded in clumps of more diffuse gas; such clumps are often termed *core complexes*. A well-studied core complex is Barnard 5 (or B5) which has a cluster of five dense cores

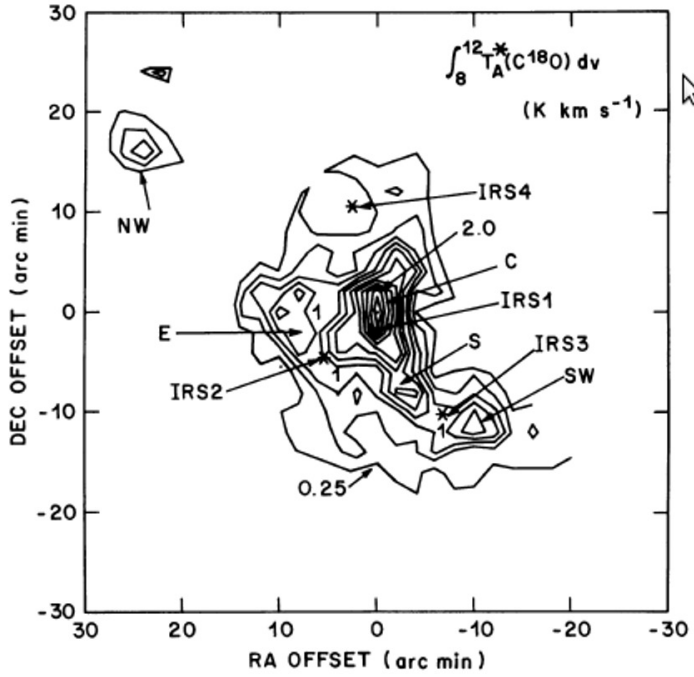


Figure 1.1. [Integrated $C^{18}O$ intensity contour map of the Barnard 5 core complex (image from Goldsmith et al. 1986). Dense cores are indicated by the directional labels C, S, SW, E, NE. Infrared point sources are Labelled IRS1, IRS2, IRS3 and IRS4.

(Goldsmith et al. 1986) and four infrared point sources as determined from an IRAS (Infrared Astronomical Satellite) survey (Beichman et al. 1984).

1.1.1 The classification of dense cores

The infrared point sources are attributed to low-mass nascent stars or *protostars*; a distinction is made between stars and protostars in that protostars derive their luminosity from gravitational collapse while stars derive their luminosity from nuclear fusion. Bipolar outflows of gas originate from at least three of the four IRAS sources; only one of the dense cores has an associated IRAS source co-located at the core centre as determined by the peak molecular line emission of NH_3 . The remainder of the cores without an associated infrared source are termed *starless* (Beichman et al. 1986). The cores have a temperature $T \sim 14$ K, masses ranging from 7 to $54 M_\odot$ and number density of hydrogen molecules ranging from $3 \times 10^3 \text{ cm}^{-3} \lesssim n(H_2) \lesssim 7 \times 10^3 \text{ cm}^{-3}$; the inter-core medium has a number density of hydrogen molecules, $n(H_2) \sim 10^3 \text{ cm}^{-3}$. An extensive study of dense cores by Myers & Benson (1983) associated starless cores with narrow emission lines of

NH₃, indicating that emission is dominated by either thermal with subsonic microturbulent motions or thermal with collapse motions. A further classification of starless cores by Ward-Thompson et al. (1994) separated those cores that were dynamically stable and those cores on the verge of forming a protostar: a *pre-protostellar* core – a term which is shortened to *pre-stellar* in much of the literature. Protostellar cores are also classified by the shape of their spectral energy distribution (SED): a log-log plot of λF_λ against λ where F_λ is the flux at wavelength λ . Adams et al. (1987) used the spectral index, $m = \frac{d(\log \lambda F_\lambda)}{d(\log \lambda)}$, between $\lambda = 2 - 10 \mu\text{m}$ to define three classes of protostellar core (Figure 1.2). Class I has $m \geq 0$ with an energy distribution that is broader than that of a blackbody. These cores are deeply embedded in circumstellar dust and often undergoing molecular outflows. The emission from Class I cores are dominated by accretion from the dust envelope. Class II has $-1.5 \leq m < 0$ and is identified with classical T-Tauri stars – protostars where emission can be modelled by a single temperature black-body plus excess infrared emission from a dust disk; Class III has $m < -1.5$ and is identified with weak-line T-Tauri stars – protostars surrounded by a disk that is weak or no longer in existence. The emission from Class III sources are well fitted to a blackbody spectrum, implying that the energy emitted mainly comes from the central protostar. Classes I to III represent an evolutionary sequence of a protostellar low-mass core with class I the youngest and class III the oldest.

An earlier evolutionary class, Class 0, was added later (Andre et al. 1993) for protostellar cores with emission peaking at longer wavelengths: these cores represent an initial infall stage where the mass contained in the embedded source is less than the mass contained in the collapsing envelope. Class 0 cores are colder ($T < 30 \text{ K}$) than Class I cores, are reasonably isothermal (unlike a Class I core the SED can be modelled by a single-temperature grey-body) and are capable of driving highly collimated and energetic bipolar molecular outflows which usually implies some form of dynamical activity. These objects have been the subject of extensive research in order to unambiguously detect infall in the earliest stages of low-mass star formation. While core SEDs are useful in identifying collapse candidates and validating a particular collapse scenario, the only way to reliably detect infall in these objects is by observation and modelling of molecular line profiles (Rawlings 1996b). Given the ubiquity of molecular outflows in Class 0 cores, it would seem difficult observationally to identify infall using molecular line profiles. However, current theories suggest that during this stage of star formation, infall is directed onto an accretion disk

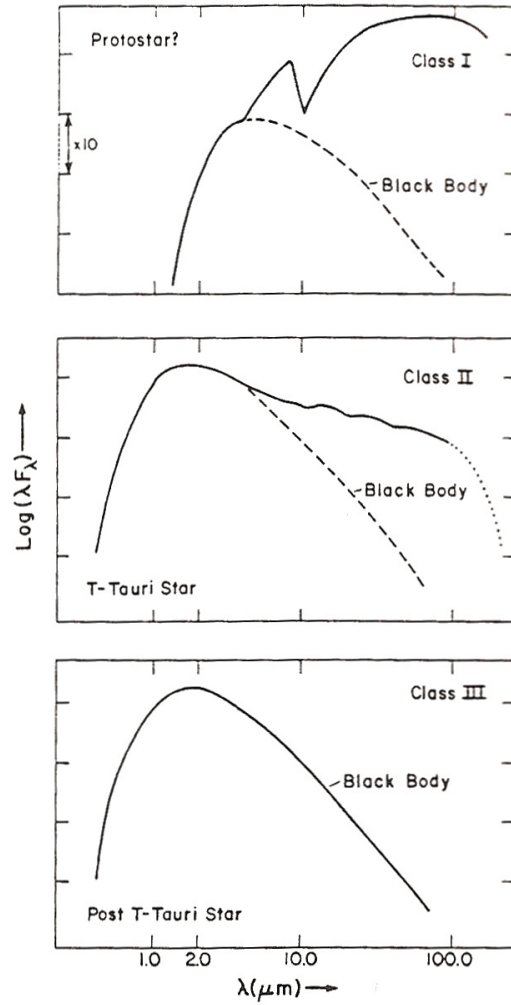


Figure 1.2. Classification of protostellar cores by their spectral energy distributions (image from André 1994).

while outflow is directed along the axis of rotation (Zhou et al. 1993).

1.1.2 B335 – an isolated Class 0 protostellar core

While bipolar outflows dominate the spectral emission of many Class 0 cores, B335, an isolated Class 0 core, has been shown to have a highly collimated outflow roughly in the plane of the sky (Cabrit et al. 1988) allowing the spectral emission from the region potentially associated with infall to be distinguished from the emission associated with outflow. With the realisation that the dynamics in B335 can be separated in this way, the core has been the subject of extensive line surveys to investigate the dynamics in the core (Zhou et al. 1993; Saito et al. 1999; Evans et al. 2005) and extended envelope (Saito

et al. 1999). The core is generally recognised as an excellent test case for theories of low-mass star formation. Zhou et al. (1993) argue the case for infall in this core by modelling the spectra from CS and H₂CO rotational transition lines using a dynamical inside-out collapse model proposed by Shu (1977) (see section 1.2 for a detailed description of this model) with the simplifying assumption that molecular abundances are independent of position within the core. The spectral signature for optically thick lines in a cold dense core undergoing spherical collapse is that of an asymmetric double-peaked line profile: the blueshifted emission peak dominates over the redshifted emission peak (see section 1.3 for an explanation of why this spectral signature coupled with a single-peaked optically thin line indicates infall). Their model gives an excellent fit to the observed emission profiles. Furthermore, they argue that the asymmetric line profiles cannot have arisen from other scenarios such as expansion, turbulence, rotation or a static model with foreground absorption. Despite the compelling evidence for infall in the core, Rawlings (1996*b*) cautions the reader from using these results as proof of the inside-out infall model: since the radiative transfer calculations assume the validity of the collapse model from the outset, at most the conclusion to be drawn is that these line profiles are consistent with inside-out collapse. Additionally, the chemical abundances are expected to have significant radial dependence in a dynamically evolving core due to both gas-phase reactions and freeze-out of gas-phase species onto the surfaces of grains. Subsequent line profile modelling using radially varying molecular abundances (Evans et al. 2005) had similar success when matching with the observed line profiles. However, the authors highlighted a number of problems as a result of assuming inside-out infall. Firstly and with particular relevance to the contents of this thesis, the asymmetric double-peaked spectra from optically thick lines tended to have *dip* velocities, v_{dip} , redshifted from the core local standard of rest velocity, v_{LSR} . This trend was clearest in the HCO⁺ transition lines with v_{dip} increasing from 0.05 km s⁻¹ for HCO⁺ (1-0) to 0.25 km s⁻¹ for HCO⁺ (4-3). The interpretation of this feature is that absorption in a region of infalling gas is responsible for the shift from v_{LSR} . Furthermore, this feature could not be reproduced by the Shu dynamical model which requires the gas to be static in the outer core. Secondly, an independent study of the dust continuum emission from B335 (Shirley et al. 2002) gave estimates for the *infall radius* that were inconsistent with the best-fit Shu model. In a Shu inside-out model, collapse initiates at the centre of the core; the pressure loss at the centre triggers a collapse expansion wave, CEW, travelling from the core centre to the core boundary at the local sound speed. The infall radius is

defined as the radial distance at the position of the head of the CEW. Shirley et al. (2002) found the infall radius to be much smaller than the best-fit Shu model used to calculate the line profiles. It should be noted however, that inclusion of a disk when modelling the dust continuum emission gives consistent estimates of the infall radius (Harvey et al. 2003) but is inconsistent with the radial variation in gas density predicted by the Shu model. Other problems exist with the assumption of a purely spherical model: the dynamical age of the bipolar outflow indicates that it must have been triggered at about the same time as the onset of inside-out infall (Rawlings 1996a). Consequently, any spherically symmetric model cannot possibly describe both the infall onto an accretion disk and outflow along an axis perpendicular to the accretion disk.

1.1.3 Pre-stellar cores

Pre-stellar cores are at an evolutionary stage prior to Class 0 cores. Due to the uncertainties in observational data, it is sometimes difficult to distinguish those cores that are pre-stellar (gravitationally bound) from those that are gravitationally unbound. Enoch et al. (2008) measured the total flux at $\lambda = 1.1$ mm for each of the starless cores in the Perseus molecular cloud in order to derive estimates for the core mass, M_{core} . Core temperatures and velocity dispersion data, derived from $\text{NH}_3(1,1)$ and $\text{NH}_3(2,2)$ inversion lines, were taken from Rosolowsky et al. (2008) and used to derive the virial mass, M_{vir} , for each core having well-defined NH_3 linewidths. Of the 38 starless cores in Perseus for which estimates for both M_{core} and M_{vir} were available, 32 cores were found to be gravitationally bound, having $M_{core} > 0.5M_{vir}$. The authors acknowledged that uncertainties in the estimates of the dust opacity at $\lambda = 1.1$ mm could result in all starless cores being classified as pre-stellar. Perhaps more convincingly, the same analysis on protostellar cores in Perseus resulted in a similar ratio of gravitationally bound to unbound cores, suggesting that all the starless cores will eventually form stars and are thus pre-stellar.

1.1.4 General properties of starless cores

A survey of starless cores by Benson & Myers (1989) gives a mean hydrogen nuclei number density, $n(\text{H}) \sim 3 \times 10^4 \text{ cm}^{-3}$, a mean size $r \sim 0.12 \text{ pc}$ and a mean gas kinetic temperature, $T_k \sim 11 \text{ K}$. Unlike protostellar cores, there is no internal source of radiation from an embedded protostellar source; the dominant source of heating is provided by the external interstellar radiation field (Evans et al. 2001; Launhardt et al. 2013). Observations and

modelling of the dust continuum radiation from several pre-stellar cores indicates that the dust temperature varies from $T_{\text{centre}} \sim 7$ K at the core centre to $T_{\text{edge}} \sim 13$ K at the core edge (Evans et al. 2001). More recent observations from the Herschel Space Observatory indicate slightly higher dust temperatures with $T_{\text{centre}} \sim 8 - 12$ K and $T_{\text{edge}} \sim 14 - 18$ K (Launhardt et al. 2013). The narrow NH_3 linewidths of dense cores observed by Myers & Benson (1983), indicated that these cores were either in the early stages of collapse or they were in a state of *near-critical dynamical equilibrium*: the force of gravity being balanced by a combination of thermal pressure and subsonic turbulence or thermal pressure alone.

1.1.5 Barnard 68 – a gravitationally stable pre-stellar core

The Bok globule, Barnard 68 (B68), is thought to be an example of a starless core in near-critical dynamical equilibrium. Bok globules (Bok & Reilly 1947) like B68 are nearby (~ 150 pc), isolated and are generally spherical, each harbouring a few cores (Goldsmith et al. 1986; Stutz et al. 2010). Those globules showing no signs of star formation activity are ideally suited to studying the initial conditions prior to the onset of collapse and the process of low-mass star formation. Alves et al. (2001*b*) observed the near-infrared extinction of B68 to derive a density distribution that was consistent with a marginally unstable Bonnor-Ebert sphere (Bonnor 1956; Ebert 1955), indicating (with the assumption that the gas kinetic temperature is isothermal) that the core is in hydrostatic equilibrium with a gas temperature of $T_k = 16$ K determined from the best fit to a Bonnor-Ebert sphere. Using observations of the inversion lines of NH_3 , Hotzel et al. (2002) determined the gas kinetic temperature in B68 to be $T_k = 10 \pm 1.2$ K and the NH_3 linewidths to be very close to that expected for a thermally supported core, again implying the core is close to being in hydrostatic equilibrium. While NH_3 has been found to be a good tracer of gas in the inner region of a starless core, CO is a better tracer of gas in the outer core (Tafalla et al. 2002; Bergin et al. 2006). Tafalla et al. (2002) mapped the 1.2 mm dust continuum emission and the integrated emission from lines of NH_3 (1,1) and (2,2), C^{18}O (1-0), C^{18}O (1-0), CS (2-1) and N_2H^+ (1-0) for a sample of five nearly spherical, starless cores. The NH_3 and N_2H^+ emission maps are shown to be reasonably consistent with the 1.2 dust continuum emission peak, indicating that both molecules are good tracers of dense gas in the inner core. However, the emission maps of C^{18}O and CS are shown to have minima at the dust emission peak, indicating strong depletion of these gas-phase molecular species in the inner core. The suggested reason for the depletion of CS and CO is the selective

freeze-out of these molecules onto dust grains at densities above $n(\text{H}) \sim 2 - 6 \times 10^4 \text{ cm}^{-3}$. Bergin et al. (2006) observed multiple transition lines of C^{18}O and ^{13}CO in conjunction with a chemical and radiative transfer model to derive the radial variation for the gas temperature in B68. The CO emission lines were also found to be weak in the inner core, consistent with the conclusions of Tafalla et al. (2002), that CO is depleted at the core centre. A derived gas kinetic temperature of $T_k \sim 7 - 8 \text{ K}$ was found to be lower than the dust temperature, $T_{\text{outer}} \sim 14 \text{ K}$, in the outer core. This is explained due to the abundant CO in the outer core acting to cool the gas, however the gas density is too low for gas-grain collisions to tightly couple the dust and gas temperatures. In the inner core, the gas temperature should be close to the assumed dust temperature, $T_{\text{inner}} \sim 8 \text{ K}$, since the increased collision rate between gas and dust in the dense inner core should be sufficient to provide tight coupling between the gas and dust temperatures. Assuming the accuracy of the measurements of the gas temperature based on the NH_3 inversion lines are better than 2 K, a temperature of $T_{\text{NH}_3} = 10 \text{ K}$ in the inner core, requires the dust-gas coupling factor in the model to be reduced by a factor of 10. The reduction in the dust-gas coupling factor is consistent with the idea that small grains coagulate into larger grains, therefore offering less surface area when colliding with gas particles.

The dynamical properties of B68 have been studied by analysing observations of molecular line profiles over the entire core. Although the core is close to being in thermal equilibrium, Lada et al. (2003) found alternating blueshifted and redshifted CS line profiles across the core while Redman et al. (2006) found a similar pattern for HCO^+ : these observations are interpreted as small-amplitude oscillations of a thermally supported, gravitationally stable core. A further conclusion drawn is that cores like B68 can survive over several sound-crossing times under the turbulent conditions of the interstellar medium (ISM). Turbulence in the ISM can disrupt and dissipate cores if the size of the turbulent eddies are comparable to the radius of the core (Davidson 2004): eddies with size much larger than the core radius may alter the mean position of the core but will not lead to core disruption ; eddies much smaller than the core radius will tend to cause *ripples* at the core edge. The longevity of B68 suggests that in this region of the ISM, insufficient energy exists in eddies having sizes capable of core disruption. Myers (1983) speculate on the reasons why the non-thermal component of NH_3 linewidths are frequently subsonic in dense cores, which may also have relevance to the survivability of dense cores in the ISM. In regions of active star formation such as Taurus, cores tend to be denser and have

narrower linewidths, with the implication that dense cores evolve into low-mass stars by dissipation of turbulence. An isolated dense core such as B68, may be cut off from the re-supply of turbulent eddies at the largest scale; since turbulent energy is transferred from large to small scales through turbulent cascade, eddies having sizes comparable to the core radius (the critical disruption size) will dissipate their energy in approximately a freefall time. Furthermore, cores having a high density contrast with the surrounding gas may decouple from the cascade process: disrupting eddies will have lower densities compared to the core and therefore coupling between the eddy and the densest region of the core will be relatively inefficient. The removal of turbulent support from a core allows a core to contract and become denser which in turn enhances the survivability of the core against turbulent dissipation.

1.1.6 Lynds 1544 – a pre-stellar core undergoing collapse?

Lynds 1544 (L1544) is a starless, dense core embedded in a dark cloud of the same name within the Taurus molecular cloud. Tafalla et al. (1998) demonstrated how this core has quite different dynamical properties from those of a gravitationally stable core such as B68. Tafalla et al. (1998) used a multiline study over the L1544 core, including both optically thin and thick lines of CO, CS and their isotopes to investigate the dynamical structure. It was found that the deep absorption lines of CS (2-1) and the asymmetry of the emission peaks could be modelled by assuming that the background emitting gas had a two-component constant velocity field directed towards the absorbing, constant velocity foreground gas. The velocity difference between the background and foreground gas was found to be around $v_{inner} \sim 0.01 \text{ kms}^{-1}$ in the inner region of the core and $v_{outer} \sim 0.1 \text{ kms}^{-1}$ in the outer region of the core. The high central density of the core coupled with the deep asymmetric line profiles are exactly the features present in collapsing protostellar cores, suggesting that L1544 is undergoing gravitational collapse. The intensity of the optically thin transitions, C³⁴S (2-1) and C¹⁸O (1-0), taken at the core centre and at several telescope positions offset by 50 arcsec from the core centre, were used to derive a power-law relationship between the density, $n(\text{H})$, and radial distance, R , of the form $n(\text{H}) \propto R^{-1.5}$. While this relationship is consistent with the expected fall-off in density within the infall radius of the Shu inside-out collapse model, an inconsistency exists which seems difficult to reconcile with the use of the Shu model for this particular core: the estimated time it takes for the CEW to reach 0.05 - 0.1 pc (the estimated radial

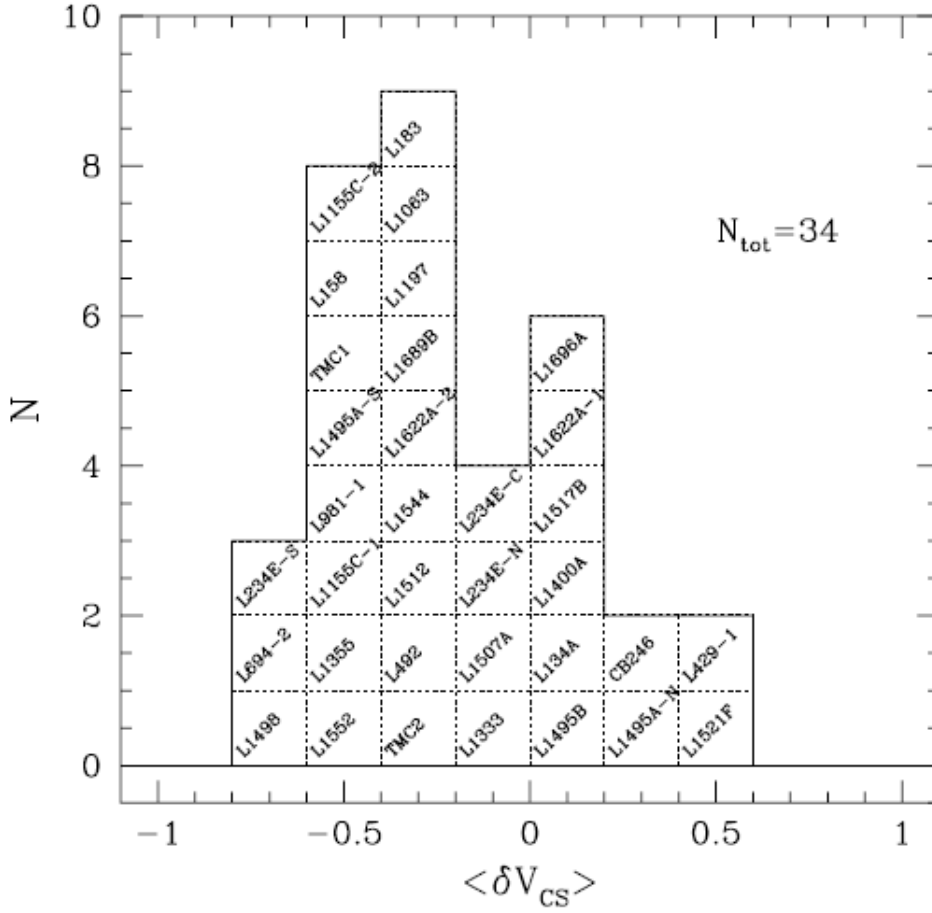


Figure 1.3. Number distribution of $\langle \delta V_{CS} \rangle$, the mean normalised velocity difference between lines of CS (2-1) and N_2H^+ (1-0) in a sample of starless cores (image from Lee et al. 2001).

position of the maximum contrast in CS (2-1) peak temperatures) and achieve an infall speed of $v_{infall} \sim 0.1 \text{ km s}^{-1}$ is between 0.3 and 0.5 Myr; in this time, a point source with luminosity $L \sim 7 - 14 L_{\odot}$ should be easily detectable by IRAS. In other words, if the Shu model is correct, L1544 should be a protostellar core. Other collapse models were also considered, including an ambipolar diffusion driven collapse model proposed by Ciolek & Mouschovias (1994). This model assumes that the initial stages of collapse are controlled by ambipolar diffusion, that is the process whereby magnetic flux is gradually removed from the inner core due to neutral particles collapsing quasi-statically inward through the charged particles. The timescale for ambipolar diffusion in a dense core (and therefore collapse in general) is much longer compared to the timescale for collapse in a Shu model – the ambipolar diffusion timescale is proportional to the ionization fraction according

to equation 1.7. However, this model was also found to be inconsistent with the L1544 observations since the maximum infall speed $v_{infall} \sim 0.1 \text{ kms}^{-1}$ was found to be a factor of 5 higher than the infall speed predicted by the ambipolar diffusion model.

1.1.7 Are there other pre-stellar cores like Lynds 1544?

The discovery of the extended velocity field in L1544 was followed up by an extensive line mapping survey in order to determine whether similar features could also be found in other starless cores (Lee et al. 2001). Spectral emission lines of CS (2-1), N_2H^+ (1-0) and C^{18}O (1-0) were mapped for 53 dense starless cores. A sensitive measure of the line shifts that are indicative of a collapsing core is to use the normalised velocity difference between an optically thick line such as CS (2-1) and an optically thin line such as N_2H^+ (1-0), $\delta V_{\text{CS}} = (V_{\text{CS}} - V_{\text{N}_2\text{H}^+})/V_{\text{N}_2\text{H}^+}$. Here, V_{CS} is the velocity at the maximum intensity of the CS emission line, as determined from a Gaussian fit to either the single-peaked CS line profile or the dominant peak in the case of a double-peaked CS line profile; $V_{\text{N}_2\text{H}^+}$ is the velocity at the maximum intensity of the N_2H^+ line, as determined from a Gaussian fit of the hyperfine components of the line. Observations of CS and N_2H^+ were taken at many positions over the cores with a telescope beam size of approximately 52 arcsec for both CS (2-1) and N_2H^+ (1-0) line frequencies. Only those observations of CS (2-1) and N_2H^+ (1-0) for which the signal to noise ratio was better than 5, were taken forward and used in the calculation of δV_{CS} . Figure 1.3 shows a histogram of the number distribution of the mean δV_{CS} for each core, $\langle \delta V_{\text{CS}} \rangle$. The histogram shows a dominant peak in negative values of $\langle \delta V_{\text{CS}} \rangle$, indicating that blueshifted CS spectra dominate in this sample of cores. The authors point out however, that this result should not be taken as an indication that most starless cores are collapsing, since the initial choice of cores is biased towards those which were thought to be possible collapse candidates. However, of particular relevance to the contents of this thesis, is the significant proportion (about a third) of the cores that show overall dominant redshifted spectra, indicating expansion in at least some of the cores.

Within the 34 cores for which the analysis of δV_{CS} was possible, two sub-populations of cores were defined as *strong infall candidates* and *probable infall candidates*: the former sub-population having very significant blue excess and double-peaked CS (1-0) line profiles; the latter sub-population having very significant blue excess but single-peaked CS (1-0) line profiles. For each core in these groups, the infall radius was determined by measuring the

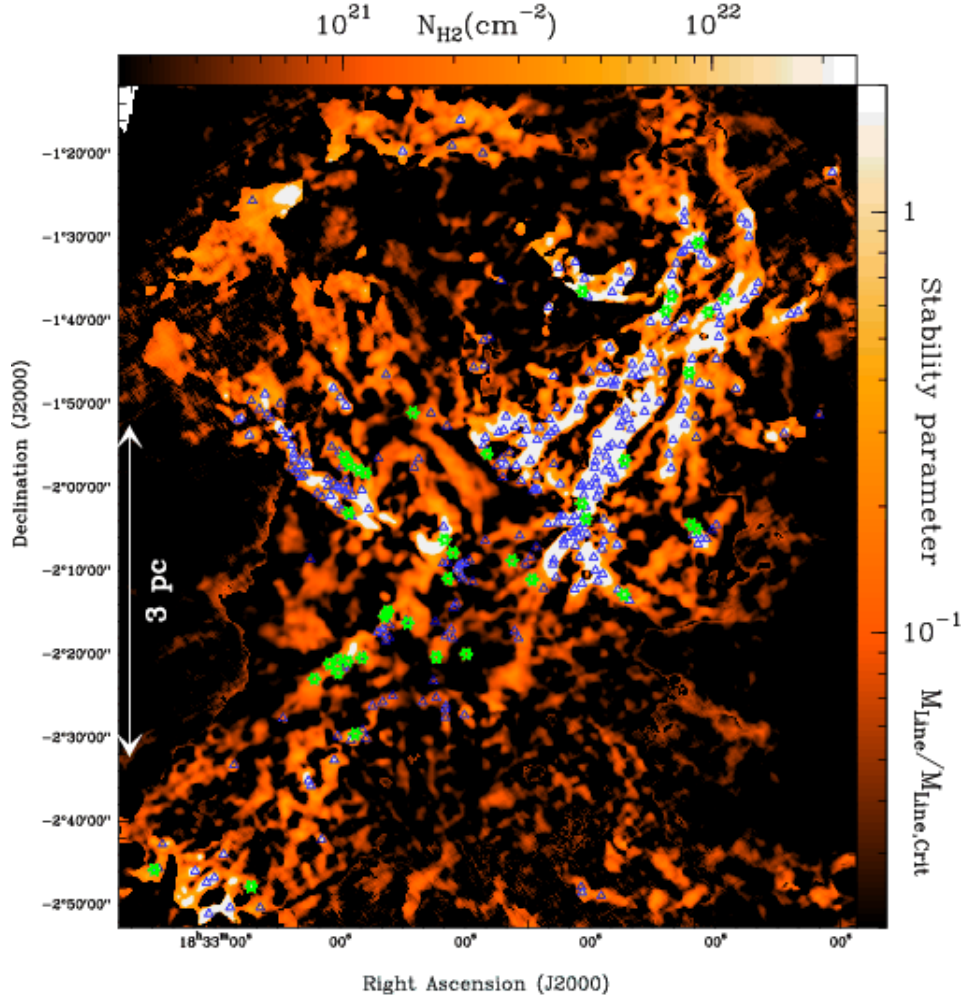


Figure 1.4. Column density map and stability map from Herschel observations in the Aquila cloud complex (image from André et al. 2010). The blue triangles mark the positions of the pre-stellar cores while the green stars mark the positions of the Class 0 protostars.

spatial separation in points where the CS line profiles are significantly skewed to the blue: for all line profiles for which $\delta V_{\text{CS}} > 5\sigma_{\delta V_{\text{CS}}}$ ($\sigma_{\delta V_{\text{CS}}}$ is the standard deviation of the error in the calculation of δV_{CS}), the infall radius was taken as half the maximum distance between any two such points within the core. The infall radius was found to be about 0.06-0.10 pc using this method. An estimate of the infall velocity was derived using a simple two-layer model of background gas moving towards the telescope and foreground gas moving away from the telescope. A best-fit radiative transfer model was found for the averaged CS (1-0) spectra for each of the strong and probable infall candidates. It was found that most of the cores had velocities in the range $0.05 - 0.09 \text{ km s}^{-1}$, although this value is half the one

dimensional velocity difference between the foreground and background gas layers which could be lower than the actual three dimensional infall velocity by a factor of 1-2. Both the infall radii and infall velocities are similar to those found for L1544, the inference being that L1544 is not unusual in showing strong signs of infall over an extended region of the core. In common with L1544, these results also appear to be wholly inconsistent with the Shu inside-out collapse model. Infall velocities are also inconsistent with the quasi-static ambipolar diffusion model proposed by Ciolek & Mouschovias (1994). However, a later model (Ciolek & Basu 2000) specifically targeted the observational results for L1544 (Tafalla et al. 1998; Williams et al. 1999) and found that if the background magnetic field is reduced and the core is considered to be in a later stage of collapse, then the velocity distribution predicted by the model is consistent with observations.

1.1.8 Giant molecular clouds and filamentary structure

Core complexes can themselves be clustered into giant molecular clouds (GMCs) with masses in excess of $10^4 M_\odot$ and a mean density of hydrogen nuclei, $n(\text{H}) \sim 80 \text{ cm}^{-3}$ (McKee & Ostriker 2007). Recent observations by the Herschel Space Observatory reveal in detail the connection between pre-stellar cores, protostars and the filamentary structures within molecular cloud complexes (André et al. 2010). As part of Herschel's Gould Belt Survey, observations of the Aquila cloud complex using SPIRE at 250-500 μm and PACS at 70-160 μm show a network of filaments with widths of about 0.05 pc and lengths of 2 pc or less (Men'shchikov et al. 2010). A total of 541 starless cores were identified in this region; all cores appear to be situated along the filaments. In the absence of spectral linewidths with which to calculate a virial mass, cores were determined as gravitationally bound by comparing the core mass, as estimated by fitting grey-body SEDs to the Herschel data, with a local critical Bonnor-Ebert mass calculated from the Herschel column density maps of the gas external to the core. Most of the cores ($\sim 60\%$) are found to be gravitationally bound and thus pre-stellar. In contrast to the Aquila field, observations and analysis of the Polaris cloud reveal 302 starless cores, most of which are gravitationally unbound. The column density of the Polaris cloud, $n(\text{H}_2) \sim 10^{21} \text{ cm}^{-2}$, is less than for the Aquila cloud, $n(\text{H}_2) \gtrsim 10^{22} \text{ cm}^{-2}$, and while the Aquila cloud harbours between 45 and 60 Class 0 protostars, no protostars are found in the Polaris cloud. Filaments are unstable to axisymmetric perturbations if their line mass, M_{line} , is greater than the critical unmagnetised line mass, $M_{\text{line,crit}}^{\text{unmag}}$, where $M_{\text{line,crit}}^{\text{unmag}} = 2C_s^2/G$, C_s is the sound speed and G is the gravitational

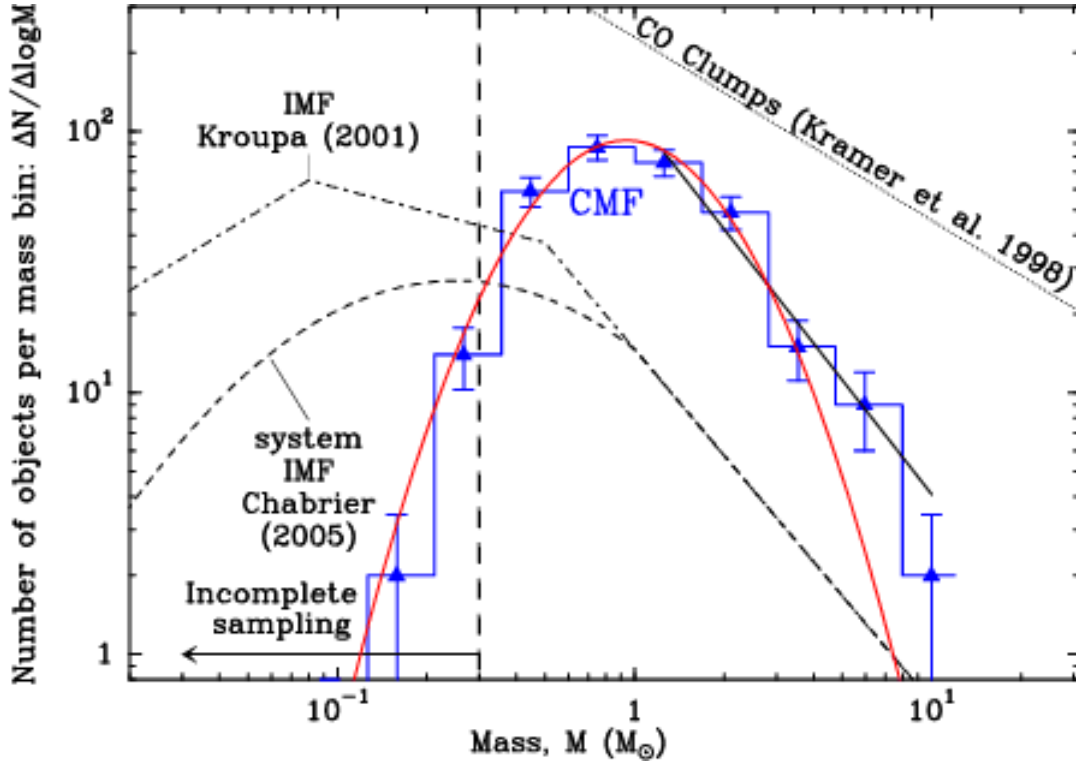


Figure 1.5. Differential mass function ($dN/d\log M$) of the pre-stellar core population in the main sub-field of Aquila. The best-fit power law to the high-mass end of the CMF gives $\xi_{core}(m_{core}) \propto m_{core}^{-2.45}$. This compares to high-mass end of the stellar IMF of the form $\xi(m) \propto m^{-2.3}$ (Kroupa 2001). Image taken from Könyves et al. (2010).

constant (Inutsuka & Miyama 1997). André et al. (2010) determined the gravitational stability of the filaments by multiplying the filament width by the column density of the filament. Figure 1.4 shows the stability of the filaments in units of the critical unmagnetised line mass for a gas temperature of 10 K, $M_{line,crit}^{unmag} \simeq 15 M_{\odot}/\text{pc}$. The positions of the Class 0 protostars and pre-stellar cores are mapped on top of the filaments. Nearly all of the pre-stellar cores are situated along the most gravitationally unstable filaments. The picture emerging from these observations is that of filament formation followed by fragmentation of the densest filaments to form pre-stellar cores.

1.1.9 The core mass function

The large population of pre-stellar cores found by Herschel in the Aquila rift cloud complex (the main sub-field in the Aquila cloud), allowed Könyves et al. (2010) to derive the pre-stellar *core mass function* (CMF) with better precision than previous surveys using

ground-based telescopes. The core mass function is a measure of the mass distribution of cores within a cloud complex. As found in previous studies of the pre-stellar CMF (Enoch et al. 2008), the shape of pre-stellar CMF matches closely that for the stellar *initial mass function* (IMF). The stellar IMF is a measure of the mass distribution of stars that form in one star-formation event (Kroupa 2002). For stars having mass $m \geq M_\odot$, Kroupa (2001) derived an average or Galactic-field, single-star IMF of the form $\xi(m) \propto m^{-2.3 \pm 0.7}$ where $\xi(m)dm$ is the number of stars with masses in the interval m to $m + dm$. This compares to the Aquila rift pre-stellar CMF of the form $\xi_{core}(m_{core}) \propto m_{core}^{-2.45 \pm 0.2}$ for cores with mass $m_{core} \geq 2M_\odot$. The similarity in shape between the pre-stellar CMF and the IMF (Figure 1.5) suggests a one-to-one correspondence between m_{core} and m_{star} of the form $m_{star} = \epsilon m_{core}$ with the implication that $\epsilon \sim 0.2 - 0.4$ is the star-forming efficiency in Aquila (André et al. 2010).

1.2 Star formation theories and the role of ambipolar diffusion

1.2.1 High-mass and low-mass stars

Star formation theories for low-mass and high-mass stars are generally treated separately; the dividing line between low-mass and high-mass stars is taken somewhat arbitrarily to be $8M_\odot$. Protostars forming stars with masses much below $8M_\odot$ have luminosities that are dominated by accretion of gas onto a hydrostatic core. These low-mass protostars are formed from cores with masses in the order of $M_{core} \simeq M_\lambda$ where $M_\lambda = (4\pi/3)(\lambda_J/2)^3\rho_0$ is the thermal Jeans mass, $\lambda_J = \pi C_s/(G\rho_0)^{0.5}$ is the thermal Jeans length, ρ_0 is the initial gas density and C_s is the sound speed in the gas (McKee & Ostriker 2007). Protostars forming stars with masses above $8M_\odot$ have luminosities dominated by nuclear fusion. Where molecular cores give birth to high-mass protostars, their core mass is much greater than M_λ . It is low-mass star formation to which this thesis is directed.

1.2.2 The Larson-Penston flow

Early theoretical studies of cold, dense, isothermal cores undergoing gravitational collapse indicated that the gas density, ρ , varies with radial distance R as approximately $\rho \propto R^{-2}$ (Larson 1969). Prior to the formation of the protostar, there is a central, thermally

supported region of size $R_0 \simeq \lambda_J$; the R^{-2} density gradient is created as the pressure wave triggered by collapse propagates inward, triggering collapse on smaller scales (Larson 2003). Larson (1969) provided a numerical solution following the collapse from an initially uniform density, starless core through to the formation of a star. The collapse can be divided into three phases. The first phase is that of *isothermal collapse*; as the core collapses to form the R^{-2} density profile, the compressional heating of the gas is balanced by radiative cooling by dust grains such that the gas temperature can be considered approximately constant at 10 K. A second, *adiabatic collapse* phase is identified when the gas at the core centre becomes radiatively optically thick, at a gas density of about $\rho \sim 10^{-13} \text{ g cm}^{-3}$. A rapid increase in temperature in the core centre gives rise to a pressure gradient that is strong enough to decelerate the infalling material close to the core centre. At a temperature of about $T = 200 \text{ K}$ a first, small core forms in hydrostatic equilibrium which is accompanied by a shock at its outer edge. The central hydrostatic core continues to gain mass from infalling material while at the same time increasing in temperature due to compressional heating. When the gas temperature in the core reaches $T = 2000 \text{ K}$, dissociation of H_2 cools the gas and a second collapse phase begins in a small amount of material at the core centre. When the gas temperature reaches $T = 20,000 \text{ K}$ and a gas density of $\rho \sim 10^{-2} \text{ g cm}^{-3}$, dissociation of H_2 is complete and a second, inner hydrostatic core is established, accompanied by a second shock front at the edge of the inner hydrostatic core. The third phase involves the *accretion* of the remaining gas onto the second stellar core. During the isothermal collapse phase, it was noticed that the radial change in density and velocity in the inner part of the core tended towards a constant limiting distribution. Subsequent mathematical analysis showed that an *asymptotic* similarity solution existed such that the density, $\rho(t)$, velocity, $v(t)$ and mass distribution, $m(t)$, at time t could be expressed in terms of dimensionless scale factors $a(t)$, $b(t)$, $c(t)$ and $d(t)$: $v(t) = b(t)v_1(s)$, $\rho(t) = c(t)\rho_1(s)$ and $m(t) = d(t)m_1(s)$ where $s = R/a(t)$ and $v_1(R)$, $\rho_1(R)$ and $m_1(R)$ are the radial distributions in velocity, density and mass respectively at time t_1 ; the dimensionless scale factors are all unity at time t_1 . In the limiting case when a dimensionless radial parameter, x , is much larger than unity, the infall velocity tends towards a constant velocity of $3.28C_s$ and the density distribution tends towards:

$$\rho(R) = \frac{4.43C_s^2}{2\pi GR^2} \quad (1.1)$$

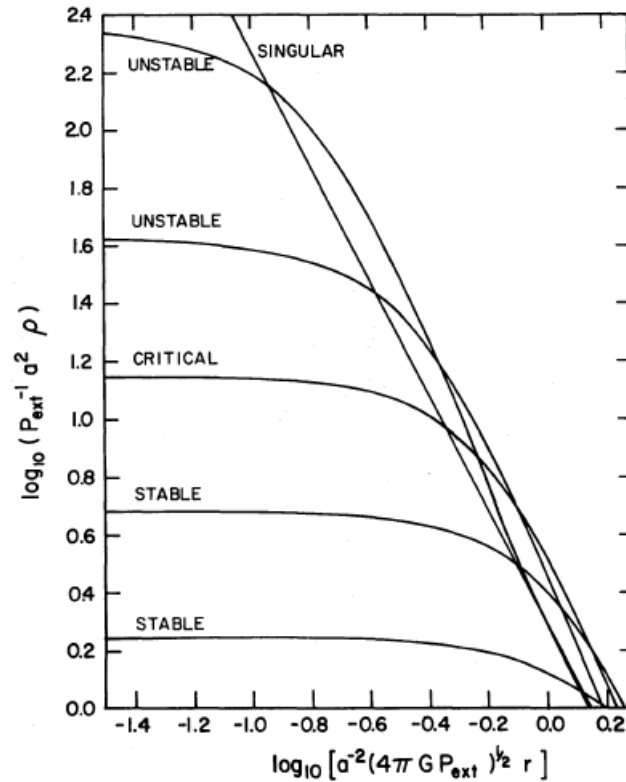


Figure 1.6. Examples of stable and unstable Bonnor-Ebert (BE) spheres. Unstable BE spheres have a central density to boundary density contrast in excess of 14.3 ($= 10^{1.16}$). In the limit of infinite central density, the unstable Bonnor-Ebert sphere takes the form of the singular isothermal sphere, $\rho(R) = C_s^2/(2\pi GR^2)$. Image taken from Shu (1977).

where $x = (s/\tau C_s)$ and $\tau = -(da/dt)^{-1}$ is a positive constant. In the limiting case when $x \ll 1$, corresponding to radial positions close to the core centre, the infall velocity tends towards a linear function of x while the density tends towards a constant value (independent of x but still changing over time). The same self-similar solution was also found by Penston (1969) and is often termed the *Larson-Penston* (LP) model or flow.

1.2.3 The Shu inside-out collapse model

Shu (1977), hereafter Shu, argued that only special initial and boundary conditions could give rise to the LP flow: that supersonic gas inflow at large radii, of nearly 3.3 times the sound speed, is brought to rest at the core centre without a shock requires a highly artificial arrangement of self-gravity and pressure gradient. Shu investigated alternative, analytic, self-similar collapse solutions using as starting conditions, cores with an initial

density profile of the form $\rho \propto R^{-2}$. For isothermal cores of mass M , bounded by a constant external pressure P_{ext} , hydrostatic equilibrium is possible if $M \leq M_{crit}$ where M_{crit} is the critical Bonnor-Ebert mass (Bonnor 1956; Ebert 1955):

$$M_{crit} = 1.18 \frac{C_s^4}{G^{3/2}} P_{ext}^{-1/2} \quad (1.2)$$

Furthermore, for those cores with $M \leq M_{crit}$, stable hydrostatic equilibrium is only possible when the central to boundary density contrast does not exceed 14.3 (Figure 1.6). In the limit of infinite central density, the unstable Bonnor-Ebert sphere takes the form of the hydrostatic, singular isothermal sphere (SIS), $\rho(R) = C_s^2/(2\pi GR^2)$. When unstable hydrostatic cores are subject to a small perturbation, the density contrast between centre and boundary increases and approaches ever closer the density profile of a SIS. In the case when $M > M_{crit}$, as long as the sound speed is short in comparison to the gravitational collapse time in the envelope, the density profile also approaches a $\rho \propto R^{-2}$ distribution. Using the similarity variable, $x = R/(C_s t)$, self-similar solutions of the form: $\rho(R, t) = \alpha(x)/(4\pi G t^2)$, $M(R, t) = C_s^3 t m(x)/G$ and $V(R, t) = C_s v(x)$ are found. The functions $\alpha(x)$, $m(x)$ and $v(x)$ are found from the solutions to a pair of ordinary differential equations that are identical (apart from notational and sign conventions) to those used to derive the LP flow. Solutions are divided into two main categories: plus (+) solutions are those solutions having a positive derivative in the infall velocity, $d(-v)/dx > 0$ at large radii; minus (-) solutions are those solutions having a negative $d(-v)/dx$. However, a special static case is identified having the following properties: $v = 0$, $\alpha = 2/x^2$ and $m = 2x$; this case is identical to the hydrostatic SIS. In addition, a singular solution of the form $x - v = 1$ and $\alpha = 2/x$ is identified. However, this solution does not allow the original fluid equations to be solved. The interpretation of this singular solution is that of *critical points* on the locus, $x - v = 1$, through which solutions can only pass smoothly if the condition $\alpha = 2/x$ is satisfied. For minus solutions without critical points, assuming that gas velocities are negligible at $t = 0$, the following asymptotic behaviour is found: $\alpha \sim A/x^2$, $v \sim -(A - 2)/x$ and $m \sim Ax$ where A is a constant with a value greater than 2 in order for the infall velocity gradient to be negative. This requires an initial density

distribution of the form:

$$\rho(R, 0) = \frac{AC_s^2}{4\pi GR^2} \quad (1.3)$$

– the density distribution for a SIS, and since $A > 2$, the density distribution has a mass in excess of a SIS in hydrostatic equilibrium. Shu associates these solutions with the collapse of cores for which $M > M_{crit}$. In the limit that $x \rightarrow 0$, the minus solutions have the following properties: $m \rightarrow m_0$, $\alpha \rightarrow (m_0/2x^3)^{1/2}$ and $v \rightarrow -(2m_0/x)^{1/2}$. The physical interpretation of this limiting case is one where a reduced mass, m_0 , has fallen onto a protostellar core and gas immediately outside the protostellar core is accelerated to nearly freefall velocities. Crucially, unlike the LP flow, these solutions pass smoothly from subsonic at large radii to supersonic at small radii. On the other hand, plus solutions (for which $A < 2$), cannot describe collapse flows, although their time-reversed counterparts could be used for wind or expansion solutions. In general, minus solutions with critical points cannot follow collapse either, with the exception of one special solution, which Shu terms the *expansion-wave collapse* solution but is often referred to in much of the literature as the *inside-out collapse* solution. This solution passes through the limiting critical point, $x_* \rightarrow 1^-$, i.e. the critical point $x = 1$ is reached from values of x having $x < 1$. The exact same solution is also obtained in the limiting case when $A \rightarrow 2^+$, i.e. the solution $A = 2$ is reached using solutions having $A > 2$. In the inside-out collapse solution, the initial R^{-2} profile is reached quasi-statically, perhaps due to magnetic field effects or turbulence resisting the force of gravity such that the initial profile resembles that of an unstable singular isothermal sphere. In practice, the singular isothermal sphere is truncated at a radial distance at which the gas pressure internal to the SIS matches the external pressure of the inter-core medium. An unspecified event triggers collapse at the core centre and a collapse expansion wave (CEW) propagates outward at the speed of sound, triggering infall at the head of the wave. Behind the wave, the infall velocity approaches that of freefall due to gravity alone, resulting in a radial density profile of the form $\rho \propto R^{-1.5}$; in front of the wave, the density profile continues to be that of a SIS. Infalling gas accretes onto the protostellar core at a constant rate; the remaining gas making up the total mass behind the CEW has approximately the same mass as that accreted onto the protostellar core.

The inside-out solution of Shu has played and continues to play an important role in the development of star formation theory; its self-similar nature is intuitive and relatively simple to implement in code that requires a dynamical model of collapse onto a protostellar core. However, as touched on in section 1.1, the model is not without its observational difficulties. Additionally, the requirement for a SIS to describe initial conditions prior to collapse is problematic since it implies an infinite density at the core centre. The model does however, provide the prototype for other collapse models that start from a more realistic, finite central-density configuration such as models that assume an initial, marginally stable Bonnor-Ebert sphere (Hunter 1977; Foster & Chevalier 1993).

1.2.4 Including magnetic fields in star formation theories

Two classical problems exist that any complete theory of star formation must solve (McKee & Ostriker 2007, Spitzer 1998) : if angular momentum and magnetic flux are conserved from the interstellar medium in which stars form, stars should have much higher rates of rotation and magnetic field strength than that observed. A way out of both these problems is to include the effects of magnetic fields in star formation theory: magnetic flux can be removed by *ambipolar diffusion*, the term used to describe the process where magnetic flux and charged particles drift through the neutral gas – the motion of charged particles and magnetic flux being tightly coupled due to flux freezing (Spitzer 1998); magnetic fields can remove angular momentum through the outward transfer of gas via torsional Alfvén waves, along magnetic field lines that have become twisted by rotation, a process known as *magnetic braking* (Gillis et al. 1974, Mouschovias & Paleologou 1979).

1.2.5 The magnetic field strength problem

With regard to the problem concerning the magnetic field strength, consider the momentum equation governing the change in fluid velocity \mathbf{v} of gas in the presence of a magnetic field \mathbf{B} (Spitzer 1998):

$$\rho \frac{\partial \mathbf{v}}{\partial t} = -\rho \nabla \phi - \nabla P - \frac{1}{8\pi} \nabla B^2 + \frac{1}{4\pi} \mathbf{B} \cdot \nabla \mathbf{B} \quad (1.4)$$

where $\frac{\partial \mathbf{v}}{\partial t}$ is the Lagrangian time derivative of \mathbf{v} , ρ is the gas density, ϕ is the gravitational potential and $P = P_G + P_R + P_T$ takes into account the gas pressure (P_G), the radiation

pressure from energetic particles such as cosmic rays (P_R) and the pressure contribution from turbulence (P_T). The gas pressure is given by the perfect gas law:

$$P_G = \frac{\rho k T}{\mu} \quad (1.5)$$

where k is the Boltzmann constant, T is the gas temperature and μ is the mean mass per particle. The last two terms on the right hand side of equation 1.4 are the magnetic pressure and tension terms attributed to the Lorentz force, $\mathbf{j} \times \mathbf{B}$, acting on charged particles having current density \mathbf{j} . Consider an initially uniform magnetic field in a molecular cloud with straight, parallel field lines. With the additional idealised assumption that over time, field lines continue to be straight and parallel while B can vary from place to place, the magnetic pressure term acts in a direction perpendicular to the magnetic field lines while there is no force due to magnetic tension since $\mathbf{B} \cdot \nabla \mathbf{B} = 0$. As a condensation within the cloud contracts under the force of gravity, the field lines are drawn closer together. Assuming that both charged and neutral particles are tightly coupled under conditions typical of molecular clouds, and that the magnetic flux can be considered as frozen into the plasma (a condition known as *flux freezing*), the decrease in cross-sectional area A , threaded by the magnetic flux density B , gives rise to an increase in B in order that the magnetic flux remains constant, $\Phi_B = BA$; a negative magnetic pressure gradient is set up that resists the gravitational collapse of the condensation. The magnetic flux may be so great as to resist the force of gravity if the cloud mass is below a critical value:

$$M_\phi \sim \Phi_B / (2\pi G^{0.5}) \quad (1.6)$$

(Nakano & Nakamura 1978; Tomisaka et al. 1988). Clouds with mass below M_ϕ are termed *magnetically subcritical* while clouds with mass M_ϕ or above are *magnetically supercritical*. Magnetically subcritical clouds can eventually collapse if the mass to magnetic flux ratio can be increased, either through an increase in the cloud mass (while keeping Φ_B constant) due to the collapse of gas along parallel magnetic fields lines or through a decrease in Φ_B (while keeping the mass constant) due to ambipolar diffusion. Ciolek & Mouschovias (1993) argue that a rapid collapse of gas parallel to the magnetic field lines will result in a thin-disk morphology for the cloud; collapse in the plane of the disk is slowed down by ambipolar diffusion and gradually reduces Φ_B until the cloud becomes supercritical in the

centre while the outer envelope remains in a subcritical state. An approximate timescale, t_{AD} , for the magnetic flux to be removed from a cylinder with constant density and a uniform, parallel magnetic field is given by (Spitzer 1998):

$$t_{AD} = \frac{\langle \sigma w \rangle}{2\pi G m_H} \frac{n_i}{n_H} (1 + 4n_{\text{He}}/n_H)^{-2} \quad (1.7)$$

where $\langle \sigma w \rangle$ is the ion-neutral collision cross-section, n_{He}/n_H is the relative abundance of He atoms relative to H atoms, n_i/n_H is the ionization fraction and m_H is the mass of a hydrogen atom. In diffuse atomic clouds for which the visual extinction is much less than unity, ultraviolet radiation from the background interstellar radiation field is sufficient to dissociate molecules, leaving hydrogen mainly as H I. Assuming that the ionization fraction is dominated by C^+ ions in diffuse atomic gas clouds, then $\langle \sigma w \rangle = 2.2 \times 10^{-9} \text{ cm}^3 \text{ s}^{-1}$ for C^+ -H collisions can be used as an approximate ion-neutral collision cross-section. Using $n_{\text{He}}/n_H = 0.1$ and an ionization fraction of $n_i/n_H \sim 1 \times 10^{-4}$, typical of diffuse clouds, gives an ambipolar diffusion timescale of $5 \times 10^9 \text{ yr}$. Although this calculation is based on idealised assumptions, the ambipolar diffusion timescale should be correct to an order of magnitude, indicating that magnetically subcritical clouds with diffuse gas should be long-lived and that ambipolar diffusion is inefficient at removing magnetic flux. Clumps within molecular clouds with a visual extinction of $A_v \sim 1$ have an ionization fraction of about 10^{-5} , mainly due to sulphur ions, carbon atoms now being locked up in CO molecules resulting from a reduced rate of CO photodissociation due to self-shielding and absorption of CO-dissociating photons by H and H_2 (Hartquist et al. 1993). CO photodissociates via discrete absorption into predissociating bound states – at a certain visual extinction into the cloud, the line density of CO is sufficient to prevent CO-dissociating photons from penetrating deeper into the cloud, a process known as *self-shielding* (van Dishoeck & Black 1988). Hydrogen is now also mainly in molecular form, H_2 , again due to self-shielding of the background interstellar radiation field. Essentially these clumps are also long-lived and stable, having $t_{AD} \sim 7.5 \times 10^8 \text{ yr}$. In this calculation, equation 1.7 has been adjusted for a collision cross-section between H_2 and HCO^+ : $\langle \sigma w \rangle = 1.69 \times 10^{-9} \text{ cm}^3 \text{ s}^{-1}$; the H_2 - HCO^+ collision cross-section being representative of the collision cross-section between H_2 and metallic ions. At a visual extinctions of $A_V \sim 5$, the ionization fraction drops to about 10^{-7} and the clumps are able to collapse quasistatically having $t_{AD} \sim 7.5 \times 10^6$

yr. In dense molecular cores, freeze-out of ions onto the surfaces of grains results in the ionization fraction dropping to around $10^{-9} \lesssim n_i/n_H \lesssim 10^{-8}$ (Rawlings et al. 1992; Caselli et al. 2002c; de Boisanger et al. 1996) giving $7.5 \times 10^4 \text{ y} \lesssim t_{AD} \lesssim 7.5 \times 10^5 \text{ y}$, indicating that ambipolar diffusion is significantly more efficient in removing magnetic flux and is comparable to the freefall timescale, $t_{ff} = 4 \times 10^4 \text{ y}$, at a density of $n_H \sim 10^6 \text{ cm}^{-3}$ where

$$t_{ff} = \sqrt{\frac{3\pi}{32G\rho_0}} \quad (1.8)$$

is the time taken for a sphere with uniform initial density, ρ_0 , to collapse due to gravity alone (Spitzer 1998). At even higher densities, typical of the accretion phase of star formation, the almost complete decoupling of ions from neutral particles leads to an increase in the mass to magnetic flux ratio in the protostellar core: ambipolar diffusion allows flux to accumulate in the accretion disk while neutral gas continues to flow through the field and onto the protostar (Li & McKee 1996, Ciolek & Koenigl 1998).

1.2.6 The angular momentum problem

With regard to the angular momentum problem, consider a spherical cloud of mass M and uniform density ρ , embedded in external gas having density $\rho_0 \ll \rho$. A uniform magnetic field \mathbf{B} threads both the cloud and external gas. Initially the angular velocity is $\boldsymbol{\Omega}$ within the cloud and zero external to the cloud; $\boldsymbol{\Omega}$ is assumed to be parallel with \mathbf{B} . As the cloud rotates, a discontinuity in magnetic tension at the boundary between the cloud and external gas is created. The field lines become twisted and a perturbation $\delta\mathbf{B}$, transverse to the direction of \mathbf{B} , travels at the Alfvén velocity, V_A :

$$V_A^2 = \frac{B^2}{4\pi\rho_0} \quad (1.9)$$

out along the field lines (Spitzer 1998). Assuming that ions and neutral particles are tightly coupled within the cloud, the Alfvén wave accelerates the external gas within a cylindrical shell, having radius r and thickness dr , up to angular velocity Ω at a rate of $2\pi\rho_0 r V_A dr \text{ g s}^{-1}$ giving a rate of angular momentum transfer of $2\pi\rho_0 \Omega r^3 V_A dr \text{ g cm}^2 \text{ s}^{-2}$. Integrating over the radius of the cloud R and evaluating the integral at the initial time,

$t = 0$, gives an expression for $d\Omega/dt|_{t=0}$, the initial rate of change of angular velocity. An estimate of the time taken for the initial angular velocity Ω_0 to be reduced to zero by magnetic braking is then given by:

$$t_B = \frac{-\Omega_0}{d\Omega/dt|_{t=0}} = \frac{2M}{5\pi R^2 \rho_0 V_A} \quad (1.10)$$

where it is assumed that the cloud undergoes rigid-body rotation. For clouds having $M \sim M_\Phi$, substituting $\Phi_B = \pi B R^2$ into equation 1.6 gives t_B as a function of t_{ff} , the freefall time of a sphere with gas density ρ (equation 1.8): $t_B \sim 0.4(\rho/\rho_0)^{0.5} t_{ff}$. Given the initial assumption that $\rho_0 \ll \rho$, then t_B is found to be substantially greater than the freefall time. Mouschovias & Paleologou (1979) found that angular momentum is more efficiently removed in magnetised molecular clouds when the axis of rotation is aligned perpendicular to the direction of a uniform magnetic field with straight, parallel field lines. Consequently, magnetic braking is expected to preferentially remove the component of the angular momentum vector that is perpendicular to the direction of the magnetic field lines, leaving mainly gas having an angular momentum vector that is parallel to the magnetic field lines.

1.2.7 Support from Alfvén waves

While magnetic fields provide support against gravitational collapse perpendicular to the direction of fields lines through the magnetic pressure term, the magnetic tension term in equation 1.4 provides no support along straight, parallel magnetic field lines. Given that magnetic fields in molecular clouds are generally well-ordered (Vrba et al. 1976; Moneti et al. 1984; Li et al. 2009), it might be expected that clumps within molecular clouds having mass $M_{clump} < M_\Phi$ will collapse preferentially along field lines resulting in flattened structures. However, clumps are in general not flattened structures (Shu et al. 1987). A possible solution to this problem is provided by turbulent support from long-lived Alfvén waves travelling in the direction of the magnetic field lines (Shu et al. 1987; Fatuzzo & Adams 1993; Coker et al. 2000). Observations of CO linewidths in molecular clouds show a relationship between the size of the cloud R and the CO linewidth ΔV of the form $\Delta V \propto R^\alpha$ over a wide range of mass scales with $\alpha \sim 0.5$ (Myers & Benson 1983; Dame et al. 1986). Furthermore, the linewidths are shown to be consistent with clouds in virial equilibrium, $\Delta V \sim (2GM/R)^{0.5}$. The linewidth-size relationship and the

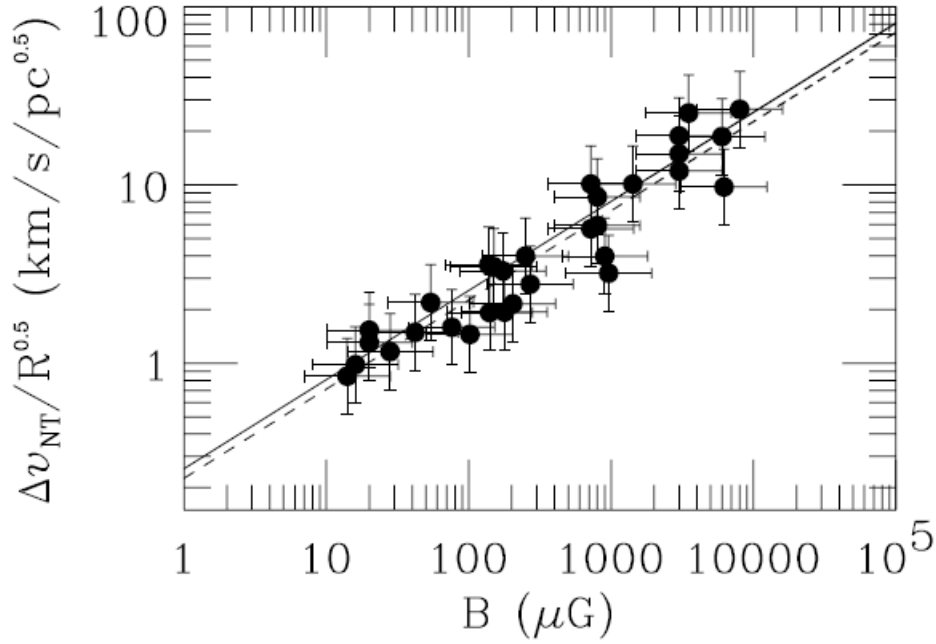


Figure 1.7. Log-log plot of the quantity $\Delta V_{NT}/R^{0.5}$ against the magnetic flux density B . Least-squares fit to the data points (dashed line) is in excellent agreement with the theoretical prediction (solid line) by Mouschovias & Psaltis (1995). Image taken from Mouschovias et al. (2006).

tendency for cloud velocities to have virial values could both be explained if the non-thermal component of linewidths can be attributed to Alfvén waves (Shu et al. 1987; Mouschovias & Psaltis 1995; Mouschovias et al. 2006). If the expression for the Alfvén velocity (equation 1.9) is re-written in terms of the magnetic flux, $\Phi_B = \pi R^2 B$, then it can be shown that for magnetically supported clouds having mass $M \sim M_\Phi$, the mean Alfvén velocity is comparable to the velocity required for virial equilibrium:

$$V_A \simeq V_{VT} = (GM/R)^{0.5} \quad (1.11)$$

(Shu et al. 1987). Additionally from equation 1.6, if B does not vary significantly in star-forming regions, clouds having a mass near the critical value should have similar column densities, $M/\pi R^2 \propto \rho R = \text{constant}$. This in turn, offers a simple explanation for the linewidth-size relationship since $\Delta V \sim 2^{0.5} V_A \propto \rho^{-0.5} \propto R^{0.5}$. Further substitution of $M \sim M_\Phi$ into equation 1.11 allows M to be replaced in favour of B , giving a more general relationship between linewidth, magnetic field strength and size: $\Delta V \propto (BR)^{0.5}$. Mouschovias et al. (2006) used derived values of B , R and the non-thermal component

of the linewidth, ΔV_{NT} , from 31 sources covering a wide range of B values to show that overall, no significant relationship of the form $\Delta V_{NT} \propto R^\alpha$ could be found for the entire data set. However, when sources are categorised by their magnetic field strength (weak-field, moderate-field, strong-field), a discernible pattern emerges that suggests different scaling laws for each of the categories. Furthermore, combining all sources together in a log-log plot of the quantity $\Delta V_{NT}/R^{0.5}$ against B (Figure 1.7) shows a remarkably good, least-squares fit to the data points which is consistent with the relationship $\Delta V_{NT} \propto (BR)^{0.5}$ and in excellent agreement with more detailed predictions of the form:

$$\Delta V_{NT} \simeq 1.4 \left(\frac{B}{30 \mu\text{G}} \right)^{0.5} \left(\frac{R}{1\text{pc}} \right)^{0.5} \text{ km s}^{-1} \quad (1.12)$$

(Mouschovias & Psaltis 1995). Hydromagnetic waves are able to propagate in molecular clouds as long as the period of the wave P , is much longer than the timescale for momentum transfer between ions and neutrals (Arons & Max 1975; Kulsrud & Pearce 1969):

$$\frac{2\pi}{P} \ll 2\mu_{ni}n_i < \sigma w > = 2 \times 10^{-11} \left(\frac{x}{10^{-5}} \right) \left(\frac{n_H}{10^3 \text{ cm}^{-3}} \right) \left(\frac{< \sigma w >}{10^{-9} \text{ cm}^3 \text{ s}^{-1}} \right) \text{ s}^{-1} \quad (1.13)$$

where $\mu_{ni} = m_i/(m_i + m_n)$, m_n and m_i are the mean molecular weights of neutral and charged particles respectively and x is the ionization fraction, $x = n_i/n_H$. Waves satisfying this condition propagate through the molecular cloud at the Alfvén velocity, V_A . Substituting V_A and P into the equation $\lambda = V_A/P$ gives the minimum wavelength for which ions and neutrals can be closely coupled in order to propagate through the cloud: $\lambda_{min} \sim 2.5 \times 10^{-2} \text{ pc}$ for a magnetic flux density of $B_0 = 40 \mu\text{G}$ and the parameter normalisations for x and n_H given in equation 1.13. Ion-neutral friction will damp these waves by a factor e^{-1} on a timescale:

$$\tau(P) = 1.6 \times 10^5 \left(\frac{P}{10^5 \text{ yr}} \right) (\mu_{ni}) \left(\frac{x}{10^{-5}} \right) \left(\frac{n_H}{10^3 \text{ cm}^{-3}} \right) \left(\frac{< \sigma w >}{10^{-9} \text{ cm}^3 \text{ s}^{-1}} \right) \text{ yr} \quad (1.14)$$

(Arons & Max 1975). Short wavelengths ($\lambda < 1 \text{ pc}$) will be damped on a timescale less than the typical lifetime of a molecular cloud unless waves are replenished by a continuous source of hydromagnetic oscillations. A possible source of Alfvén waves are those generated by clumps or cores undergoing magnetic braking. Another possibility is that large scale

($\lambda \geq 1$ pc) Alfvén waves left over from the cloud formation process survive (Mouschovias 1975) – long wavelengths suffering only weak damping rates according to equation 1.14. Hartquist et al. (1993) argue that clumps having $A_V \sim 1$ and $x \sim 10^{-5}$ are long-lived due in part to the support from Alfvén waves. As the ionization fraction in a clump drops to about $x \sim 1 \times 10^{-7}$, Alfvén waves are rapidly dissipated due to the decoupling of ions and neutrals, effectively removing turbulent support and allowing clumps to collapse under the force of gravity.

1.2.8 Turbulence and core rotation

Dense cores are shown to have relatively quiescent, thermal linewidths (Myers 1983) indicating that turbulent support, although thought to play a major role in the evolution and support of molecular clouds on the scale of GMCs and core complexes, is unable to play a significant role in the later stages of low-mass star formation (McKee & Ostriker 2007). Similarly, during the pre-stellar phase of star formation, support against collapse from rotation is thought to be negligible compared to the force of gravity: β , the ratio of rotational to gravitational energy in dense cores is typically $\beta \sim 0.02 - 0.03$ (Goodman et al. 1993; Caselli et al. 2002a).

1.3 Observations of star forming regions

1.3.1 Spectroscopic studies of dense cores

The dust in dense clouds such as Barnard 68 is sufficient to extinguish nearly all of the background starlight in the visible band of the electromagnetic spectrum. However, radiation at longer wavelengths such as the infrared and millimetre are left relatively unaffected by the dust. The spectroscopic study of dense clouds in the infrared and millimetre wavelengths are of particular interest to astronomers since these clouds are the birthplaces of stars: cold dense clouds emit radiation in the millimetre and submillimetre or radio wavelengths while background starlight or embedded protostars are observable in the infrared through absorption lines from the gas in pre-stellar cores (Herbst 2001). The chemical composition in dense clouds is overwhelmingly molecular, over 140 molecular species having been detected (Snow & Bierbaum 2008). Molecular hydrogen is the most abundant species, with CO being the next most abundant species, having an abundance of 10^{-4} relative to H_2 . The relative abundance of CO reflects the relative abundance of the constituent

elements, C and O, in the interstellar medium. At temperatures of around 10K - 30K, characteristic of the temperatures inside dense molecular clouds, *polar* molecules (those molecules having a non-zero dipole moment) are commonly observed through emission or absorption of rotational transition lines. As a consequence of the symmetrical molecular structure in H₂, no dipole moment exists and therefore H₂ cannot be directly observed via rotational transition lines. However, observations of the rotational transition lines of polar molecules, in combination with models of *radiative transfer*, allows astronomers to indirectly establish the density and temperature structure within a cloud. The total energy radiated by photons (per cm³ per unit solid angle per second) at frequency ν_{jk} between rotational upper level k and lower level j of molecule X due to *spontaneous emission* is dependent on n_k , the population density of molecule X at level k , and A_{kj} , the Einstein radiation coefficient giving the probability of a spontaneous downward transition between levels k and j per particle per second (Spitzer 1998):

$$\int j_\nu d\nu = \frac{h\nu_{jk}n_kA_{kj}}{4\pi} \quad (1.15)$$

where h is the Planck constant, j_ν is defined as the emissivity and the integral on the left hand side of the equation extends over the emission line. The total energy of photons at frequency ν_{jk} , absorbed by molecule X (per cm³ per unit solid angle per second) is given by:

$$I_\nu(\nu_{jk}) \int k_\nu d\nu = \frac{h\nu_{jk}(n_jB_{jk} - n_kB_{kj})I_\nu(\nu_{jk})}{c} \quad (1.16)$$

where n_j is the number density of molecule X at energy level j , c is the speed of light, B_{jk} and B_{kj} are Einstein probability coefficients for stimulated absorption and emission respectively, I_ν is the specific intensity of the radiation field, $I_\nu(\nu_{jk})$ is the specific intensity evaluated at frequency ν_{jk} , k_ν is the absorption coefficient and the integral on the left hand side of the equation extends over the absorption line profile at central line frequency ν_{kj} for molecule X . The number density n_j will change over time due to the radiative processes described in equations 1.15 and 1.16. Additionally, collisions with H₂ molecules may also excite or deexcite molecule X to different energy levels. The rate of change of n_j with respect to time, dn_j/dt , can be calculated by considering the summation of all, radiative

or collisional, excitation and deexcitation processes over multiple energy levels. Under steady-state conditions, $dn_j/dt = 0$ and n_j is given by:

$$n_j \left\{ \sum_k (n_{\text{H}_2} \gamma_{jk} + B_{jk} U_\nu) + \sum_{k < j} A_{jk} \right\} = \sum_k n_k (n_{\text{H}_2} \gamma_{kj} + B_{kj} U_\nu) + \sum_{k > j} n_k A_{kj} \quad (1.17)$$

where γ_{jk} is the H_2 - X collisional rate coefficient for collisions that excite molecule X from level j to k , γ_{kj} is the H_2 - X collisional rate coefficient for collisions that deexcite molecule X from level k to j , $U_\nu = \int I_\nu d\omega/c$ is the radiant energy density per unit frequency interval; the integral in the right hand side of this equation extends over all solid angles ω . A useful way of describing any level population n_j is by defining the departure coefficient $b_j = n_j/n_j^*$ as the ratio of the level population to n_j^* , the expected level population in thermodynamic equilibrium. In thermodynamic equilibrium, the relative populations of n_k^* and n_j^* are given by the Boltzmann equation:

$$\frac{n_k^*}{n_j^*} = \frac{g_k}{g_j} e^{-(E_k - E_j)/kT_k} \quad (1.18)$$

where E_j is the energy at level j , g_j is the statistical weight at level j , k is the Boltzmann constant and T_k is the gas kinetic temperature. Substituting the departure coefficients b_j and b_k into the Boltzmann equation in order to eliminate n_j^* and n_k^* gives an expression for the ratio n_k/n_j in terms of the gas kinetic temperature and the ratio of the departure coefficients:

$$\frac{n_k}{n_j} = \frac{b_k}{b_j} \frac{g_k}{g_j} e^{-(E_k - E_j)/kT_k}. \quad (1.19)$$

Evidently when $b_k/b_j = 1$, the ratio of the level populations n_k/n_j is indistinguishable from the level populations in thermodynamic equilibrium; the condition that a system is not in thermodynamic equilibrium but $b_k/b_j = 1$ is termed *local thermodynamic equilibrium* (LTE). Another useful tool for describing the ratio n_k/n_j between any two levels is the *excitation temperature*, T_{ex} : given the level populations of two levels n_k and n_j , T_{ex} satisfies the Boltzmann equation so that:

$$\frac{n_k}{n_j} = \frac{g_k}{g_j} e^{-(E_k - E_j)/kT_{ex}}. \quad (1.20)$$

Comparing equation 1.20 to equation 1.19 implies that in LTE, $T_{ex} = T_k$. Above some critical number density of hydrogen molecules, $n_c = A_{kj}/\gamma_{kj}$, the rate of change in number density between levels k and j due to collisional deexcitation exceeds that due to spontaneous emission; for densities much above n_c , collisional processes will dominate over radiative processes and the ratio n_k/n_j will approach that for LTE; in this case $T_{ex} \sim T_k$ and the lines are said to be *thermalised*. Weakly polar molecules such as CO radiate slowly, especially at low rotational levels, and require only small n_c in order for emission lines to be observable. On the other hand, strongly polar molecules such as N_2H^+ have higher critical densities and are therefore better at probing the density structure in the densest regions of cloud cores. Using a combination of lines from both weakly polar and strongly polar molecules, indirect observations of the gas density structure can be determined. This technique is not infallible, as Myers et al. (1991) demonstrate with a survey of NH_3 (1,1), CS (1-0) and $C^{18}O$ (1-0) line emission from 16 dense cores. While the half-maximum contour plots for $C^{18}O$ (1-0) emission is shown to be the most extended of the three lines, in agreement with the calculated values for n_c , CS (1-0) emission is shown to be consistently more extended than NH_3 (1,1), in disagreement with the analysis of n_c for the two lines. A reason suggested for this discrepancy is that selective freeze-out of CS onto the surfaces of grains is sufficient to alter significantly the emission profiles for CS (1-0) (Tafalla et al. 2002). Freeze-out of CS flattens the emission profile in the central, densest region of the core, resulting in the distance of the half-maximum contour line increasing by a factor of about 2. On the other hand, NH_3 survives significant freeze-out onto grains at higher densities due to the lower binding energy between nitrogen-bearing species and grain mantles.

1.3.2 The equation of radiative transfer

As a ray of light travels through a cloud to an observer, the specific intensity may decrease due to absorption by gas according to equation 1.16 and by scattering and absorption of photons due to dust grains. In the case of radio waves, having wavelengths in the millimetre and submillimetre, scattering and absorption by dust grains of size $\sim 0.1 \mu m$ is negligible. The specific intensity will also increase due to gas emission according to equation 1.15. Overall, the rate of change in intensity taken along a ray of radiation is described by the

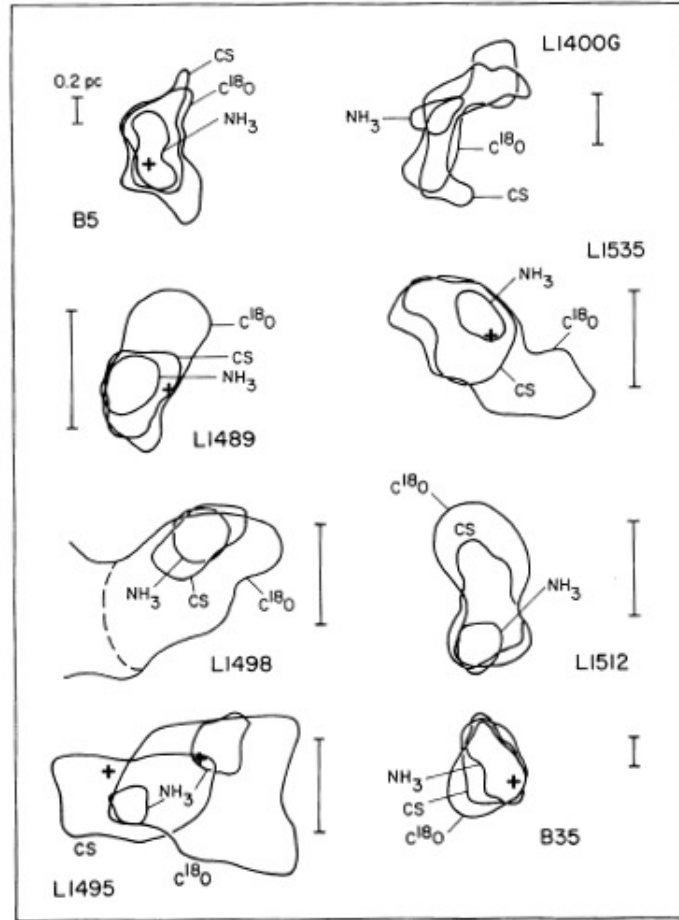


Figure 1.8. Half-maximum intensity contour plots for eight dense cores. Calculated values for the critical density for each of the molecular transition lines NH_3 (1,1) and CS (1-0) indicate that NH_3 (1,1) should have more extended emission than CS (1,0). Observations of dense cores consistently indicate that NH_3 (1,1) emission is less extended than CS (1-0). Image taken from Myers et al. (1991).

equation of radiative transfer:

$$\frac{dI_\nu}{ds} = -k_\nu I_\nu + j_\nu \quad (1.21)$$

where s is the distance along the beam of radiation. The optical depth or opacity, τ_ν , of the absorbing gas is defined by: $d\tau_\nu = -k_\nu ds$. The definition of τ_ν is defined in the reverse direction to s such that $\tau_\nu = 0$ indicates the position of an observer and τ_ν increases with increasing depth into the cloud. An absorbing gas is said to be *optically thin* if $\tau_\nu \ll 1$ and *optically thick* when $\tau_\nu \gg 1$. Multiplying both sides of equation 1.21 by $e^{-\tau}$ and integrating over τ_ν from the position of the observer, $\tau_\nu = 0$, to the position at the far

side of the cloud, $\tau_\nu = \tau_{\nu r}$, gives an expression for the specific intensity as seen by the observer:

$$I_\nu = I_\nu(0)e^{-\tau_{\nu r}} + \int_0^{\tau_{\nu r}} \frac{j_\nu}{k_\nu} e^{-\tau_\nu} d\tau_\nu \quad (1.22)$$

where $I_\nu(0)$ is the specific intensity on the far side of the cloud corresponding to when $\tau_\nu = \tau_{\nu r}$. The ratio j_ν/k_ν is also known as the source function, S_ν , and is generally a function of τ_ν . However, under local thermodynamic equilibrium, j_ν/k_ν has the same value as a system in strict thermodynamic equilibrium. In this case I_ν is given by the Planck function:

$$B_\nu(T_k) = \frac{2h\nu^3}{c^2} \frac{1}{e^{h\nu/kT_k} - 1} \quad (1.23)$$

where T_k is the gas kinetic temperature. Thermodynamic equilibrium implies that I_ν must be constant; setting $dI_\nu/ds = 0$ in equation 1.21 then gives the relationship known as Kirchoff's law: $j_\nu = k_\nu B_\nu(T_k)$.

1.3.3 Measurements of core excitation temperatures and opacities

With the assumption that the gas temperature is constant over the cloud, substituting j_ν/k_ν into equation 1.22 gives:

$$T_b = T_{b0}e^{-\tau_{\nu r}} + T_k(1 - e^{-\tau_{\nu r}}) \quad (1.24)$$

where T_b is the *brightness temperature* which is defined by replacing T_k with T_b in the Raleigh-Jeans law, and equating I_ν to $B_\nu(T_b)$ under the condition that $h\nu \ll kT_k$:

$$I_\nu = B_\nu(T_b) = \frac{2\nu^2 k T_b}{c^2} \quad (1.25)$$

and T_{b0} is the brightness temperature on the far side of the cloud (Spitzer 1998). In radio astronomy, since the condition $h\nu \ll kT_k$ is generally satisfied for the lines being observed, the brightness temperature is often used in preference to the specific intensity. Physically, T_b can be thought of as the temperature at which a black body needs to emit radiation in order that its intensity matches I_ν . In the limiting case of an extremely optically thick

line, $\tau_{\nu r} \gg 1$, it can be seen from equation 1.24 that $T_b \simeq T_k$.

In the case where $T_k \neq T_{ex}$ it can be shown that the source function, $S_\nu = j_\nu/k_\nu$, is given by:

$$S_\nu = j_\nu/k_\nu = \frac{2h\nu^3}{c^2} \frac{1}{\frac{b_j}{b_k} e^{h\nu/kT_k} - 1} \quad (1.26)$$

under the assumption that the absorption and emission profiles have the same frequency distribution (Spitzer 1998). Using equations 1.19 and 1.20 to arrive at an alternative expression for the ratio of departure coefficients:

$$\frac{b_j}{b_k} = e^{h\nu/kT_{ex} - h\nu/kT_k} \quad (1.27)$$

allows S_ν to be expressed as

$$S_\nu = j_\nu/k_\nu = B_\nu(T_{ex}). \quad (1.28)$$

With the assumption that T_{ex} is constant through the cloud, a more general version of equation 1.24 can then be given in terms of T_{ex} :

$$T_b - T_{b0} = (T_{ex} - T_{b0})(1 - e^{-\tau_{\nu r}}) \quad (1.29)$$

where $-T_{b0}$ has been added to each side of equation 1.24 in order to give an expression for the brightness contrast: the observed difference in brightness temperature between the source and background emission. Using spectral line observations of CO (1-0), C¹⁸O (1-0) and ¹³CO (1-0) directed towards the centre of the L1544 core, Tafalla et al. (1998) estimated the temperature properties of the inner and outer region of the L1544 core. The opacities and excitation temperature in the core can then be determined from equation 1.29 using the ratio of the observed peak brightness contrast between the C¹⁸O (1-0) and ¹³CO (1-0) lines and the following assumptions: a) both lines have the same excitation temperature; b) the ratio of the ¹³CO (1-0) opacity to the C¹⁸O (1-0) opacity is approximately equal to the ratio of the terrestrial abundance ratio of ¹³CO : C¹⁸O = 5.5. Using this method, the excitation temperature was found to be $T_{ex} = 12.5$ K and the opacities towards the centre of the core were found to be 0.8 and 4.4 for the C¹⁸O (1-0) and ¹³CO

(1-0) lines respectively. The opacity of the CO (1-0) line is estimated at around 400, indicating that emission is dominated by the outer 1% of the core. From the peak brightness temperature in the CO (1-0) line, the excitation temperature in the outer core is estimated to be between 11 K and 16.7 K. Assuming all CO lines to be thermalised, these results indicate that either the temperature profile is approximately constant or the temperature increases towards the observer.

1.3.4 Using Ammonia line profiles to probe the temperature structure

Ammonia is particularly important when determining the gas temperature in dense cores (Ho & Townes 1983). The structure of an ammonia molecule is that of a pyramid with three hydrogen atoms at its base and a nitrogen atom at its apex. The rotational energy of NH_3 can be expressed using the notation $\text{NH}_3 (J, K)$: quantum number J gives the total angular momentum; quantum number K gives the projection of the total angular momentum onto the molecular axis. Two distinct species of NH_3 exist: the species having all spin axes of H atoms aligned parallel to each other is termed *ortho*- NH_3 ; the species having anti-parallel H spin axes is termed *para*- NH_3 . Each species can exist in rotational states defined by a mutually exclusive set of K -values: *ortho*- NH_3 can exist in a state for which $K = 3n$ where $n \geq 0$ is an integer; *para*- NH_3 can exist in states for which $K \neq 3n$. Transitions between K -ladders are slow such that the K -ladders can be considered independent of each other. The lowest rotational state in each K -ladder, $\text{NH}_3 (n,n)$, decay slowly due to $\Delta K = \pm 3$ transitions and are termed *metastable* while states for which $J > K$ are termed *nonmetastable* since they decay rapidly due to $\Delta J = 1$ transitions. Quantum mechanical tunnelling allows the nitrogen atom to pass through the base to the opposite side. However, the nitrogen atom maintains its direction of spin during this *inversion* transition, the difference between the two vibrational states giving rise to a transition frequency that lies in the radio band of the electromagnetic spectrum. By measuring the relative intensities between the main *para*- NH_3 (1,1) line and a hyperfine component of the line, an estimate of the optical depth can be made; using the optical depth and the relative intensities between the *para*- NH_3 (1,1) and *para*- NH_3 (2,2) lines, the rotation temperature for the *para*- NH_3 (1,1) \rightarrow *para*- NH_3 (2,2) transition can be calculated. Since the radiative transition between these two metastable states is forbidden, the only transitions allowed are collisional, hence the rotation temperature is equivalent to the gas kinetic temperature.

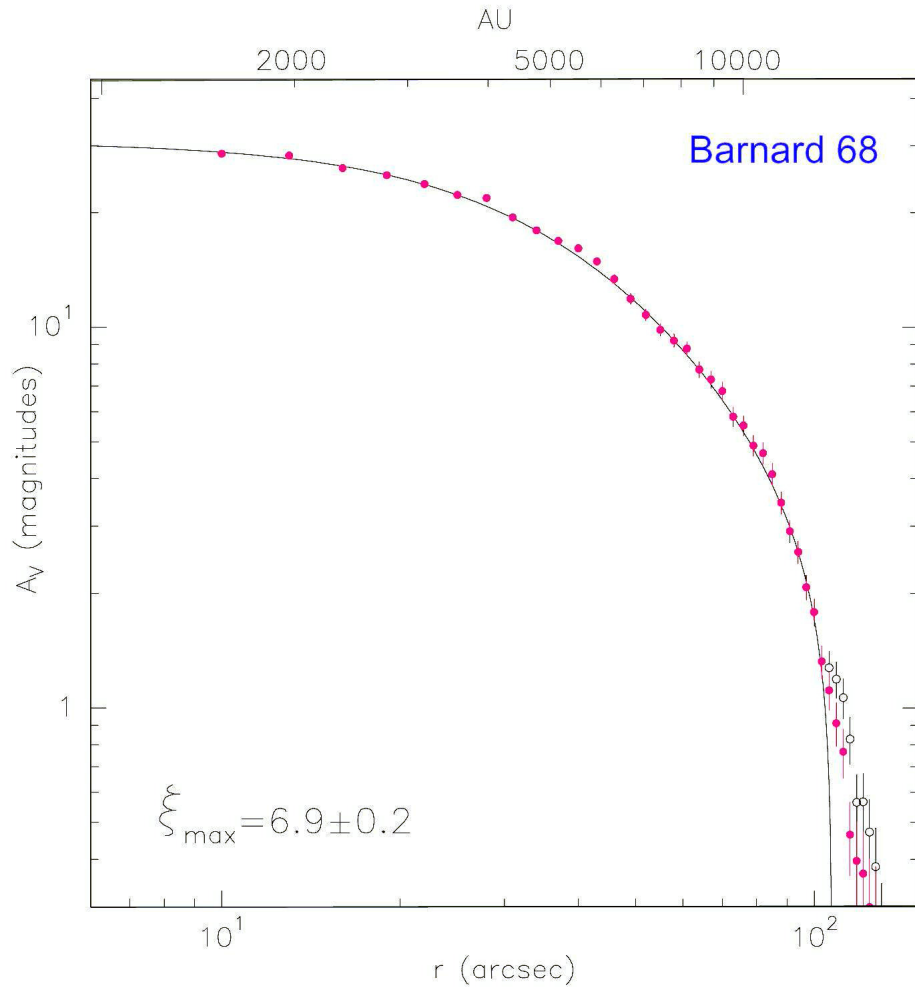


Figure 1.9. Near-infrared extinction of Barnard 68 (image from Alves et al. 2001*a*). Image courtesy of ESO.

1.3.5 Modelling the gas density structure

In general, the analysis of temperature structure within a core is complicated due to observations sampling emission through gas which may have a varying density and temperature structure. Often, a model of the gas distribution is used to complement the observations, the model being derived from the dust continuum emission (Tafalla et al. 2002) or from mapping the near-infrared extinction in the core (Alves et al. 2001*a*). Figure 1.9 shows the near-infrared extinction as a function of radial distance for Barnard 68. The density profile as derived from the near-infrared extinction compares well with a theoretical density distribution, a stable Bonnor-Ebert sphere (Bonnor 1956, Ebert 1955). The flat density profile in the core centre and the steep fall-off in density at the core edge are typical of

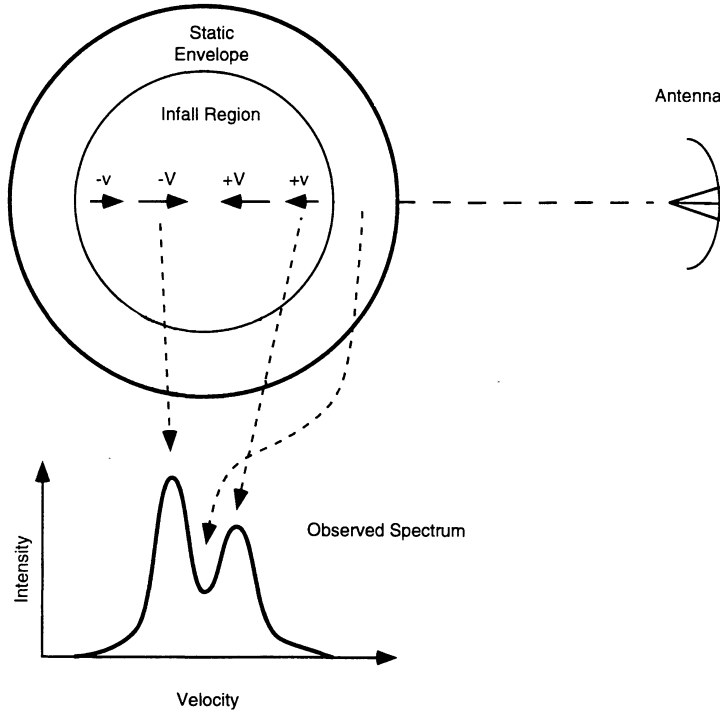


Figure 1.10. Spectral signature of collapse in a protostellar core (image from Rawlings 1996*b*). For optically thick lines, the static envelope creates an absorption dip, giving rise to two peaks in the line profile.

pre-stellar cores, although it should be noted that for most cores a stable Bonnor-Ebert sphere is inconsistent with the observed core temperature (Kirk et al. 2005). Protostellar cores on the other hand, tend to have a radial density distribution inferred from dust continuum emission that is closer to the R^{-2} profile of a SIS: Shirley et al. (2000) used dust continuum emission at $450\ \mu\text{m}$ and $850\ \mu\text{m}$ to derive a density distribution of the form $n \sim R^{-2.1}$ for Class 0 and I protostellar cores.

1.3.6 Using line profiles to probe the velocity structure

A common observational technique for determining whether a core is collapsing is by analysing the spectral line profiles of molecular species. Rawlings (1996*b*) discusses the use of observed spectral line profiles coupled with dynamical and chemical models to provide diagnostics of the infall dynamics of protostellar cores: infall candidates have a distinctive fingerprint which is obtained by observing at least two lines of molecular species that probe the contracting part of the core. One of the lines is optically thin, originating from transitions between higher rotational levels that are able to trace the

dense, warmer region of the protostellar core; the optically thin peak is symmetric and single-peaked and does not on its own necessarily indicate infall. The single peak is important in distinguishing between the spectral signature of a single core and that of two cores or gas condensations being observed in close proximity. The other transition must be optically thick; under suitable conditions this line will exhibit an asymmetric, double-peaked profile with the blueshifted peak dominating over the redshifted peak: the two peaks corresponding to emission from the redshifted and blueshifted hemispheres of a collapsing core. The central velocity of the emission peak for the optically thin line is representative of the local standard of rest velocity (V_{LSR}); V_{LSR} lies between the velocities of the emission peaks for the optically thick line, indicating that emission is from the same volume of gas. For the optically thick line, the blueshifted peak will dominate over the redshifted peak if the following conditions are satisfied (Zhou & Evans 1994): there is a velocity gradient in the line forming region of the core, so that the infall rate increases towards the centre; the excitation temperature in the line forming region increases towards the centre. That two peaks are observed rather than one as in the optically thin case, is explained due to absorption in the static or near-static outer region of the core (Figure 1.10). The dominance of the blueshifted peak over the redshifted peak can be explained by assuming the velocity gradient to be large: the blueshifted and redshifted hemispheres will be radiatively decoupled and the emission from the blueshifted and redshifted hemispheres can then be considered separately. The emission from the blueshifted hemisphere is dominated by the gas from the inner core – gas which is denser, warmer and has higher infall velocity and excitation temperature than the outer core. The emission from the redshifted hemisphere is dominated by gas from a region further away from the core centre than for blueshifted hemisphere – consequently the emission traces slower moving, lower excitation temperature gas. While this analysis originally applied to collapsing protostellar cores, the analysis still holds for the interpretation of asymmetric line profiles in pre-stellar cores. In pre-stellar cores, the kinetic temperature in the inner core cannot be assumed to be higher than in the outer core. Nevertheless, for unthermalised molecular transition lines the excitation temperature can still increase towards the core centre, even while assuming a decreasing kinetic temperature. Line profile studies of pre-stellar cores indicate that in some cases, the gas dynamics are more complex than this simple analysis suggests. Redman et al. (2004) observed the pre-stellar core L1689B in HCO^+ and found both dominant redshifted and blueshifted peaks in the

line profile at different angular positions; furthermore, a distinct line could be drawn separating the dominant redshifted and blueshifted line profiles. This separation, so the authors argue, is evidence for core rotation. Lada et al. (2003) observed Barnard 68 (B68) in CS across the core and found blueshifted profiles in the core centre and redshifted profiles at the core edge. The reversal in the dominant hemisphere is attributed to small-amplitude oscillations about a stable equilibrium value at the core edge. Redman et al. (2006) later confirmed core oscillations with observations in HCO^+ across the core. Multiple line observations of B68 by Maret et al. (2007), Figure 1.11, added further complexity to the nature of the gas dynamics. The authors found that the $\text{N}_2\text{H}^+(1-0)$, $\text{DCO}^+(2-1)$ and $\text{HCO}^+(4-3)$ lines observed at the dust extinction peak, have a dominant redshifted peak, indicating expansion in the dense, central region of the core.

1.3.7 Strength of magnetic fields

Measuring the strength and direction of the magnetic field in molecular clouds is critically important in distinguishing between the different theories of star formation. Measurements of the Zeeman splitting effect on OH spectral lines have been used to detect the magnetic flux density along the line of sight, B_{LOS} , in 15 molecular clouds (Crutcher 1999). The authors find that on average, the ratio of cloud mass to the critical value is $M/M_\phi \simeq 2$. The simple interpretation of this result is that magnetic pressure provides half the support against gravity; the other half being provided by superthermal magnetohydrodynamic (MHD) waves. The authors stress however, that the various assumptions about the particular value of M_ϕ and the choice of cloud morphology could affect this result to the point that $M/M_\phi \simeq 1$ cannot be ruled out. Zeeman measurements in the pre-stellar core L1544 were used to derive a mean $B_{LOS} \sim 11 \mu\text{G}$ (Crutcher & Troland 2000): this result could be consistent with an ambipolar diffusion model of star formation (Ciolek & Basu 2000) if the magnetic field is inclined at 16° to the plane of the sky. However, the low B_{LOS} measurements could be due to depletion of OH in the central, densest region of the core, giving a mean B_{LOS} which is representative of the lower density core envelope only: thus B_{LOS} at the core centre could be higher.

1.3.8 Geometry of magnetic field lines

The geometry of the magnetic field in the plane of the sky can be mapped in cloud cores using submillimetre polarimetry. Using this method, Ward-Thompson et al. (2000) found

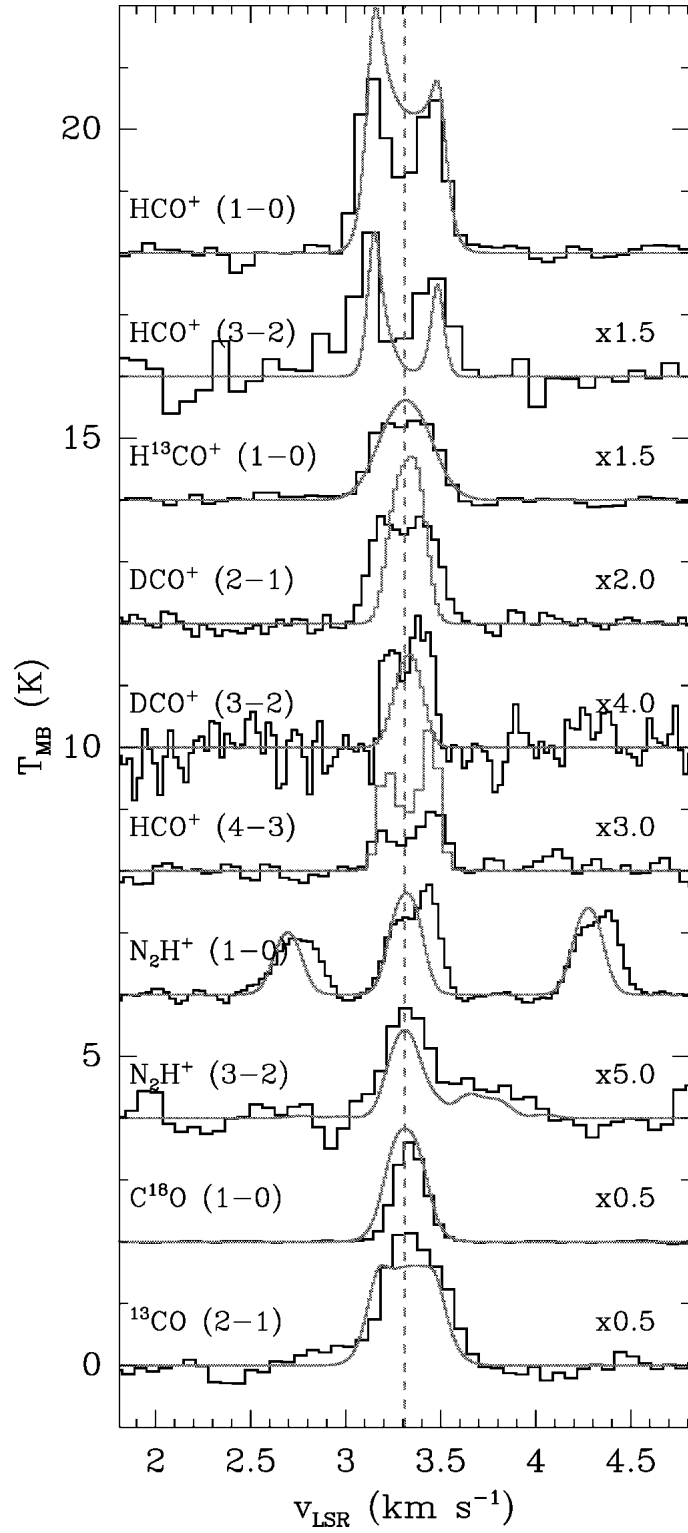


Figure 1.11. Molecular line profiles at the centre of Barnard 68 (image from Maret et al. 2007). Solid black lines are measured line profiles; solid grey lines are a best fit model.

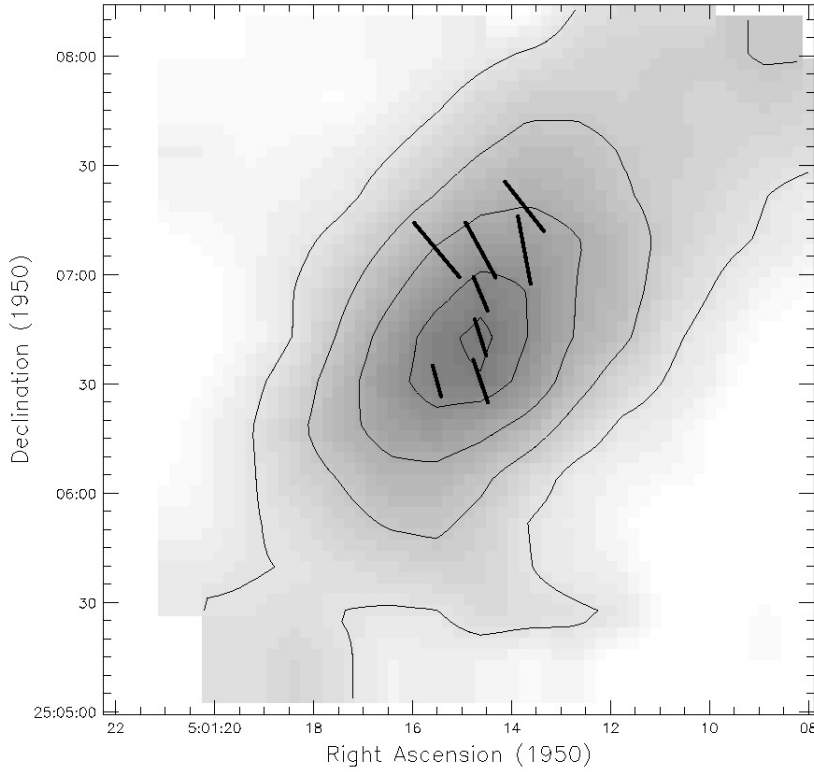


Figure 1.12. Magnetic field orientation in L1544 using submillimetre polarimetry (image from Ward-Thompson et al. 2000). Contours trace the dust continuum emission while bold lines mark the orientation of the magnetic field.

the magnetic field in L1544 to be fairly uniform and inclined at an angle $\sim 30^\circ$ to the minor axis of the core (Figure 1.12). These observations contradict predictions of the ideal ambipolar diffusion model of Ciolek & Basu (2000) requiring the magnetic field to be aligned with the minor axis. The difference between the orientation of the minor axis and the magnetic field is also found in five other starless cores (Ward-Thompson et al. 2009) with a mean inclination angle $\sim 30^\circ \pm 3^\circ$ determined for all cores including L1544. However, the fact that the magnetic field is fairly uniform suggests that turbulence cannot be too strong as to twist magnetic field lines into random orientations, although the relative strength in polarization is shown to be weaker closer in to the core centre, possibly indicating stronger turbulent support. Ward-Thompson et al. (2000) suggest that this tendency may instead be related to increased rates of gas-grain collisions in the core centre inducing increased randomization in the grain alignment, thus reducing grain polarization.

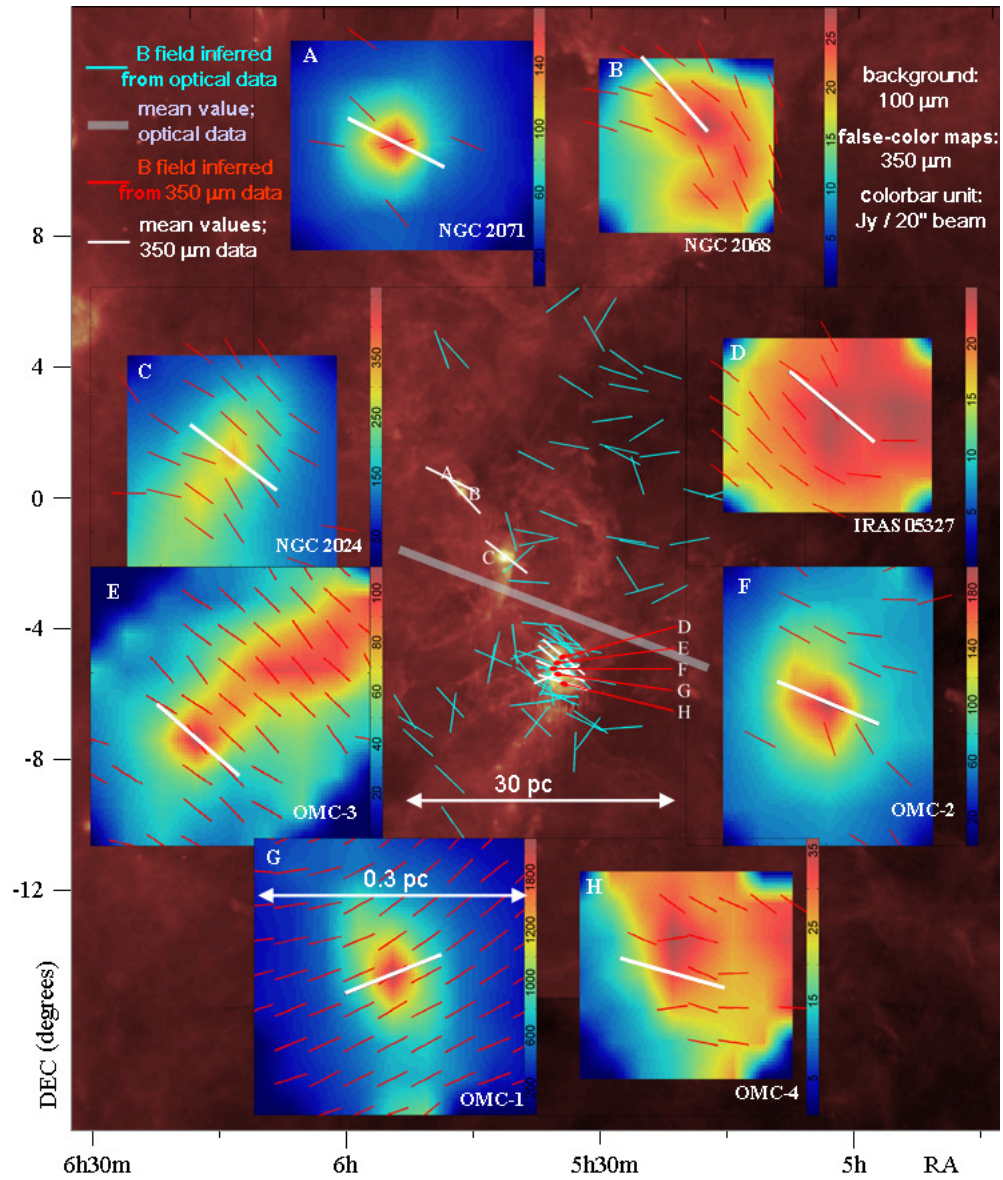


Figure 1.13. Magnetic fields in the Orion molecular cloud (image from Li et al. 2009).

1.3.9 Do magnetic fields dominate the later stages of star formation?

Further support that turbulence may not play a dominant role in the later stages of star formation comes from studying the magnetic field in the Orion molecular cloud (Li et al. 2009): a strong correlation is found between the mean magnetic field alignment in cloud cores as derived from millimetre and submillimetre polarimetry and the mean magnetic field in the inter-core medium (ICM) as derived from optical polarimetry, Figure 1.13. The authors argue that turbulence cannot strongly effect the direction of field lines if the orientation is preserved over such a large range of scales.

A counter-argument to the idea that magnetic fields play a dominant role in star formation comes from studying the alignment of disks and outflows from T-Tauri stars in the Taurus-Auriga molecular cloud (Ménard & Duchêne 2004). This study concluded that T-Tauri stars are orientated randomly with respect to the local magnetic field: if the local magnetic field plays a dominant role in the later stages of star formation, theory predicts that disks should be aligned perpendicular to the magnetic field while bi-polar outflows should be aligned parallel to the magnetic field.

1.4 Interstellar chemistry and the ionization fraction in molecular clouds

1.4.1 Molecular synthesis

Herbst (2001) considers the potential sites of molecular synthesis that could explain the abundances of molecules found in molecular clouds. The reaction rate for many chemical reactions of the form:



where R_1 and R_2 are the reacting molecules, atoms or ions and P_j are the products of the reaction, can be expressed using a rate coefficient $k/\text{cm}^3 \text{ s}^{-1}$ given by:

$$k = A(T)e^{-E_a/k_B T} \quad (1.31)$$

where $A(T)$ is a pre-exponential factor, E_a is an activation energy and k_B is the Boltzmann constant; the reaction proceeds at a rate of $n(R_1)n(R_2)k \text{ cm}^{-3} \text{ s}^{-1}$. The low temperatures in dense cores ($T \sim 10 \text{ K}$) effectively suppresses all endothermic reactions and most exothermic reactions for which $E_a \gg k_B T$. On the other hand, temperatures in the envelopes of very old stars range from a few thousand K down to 10 K in the outer envelope, allowing such reactions to take place efficiently. Furthermore, the gas density in the inner region of the envelope is high enough to allow dust particles to condense out. The molecules and dust will eventually be expelled out into space from strong winds. Alternatively, in the case of massive stars, molecules and dust may be formed and expelled into space due to supernovae events. The material expelled into space from old or dying stars will eventually undergo gravitational collapse and cloud formation. However, a major problem exists with the idea that molecules are created in the envelopes of old stars and transported to the sites of newly forming clouds: the UV interstellar radiation field is strong enough to photodissociate most molecular species. Only dust grains and possibly some large molecules would be able to withstand the harsh UV radiation in interstellar space. This leaves the synthesis of molecules within the clouds themselves as the most likely scenario which could account for the observed abundances of small molecules. Despite the inefficiency of those reactions requiring a significant activation energy in molecular clouds, some reactions are able to proceed relatively quickly (in astronomical terms). Reactions between positive ions and neutrals quite often have no activation energy while a small number of neutral-neutral reactions involving a single atom or radical and a stable neutral molecule are found to proceed quickly at temperatures of around 10 K. The reactions between ions and non-polar neutrals often proceeds at a rate first derived by Langevin (Ferguson 1975):

$$k_L = 2\pi e(\alpha/\mu)^{0.5} \approx 10^{-9} \text{ cm}^3 \text{ s}^{-1} \quad (1.32)$$

where e is the electronic charge on the ion, α is the mean dipole polarisability of the neutral and $\mu = m_{R_1}m_{R_2}/(m_{R_1} + m_{R_2})$ is the reduced mass of the reactants. The rate coefficient is derived by considering the long-range, charge-induced dipole potential as a

function of r , the distance between the molecule and the ion:

$$V(r) = -\frac{e^2\alpha}{2r^4} \quad (1.33)$$

and defining a critical impact parameter, b_0 , for the relative trajectory between the neutral and ion reactants (Gioumouzis & Stevenson 1958); relative trajectories having an impact parameter below b_0 result in the *capture* of the neutral and the reaction is able to proceed. Importantly for reactions in the low temperature environments of dense cores, k_L is independent of temperature. At temperatures of around 10 K, Langevin reactions proceed at a rate approximately 10-100 times as fast as neutral-neutral reactions having no activation energy (Herbst 2001).

1.4.2 Diffuse clouds

In the outer regions of diffuse clouds, ions are produced via photoionization from the external UV radiation. However, the UV radiation is also able to photodissociate any molecules formed, consequently the gas is predominantly in an atomic state. In the inner regions of diffuse clouds, at visual extinctions for which $0.2 \lesssim A_V \lesssim 1$, H_2 is shielded from the photodissociating UV radiation due to the H_2 in the outer region of the cloud. Hydrogen is now mainly in molecular form while other elements such as carbon are still predominantly in an ionized atomic state. Molecules such as CO, OH and HCO^+ are observed in these clouds, indicating that the molecular formation rate is now beginning to compete with the molecular destruction rate due to UV photodissociation. The terms *diffuse atomic* and *diffuse molecular* have been used to chemically differentiate the local conditions in the outer and inner regions of diffuse clouds respectively (Snow & McCall 2006).

1.4.3 Dense clouds

In dense clouds for which $A_V > 5$, the UV radiation is sufficiently attenuated by the dust grains so that ionization and direct photodissociation by the external UV radiation field is much reduced. Ionization is now driven by the bombardment of cosmic ray particles that have sufficient energy to ionize atoms and molecules with high ionization potentials such as H, He and H_2 . Photoionization and photodissociation is still possible in dense clouds due to a cosmic ray induced UV flux: cosmic rays excite electronic states of H_2 , either

directly or via collisions with secondary electrons generated by cosmic rays; the decays from the excited electronic states of H_2 produce an ionizing/dissociating UV flux (Prasad & Tarafdar 1983). Nearly all of the gas phase carbon in dense clouds is locked up in CO; this feature of the carbon composition is used to provide the chemical definition of a *dense molecular* cloud (Snow & McCall 2006).

1.4.4 Translucent clouds

The term *translucent* is applied to the local conditions in clouds with intermediate visual extinction, $1 \lesssim A_V \lesssim 5$; translucent clouds are characterised by a transition from the mainly ionized atomic state of carbon in diffuse molecular clouds to neutral atomic or the molecular CO that dominates the carbon composition in dense molecular clouds. The term *photodissociation region* (PDR), also called *photon-dominated region*, is a more general term that describes any region in the ISM, including diffuse and translucent clouds, where gas is predominantly neutral but where UV radiation plays a significant role in the chemistry or heating of that region (Hollenbach & Tielens 1997). Under this definition of a PDR, the region may also extend into dense clouds to the point where O_2 is not appreciably photodissociated, $A_V \sim 10$.

1.4.5 The role of dust grains in molecule formation

Dyson & Williams (1997) discuss the efficiency of different mechanisms of molecule formation under interstellar conditions. For ion-molecule reactions to be efficient, it requires the presence of H_2 or the product of a reaction with H_2 . The observed high abundance of species formed from reactions with H_2 in molecular clouds is difficult to explain since a) H_2 is rapidly destroyed by UV photodissociation and b) the formation of H_2 via radiative association:



is forbidden and therefore its reaction rate far too slow to counterbalance the rate of UV photodissociation. The conclusion drawn is that in diffuse, translucent and dense

molecular clouds, H_2 is predominantly formed on the surfaces of grains:



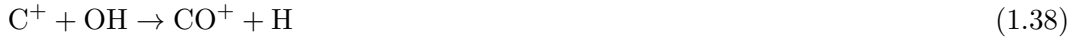
and the formation rate is sufficiently rapid such that the composition of hydrogen (beyond $A_V > 0.2$) is mostly in the form of H_2 molecules.

1.4.6 Ionization fraction

Of particular importance with regard to theories of star formation involving ambipolar diffusion is the ionization fraction: the ratio of the number density of ions to hydrogen atoms, $X(\text{e}^-)$. Ruffle et al. (1998) studied the ionization fraction as a function of the visual extinction, A_V , at the point of chemical equilibrium for a static cloud. They found a steep drop in ionization fraction at $2 \lesssim A_V \lesssim 3$ and suggested that a threshold visual extinction of $A_V \sim 3$ in the Rosette molecular cloud determines whether stars will form in a clump of gas: for $A_V \gtrsim 3$, MHD waves are rapidly dissipated due to low ionization levels (see equation 1.14) while for $A_V < 3$, MHD waves provide enough support to prevent the gravitational collapse of the cloud. In more diffuse gas for which $A_V \lesssim 1$, photodissociation of CO and photoionization of C^0 by the interstellar radiation field give rise to C^+ being the most abundant ion according to the following reactions (Hartquist et al. 1993):



The removal of C^+ is primarily through the following reactions:





The equilibrium condition in diffuse gas is for most of the carbon to be locked up in C^+ and the ionization fraction is between 10^{-4} and 10^{-5} for a gas density between $500 \leq n(\text{H}) \leq 5000 \text{ cm}^{-3}$ (Ruffle et al. 1998). Here, the ionization fraction reflects the relative abundance of the element carbon ($\sim 10^{-4}$) in the interstellar medium. For $A_V > 1$, H_2 and H shield CO from interstellar photons in addition to self-shielding from CO and the rate of production of C through reaction 1.36 is much reduced (van Dishoeck & Black 1988), consequently the overall ionization level drops. In this case, the equilibrium condition in dense gas is for most of the carbon to be locked up in CO . For $A_V \gtrsim 4$, the dominant ions are low ionization potential metals such as sodium and magnesium. For $A_V \gtrsim 5$, UV photons cannot penetrate deep enough into the cloud at a sufficient rate to maintain the high ionization levels of the more diffuse gas. However, even in regions of high visual extinction, ionization occurs either directly through collisions with cosmic rays or via cosmic ray induced UV photons: the ionization fraction at $A_V = 5$ drops to about 10^{-7} .

1.4.7 Freeze-out and desorption processes

At intermediate-to-high visual extinction, the process of *freeze-out* reduces the abundances of most atoms and molecular species. Freeze-out or depletion is the term used to describe the removal of gas phase atoms and molecules onto grains. The critical visual extinction, $A_{V,crit}$, above which freeze-out becomes important depends on the particular molecular cloud and the molecule. Teixeira & Emerson (1999) found that in the Taurus molecular cloud, freeze-out of CO and H_2O onto grain mantles will occur for $A_V > 2.6 \pm 0.8$ and $A_V > 2.7 \pm 0.6$ respectively while in the Ophiuchus molecular cloud, CO and H_2O freeze out at $A_V > 8.3 \pm 1.6$ and $A_V > 12 \pm 1$ respectively. The depletion rate of molecules, ions

and atoms from the gas phase due to freeze-out is given by:

$$\frac{dn_j}{dt} = 4.57 \times 10^4 \langle d_g a^2 \rangle T^{1/2} C n_H S_j m_j^{-1/2} n_j \text{ cm}^{-3} \text{ s}^{-1} \quad (1.41)$$

(Spitzer 1998; Umebayashi & Nakano 1980) where d_g is the dust-gas ratio, a is the grain radius in cm, $\langle d_g a^2 \rangle$ is an average of $d_g a^2$ over the grain population, T is the gas temperature, n_H is the number density of hydrogen atoms, n_j is the number density of the particle, S_j is the sticking coefficient, m_j is the mass of particle j in amu and C is a factor which takes into account electrostatic effects. The average grain charge, applicable to dark clouds, is assumed to be -1, in which case: $C = 1$ for neutral species; $C = 1 + (16.71 \times 10^{-4}/aT)$ for singly charged positive ions. The effect of the electrostatic force for a grain size of $0.1 \mu\text{m}$ and a temperature of 10K, is to increase the freeze-out rate of singly charged positive ions by a factor of around 17 compared to the freeze-out of a neutral particle with the same mass.

1.4.8 Desorption processes

The overall rate of depletion from the gas phase must also take into account *desorption*: this is the term used to describe the processes that return atoms and molecules from the surfaces of grains back into the gas phase. A number of processes have been suggested that could provide efficient desorption rates. Molecules may evaporate from the surface of a grain if there is a non-negligible probability of being in an energy state that is greater than the binding energy between the molecule and the surface of the grain (Leger et al. 1985). The binding energy is dependent on the molecular species: H_2O has a much higher binding energy than CO so that H_2O may evaporate from grains at temperatures above 100 K while CO evaporates from grains at temperatures above 20 K (Hollenbach et al. 2009). Grains may be heated by UV photons (Aannestad & Kenyon 1979), X rays and cosmic rays (Leger et al. 1985). Above a critical temperature of 27 K, radicals become mobile and are able to react explosively resulting in desorption of the entire grain mantle (Leger et al. 1985). Direct photodesorption by far ultraviolet (FUV) photons has also been considered by Hollenbach et al. (2009) while Roberts et al. (2007) investigate the major desorption processes in dark clouds, namely: desorption by the energy released from H_2 formation on the surfaces of grains; direct heating by cosmic rays; photodesorption due

to the cosmic ray induced UV flux. The suggestion of a critical visual extinction, A_{Vcrit} , above which the effects of freeze-out can be observed indicates that for $A_V < A_{Vcrit}$, desorption is more efficient than freeze-out while for $A_V > A_{Vcrit}$, freeze-out begins to dominate over desorption. Rawlings et al. (1992) modelled the NH_3 (1,1) line profile in L1498 using a chemical model that included freeze-out onto grain mantles. The authors found that the observed narrow linewidths of NH_3 (1,1) could be matched when freeze-out was included. Later observations by Tafalla et al. (2002) suggested that CS and CO are also severely depleted at the centre of several pre-stellar cores. Over the timescale of collapse indicated by the freefall time of a pre-stellar core, the freeze-out timescale is of the same order or less, indicating that freeze-out is an important consideration when modelling $X(\text{e}^-)$, especially since ions are preferentially removed over neutrals due to electrostatic attraction between positively charged ions and negatively charged dust grains (Rawlings 2000). The preferential freeze-out of ions onto grains over neutral species has some surprising affects on the abundances on some species (Rawlings et al. 1992; Rawlings & Yates 2001): whereas most ions see an increased depletion with increasing density of the cloud, HCO^+ can initially see an increase. This effect can be explained by considering the major formation and removal mechanisms for HCO^+ . HCO^+ is predominantly formed through the reaction:



and lost through



when $n(\text{H}_2\text{O})/n(\text{e}^-) > 100$ (Rawlings 1996a) and



when $n(\text{H}_2\text{O})/n(\text{e}^-) < 100$. As depletion of H_2O becomes significant, a major loss route for HCO^+ is removed and the abundance of HCO^+ rises. At later times, the ionization level drops and the removal route through electron reactions is suppressed. Since the freeze-out of CO onto grains occurs at a much slower rate than that of charged species

and the formation of H_3^+ is primarily determined by the cosmic ray ionization of H_2 , the formation of HCO^+ drops at a slower rate than the removal rate.

1.4.9 An analytic model for the ionization fraction at the centre of dark clouds

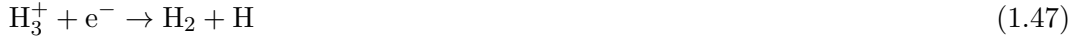
At the centre of dark clouds, H_2 is shielded from UV radiation and is predominantly destroyed using the following reaction network (Dyson & Williams 1997):



at a rate ζ per second. Subsequently



at a rate of $k' \text{ cm}^3 \text{ s}^{-1}$ per molecule, and



at a rate of $k'' \text{ cm}^3 \text{ s}^{-1}$ per molecule. Again, it is assumed that H atoms combine on the surfaces of grains and return H_2 back into the gas phase. Closed reaction networks such as those described above, can be used to set up a series of ordinary differential equations describing the time-variation of abundances in a cloud. For the above network, the rate of change in the number density of H_2^+ molecules is given by the difference between the rate that H_2^+ is destroyed subtracted from the rate that H_2^+ is created:

$$\frac{d}{dt}n(\text{H}_2^+) = \zeta n(\text{H}_2) - k' n(\text{H}_2) n(\text{H}_2^+). \quad (1.48)$$

Similarly for H_3^+ :

$$\frac{d}{dt}n(\text{H}_3^+) = k' n(\text{H}_2) n(\text{H}_2^+) - k'' n(\text{e}^-) n(\text{H}_3^+) \quad (1.49)$$

Some useful information can sometimes be gained by considering the equilibrium condition: when the time derivative components of equations 1.48 and 1.49 are zero:

$$\zeta n(\text{H}_2) = k' n(\text{H}_2) n(\text{H}_3^+) = k'' n(\text{e}^-) n(\text{H}_3^+). \quad (1.50)$$

Assuming that k' and k'' are of the same order and that $n(\text{H}_3^+) \gg n(\text{H}_2^+)$ so that the approximation $n(\text{H}_3^+) \approx n(\text{e}^-)$ holds, then

$$n(\text{e}^-) = \left(\frac{\zeta}{k''} n(\text{H}_2) \right)^{1/2} \quad (1.51)$$

or

$$X(\text{e}^-) \simeq 0.5 \left(\frac{\zeta}{k'' n(\text{H}_2)} \right)^{1/2}. \quad (1.52)$$

Assuming a cosmic ray ionization rate of $\zeta = 1.3 \times 10^{-17} \text{s}^{-1}$ (van der Tak & van Dishoeck 2000) and $k'' = 8.2 \times 10^{-8} \text{cm}^3 \text{s}^{-1}$ at a temperature of 10 K (Millar et al. 1997), then $X(\text{e}^-) = 4.5 \times 10^{-9}$ for a number density of hydrogen molecules of $n(\text{H}_2) = 2 \times 10^6 \text{cm}^{-3}$. More detailed analysis of the ionization fraction at the centre of dense molecular cores indicates that $10^{-9} \lesssim X(\text{e}^-) \lesssim 10^{-8}$ (Rawlings et al. 1992; Caselli et al. 2002*c*; de Boisanger et al. 1996).

1.5 Thesis motivation and purpose

The use of chemical models in conjunction with an assumed dynamical model is now a well-established technique that can be used to analyse spectral line profiles in order to probe the density and velocity structure within collapsing cores (Rawlings et al. 1992; Rawlings & Yates 2001; Tsamis et al. 2008). The chemical composition in a collapsing core is governed by the initial abundances of atoms and molecules, the assumed dynamical model of collapse and temperature change within the core, and the chemical models of molecule formation and destruction. Whereas most studies to date, use the output of the chemical model to analyse the spectral line profiles, few studies (e.g. Li et al. 2002) have used the ionization fractions as determined by the chemical model to feed back

into the magnetohydrodynamical model in order to study in a consistent manner the interaction between charged and neutral particles. Due in part to the lack of such studies, little is known about the spectral features that might be expected if ambipolar diffusion plays a significant role in the collapse of pre-stellar cores. Many studies have performed linewidth studies of dense cores (e.g. Myers & Benson 1983) but within the limits on frequency resolution of the observing equipment, do not find linewidth differences that would suggest a velocity difference or drift velocity between ions and neutrals. Perhaps the only statistically significant constraint on the drift velocity is an upper limit, $V_{drift} \leq 30 \text{ ms}^{-1}$, based on the observational limitations of a study of 60 dense cores (Benson et al. 1998). The authors stress that these observations do not confirm ambipolar diffusion, rather they provide an upper limit to the drift velocity that could exist without detection by their equipment. Other observations suggest that the standard model of star formation (Shu 1977), the quasi-static collapse to a singular isothermal sphere followed by an inside-out collapse that forms a protostar within a freefall time, may not be correct for at least some cores: observations of the pre-stellar core L1544 by Tafalla et al. (1998) indicate that large infall velocities exist at radii predicted to have near-static velocities by the standard model; protostellar cores have a density distribution that are more centrally condensed than the standard model (Evans et al. 2001).

Estimates of lifetimes of pre-stellar cores have been made by comparing the relative populations of starless cores with that of cores with embedded young stellar objects and extrapolating back from the ages of T Tauri stars (Kirk et al. 2005; Beichman et al. 1986; Lee & Myers 1999). Kirk et al. (2005) find the lifetime of starless cores to be roughly 3 times the free-fall time for starless cores with central volume density $n(\text{H}) \simeq 5 \times 10^4 \text{ cm}^{-3}$ and twice the free-fall time for starless cores with $n(\text{H}) \simeq 2 \times 10^5 \text{ cm}^{-3}$. A possible explanation for the slowing down of purely free-fall collapse of pre-stellar cores is ambipolar diffusion. Rawlings et al. (1992), hereafter R92, modelled the effects of ambipolar diffusion on the time-evolution of the chemistry by multiplying the gravitational constant, G , by a single retardation factor, $f_B \leq 1$, to slow down gravity-induced free-fall collapse. While this approach offers the benefit of being simple to include in dynamical models, the choice of f_B is somewhat arbitrary and applies indiscriminately to all points in a multi-point model. This thesis builds on the chemical model presented by R92, but differentiates itself by using a self-consistent chemical-MHD model describing the interaction between the neutral particles (that are not directly affected by the magnetic field) and charged

particles (that are directly affected by the magnetic field). The prime objective of this thesis is to identify features of molecular line profiles that are consistent with ambipolar diffusion-driven collapse while being absent from models without ambipolar diffusion.

The remaining chapters are organised as follows. Chapter 2 formulates the problem of ambipolar diffusion in a spherical core and gives the method of solution. Chapter 3 defines the parameters that are used by a standard model and model variations: in order that the sensitivity to model parameters can be tested, a set of model variants are defined that in general change just a single parameter compared to the standard model. The results of the standard model are presented in Chapter 4. This chapter analyses the model output for the density, velocity and species abundances as a function of radial distance from the core centre. The resulting spectral line profiles of HCO^+ and CS are also analysed and discussed in the context of observational data. Chapter 5 models the linewidth difference between optically thin lines of C^{18}O , HC^{18}O^+ , NH_3 and N_2H^+ in order to determine whether the method of linewidth differencing can be used to determine the difference between infall velocities of ions and neutral species. Chapter 6 compares the results of the model variants against the standard model and observational data. Chapter 7 models the expected dust continuum emission from all models and compares the synthetic submillimetre emission profiles with observational data. Chapter 8 models the collapse of a core and extended envelope and compares the results with the core-only models. Chapter 9 discusses the results in the context of other models that also attempt to model the dynamics and chemistry of collapsing pre-stellar cores self-consistently. This chapter also gives the conclusions.

Chapter 2

Model

He has got himself “imbrangled” as they call it – fine old English word, that. Now what has the foolish lad done here? The ninth lead should bring Queens change – let me see, let me see – 51732468, 15734286 – thats the first thirds and fourths all right – 51372468, 15374286 – and thats the first fourths and thirds – 13547826 – Ah! here is the trouble! The eighth should be at home. What has happened? – To be sure! What a beetle-headed cuckoo I am! He has forgotten to make the bob.

Dorothy L Sayers, The Nine Tailors

The model presented in this chapter is taken from Stace and Rawlings (2014a), in preparation. The model, in conjunction with the model parameters defined in Chapter 3, is used to derive the core dynamical and chemical properties for the results presented in subsequent chapters. The initial version of the code was taken from R92 and updated to include the following:

1. The chemistry at multiple points or shells within the test core is followed, allowing the radial change in ionization fraction to be used with the model of ambipolar diffusion.
2. While R92 uses the Shu inside-out collapse model to define the change in density over time, the updated code uses a new algorithm to calculate the collapse rate due to gravity, thermal pressure and ambipolar diffusion within the test core; no a priori

assumption is made regarding the density profile in collapsing core other than assuming an initially constant radial density profile. It is assumed that the core condenses out from an isolated core complex with its inter-core gas having an approximately flat density distribution. A constant density and magnetic flux density are used as boundary conditions for the collapsing core; the boundary conditions are designed to simulate a constant pressure exerted by the inter-core gas.

3. A new algorithm is used to determine the visual extinction at any shell in the core: a variable dust-gas ratio is taken into account.

These updates were implemented as part of this thesis using code written in Fortran 95.

2.1 Core morphology

The multi-point model presented here uses a grid of spherically symmetric shells – the chemistry of each shell is followed throughout the collapse. The geometry of the magnetic field is assumed to be cylindrical – magnetic field lines always stay parallel throughout the collapse (Figure 2.1a); this is far from ideal and is probably only realistic for a thin disk in the central plane of the collapsing core. Several authors (Larson 1969; Shu 1977) have assumed spherical symmetry in models of collapsing protostars while Mouschovias & Paleologou (1979) argue that a thin disk model is more appropriate when including magnetic fields. Studies by Jones et al. (2001) show the morphology to be triaxial with cores being more oblate than prolate. While the model presented here does not attempt to address the axisymmetric nature of protostellar collapse as studied by Mouschovias & Paleologou (1979), the assumption of spherical symmetry allows a simple calculation of the gravitational force on each shell and importantly, the computationally expensive chemistry calculations are only required at a single point for each shell. This approach of simplifying the geometry to spherical symmetry when modelling ambipolar diffusion has been used by other workers, e.g. Safier et al. (1997) ignore the magnetic tension term associated with contracting field lines so that spherical symmetry can be assumed.

Since the MHD equations used in this model (§2.4) apply equally to all points with the same radial distance R from the core centre, a more accurate morphology is that of a randomly orientated magnetic field (Figure 2.1b). The component of mean magnetic field vector that is perpendicular to the direction of radial infall or outflow has a magnitude

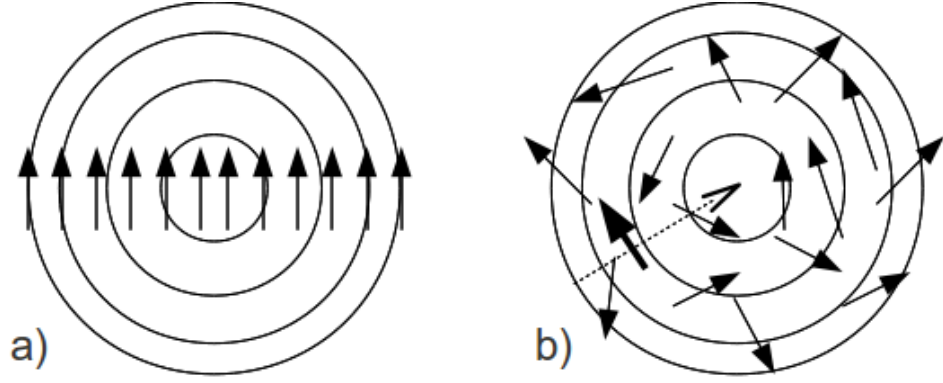


Figure 2.1. Core Morphology.

a) Model core morphology: gas enclosed by spherical shells; parallel magnetic fields lines follow cylindrical geometry in disk going into the page. b) Model core is equivalent to a randomly oriented distribution of magnetic field lines: the component of mean magnetic field vector that is perpendicular (thick arrow) to the direction of radial infall or outflow (dashed arrow) has a magnitude that is spherically symmetric.

that is spherically symmetric, i.e. each point on a sphere of radius R , experiences the same retarding effect due to the gradient in the magnetic pressure. Studies show that in star-forming regions the magnetic field is generally well ordered. However, field lines are not perfectly aligned. Chapman et al. (2011) used infrared polarimetry to study the magnetic field structure in the Taurus molecular cloud: 5 dense filamentary subregions and 2 diffuse subregions were studied. In the dense filamentary subregions, the dispersion of the polarisation angle, weighted relative to the number of observations in each subregion, is $\sim 25^\circ$. The dispersion angle is a function of the magnetic field strength: the higher the magnetic field strength, the weaker the impact turbulence has in distorting the magnetic field lines. The Pipe Nebula has a strong, well ordered magnetic field (Franco et al. 2010): in the B59 core complex, the only star-forming region of the Pipe Nebula, the mean dispersion angle is $\sim 12^\circ$. These studies indicate that at least some magnetic pressure component will be acting on gas that is flowing in a direction parallel to that of the mean magnetic field, and this magnetic pressure will increase as the gas and magnetic field lines collapse into the core centre.

2.2 Drag on neutral particles due to collisions with ions and grains

Ion-neutral drag is the force associated with the collisions between neutral gas particles and charged gas particles – the latter being coupled to the magnetic field. The strength of the ion-neutral drag depends on the relative number of ions in the cloud – the higher the ionization the stronger the effects of ion-neutral drag. In a magnetically supported cloud, the ions tend to drift outward relative to the neutral particles – a phenomenon known as *plasma drift* or *ambipolar diffusion*. Ciolek & Mouschovias (1993), hereafter CM93, give the force per unit volume element of neutral gas exerted by the ions on the neutral gas as:

$$\mathbf{F}_{ni} = \frac{\rho_n}{\tau_{ni}} (\mathbf{v}_i - \mathbf{v}_n) \quad (2.1)$$

where τ_{ni} is the mean time for a collision between a neutral gas particle and an ion, ρ_n is the mass density of neutral gas particles, \mathbf{v}_i is the bulk flow velocity of the ions and \mathbf{v}_n is the bulk flow velocity of the neutrals. Assuming an abundance of helium relative to hydrogen nuclei of X_{He} , τ_{ni} is given by:

$$\tau_{ni} = (1 + 4X_{\text{He}}) \frac{m_i + 2m_{\text{H}}}{m_i} \frac{1}{n_i \langle \sigma w \rangle_{in}} \quad (2.2)$$

where $\langle \sigma w \rangle_{in}$ is the average collision cross-section between ions of mass m_i and hydrogen molecules of mass $2m_{\text{H}}$; m_{H} is the mass of a hydrogen atom. In common with CM93 the $\text{HCO}^+ - \text{H}_2$ collision cross-section of $1.69 \times 10^{-9} \text{ cm}^3 \text{ s}^{-1}$ is taken.

The charged grains also have a component of drag which must be taken into account. The mean charge on a grain, applicable to dark clouds, is assumed to be -1 (Umebayashi & Nakano 1980); it is also assumed that the more massive grains above a threshold value do not move with the magnetic field (Ciolek & Mouschovias 1996) – this is modelled by assuming a factor g_i of the grains are below this threshold value and move with the magnetic field. The calculation of the fraction of grains which move with the magnetic field takes into account the size distribution of grains, the details of which are given for the standard model in Chapter 3 – *Model Parameters*. The force per unit volume element

of neutral gas exerted by the charged grains moving with bulk flow velocity \mathbf{v}_i is (CM93):

$$\mathbf{F}_{ng} = \frac{\rho_n}{\tau_{ng}}(\mathbf{v}_i - \mathbf{v}_n) \quad (2.3)$$

The mean time for a collision between a neutral gas particle and a charged grain is given by:

$$\tau_{ng} = \frac{m_g + 2m_H}{m_g} \frac{1}{n_g \langle \sigma w \rangle_{gn}} \simeq \frac{1}{n_g \langle \sigma w \rangle_{gn}} \quad (2.4)$$

where n_g is the number density of grains, m_g is the mean grain mass and $\langle \sigma w \rangle_{gn}$ is the average grain-neutral collision rate. The grain mass has been dropped from the approximation on the right hand side of the equation since $m_g \gg m_H$. CM93 gives $\langle \sigma w \rangle_{gn}$ as:

$$\langle \sigma w \rangle_{gn} = \pi a^2 \left(\frac{8kT}{\pi \mu m_H} \right)^{0.5} \quad (2.5)$$

where a is the grain radius, k is the Boltzmann constant, μ is the mean molecular mass of the neutral gas in units of the atomic hydrogen mass and T is the temperature of the gas. Combining equations 2.4 and 2.5 allows the grain-neutral collision time to be expressed in terms of the dust-gas ratio, d_g , and the number density of hydrogen nuclei, $n(H)$:

$$\tau_{ng} = \frac{1}{n(H) \pi \langle d_g a^2 \rangle} \left(\frac{\pi \mu m_H}{8kT} \right)^{0.5} \quad (2.6)$$

The expression $\pi \langle d_g a^2 \rangle$ is the average grain area per hydrogen nucleus. The total drag on the neutrals is then:

$$\mathbf{F}_{ni} + \mathbf{F}_{ng} = \frac{\rho_n}{\tau_{nig}}(\mathbf{v}_i - \mathbf{v}_n) \quad (2.7)$$

where $\frac{1}{\tau_{nig}} = \frac{1}{\tau_{ni}} + \frac{1}{\tau_{ng}}$; τ_{nig} can be interpreted physically as the mean time for a collision of a neutral particle with either an ion or charged grain. Note that the contribution from

electrons to the total drag, \mathbf{F}_{ne} , has been neglected since the electron mass, $m_e \ll m_H$.

2.3 Force equation on neutral gas

The force equation for neutral gas particles can now be written down as (CM93):

$$\rho_n \frac{\partial \mathbf{v}_n}{\partial t} = -\rho_n \nabla \phi - \nabla P_n + \mathbf{F}_{\text{ni}} + \mathbf{F}_{\text{ng}} \quad (2.8)$$

where P_n is the neutral gas pressure and ϕ is the gravitational potential. In a spherically symmetric cloud,

$$\phi = -\frac{GM(r)}{r} \quad (2.9)$$

where $M(r)$ is the mass interior to the cloud at radius r from the centre of the cloud and G is the gravitational constant. The gas pressure P_n is given by the perfect gas law:

$$P_n = n_n kT = \rho_n C_S^2 \quad (2.10)$$

where $C_S = (kT/\mu m_H)^{0.5}$ is the sound speed in the neutral gas.

2.4 Electric and magnetic field forces on ions, electrons and charged grains

For the charged particles (ions, electrons and charged grains) under conditions typical for core collapse, the gravitational and gas pressure terms are much less than the Lorentz force due to the electric field, \mathbf{E} , and magnetic field, \mathbf{B} . Subsequently they are dropped from the force equations (CM93):

$$\rho_i \frac{\partial \mathbf{v}_i}{\partial t} = en_i (\mathbf{E} + \frac{\mathbf{v}_i}{c} \times \mathbf{B}) - \mathbf{F}_{\text{ni}} \quad (2.11)$$

$$\rho_e \frac{\partial \mathbf{v}_e}{\partial t} = -en_e(\mathbf{E} + \frac{\mathbf{v}_e}{c} \times \mathbf{B}) - \mathbf{F}_{ne} \quad (2.12)$$

$$\rho_g \frac{\partial \mathbf{v}_i}{\partial t} = -en_g(\mathbf{E} + \frac{\mathbf{v}_i}{c} \times \mathbf{B}) - \mathbf{F}_{ng} \quad (2.13)$$

where e is the charge on an electron, c is the speed of light, \mathbf{v}_e , is the bulk flow velocity of the electrons, ρ_e is the electron density and n_e is the number density of electrons. Here, an assumption is made that in dark clouds, the average charge on a grain is $-e$ (Umebayashi & Nakano 1980) and charged grains move at velocity \mathbf{v}_i , the bulk flow velocity of ions. Note that the above expressions differ from those given by CM93 in that the Lagrangian acceleration terms on the left hand side of the equation have been included for clarity. CM93 subsequently drop the acceleration terms since they are much smaller than the terms on the right hand side. Adding equations 2.11, 2.12 and 2.13 together and making use of Ampère's Law (equation 2.14), the equation giving the total current (equation 2.15) and the condition for local charge neutrality (equation 2.16) gives a total force equation for ions, neutrals and grains (equation 2.17):

$$\nabla \times \mathbf{B} = \frac{4\pi}{c} \mathbf{j} \quad (2.14)$$

$$\mathbf{j} = e(n_i \mathbf{v}_i - n_e \mathbf{v}_e - n_g \mathbf{v}_i) \quad (2.15)$$

$$e(n_i - n_e - n_g) = 0 \quad (2.16)$$

$$\mathbf{F}_{ni} + \mathbf{F}_{ng} = \frac{(\nabla \times \mathbf{B}) \times \mathbf{B}}{4\pi} = -\frac{1}{8\pi} \frac{dB^2}{dr} \hat{r} \quad (2.17)$$

where \hat{r} is the unit vector in the radial direction in cylindrical polar coordinates. In the far right of equation 2.17, parallel magnetic field lines in cylindrical polar coordinates have been used: $\mathbf{B} = B(r, t)\hat{z}$ where \hat{z} is the unit vector parallel to the magnetic field lines – the resulting term acts as a *magnetic pressure* perpendicular to magnetic field lines. Note that again the contribution from electrons to the total force, \mathbf{F}_{ne} , has been neglected since $m_e \ll m_H$. Combining equation 2.17 with equation 2.7 gives an expression for the radial ion-neutral drift velocity:

$$v_i - v_n = -\frac{\tau_{nig}}{\rho_n} \frac{1}{8\pi} \frac{dB^2}{dr} \quad (2.18)$$

2.5 Flux freezing

A distinctive feature in many astrophysical situations is that the electrical conductivity of the charged gas or plasma is high – in other words the particles have very long mean free paths. In the limit of infinite conductivity, the magnetic field behaves as if it were frozen into the plasma – this condition is known as *flux freezing* (Longair 1992). For a cylinder of charged gas with cross-sectional area A threaded by a magnetic field with flux density B and field lines parallel to the central axis of the cylinder, as the cross-sectional area decreases due to pressure on the cylinder the magnetic flux increases such that $BA = \text{constant}$. The effect on a collapsing cloud is to resist collapse – this is due to an increase in magnetic flux density and therefore increased magnetic pressure term according to (2.17). For the density range of interest in the collapsing core, $n_n \simeq 10^3 - 10^7 \text{ cm}^{-3}$, CM93 shows that the assumption of flux freezing is an excellent approximation.

2.6 Visual extinction

The visual extinction, A_V , in the core is required in the calculation of photoreactions driven by the interstellar UV field. Spitzer (1998) gives the interstellar extinction at wavelength λ as:

$$A_\lambda = 1.086 N_d Q_e \sigma_d \quad (2.19)$$

where N_d is the column density of dust grains in cm^{-2} , Q_e is the *extinction efficiency factor* and σ_d is the geometrical cross section of the grain. The dimensionless quantity Q_e is a function of λ , the grain size and shape. This relation needs to be integrated over all solid angles and grain sizes for $\lambda = 0.555 \mu\text{m}$ to arrive at the visual extinction at any point in the core. Assuming spherical grains and that Q_e is an average over the grain distribution in the core, at the centre of the core:

$$\langle N_d \sigma_d \rangle = \pi \langle a^2 d_g \rangle n(\text{H}) R \quad (2.20)$$

where $\pi \langle a^2 d_g \rangle$ is the average grain surface area per hydrogen nucleus, d_g is the ratio of grains per hydrogen nucleus, $n(\text{H})$ is the number density of hydrogen nuclei and R is the radius of the core. Instead of selecting an extinction efficiency factor with which to calculate A_V , Q_e is defined in terms of the mean A_V value observed for dark clouds, $A_{V\text{cloud}} \approx 4$ when $n(\text{H})R_{\text{cloud}} = 8 \times 10^{21} \text{ cm}^{-2}$ (Spitzer 1998):

$$Q_e = \frac{A_{V\text{cloud}}}{1.086 \pi \langle a^2 d_g \rangle n(\text{H}) R_{\text{cloud}}} \quad (2.21)$$

where R_{cloud} is the radius of the cloud. In general, to get the visual extinction at any point in the core, integration of the dust column density over all solid angles of incident radiation must be performed. A schematic diagram for a single ray of radiation is shown in Figure 2.2. The specific intensity I_ν at any point P due to radiation travelling along AP with length S is given by:

$$I_\nu(\phi, \theta) = I_\nu(0) e^{-\tau_\nu(\phi, \theta)} \quad (2.22)$$

$$\tau_\nu(\phi, \theta) = Q_\nu \sigma_d \int_0^S d_g n(\text{H}) ds \quad (2.23)$$

where $I_\nu(0)$ is the background specific intensity at frequency ν . To arrive at an ex-

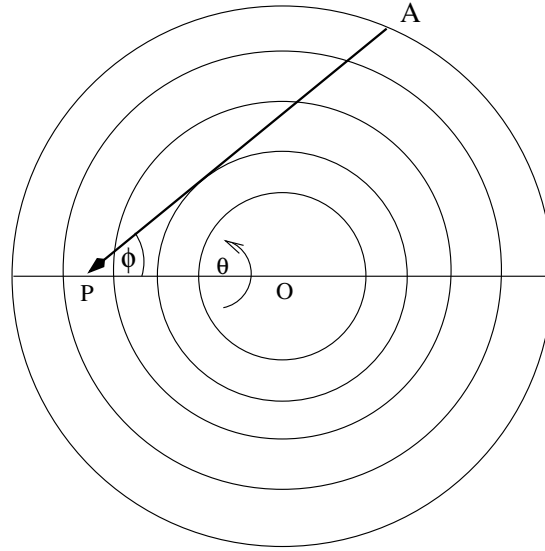


Figure 2.2. Geometry for extinction due to a single ray of radiation

pression for the total flux, equation 2.22 is integrated over all solid angles:

$$F_\nu = \frac{F_\nu(0)}{4\pi} \int_0^{2\pi} \int_0^\pi e^{-\tau_\nu \sin\phi} \sin\phi \, d\phi \, d\theta \quad (2.24)$$

$$F_\nu = \frac{F_\nu(0)}{2} \int_0^\pi e^{-\tau_\nu \sin\phi} \sin\phi \, d\phi \quad (2.25)$$

Note that to arrive at 2.25, the outer integral in equation 2.24 reduces to 2π due to symmetry around the OP axis. The extinction is then given by:

$$A_\lambda = -2.5 \log \frac{F_\nu}{F_\nu(0)} \quad (2.26)$$

In addition to the visual extinction internal to the core, an external contribution $A_{V_{ext}}$ due to the enclosing molecular cloud is assumed.

Table 2.1. Temperature T as a function of A_V

A_V	0.0	4.0	10.0	20.0	50.0
$T(\text{K})$	13.5	9.0	7.5	7.0	6.5

2.7 Temperature profile

The temperature in the core affects the gas pressure through equation 2.10 and the rates of chemical and grain reactions. A semi-empirical relationship between the visual extinction, A_V , and temperature, T , at any point in the cloud is assumed: the data in Table 2.1 are taken from figure 9 of Evans et al. (2001) for a dust temperature- A_V model where a Bonnor-Ebert sphere with central hydrogen nuclei number density $n_c = 1 \times 10^7 \text{ cm}^{-3}$ is used to model the density distribution in pre-stellar cores. The gas temperature, T_g , is assumed to be equal to the dust temperature, T_d . It is noted however, that this assumption is only valid for the denser ($n(\text{H}) \gtrsim 2 \times 10^4 \text{ cm}^{-3}$) region of the core (Takahashi et al. 1983; Doty & Neufeld 1997), where the gas-grain collision rate is high enough to maintain a strong coupling between dust and gas temperatures. Even in the densest, central region of the core, there may be some divergence between T_g and T_d due to the coagulation of small grains into larger grains, reducing the total grain surface area available for gas-grain collisions (Tafalla et al. 2002). However, one of the model variations tests the effects of using a constant $T_g = 10 \text{ K}$ temperature profile throughout the core, resulting in a small difference in the dynamical profiles, indicating that the particular choice of temperature profile is not that important in shaping the overall dynamical evolution. Interpolation using 3rd-order splines is used to derive the temperature at intermediate values to those in Table 2.1. The code used for interpolation was taken from the Public Domain Algorithm library of the Starlink software collection (Meyerdierks et al. 2005).

2.8 Chemical model

The chemical composition in the collapsing core is governed by the initial abundances of elements and the models of molecule formation – this in turn determines the ionization in the cloud and therefore the value τ_{mig} as described in the dynamical model. In most cases where the chemical behaviour of a core is being modelled, hundreds of strongly-coupled ordinary differential equations need to be solved. This is most easily done using

an integrator called GEAR (Gear 1971) – generic code which is used to solve *stiff* ordinary differential equations: this code is well-suited to solving such problems in astrochemistry. For the solution of molecular abundances in this model, 1067 reactions are used – reaction rates are primarily taken from the UMIST 1995 reaction rate file (Millar et al. 1991, 1997). Note that the effects of using more recent updates to the UMIST database (Woodall et al. 2007; McElroy et al. 2013) are discussed in chapter 9. For each reaction, three parameters are given: α , β and γ . The reaction types modelled are:

1. Neutral-neutral reactions. The rate coefficient is calculated as

$$k = \alpha(T/300)^\beta e^{-\gamma/T} \text{ cm}^3\text{s}^{-1} \quad (2.27)$$

where T is the kinetic gas temperature. The component $(T/300)^\beta$ of the above equation is associated to the kinetic energy of the reactants – i.e. the higher the kinetic energy of the the reactants the more likely a collision takes place; the $e^{-\gamma/T}$ component of the above equation is associated to an activation barrier – the excess energy over that of the ground state for a reaction to occur – in general the higher the kinetic temperature of the gas, the higher the proportion of reactants having sufficient energy to overcome the activation barrier.

2. Ion-neutral reactions. The same rate coefficient as for neutral-neutral reactions applies here – in general there is no barrier to ion-neutral reactions, so in most cases γ is zero.
3. Electron reactions, including radiative and dissociative recombination of positive ions. Here the activation barrier is implicitly zero i.e. γ is zero in the above equation for neutral-neutral reactions.
4. Ionization by cosmic-ray protons. The rate coefficient is calculated using $k = \alpha s^{-1}$.
5. Photoreactions driven by the interstellar UV radiation field. The reaction rate is calculated as $k = \alpha e^{-A_V \gamma} s^{-1}$. A departure from the UMIST 1995 database is to take a modified CO photodissociation rate based on detailed modelling of the Taurus molecular cloud by van Dishoeck & Black (1988), $k = 2 \times 10^{-10} e^{-6.5 A_V} s^{-1}$, that takes into account self-shielding and shielding from lines of H_2 and H.

6. Cosmic-ray-induced photoreactions. Photoreactions result from cosmic rays ionizing H_2 , which generate secondary electrons - these electrons then excite electronic states of H_2 , the decays of which produce an ionizing/dissociating UV flux (Prasad & Tarafdar 1983). The rate coefficient is $k = \alpha\gamma/(1 - \omega)\text{s}^{-1}$ where ω is the grain albedo: this model uses $\omega = 0.5$ - the same value as used by R92.

2.9 Grain reactions

Additionally, 80 reactions involving freeze-out of molecules, ions and atoms onto grains is governed by:

$$\frac{dn_j}{dt} = 4.57 \times 10^4 d_g a^2 T^{1/2} C n_H S_j m_j^{-1/2} n_j \text{ cm}^{-3} \text{ s}^{-1} \quad (2.28)$$

(Spitzer 1998; Umebayashi & Nakano 1980) where S_j is the sticking coefficient, m_j is the molecular mass of species j in amu and C is a factor which takes into account electrostatic effects. The average grain charge, applicable to dark clouds, is assumed to be -1, in which case: $C = 1$ for neutral species; $C = 1 + (16.71 \times 10^{-4}/aT)$ for singly charged positive ions. To arrive at a mean reaction rate, equation 2.28 needs to be averaged over all grain radii: for neutral species $C d_g a^2$ is replaced by $\langle d_g a^2 \rangle$ while for singly charged positive ions with $a \ll 10^{-4} \text{ cm}$, $\langle C d_g a^2 \rangle \simeq 16.71 \times 10^{-4} \langle d_g a \rangle / T$. He^+ and Na^+ ions that collide with grains are assumed to return to the gas phase as neutral He and Na, which with H_2 are assumed to be inert with respect to grains. S^+ ions that collide with grains also return to the gas phase as neutral S. However, neutral S freezes out onto grains. In this model, d_g varies with time due to the drift velocity of charged gas relative to the velocity of neutral gas. There is observational evidence that freeze-out of CO and H_2O onto grains will only occur where the visual extinction is above a critical value: for the Taurus dark cloud, $A_{V\text{crit}} \geq 3$ (Teixeira & Emerson 1999). In this model we assume that this critical visual extinction applies to all other molecular species.

The model does not take into account desorption effects: that is the return of molecular species to the gas phase by the heating of grain mantles. Willacy et al. (1994) conclude that: desorption effects may result in marginal changes in line profiles of commonly observed species; the effects will be most important where the cloud remains in a state of hydrostatic equilibrium over an extended period of time. It is noted that in this model,

where the timescale for collapse can be extended over several million years, desorption is likely to be important in keeping the core chemically young. It is expected that the results may underestimate the strength of the synthetic line profiles. To some extent, the adoption of a critical visual extinction helps to alleviate this effect – this ensures the chemistry is kept *young* until $n(\text{H}) \geq 10^4 \text{ cm}^{-3}$.

2.10 Model solution

The integrator GEAR is called initially for a constant density period $t_{cd} = 1 \text{ Myr}$ to solve the chemical ordinary differential equations for a grid of 100 concentric shells with outer radius r_s . A long constant density phase is chosen in order to establish a state close to chemical equilibrium. A finite difference algorithm, developed as part of this thesis specifically for the solution of this problem, is used to solve the dynamical equations 2.8 and 2.18: the collapse of each shell with constant mass is followed – i.e. the Lagrangian form of the equations are solved. A detailed description of the algorithm is given in Appendix A. The boundary condition at the core edge is based on the assumption that the core is embedded in a core complex having an approximately flat inter-core gas density distribution. The gas density and magnetic flux density are constant in the inter-core medium. This is modelled by setting a boundary region in the outermost 10 shells ($N=91..100$) of the core: all shells in the boundary region are kept at a constant gas density and magnetic flux density. Implicit in this assumption is the condition that the drift velocity between ions and neutrals is zero in this region. The choice of 10 shells in the boundary region is somewhat arbitrary, other than it needs to have at least 3 shells in order to satisfy requirements of a 3rd order spline-fitting routine applied at the boundary of the core. Tests showed that the model was left unaffected by choosing a larger number of shells in the outer boundary. The inner boundary is defined to be *reflecting* in the sense that all values at r_{-s} are equal to values at r_s – this allows the spline calculations to give accurate values at r_1 . After a dynamical time-step $\Delta t_D = 10 \text{ yr}$, the model calculates neutral and charged gas radii r_{is} for each shell. The difference between r_s and r_{is} represents the spatial drift between charged and neutral particles after a dynamical time-step. Using the flux freezing equation (§2.5), revised magnetic flux densities are calculated and mapped onto the new neutral gas radii using piecewise constant interpolation. Similarly, the spatial drift between the charged and neutral particles is used to calculate revised number densities for charged

particles at the new neutral gas radii, again using piecewise constant interpolation. The dynamical model is repeated $\Delta t_C / \Delta t_D$ times where $\Delta t_C = 10000$ yr is the chemical time-step. Subsequently, the visual extinction and temperature in the core are recalculated and GEAR is called for a period Δt_C with revised number densities of hydrogen nuclei and charged particles. Ideally, Δt_C should be small enough such that the overall change in ionization fraction as a fraction of the ionization level is small. Tests showed that reducing Δt_C to 1000 yr did not give ionization fractions significantly different to those calculated when $\Delta t_C = 10000$ yr, indicating that there was little benefit in using the smaller value.

Note that Δt_D is much shorter than Δt_C since the dynamical model is computationally less expensive than the chemical model and its solution only converges with sufficiently small time-steps. The choice of $\Delta t_D = 10$ yr was determined by trial and error: using a much larger value of Δt_D does not provide enough accuracy in the results and leads to *jump* conditions whereby a shell's radial distance advances beyond the boundary of the adjoining shell; using a smaller value resulted in longer integration times without adding noticeable benefits to the accuracy or stability of the solution. A calculation was also made to ensure that Δt_D did not violate the Courant-Freidrichs-Lewy (CFL) stability condition (Courant et al. 1928), that $\Delta t_D \leq \Delta x / \sqrt{(C_s^2 + V_A^2)}$ where Δx is the distance between adjoining shells, C_s is the sound speed and V_A is the Alfvén velocity. The stability condition prohibits the sending of information across a shell faster than the integration time step. In the case of magnetohydrodynamic equations, the maximum speed that information can be sent across a shell is given by the fast-mode Alfvén wave velocity: $V_{fast} = \sqrt{(C_s^2 + V_A^2)}$. Using sample values from the end of the standard model run, when the core is at its densest and the separation between shell is least, gives the following typical values in the outer region of the core: $\Delta x \sim 5 \times 10^{13}$ m; $V_{fast} \sim 350$ ms⁻¹. Using these parameters it can be seen that the CFL condition holds in the outer core: $\Delta t_D \leq 4500$ yr. Similarly, using values of $\Delta x \sim 1 \times 10^{14}$ m and $V_{fast} \sim 300$ ms⁻¹ for the central shell also shows that the CFL condition holds: $\Delta t_D \leq 10000$ yr.

2.11 Code validation

The computer code is tested using a number of simplified collapse scenarios and subsequently comparing the results with simple analytical models.

2.11.1 Freefall time

A test is used to check whether the dynamical time-step, Δt_D , is sufficiently small enough to ensure the accuracy of collapse timescales and infall velocities when the core is collapsing due to the force of gravity alone. This test requires the use of a constant temperature of 10 K throughout the core and the initial magnetic flux density to be set to a negligibly small value. These conditions ensure that: a) there is no pressure gradient in the central shell due to a radial temperature gradient; b) since the magnetic flux density is small, the core can collapse for a longer period ($= 0.7$ Myr) without being affected by the retarding effect of a gas pressure gradient. At later times into collapse, the pressure perturbation that originates at the core edge (due to the density being held constant in the outer 10 shells) will have reached the inner shell and will retard the collapse. Up to this point, collapse of the inner shell is governed purely by gravity – as such this provides an opportunity to test the accuracy of the finite difference algorithm when calculating infall velocities due to the force of gravity. Using equation 6.1, the time taken for the inner shell to collapse to a density of $n(\text{H}) = 1.977 \times 10^4 \text{ cm}^{-3}$ is 0.69984 Myr. This compares with a collapse time of 0.7 Myr, giving an error of 160 yr or 0.023 percent. This would indicate that setting $\Delta t_D = 10$ yr gives reasonably accurate results.

2.11.2 Sound speed

A test is used to check the response of the model due to a gas pressure perturbation, excluding the contribution from the magnetic field, i.e. to test how a sound wave propagates through the model core. The initial collapse phase can usefully be used to calculate the speed of sound at which a gas pressure perturbation propagates through the core. This test requires the use of a constant temperature of 10 K throughout the core in order that the sound speed remains constant. The initial magnetic flux density is set to a negligibly small value in order for the test to eliminate any contribution from the magnetic field to the sound speed. The radial density profile is initially flat. As collapse proceeds, a wave travels from the core edge in towards the centre: the wave is in response to having a boundary condition at the core edge that has constant pressure while the remainder of the core has pressure that increases over time due to the collapse of the core under the force of gravity. The radial density profile remains flat for those shells which have not yet been caught up by the wave. For these shells, the infall velocity will be governed by

the force of gravity. The mean velocity at which the head of the wave propagates can be estimated by recording the radial distances r_0 and r_1 of a *start* shell at time t_0 and an *end* shell at time t_1 ; these are the shells closest to the core centre that show signs of a fall-off in density relative to the flat section of the radial density profile. The mean velocity of the wave as it travels between the two shells, relative to a fixed frame of reference is then $V_s = (r_0 - r_1)/(t_1 - t_0)$. The bulk flow velocity of the gas is non-zero, therefore an adjustment is made to subtract the mean infall velocity between the start and end shells to arrive at an estimate of the sound speed: $C_s = V_s - 0.5(V_0 + V_1)$ where V_0 and V_1 are the (positive) infall velocities at the start and end shells respectively. The calculation of the adjusted sound speed is likely to be subject to errors due to the uncertainty around the actual variation in infall velocity of the density perturbation. The uncertainty can be minimised by choosing test shells early on in the collapse so that the difference between V_0 and V_1 is small. The estimate of C_s is also subject to errors due to the resolution of the spherical grid, i.e. the measurement of the exact position of the head of the wave is uncertain by the distance between the shells. A reasonably long time interval is therefore required in order to minimise resolution errors. An example calculation uses start and end shells between 0.1 Myr and 0.2 Myr into collapse – the following parameters are taken from the model output: $r_0 = 7.592 \times 10^{15}$ m, $r_1 = 6.807 \times 10^{15}$ m, $V_0 = 40$ ms⁻¹, $V_1 = 75$ ms⁻¹. Using these parameters, the estimated sound speed, $C_s = 191$ ms⁻¹, compares well with the actual sound speed of 188 ms⁻¹. However, the estimate of C_s may be out on average by $\sim \pm 9$ ms⁻¹ due to resolution errors, indicating that the model is accurate to within $\sim \pm 4.7$ percent of the actual sound speed.

2.11.3 Magnetosonic speed

A test is used to check the response of the model due to a perturbation in both the gas pressure and magnetic flux density, i.e. to test how a magnetosonic wave propagates through the model core. The test is almost identical to the test used to assess the accuracy of the sound speed in the core (§2.11.2); in this case the initial magnetic flux density is set to $B = 6.44$ μG . During the early stages of collapse, neutrals and ions will be tightly coupled due to the high ionization levels – this period can be used to analyse the behaviour of the model core under ideal MHD conditions (no ambipolar diffusion). Since the direction of the magnetosonic wave is perpendicular to the direction of field lines, the test will check the accuracy of the fast mode Alfvén wave speed, $V_{ms} = (V_A^2 + C_s^2)^{0.5}$ where V_A is the

Alfvén velocity. One difference between this test and the sound speed test is the need to take into account the variation in V_A as the core collapses. The estimated value of V_{ms} is therefore compared with an analytic value that uses a mean V_A between the start and end shells. The estimate of the magnetosonic speed is given by: $V_{ms} = V_s - 0.5(V_0 + V_1)$ where the definitions of V_s , V_0 and V_1 are identical to those used in §2.11.2. The estimate of the magnetosonic speed is subject to the same errors that affect the accuracy on the estimate of the sound speed. An example calculation uses start and end shells between 0.1 Myr and 0.2 Myr into collapse – the following parameters are taken from the model output: $r_0 = 7.223 \times 10^{15}$ m, $r_1 = 6.085 \times 10^{15}$ m, $V_0 = 38$ ms⁻¹, $V_1 = 66.5$ ms⁻¹. Using these parameters, the estimated magnetosonic speed, $V_{ms} = 308.5$ ms⁻¹, compares with the average analytic value for the magnetosonic speed of 304.5 ms⁻¹. However, the estimate of V_{ms} may be out on average by $\sim \pm 10$ ms⁻¹ due to resolution errors, indicating that the model is accurate to within $\sim \pm 3.3$ percent of the analytically derived magnetosonic speed.

2.11.4 Magnetic flux conservation

A test is used to check that the total magnetic flux is conserved. As the core collapses, the magnetic field will drift outwards relative to the motion of the neutral gas. However, the magnetic flux, $\phi = BA$, where B is the magnetic flux density and A is the area perpendicular to the magnetic field lines, should remain constant when summed over all shells in the collapsing core. The test ignores the contribution to ϕ from the outermost 10 shells since B is set to a constant value in these shells. Results from the standard model (§4) are used to test magnetic flux conservation: the total flux at the start of the model run, ϕ_0 , is compared to the total flux at the end of collapse, ϕ_1 , giving a ratio of $\phi_0/\phi_1 = 0.999938$, indicating that the error in total magnetic flux is ~ 0.006 percent.

2.11.5 Dust conservation

A test is used to check that the total number of dust grain particles is conserved. As the core collapses, the magnetic field will drift outwards relative to the motion of the neutral gas. Charged dust grains are tied to the motion of the magnetic field while massive grains and neutral grains will follow the motion of the neutral gas. However, the total number of dust grains should be conserved. The total number of grains in the core is equal to the summation of the dust-gas ratio, Dg , within each shell multiplied by the mass of each

shell. Since the mass of each shell is the same, the summation of Dg over all shells should remain constant. The test ignores the contribution to the total dust-gas ratio from the outermost 10 shells since Dg remains constant in these shells. Results from the standard model (§4) are used to test dust conservation: the summation of the dust-gas ratios at the start of the model run, Dg_0 , is compared to the summation of dust-gas ratios at the end of collapse, Dg_1 , giving a ratio of $Dg_0/Dg_1 = 0.999998$, indicating that the error in total dust mass is ~ 0.0002 percent.

2.11.6 Modelling a Bonnor-Ebbert sphere

A test is used to check the behaviour of the model when the initial density profile is that for an isothermal core in hydrostatic equilibrium, i.e. the density profile for a Bonner-Ebbert (BE) sphere (see Figure 1.6). This test requires the use of a constant temperature of 10 K throughout the core giving a sound speed of $C_s = 188 \text{ ms}^{-1}$. The initial magnetic flux density is set to a negligibly small value in order to remove any support against gravitational collapse due to a gradient in the magnetic pressure. A density profile for a stable BE sphere is chosen with a density contrast of $n_0/n_{ext} = 6.0$ where n_0 is the number density of hydrogen nuclei, $n(\text{H})$, at the core centre and n_{ext} is $n(\text{H})$ external to the core. The density of the outer 10 shells are kept constant at $n(\text{H}) = 2.8 \times 10^3 \text{ cm}^{-3}$. Each of the 100 shells of the model has a mass of $M_{\text{BE}}/90$ where $M_{\text{BE}} = 2.74M_{\odot}$ is the mass of the BE sphere; the boundary of the BE sphere, $R_{\text{BE}} = 4.875 \times 10^{17} \text{ cm}$, is at shell 90. The density profile is calculated by solving numerically the Lane-Emden equations for an isothermal sphere (Binney & Tremaine 1987; Liu 1996):

$$\frac{d^2\omega}{d\xi^2} + \frac{2}{\xi} \frac{d\omega}{d\xi} = e^{-\omega} \quad (2.29)$$

where $\xi = (\frac{4\pi G \rho_0}{C_s^2})^{0.5} R$ is the dimensionless radius, ρ_0 is the mass density at the centre of the sphere and ω is related to the density ρ at radial distance R by $\rho = \rho_0 e^{-\omega}$. Since the BE sphere is in hydrostatic equilibrium, the initial calculation of the pressure gradient by the finite difference algorithm (Appendix A) can be checked for accuracy: from equation 2.8, in the absence of any drag due to ions or charged grains on neutral particles, equilibrium requires that the pressure gradient term is equal in magnitude to the gravitational force at each shell. Excluding shells 1,2 and 90 (the innermost 2 shells and the shell at the boundary of the BE sphere), the root mean square error in the percentage difference between the force due to the pressure gradient (as calculated by the model) and the force of gravity is found to be 0.2 percent. The force due to the pressure gradient at the boundary of the BE sphere (shell 90) is 49 percent of the gravitational force – this is due to the smoothing out of the radial change in density between the boundary of the BE sphere (which falls off as approximately $n(\text{H}) \propto R^{-2}$) and the flat radial density profile in the outer 10 shells of the core. There is also a general tendency for the error to increase with decreasing distance to the core centre: the force due to the pressure gradient at shell 2 is 96.5 percent of the

gravitational force while for the innermost shell the pressure gradient accounts for 76.4 percent of the gravitational force. The reason for the larger errors in the inner shells is due to the finite difference algorithm using mean density values (between successive shell boundaries) to calculate the pressure gradients. As the radial distance between adjoining shells becomes larger and the density profile flattens out, as in the case for shells that are closer to the core centre, the differences between mean density values and *spot* values at shell boundaries become more significant. It is this difference that affects the accuracy of the finite difference algorithm. The spline-fitting routine that calculates the density and pressure gradient at the inner shell helps reduce this error: without using the spline-fitting routine the pressure gradient accounts for only 50 percent of the gravitational force. Nevertheless, despite these errors inherent at the boundaries of the BE sphere, Figure 2.3 shows that after time $t = 3$ Myr, the density profile (solid line) remains similar to the initial density profile of the BE sphere (dashed line), indicating that the model closely approximates a core in hydrostatic equilibrium. There is a marginal departure between the density profiles in the inner shell, due to the larger error in the calculated pressure gradient. However, the core is very nearly static, having infall velocities: $|v_n| \lesssim 2 \text{ ms}^{-1}$. Although not noticeable in the plot of density profiles, the boundary of the BE sphere has moved inward by 0.014 percent of its initial value. This is understandable since initially the magnitude of the force due to the pressure gradient at the boundary of the BE sphere is approximately half that of the gravitational force, giving rise to a net force that compresses the BE sphere. However, this compression appears to have little impact on the overall shape of the density profile.

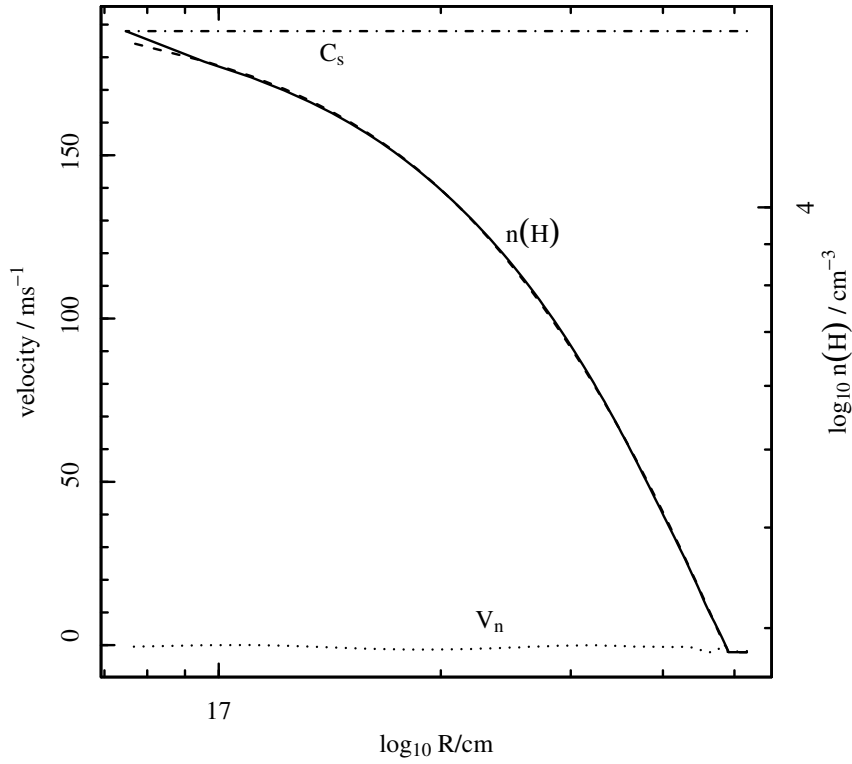


Figure 2.3. Modelling a Bonnor-Ebert sphere with a central density to external density contrast of $n_0/n_{ext} = 6.0$.

Dashed line shows the initial density profile; solid line shows the the density profile after time $t = 3$ Myr into the model run. Dotted line plots the infall velocity, V_n . Dot-dashed line shows the sound speed, C_s .

Chapter 3

Model Parameters

Whether we are based on carbon or silicon makes no fundamental difference. We should each be treated with appropriate respect.

2010, Arthur C Clarke & Peter Hyams

The initial physical conditions for the test core (mass, external visual extinction, magnetic field strength) are loosely based on observations of the pre-stellar core, L1544. The particular choice of L1544 is due to the strong observational evidence suggesting infall dynamics in the inner and outer regions of the core (Tafalla et al. 1998; Williams et al. 1999; Crapsi et al. 2005; Caselli et al. 2012). Using physical conditions consistent with L1544, allows the results to be compared with several other models that attempt to follow the dynamical evolution of the same core (see section 9.1). However, the initial chemical conditions of the test core are not based on observations of any specific core, rather they use typical values for those cores which have been observed. The approach taken here is to define a set of parameters for a *standard* model; the parameters are representative of a typical pre-stellar core. The parameter set is then varied, often by changing a single parameter, so that the sensitivity to a change in a particular parameter can be tested. The variation in parameter values are chosen to be within the upper and lower bounds of that suggested by supporting observational or theoretical data. The parameter sets are taken from Stace and Rawlings (2014a), in preparation.

Table 3.1. Elemental abundances relative to hydrogen

Element	Relative abundance
H	1.0
He	0.0763
C	3.75×10^{-4}
N	1.15×10^{-4}
O	6.74×10^{-4}
Na	2.19×10^{-7}
S	1.62×10^{-6}

3.1 Chemistry

3.1.1 Standard model

The initial conditions assume that C, N, O, Na and S are all in ionized atomic form while H is molecular and He is atomic. The initial number density of hydrogen atoms, $n(\text{H}) = 2.8 \times 10^3 \text{ cm}^{-3}$, and the gas phase elemental abundances relative to hydrogen are taken from R92. Note that the initial chemical conditions are different to the R92 model, which assumed a cycle of chemical enrichment from stellar-winds and high gas-phase abundances of some species such as NH_3 due to the shock-induced sputtering of material from grains. Here, a long constant density phase (1 Myr) prior to the onset of collapse ensures that molecular species have reached near-equilibrium values. The initial gas phase elemental abundances relative to hydrogen are given in Table 3.1. The mean molecular mass, $\mu = 2.2648$, is derived from the tabulated relative abundances of hydrogen and helium nuclei. In common with R92, the sticking coefficient in equation 2.28, S_i , is taken to be $\frac{1}{3}$ for neutral species and 1 for positive ions. A cosmic ray ionization rate of $\zeta = 1.3 \times 10^{-17} \text{ s}^{-1}$ is chosen: ζ is at the low end of observations from van der Tak & van Dishoeck (2000).

3.1.2 Model variations

The variations on the chemical model are given in Table 3.2. Variations on the Na and S abundances are used to simulate environments where metals are severely depleted from the gas phase. Since cosmic rays drive the ionization at high visual extinctions in dense cores, a low value for the cosmic ray ionization rate tests the sensitivity of the model to a reduced ionization fraction during the later stages of core collapse. The use of a constant

Table 3.2. Variations on the standard chemical model

Identifier	Description
temp1	the temperature is 10K throughout the core
xna1	the relative sodium abundance, $X(\text{Na})$, is reduced by a factor of 0.01
xs1	the relative sulphur abundance, $X(\text{S})$, is reduced by a factor of 0.01
zeta1	the cosmic ray ionization rate, ζ , is increased to $1 \times 10^{-16} \text{s}^{-1}$
zeta2	the cosmic ray ionization rate is decreased to $1 \times 10^{-18} \text{s}^{-1}$

temperature in the model tests whether the use of an A_V -dependent temperature profile has a significant impact on the chemistry.

3.2 Grain chemistry

The standard model assumes the freeze-out of molecules, ions and atoms onto grains according to equation 2.28. A variation on this model is investigated that assumes that the products of ion-electron recombination at the surface of grains are returned to the gas phase; the reaction rates for ion-electron recombination are governed by equation 2.28. The motivation behind this variation is due to the uncertainty about whether ions freeze-out or whether the energy released in ion-electron recombination reactions is sufficient to return them to the gas phase: Aikawa et al. (1999) conclude that in conditions relevant to dark clouds, HCO^+ is most likely to return to the gas phase as H and CO. This assumption is also consistent with other studies of collapsing cores (e.g. Aikawa et al. 2001, Ruffle et al. 1999).

Sticking coefficients are also uncertain and may range from 0.1 to 1.0 (Millar & Williams 1993); neutral-grain sticking coefficients of 0.1 and 1.0 are tested.

A further variation tests the case where equation 2.28 is modified to take into account the difference in velocity between charged grains and neutral particles, i.e. the ambipolar diffusion drift velocity, V_{drift} . Flower et al. (1985) determined an effective temperature,

T_{eff} , between ions and neutral particles that included V_{drift} :

$$\frac{3}{2}kT_{eff} = \frac{3}{2}kT_r + \frac{1}{2}m_r V_{drift}^2 \quad (3.1)$$

where: $T_r = (m_i T_n + m_n T_i)/(m_i + m_n)$ is the effective temperature between the ion and neutral particle and $m_r = m_i m_n/(m_i + m_n)$ is the reduced mass of the ion and neutral particle; m_i and m_n are the mass of the ion and neutral particle respectively; T_i and T_n are the kinetic temperature of the ion and neutral particle respectively. Substituting the grain mass, m_g , in place of the ion and assuming that $m_g \gg m_n$ gives:

$$\frac{3}{2}kT_{eff} = \frac{3}{2}kT + \frac{1}{2}m_j V_{drift}^2 \quad (3.2)$$

where m_j has been used in place of m_n to indicate the mass of neutral molecule j and the subscript n has been dropped from T_n . Equation 2.28 can now be written as:

$$\frac{dn_j}{dt} = \pi V_{jg} d_g a^2 C n_H S_j n_j \text{ cm}^{-3} \text{ s}^{-1} \quad (3.3)$$

with

$$V_{jg} = 1.46 \times 10^4 T^{1/2} m_j^{-1/2} + |V_{drift}| \quad (3.4)$$

– V_{jg} is the mean velocity difference between neutral molecule j and grains. The variations on the grain chemistry are summarised in Table 3.3.

3.3 Dust grain sizes and distribution

3.3.1 Standard model

The grain-size distribution is affected by processes that lead to an increase in mean grain size (grain growth) through grain accretion and grain coagulation, and a decrease in mean grain size without loss of total grain material (*disruption*) through *shattering* of grains by grain-grain collisions. Grains may also lose part or all of their mass back into the gas phase

Table 3.3. Variations on the standard grain chemistry

Identifier	Description
grainchem1	electron-ion combination at the grain surface returning products to the gas phase
grainchem2	freeze-out of neutrals onto grains enhanced due to neutral-grain drift velocity
stick1	neutral-grain sticking coefficient is increased to 1.0
stick2	neutral-grain sticking coefficient is decreased to 0.1

(*destruction*) via *sputtering*, the removal of near-surface molecular species from gas-grain collisions, and vapourisation of grain material from grain-grain collisions having sufficiently high impact velocities. Sputtering and shattering of grains are important processes in the warm ($\sim 10^4$ K) interstellar medium and in interstellar shocks (Jones et al. 1996). In the cold, quiescent environment of pre-stellar cores, disruption and destruction processes are assumed to have a negligible affect on the grain-size distribution. In this model, the grain-size distribution is assumed to be static. However a caveat applies to this assumption: in the dense interior of pre-stellar cores, grain agglomeration is likely to occur over the model collapse timescales (~ 4 Myr), leading to fewer but larger grains.

The average grain area per hydrogen nucleus $\pi\langle a^2 d_g \rangle$ is calculated using a grain-size distribution model for both silicate and carbonaceous grains from Weingartner & Draine (2001). Model 16 is chosen: this model has a ratio of visual extinction to reddening, $R_V = 5.5$, that is typical of dense clouds. A lower and upper grain radii of 5×10^{-7} cm and 1×10^{-4} cm are used to calculate $\langle a^2 d_g \rangle = 2.78 \times 10^{-22}$ cm²; this parameter is used to calculate A_V and freeze-out reaction rates. Note that this value is slightly higher than that used by R92: $\langle a^2 d_g \rangle = 2.2 \times 10^{-22}$ cm² for a depletion coefficient, $D = 1.0$. The average grain radius per hydrogen nucleus is calculated as $\langle a d_g \rangle = 1.7 \times 10^{-16}$ cm; $\langle a d_g \rangle$ is used to calculate the ion-grain reaction rates in equation 2.28. The relative freeze-out rates between ion-grain and neutral-grain reactions is given by:

$$16.71 \times 10^{-4} \langle a d_g \rangle / (T \langle a^2 d_g \rangle) = 102 \left(\frac{T}{10 \text{ K}} \right)^{-1} \quad (3.5)$$

Note that the neutral-grain reaction rate is of the same order to that used by R92, but

the ion-grain reaction rate is roughly 7 times that determined in R92: this is due to the use of a grain-size distribution model that includes a higher proportion of smaller grains.

The fraction, g_i , of grains that are assumed to be strongly coupled to the magnetic field is also dependent on the size distribution of grains. The condition for the charged grains to be decoupled from the magnetic field is when a grain collides with a neutral particle before it completes a full gyration about a magnetic field line (Aannestad & Purcell 1973):

$$\omega_g \tau_{gn} \ll 1 \quad (3.6)$$

where ω_g is the grain gyration frequency:

$$\omega_g = \frac{eB}{m_g c} \quad (3.7)$$

and τ_{gn} is the mean time for a grain to collide in a field of neutral particles (CM93):

$$\tau_{gn} = \frac{m_g n_g}{\mu m_H n_n} \tau_{ng} \quad (3.8)$$

Conversely, the condition that the grain is well-coupled to the magnetic field is when $\omega_g \tau_{gn} \geq 1$. Combining with equations 2.4 and 2.5 gives:

$$\frac{a}{10^{-6} \text{ cm}} \leq 6.6 \left(\frac{T}{10 \text{ K}} \right)^{-0.5} \left(\frac{B}{10^{-6} \text{ G}} \right)^{0.5} \left(\frac{n_n}{10^3 \text{ cm}^{-3}} \right)^{-0.5} \quad (3.9)$$

Using values of $n_n \simeq 10^3 \text{ cm}^{-3}$, $B \simeq 5 \times 10^{-6} \text{ G}$ as approximate initial values in the core and $n_n \simeq 10^6 \text{ cm}^{-3}$, $B \simeq 50 \times 10^{-6} \text{ G}$ as approximate values at the end of the collapse and assuming that $T \simeq 10 \text{ K}$ throughout, the corresponding limits on the grain radius are $a \leq 15 \times 10^{-6} \text{ cm}$ and $a \leq 1.5 \times 10^{-6} \text{ cm}$ respectively. Using the same grain-size distribution model from Weingartner & Draine (2001), the percentage of the total grain population that are below these values are 99.8% and 90.2% respectively. There is also an electrostatic attraction between charged grains and quasiparticles with charge $(n_g/n_i)e$ that strengthens the coupling between the charged grains and the magnetic field (Ciolek & Mouschovias 1994). This allows the charged grains to be coupled to the magnetic field

even when $\omega_g \tau_{gn} \ll 1$: the condition for grain coupling then becomes:

$$\frac{n_g}{n_i}(\omega_i \tau_{in})(\omega_g \tau_{gn}) \geq 1 \quad (3.10)$$

Ciolek & Mouschovias (1994) show that grains continue to be partially tied to the magnetic field for $n_n \leq 3 \times 10^9 \text{ cm}^{-3}$. For the standard model, $g_i = 0.9$ is taken as a reasonable approximation given that some grains will have no charge (Umebayashi & Nakano 1980).

3.3.2 Model variations

The effect of increasing the lower grain radius to $1 \times 10^{-6} \text{ cm}$ is investigated, since grain aggregation is likely to occur in dense cores over several millions years. This gives $\langle a^2 d_g \rangle = 2.13 \times 10^{-22} \text{ cm}^2$. The corresponding relative freeze-out rates between ion-grain and neutral-grain reactions is given by:

$$16.71 \times 10^{-4} \langle a d_g \rangle / (T \langle a^2 d_g \rangle) \simeq 60 \left(\frac{T}{10 \text{ K}} \right)^{-1} \quad (3.11)$$

The fraction g_i of grains that are assumed to be strongly coupled to the magnetic field is also dependent on the size distribution of grains. The standard model uses a maximum grain radius, $a = 1.5 \times 10^{-6} \text{ cm}$, above which grains do not move with the magnetic field. Using the grain distribution from DWE01, the fraction of grains that move with the magnetic field is recalculated using the lower grain radius: the percentage of the total grain population that is below the threshold radius is 58.3%; for this run of the model $g_i = 0.6$ is taken.

A further variation on the grain-size distribution assumes that grains with radius $a \leq 1.0 \times 10^{-6} \text{ cm}$ have no charge and therefore do not move with the magnetic field; this is consistent with the analysis by Umebayashi & Nakano (1980) who showed that for grains with radius $a > 1.0 \times 10^{-6} \text{ cm}$ the mean charge is -1. For models where the sticking coefficient of electrons onto grains ranges between 0.3 and 1.0, the fraction of grains with no charge on a grain with radius $a = 1.0 \times 10^{-6} \text{ cm}$ varies between 0.8 and 0.5 respectively; the fraction of grains with no charge increases with decreasing grain radius for $a < 1.0 \times 10^{-6} \text{ cm}$. Using DWE01, the percentage of grains with $a > 1.0 \times 10^{-6} \text{ cm}$

Table 3.4. Variations on the dust grain sizes and distribution

Identifier	Description
graindist1	lower grain radius increased to 1×10^{-6} cm; $g_i = 0.6$; $\langle a^2 d_g \rangle = 2.13 \times 10^{-22}$ cm ²
graindist2	grains with radius $a \leq 1.0 \times 10^{-6}$ cm have no charge; $g_i = 0.25$

is 25%, i.e. $g_i = 0.25$. The rate of freeze-out of ions onto grains is modified to a weighted average: 25% continue to freeze-out onto grains according to equation 2.28 with the charge parameter, $C = 1$; the remaining 75% freeze-out onto grains with charge parameter, $C = 0$. The variations on the dust grain sizes and distribution are given in Table 3.4.

3.4 Physical parameters

3.4.1 Standard model

A mass of $7.68M_{\odot}$ is chosen as the core mass: the mass is chosen to be 8 times the original core mass as studied in R92. The mass is similar to the core mass of L1544 as determined by Tafalla et al. (1998); L1544 is embedded in a dark cloud with $M_{cloud} \approx 28M_{\odot}$ and $n_H \approx 10^3$ cm⁻³. The contribution to A_V from the dark cloud is calculated as $A_{V_{ext}} = 0.9$. An initial density of $n(H) = 2.8 \times 10^3$ cm⁻³ is chosen so as to be consistent with the initial chemical conditions from R92; the initial radius of the cloud is then calculated as $R = 0.277$ pc (8.45×10^{17} cm). An initial magnetic flux density, $B = 6.1 \times 10^{-6}$ G, is chosen: this is lower than the observed line-of-sight value for L1544 of $B_{LOS} = 11 \times 10^{-6}$ G (Crutcher & Troland 2000) since B_{LOS} is for the higher current mean density of the core, $n(H) = 2 \times 10^4$ cm⁻³. The value of B is chosen to be marginally magnetically supercritical in the sense that core collapse is eventually halted and followed by an expansion phase before reversing again into collapse; the final collapse phase progresses towards infall velocities similar to that for free-fall collapse. The choice of B also gives an approximate mass to magnetic flux ratio of $M/\phi \approx 1.77$ in units of the critical mass to magnetic flux ratio, $1/2\pi G^{0.5}$; this is consistent with observations of several pre-stellar cores including L1544 (Crutcher et al. 2004). The constant density phase, $t_{cd} = 1 \times 10^6$ yr, is the period of time used to allow the chemistry in the core to settle to near-equilibrium values before collapse

Table 3.5. Physical parameters of the standard model

Parameter	Value
Mass	$M_{core} = 7.68M_{\odot}$
Initial Radius	$R = 0.277 \text{ pc } (8.54 \times 10^{17} \text{ cm})$
Constant density phase	$t_{cd} = 1 \times 10^6 \text{ yr}$
Magnetic flux density	$B = 6.1 \times 10^{-6} \text{ G}$
External visual extinction	$A_{Vext} = 0.9$
Critical visual extinction	$A_{Vcrit} = 3$

Table 3.6. Variations on the magnetic flux density

Identifier	Description
b1	$B_0 = 1.4 \times 10^{-6} \text{ G}$
b2	$B_0 = 2.8 \times 10^{-6} \text{ G}$
b3	$B_0 = 4.2 \times 10^{-6} \text{ G}$
b4	$B_0 = 5.6 \times 10^{-6} \text{ G}$

of the core proceeds. The physical parameters of the standard model are summarised in table 3.5.

3.4.2 Model variations

The effect of changing B_0 , the initial magnetic flux density and A_{Vcrit} , the critical visual extinction is investigated. The variations on B_0 are listed in Table 3.6. Two variations on A_{Vcrit} are considered. Model *avcrit1* models freeze-out onto grains using $A_{Vcrit} = 8.0$ and between $8.0 \leq A_V \leq 12.0$ the rate of freeze-out is multiplied by a factor between 0 and 1; the factor increases linearly with A_V between $8.0 \leq A_V \leq 12.0$. Beyond $A_V > 12.0$, the factor is equal to 1. These particular parameters are chosen in order to model freeze-out in the Ophiuchus molecular cloud, for which CO and H₂O freeze out at $A_V > 8.3 \pm 1.6$ and $A_V > 12 \pm 1$ respectively (Teixeira & Emerson 1999). Model *avcrit2* uses the same value of A_{Vcrit} as the standard model but the rate of freeze-out is multiplied by a factor between 0 and 1; the factor increases linearly with A_V between $3.0 \leq A_V \leq 7.0$. Beyond $A_V > 7.0$, the factor is equal to 1. These parameters are chosen in order that a less rapid change in freeze-out rates can be tested.

3.5 Model summary

Table 3.7 summarises all model variations in a single table for ease of reference.

Table 3.7. Model variations

Model id	Description
b1	Initial magnetic flux density $B_0 = 1.4 \mu\text{G}$
b2	Initial magnetic flux density $B_0 = 2.8 \mu\text{G}$
b3	Initial magnetic flux density $B_0 = 4.2 \mu\text{G}$
b4	Initial magnetic flux density $B_0 = 5.6 \mu\text{G}$
grainchem1	electron-ion recombination at the grain surface returning products to the gas phase
grainchem2	freeze-out of neutrals onto grains enhanced due to neutral-grain drift velocity
graindist1	lower grain radius increased to $1 \times 10^{-6} \text{ cm}$; the fraction of grains that move with the magnetic field is reduced to 0.6;
graindist2	grains with radius $a \leq 1.0 \times 10^{-6} \text{ cm}$ have no charge; the fraction of grains that move with the magnetic field is reduced to 0.25
stick1	neutral-grain sticking coefficient is increased to 1.0
stick2	neutral-grain sticking coefficient is decreased to 0.1
temp1	the temperature is kept at 10K throughout the core
xna1	the relative sodium abundance, $X(\text{Na})$, is reduced by a factor of 0.01
xs1	the relative sulphur abundance, $X(\text{S})$, is reduced by a factor of 0.01
zeta1	the cosmic ray ionization rate, ζ , is increased to $1 \times 10^{-16} \text{ s}^{-1}$
zeta2	the cosmic ray ionization rate is decreased to $1 \times 10^{-18} \text{ s}^{-1}$
avcrit1	freeze-out increases by a factor between 0 and 1, increasing linearly between $8.0 \leq A_V \leq 12.0$
avcrit2	freeze-out increases by a factor between 0 and 1, increasing linearly between $3.0 \leq A_V \leq 7.0$

Chapter 4

Results for the standard model

There is nothing like looking, if you want to find something. You certainly usually find something, if you look, but it is not always quite the something you were after.

The Hobbit, J.R.R. Tolkien

In this chapter the dynamical and chemical results for the standard model are presented. These results have been taken from Stace and Rawlings (2014a), in preparation. In section 4.1, an analysis of how the model behaves over time is presented. In section 4.2, an analysis of the radial profile of the core at two snapshots in time is presented: a core undergoing expansion and a core undergoing collapse. In section 4.3, synthetic line profiles are generated using code from Rawlings & Yates (2001).

4.1 Core dynamics over time

Figure 4.1 shows how the core behaves dynamically over time: the central density, central magnetic flux density, maximum ambipolar diffusion *drift* velocity together with the maximum and minimum ion and neutral gas velocities are plotted against time in Myr. The purpose of this figure is to help identify the periods in a core's evolution where significant velocity differences might be observed between charged and neutral molecular species. This figure shows the core initially collapsing to a central hydrogen nuclei number density of $n(\text{H}) \simeq 8 \times 10^4 \text{ cm}^{-3}$, followed by an expansion phase out to a density similar

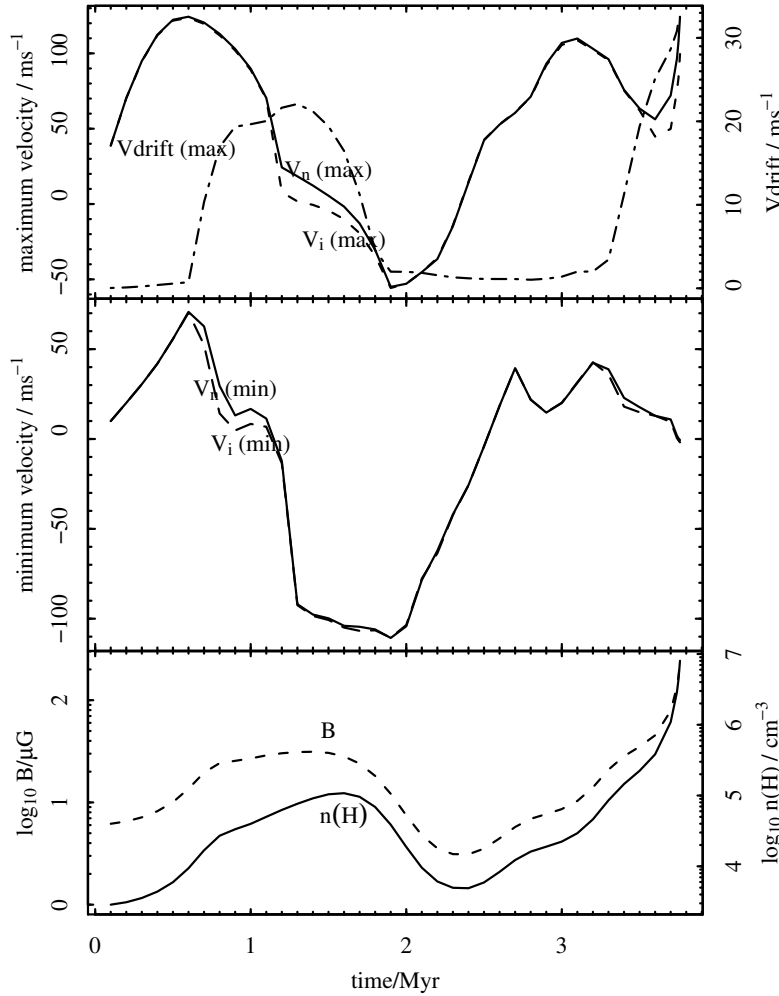


Figure 4.1. Dynamical evolution of the model core.

Negative velocities indicate expansion; positive velocities indicate infall. Upper graph plots the maximum ion velocity, V_i (max), as the dashed line and the maximum neutral velocity, V_n (max), as the solid line against the y-axis on the left; the maximum drift velocity, V_{drift} (max), is plotted as the dash-dot line against the y-axis on the right.

Middle graph plots the minimum ion velocity, V_i (min), as the dashed line and the minimum neutral velocity, V_n (min) as the solid line. For the central shell, the lower graph plots the magnetic flux density, B , as the dashed line and the hydrogen nuclei number density, $n(H)$, as the solid line.

to the starting conditions, $n(\text{H}) = 2.8 \times 10^3 \text{ cm}^{-3}$, before reversing again into a second collapse phase that proceeds to a density $n(\text{H}) > 10^7 \text{ cm}^{-3}$. At this point, the combined support from the magnetic and thermal pressure gradients is no longer able to prevent the core from collapsing to form a star. The change of the core from gravitational stability to instability is due to the reduction in the magnetic pressure support in the inner core as a result of the re-distribution of the magnetic field during the initial collapse and expansion phases. During the second collapse phase, the central magnetic flux density is reduced relative to the initial collapse phase. Note that it is not clear whether the initial collapse and expansion phase is simply the result of the model settling towards a more realistic distribution of gas and magnetic field rather than the simple starting conditions of constant $n(\text{H})$ and B . This effect was investigated by increasing B to a level where the second and subsequent collapse phases also reverse into expansion; effectively the core is magnetically subcritical and oscillates between collapse and expansion. This dynamical behaviour is similar to that found in a model of cloud collapse by Prasad et al. (1991), who divided their models between those clouds on a star-forming track and those clouds having strong magnetic fields so that at late, denser stages of cloud collapse, the combined force from the gradients in magnetic and thermal pressure is sufficient to overcome the force of gravity, and the cloud expands back out to low densities. A key difference in this model is the inclusion of ambipolar diffusion which allows the magnetic field to be re-distributed out from the core centre, allowing an initially magnetically subcritical core to become magnetically supercritical. Observations of high-mass protostellar cores for which $M_{\text{core}} > 8M_{\odot}$ (Fuller et al. 2005), low-mass protostellar cores (Mardones et al. 1997) and starless cores (Lee et al. 2001) show that a high proportion of cores ($\sim 25 - 30\%$) have self-absorbed molecular lines where the redshifted peak dominates over the blue, possibly indicating expansion. In conclusion, the initial expansion phase is a feature that can be usefully analysed as typical of expansion in general.

A peak in the maximum drift velocity occurs at $t = 1.3 \text{ Myr}$ – slightly ahead of the peak in central density occurring at $t = 1.6 \text{ Myr}$; at late times, during the second collapse phase, the maximum drift velocity increases with increasing central density. Note that a particular feature of this model is that during the period $1.2 \text{ Myr} \leq t \leq 1.5 \text{ Myr}$ in expansion and period $2.4 \text{ Myr} \leq t \leq 2.5 \text{ Myr}$ in collapse, both positive maximum and negative minimum velocities are present at the same time – i.e. the core is both collapsing and expanding in different regions of the core, at the same time. This implies that where

observations are taken over multiple regions of the core, this feature could result in both blueshifted and redshifted asymmetric line profiles.

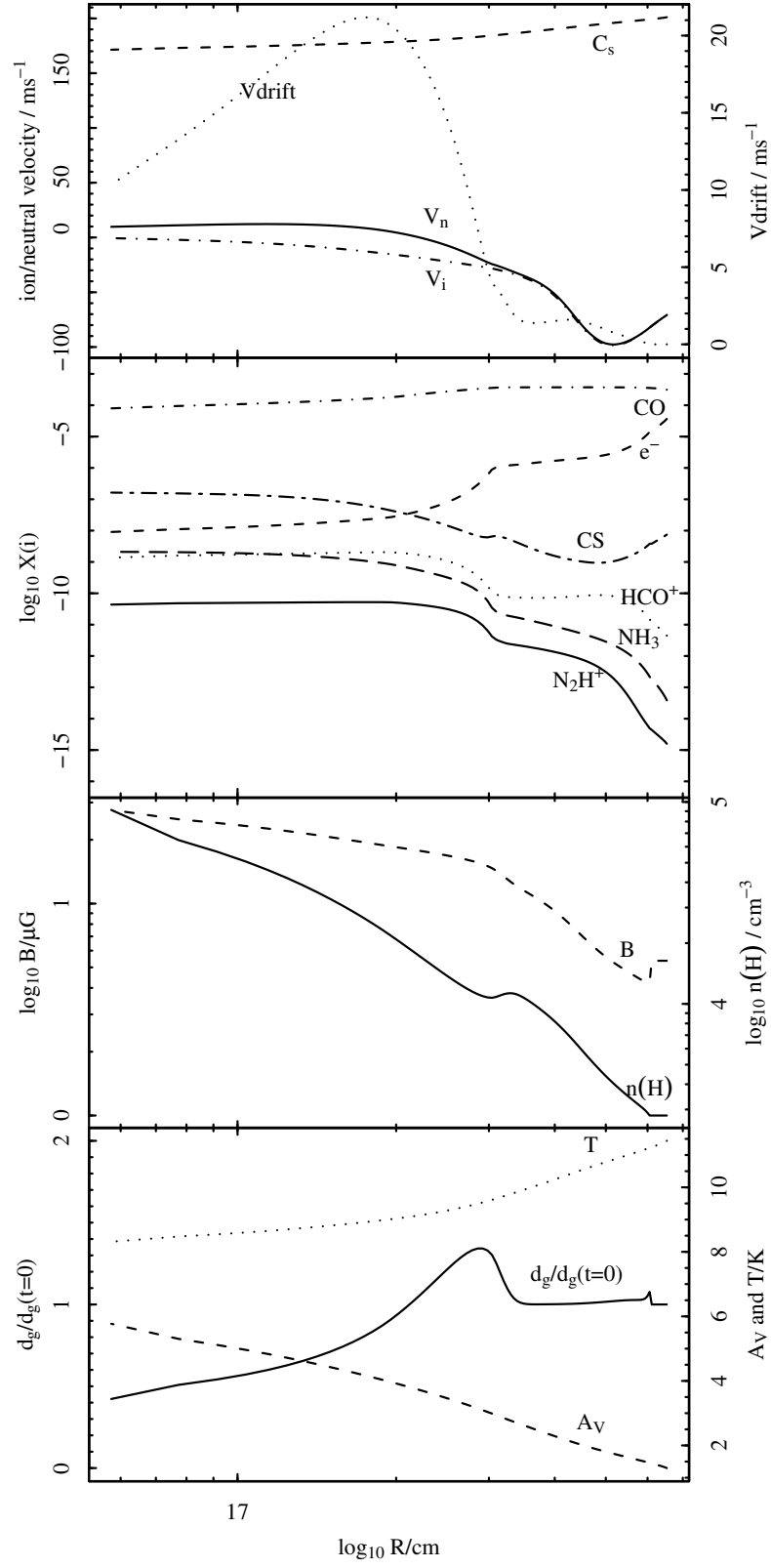
4.2 Chemical and dynamical radial profiles

Two epochs are chosen at which to analyse the radial change in density, magnetic field, velocity, ionization fraction and abundances of important molecular tracers of star-forming regions: CO, HCO⁺, CS, N₂H⁺ and NH₃. The first epoch is at $t = 1.4$ Myr – this epoch is between the times of maximum drift velocity and maximum central density during the expansion phase; the second epoch is at $t = 3.75$ Myr – this epoch is chosen due to the mean density of the central shell, $n_c(\text{H}) = 4.3 \times 10^6 \text{ cm}^{-3}$, being consistent with observations of L1544 (e.g. Ward-Thompson et al. 1999; Evans et al. 2001; Tafalla et al. 2002) giving a density at the centre of the core of around $n_o(\text{H}) \sim 3 \times 10^6 \text{ cm}^{-3}$. Later, revised estimates for the central density of L1544 by Crapsi et al. (2007), based on the same 1.2 mm dust-continuum observations as used by Tafalla et al. (2002) but using a temperature structure that increases from $T = 5.5$ K at the core centre to $T = 12$ K at the core edge, derived a best-fit density profile of the form:

$$n(\text{H}) = \frac{n_0(\text{H})}{1 + (R/R_0)^\alpha} \quad (4.1)$$

where $n_0(\text{H}) = 4.2 \times 10^6 \text{ cm}^{-3}$ is the density at the core centre and $R_0 = 1950$ AU (14 arcsec at a distance of 140 pc) is the radius of a flat inner region. Note that at the distance of the inner shell in this model, $R_c = 1060$ AU, the equivalent mean density, $\langle n(\text{H}) \rangle = 3.76 \times 10^6 \text{ cm}^{-3}$, is in good agreement with the mean density in the inner shell. However, Keto & Caselli (2010) derive a higher central density, $n_o(\text{H}) = 4 \times 10^7 \text{ cm}^{-3}$, but point out that it is difficult to constrain the central density using dust continuum observations having a beam size equivalent to ~ 1000 AU at a distance of 140 pc: for a central density of $n_o(\text{H}) = 4 \times 10^7 \text{ cm}^{-3}$, the average density within a radius of 500 AU is $\langle n_o(\text{H}) \rangle = 5.6 \times 10^6 \text{ cm}^{-3}$ – little different to the average density of $\langle n_o(\text{H}) \rangle = 6.8 \times 10^6 \text{ cm}^{-3}$ derived from a central density of $n_o(\text{H}) = 4 \times 10^8 \text{ cm}^{-3}$.

In Figures 4.2 and 4.3, the chemical and dynamical radial profiles of the core at times $t = 1.4$ Myr and $t = 3.75$ Myr are presented respectively. In the following sections a detailed analysis of these figures is given, since an important feature of the model is the

**Figure 4.2.** Chemical and dynamical radial profile at $t = 1.4$ Myr.

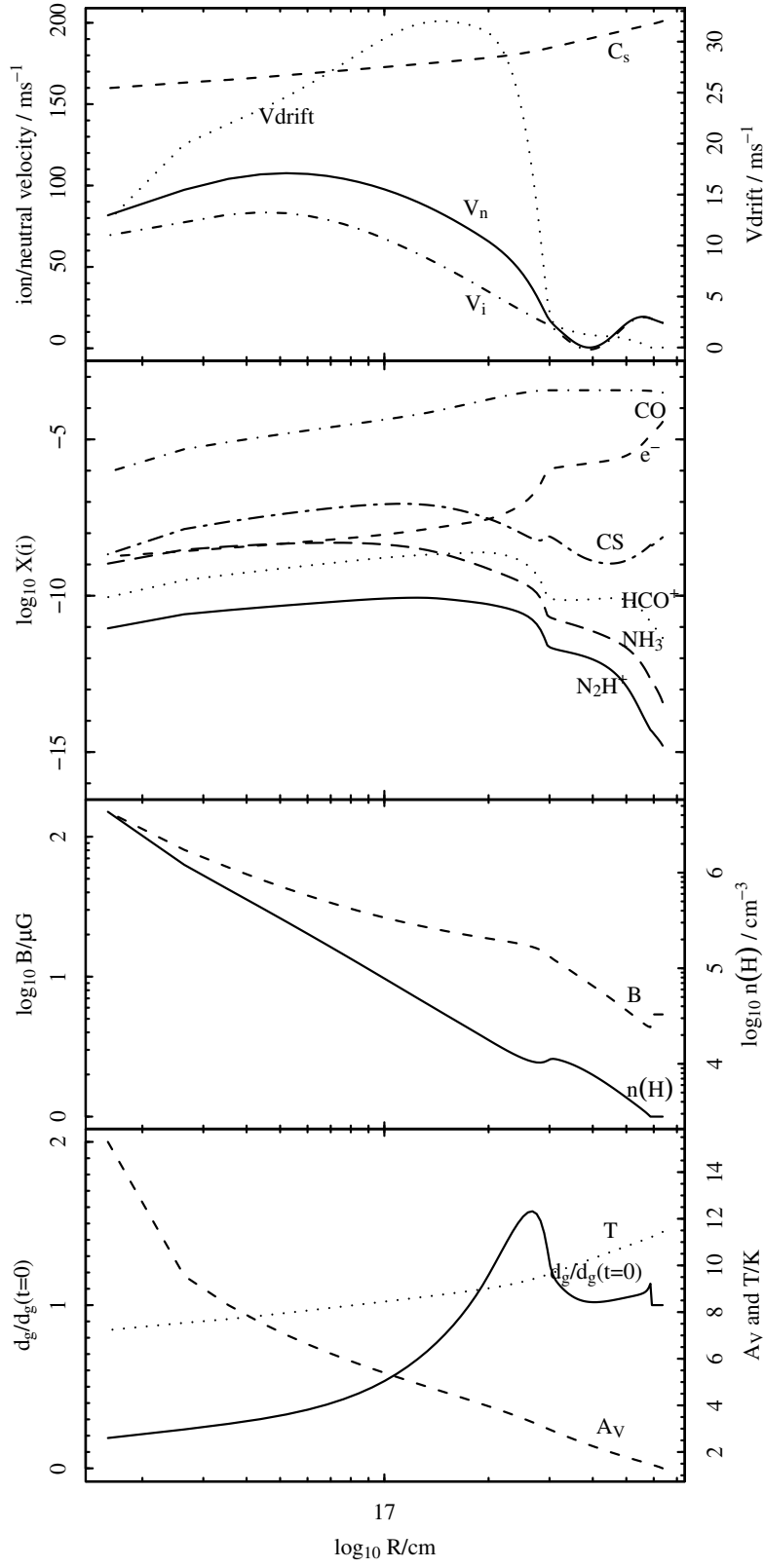


Figure 4.3. Chemical and dynamical radial profile at $t = 3.75$ Myr.

interplay between the ionization structure and the dynamics in the core. The ionization structure determines the strength of coupling between charged and neutral particles. Weak coupling between ions and neutrals allows ions and charged grains to drift through the neutral gas. This in turn affects the chemistry within each shell and therefore the ionization fraction is also affected. This feedback mechanism is an important differentiator between this model of core collapse and MHD models where the chemical feedback is not taken into account.

4.2.1 The expansion phase

In Figure 4.2, the upper graph shows the radial profile of the charged and neutral gas velocities – the neutral gas infall velocity is close to 10 ms^{-1} at the centre and reaches a maximum outflow velocity of -100 ms^{-1} at $R = 5 \times 10^{17} \text{ cm}$. Note that outflow velocities remain below the sound speed in the gas (labelled C_s). The drift velocity is plotted against the second y -axis; the maximum drift velocity of 21 ms^{-1} occurs at $R \approx 1.5 \times 10^{17} \text{ cm}$. Note that drift velocities in the outer core are small ($V_{drift} \leq 1 \text{ ms}^{-1}$), when $R > 5 \times 10^{17} \text{ cm}$ and $A_V \leq 1.5$, due to the strong coupling between neutrals and ions. This indicates that the initial condition set in the boundary region (the outer 10 shells), that $V_{drift} = 0$, is a good approximation.

The upper middle graph plots the abundance of molecular species as a fraction of the hydrogen nuclei number density, $n(\text{H})$. A rapid fall in ionization (labelled e^-) at the edge of the core, between $R = 6.5 \times 10^{17} \text{ cm}$ and $R = 5 \times 10^{17} \text{ cm}$ occurs at a visual extinction between $1.3 \leq A_V \leq 1.8$: this is attributed to the steep drop in the rate of photodissociation of CO by UV photons, primarily as a result of radiation shielding by H_2 and H lines as well as CO self-shielding (van Dishoeck & Black 1988). The drop in the CO destruction rate results in a drop in the formation rate of C^+ – the dominant ion at this visual extinction (Ruffle et al. 1998). A second rapid decrease in the ionization fraction between $R = 3.2 \times 10^{17} \text{ cm}$ and $R = 2.2 \times 10^{17} \text{ cm}$ occurs at a visual extinction between $3 \leq A_V \leq 4$: the rapid decrease is attributed to the freeze-out of molecules onto the surface of dust grains for $A_V \geq 3$. A rapid decrease in the ionization level has previously been noted by Ruffle et al. (1998) in a model of a collapsing core and was explained by the decrease in ionizing UV-photons due to the increase in UV extinction by dust as photons travel deeper into the core. In this model, this effect is found not to be as dominant as the decrease in ionization due to freeze-out.

For most species, the fractional abundances are approximately constant for $A_V > 4$. For $R > 3.5 \times 10^{17}$ cm, ions are tightly coupled to neutral gas particles as can be seen from the rapid decrease in drift velocity from 21 ms^{-1} at $R = 2 \times 10^{17}$ cm to 2 ms^{-1} at $R = 3.5 \times 10^{17}$ cm: the shell at $R = 3.5 \times 10^{17}$ cm corresponds to an ambipolar diffusion barrier, i.e. only weak relative movement between charged particles (ions and grains) and neutral particles occurs beyond this point.

The lower middle graph plots B – the magnetic flux density; B is held constant at $6.1 \text{ } \mu\text{G}$ in the outer 10 shells and increases toward the centre, peaking at $28 \text{ } \mu\text{G}$ in the central shell. The hydrogen nuclei number density, $n(\text{H})$, is plotted against the second y -axis; $n(\text{H})$ is held constant at $2.8 \times 10^3 \text{ cm}^{-3}$ in the outer 10 shells and increases toward the centre, peaking at $8 \times 10^4 \text{ cm}^{-3}$ in the central shell. Between $R = 3 \times 10^{17}$ cm and $R = 4 \times 10^{17}$ cm, a small dip in density occurs – this region coincides with the change in velocity from infall to outflow shown in the upper graph: essentially a drop in density is observed in the region just inward of this peak due to material flowing in opposite directions.

The lower graph plots the dust-gas ratio, d_g , normalised relative to the initial dust-gas ratio, $d_g(t = 0)$; d_g is lowest in the centre of the core and increases with increasing radial distance, peaking at a visual extinction, $A_V \sim 3$. This peak coincides with the rapid decrease in ionization fraction. The increase in d_g in this region is due to charged dust grains drifting outward relative to the neutral gas: a build-up of dust accumulates just inward of the ambipolar diffusion barrier at $R = 3.5 \times 10^{17}$ cm. The visual extinction, A_V , and temperature, T , are plotted against the second y -axis; note that due to the decrease in dust-gas ratio in the centre of the core, A_V is lower in the centre of the core compared to a core with a constant dust-gas ratio, $d_g = d_g(t = 0)$. The temperature is a function of A_V as defined in Table 2.1.

4.2.2 The collapse phase

Figure 4.3 plots the same series of graphs as in Figure 4.2 but at time $t = 3.75 \text{ Myr}$, corresponding to a central $n(\text{H}) \sim 3 \times 10^6 \text{ cm}^{-3}$. The neutral gas infall velocity peaks at $R = 5 \times 10^{16}$ cm; the peak value of 100 ms^{-1} is below the sound speed in the gas. In the outer region of the core, at $R = 4 \times 10^{17}$ cm, both ion and neutral gas infall velocities are $\sim 0 \text{ ms}^{-1}$ rising slightly out to the core edge. The maximum drift velocity of 32 ms^{-1} occurs at $R = 1.2 \times 10^{17}$ cm. Again, drift velocities in the outer core are small

($V_{drift} \leq 1 \text{ ms}^{-1}$), when $R > 5 \times 10^{17} \text{ cm}$ and $A_V \leq 2$, due to the strong coupling between neutrals and ions.

In common with the expansion phase (Figure 4.2), there is a two-stage rapid fall in ionization fraction: at the core edge; between $R = 3 \times 10^{17} \text{ cm}$ and $R = 2 \times 10^{17} \text{ cm}$ coinciding with a visual extinction of between $3 \leq A_V \leq 4$. Beyond $A_V > 5$ at $R = 2 \times 10^{17} \text{ cm}$ most species (NH_3 being the exception) decline rapidly with decreasing R due to freeze-out onto grains. NH_3 remains approximately constant before slowly freezing out towards the core centre. Between $R = 3 \times 10^{17} \text{ cm}$ and $R = 2 \times 10^{17} \text{ cm}$, the same dip in density occurs as that observed at $t = 1.4 \text{ Myr}$.

It is found that the density distribution follows $n(\text{H}) \propto R^{-2.14}$ in the region inside the density dip while for the region outside the density dip, a similar distribution, $n(\text{H}) \propto R^{-2.19}$, is followed. The magnetic flux density varies between $B \propto R^{-0.94}$ for the inner region ($R \leq 9.5 \times 10^{16} \text{ cm}$), $B \propto R^{-0.47}$ in the middle core ($1.0 \times 10^{17} \text{ cm} \leq R \leq 2.4 \times 10^{17} \text{ cm}$) and for the region outside the the density dip, the magnetic flux density follows $B \propto R^{-1.73}$. The radial profiles in B and $n(\text{H})$ imply the following relationships between B and $n(\text{H})$: $B \propto n(\text{H})^{0.44}$ in the inner core, $B \propto n(\text{H})^{0.22}$ in the middle core and $B \propto n(\text{H})^{0.79}$ in the outer core. In common with the expansion phase (Figure 4.2), the radial change in B is much steeper in the outer core than either the middle or inner core. The change in gradient occurs at the ambipolar diffusion barrier: inward from this point, neutrals are able to drift through the ions and charged grains allowing greater decoupling between the neutral gas and magnetic field; outward from the ambipolar diffusion barrier, neutrals, ions and charged grains are tightly coupled so that strong coupling between the neutral gas and magnetic field is expected.

The lower graph shows that the radial change in dust-gas ratio, d_g , is enhanced over that shown at $t = 1.4 \text{ Myr}$. Removal of grains at the core centre reduces the dust-gas ratio to approximately 20% of its initial value. Accumulation of grains at the ambipolar diffusion barrier now accounts for a 50% enhancement in the dust-gas ratio over its initial value. The implications of the changing dust-gas ratio are discussed in the summary section.

Table 4.1. Comparison between HCO^+ rest frequencies between Evans et al. (2005) and Cazzoli et al. (2012) and the calculated adjusted dip velocities, v_{dip} , taking into account the newer rest frequencies.

Line	ν / GHz (Evans et al. 2005)	ν / GHz (Cazzoli et al. 2012)	v_{dip} / kms^{-1}	v_{dip} (adjusted) / kms^{-1}
HCO^+ (1-0)	89.188512	89.1885247	0.05	0.09
HCO^+ (4-3)	356.734288	356.7342230	0.25	0.20

4.3 Synthetic line profiles

The radial chemical profiles are converted into line profiles that could be observed with typical existing single dish telescopes (such as JCMT or FCRAO), using spherical radiative transfer code, SMMOL (Rawlings & Yates 2001), and the collisional rate data files therein for HCO^+ and CS (Monteiro 1985; Green & Chapman 1978). The dust temperature is assumed to be the same as the gas temperature. It should be noted however, that this assumption is only valid in the denser ($n(H) \gtrsim 2 \times 10^4 \text{ cm}^{-3}$) region of the core (Takahashi et al. 1983; Doty & Neufeld 1997), where the gas-grain collision rate is high enough to maintain a strong coupling between dust and gas temperatures. A weak, constant turbulent velocity of 0.065 kms^{-1} applies throughout the core, consistent with the original assumptions about turbulence in R92. The background radiation field uses that defined by Mathis et al. (1983) with the addition of a black body of 2.7 K to simulate the cosmic background radiation. Beam parameters for an artificial beam are chosen: the beam efficiency is set to 1.0 in order to generate beam temperatures on the T_{mb} scale. A Gaussian beam profile is assumed with beam sizes derived from a 14m telescope (such as the FCRAO 14m telescope).

4.3.1 Synthetic HCO^+ line profiles

Figure 4.4 shows the HCO^+ line profiles for transitions (1-0) to (4-3); the left hand side plots transitions at time $t = 1.4 \text{ Myr}$; the right hand side plots transitions at time $t = 3.75 \text{ Myr}$. There is a noticeable change in dip velocity: in collapse, the dip velocity is seen to increase from $+0.025 \text{ kms}^{-1}$ for HCO^+ (1-0) to $+0.07 \text{ kms}^{-1}$ for HCO^+ (4-3). In expansion, the dip velocity change is less pronounced, increasing from -0.04 kms^{-1} at HCO^+ (1-0) to -0.03 kms^{-1} at HCO^+ (2-1) and -0.02 kms^{-1} at HCO^+ (3-2). The change in dip velocity is attributed to the extended velocity field; the dip velocity is determined

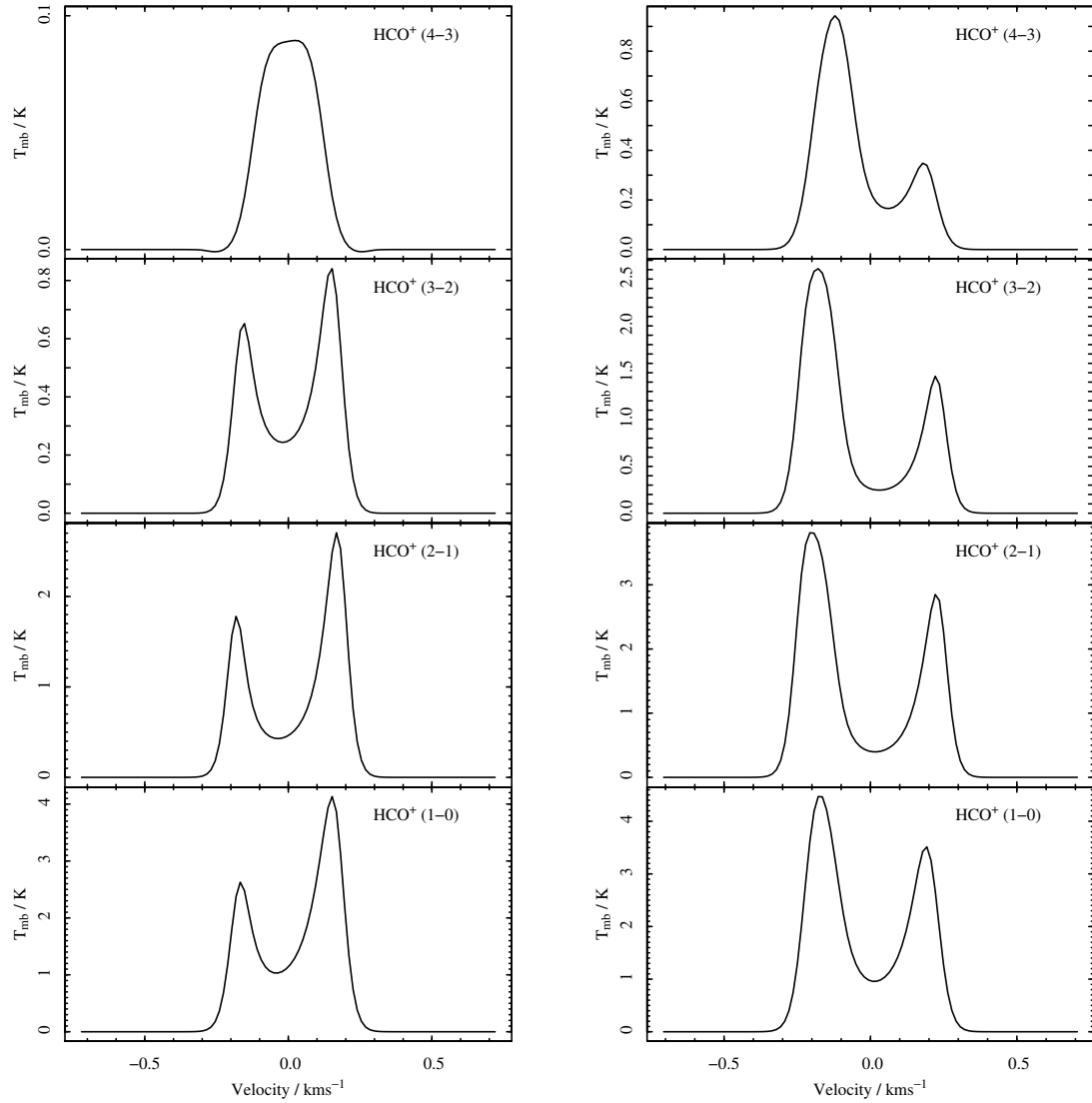


Figure 4.4. HCO^+ line profiles. Left hand side plots line profiles at $t = 1.4$ Myr – corresponding to an expansion phase; right hand side plots line profiles at $t = 3.75$ Myr – corresponding to a collapse phase.

Note the change in dip velocity: in collapse the dip velocity is seen to increase from $+0.025 \text{ km s}^{-1}$ for HCO^+ (1-0) to $+0.07 \text{ km s}^{-1}$ for HCO^+ (4-3). In expansion the dip velocity change is less pronounced, increasing from -0.04 km s^{-1} at HCO^+ (1-0) to -0.03 km s^{-1} at HCO^+ (2-1) and -0.02 km s^{-1} at HCO^+ (3-2). The change in dip velocity is attributed to the extended velocity field; the dip velocity is determined by the radial position at which most absorption for a particular line transition occurs.

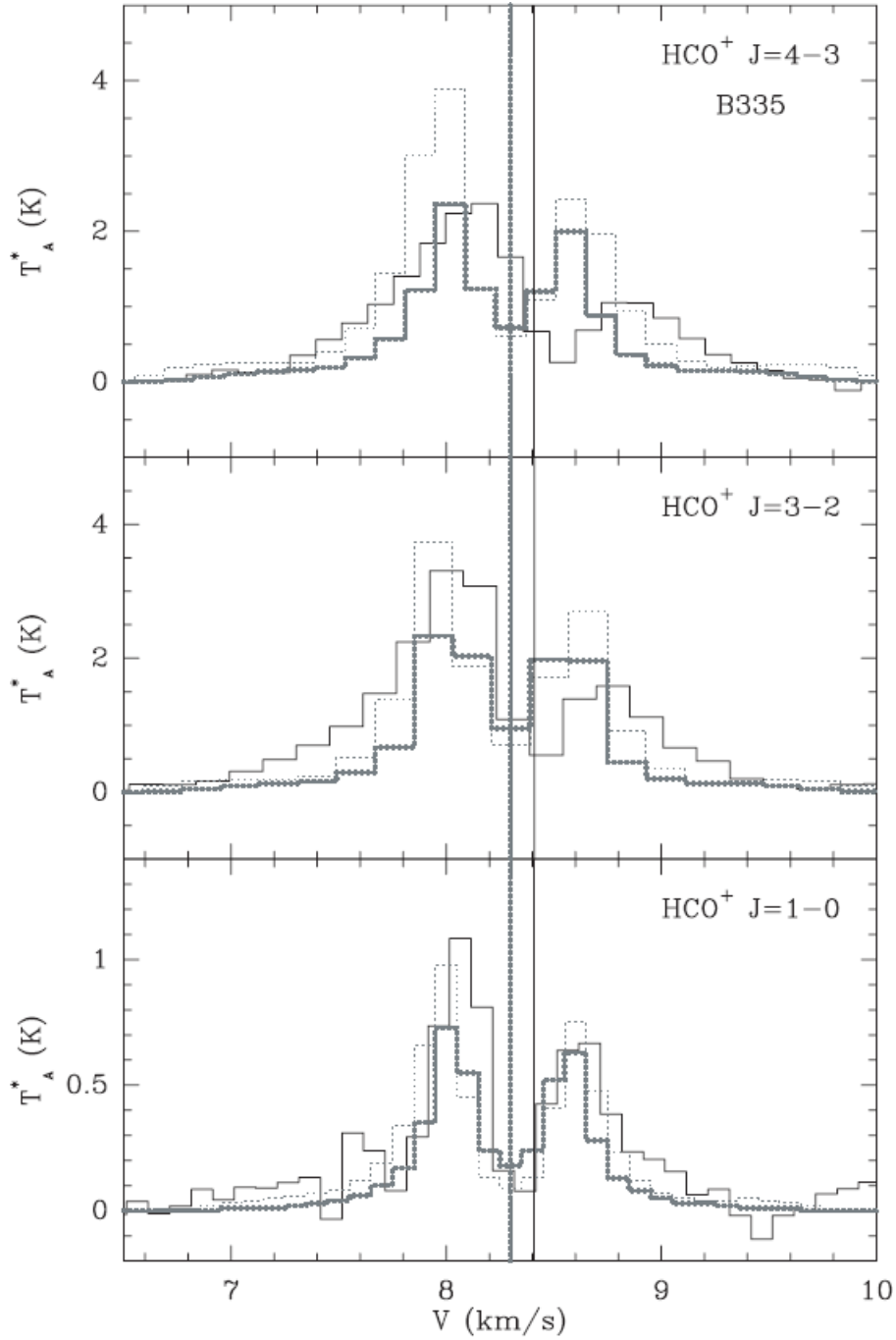


Figure 4.5. Observed HCO^+ line profiles (solid black lines) at the centre of B335 (image from Evans et al. 2005).

Two best-fit models that utilise a Shu inside-out collapse model are also shown: the model denoted by the light dotted line uses a step-function to model the molecular abundances in the core while the model denoted by the heavy dotted line uses an evolutionary chemical model to derive molecular abundances. Neither model can reproduce the observed shift in dip velocity. The dotted vertical line at 8.3 km s^{-1} gives the mean velocity of the core as determined from observations of optically thin lines.

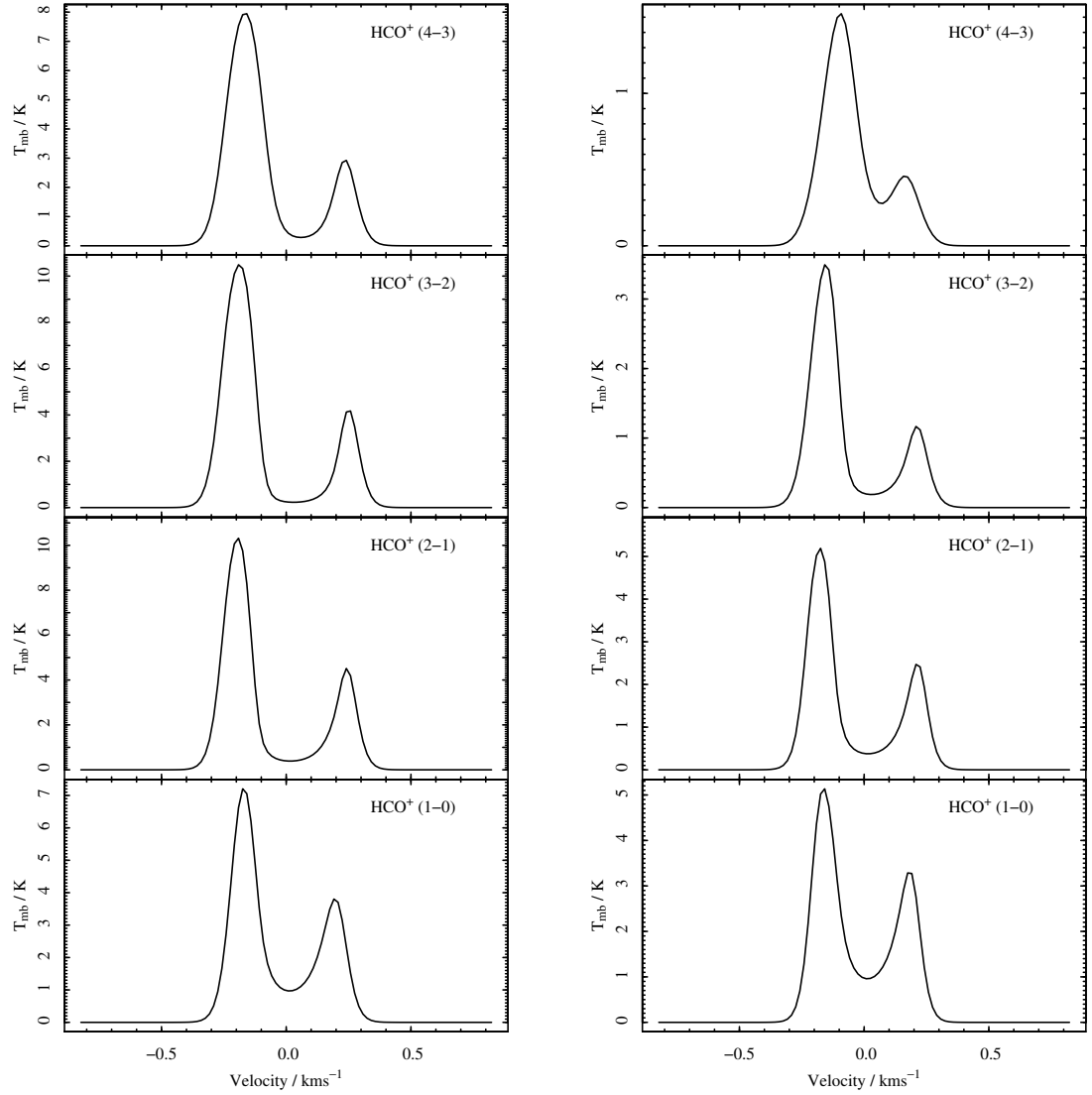


Figure 4.6. HCO^+ line profiles using a gas temperature that rises linearly with radial distance from 5000 AU to the core centre. The temperature at the core centre is ~ 20 K.

Right hand set of plots use the same temperature profile but tests the sensitivity to an increased depletion of HCO^+ within the central 5000 AU of the core: the HCO^+ abundance is reduced by a factor of 10.

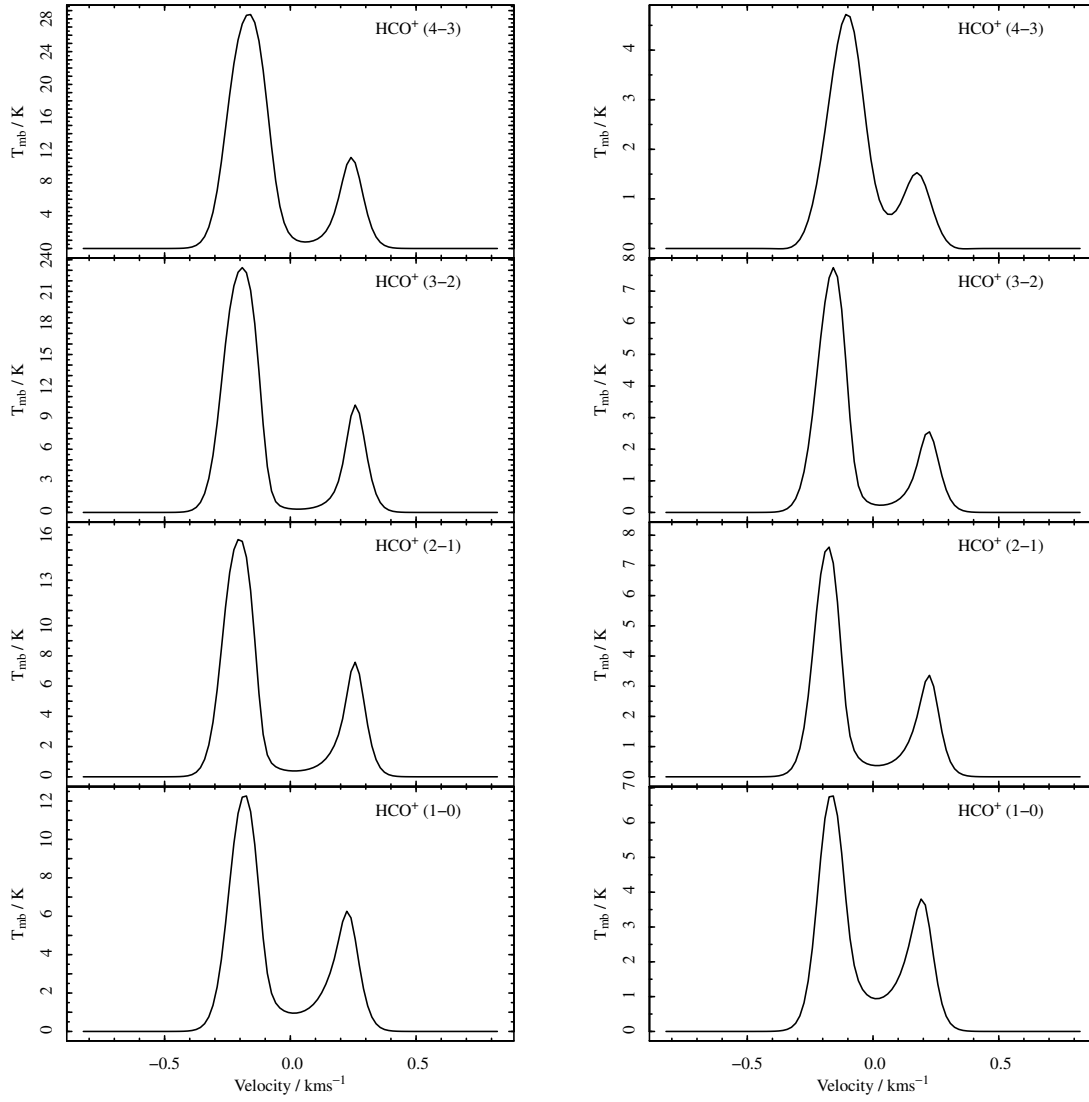


Figure 4.7. As Figure 4.6 but using angular resolutions consistent with ALMA.

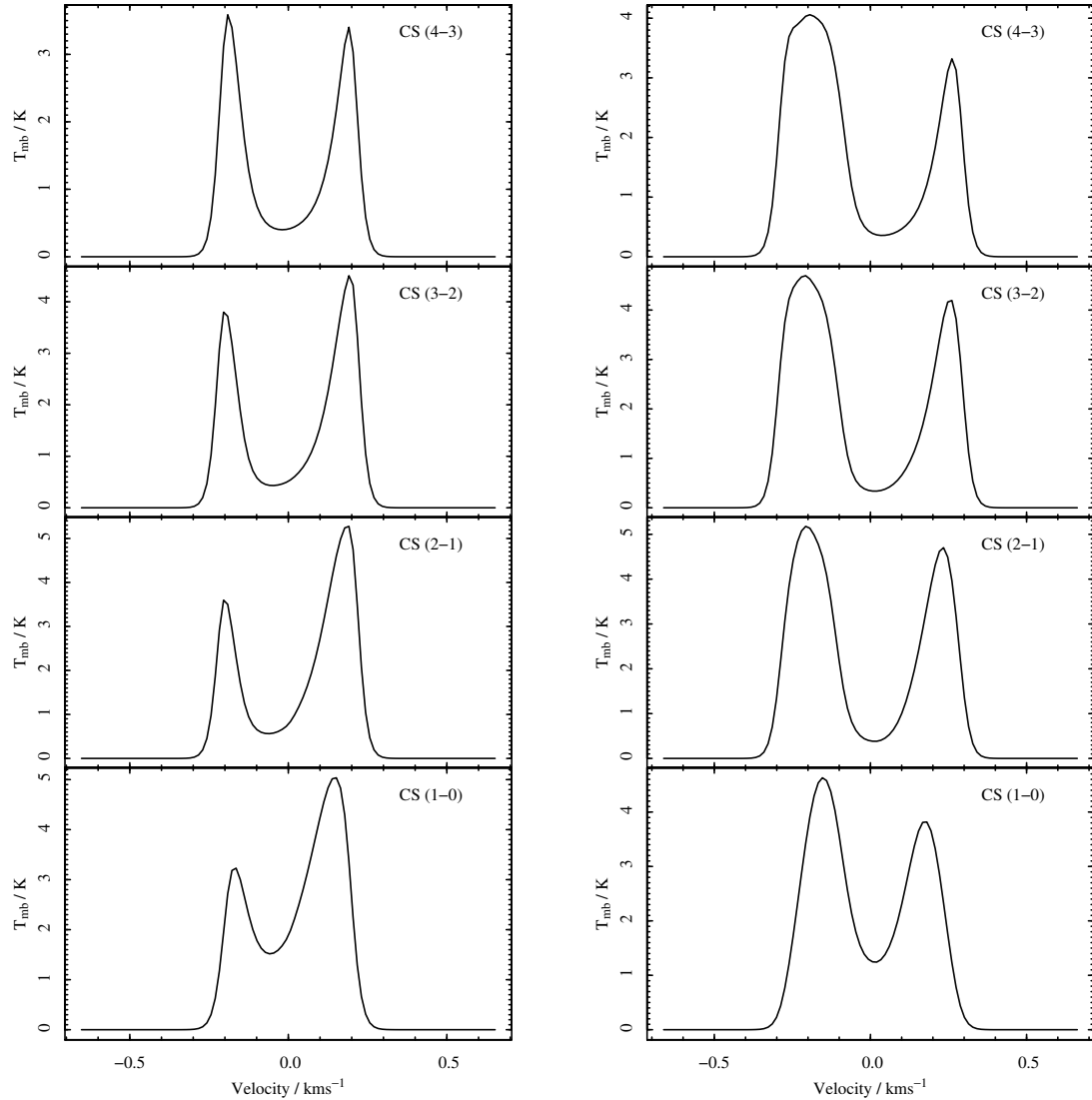


Figure 4.8. CS line profiles. Left hand side plots line profiles at $t = 1.4$ Myr – corresponding to an expansion phase; right hand side plots line profiles at $t = 3.75$ Myr – corresponding to a collapse phase.

Note the deep absorption and offset of the dip velocity from the centre: in collapse the dip velocity is $+0.02 \text{ km s}^{-1}$ for CS (1-0) – this does not change appreciably for the CS (2-1) and CS (3-2) lines while a small increase to 0.03 km s^{-1} is seen for CS (4-3). The offset in dip velocity for the lower transitions is attributed to the lower velocity gas in the outer region of the core dominating absorption. In expansion, the offset of the dip velocity from the centre is greatly enhanced: for CS (1-0) the dip velocity is offset -0.05 km s^{-1} from the centre. The offset decreases to -0.07 km s^{-1} at CS (2-1) before increasing to -0.05 km s^{-1} at CS (3-2) and -0.02 km s^{-1} at CS (4-3).

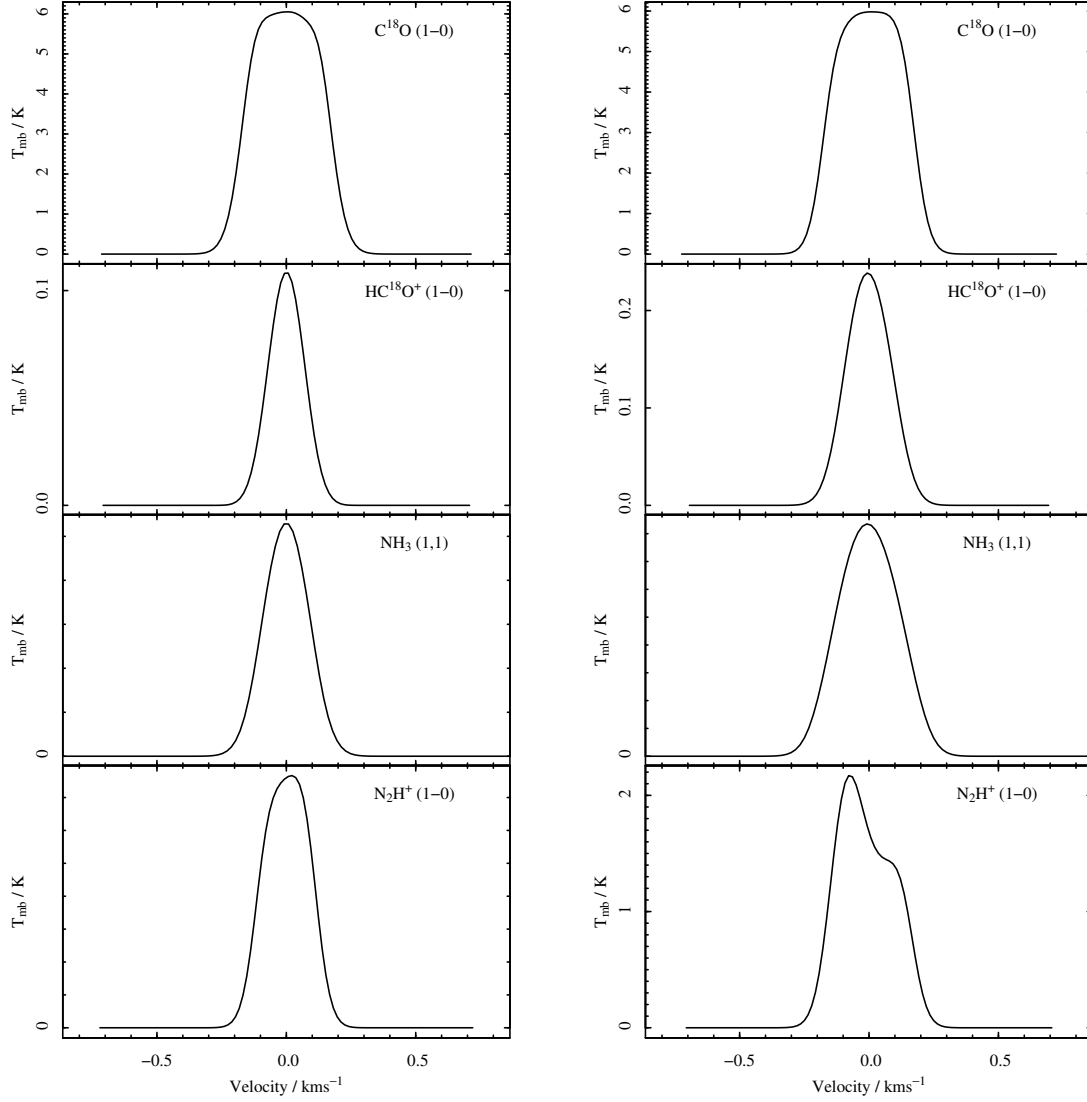


Figure 4.9. C¹⁸O, HC¹⁸O⁺, NH₃ and N₂H⁺ line profiles. Left hand side plots line profiles at $t = 1.4$ Myr – corresponding to an expansion phase; right hand side plots line profiles at $t = 3.75$ Myr – corresponding to a collapse phase.

by the radial position at which most absorption for a particular line transition occurs. Observations of the Bok globule, B335, by Evans et al. (2005) show a similar trend for HCO^+ transitions (Figure 4.5); observations show the core to have an embedded far-infrared source with a bi-polar outflow (Keene et al. 1983) – the core is thought to be collapsing. The HCO^+ dip velocity changes from 0.05 km s^{-1} at $\text{HCO}^+(1-0)$, 0.15 km s^{-1} at $\text{HCO}^+(3-2)$ to 0.25 km s^{-1} at $\text{HCO}^+(4-3)$. The rest frequencies of the $\text{HCO}^+(1-0)$ and $(4-3)$ lines have now been measured with higher accuracy than those used by Evans et al. (2005); the use of the newer rest frequencies result in significant shifts in the estimates for the dip velocities. Table 4.1 compares the newer rest frequencies, taken from Cazzoli et al. (2012), with those used by Evans et al. (2005) and calculates the adjusted dip velocities if the more recent rest frequencies are taken. These adjusted dip velocities indicate that B335 is in a much more advanced state of dynamical collapse than the test core, with an infall speed of at least 200 ms^{-1} . Zhou et al. (1993) also found significant shifts in dip velocities for CS and H_2CO line profiles at the centre of B335. The same trend is found with the more optically thick transitions having lower shifts in dip velocities. This is attributed to optically thick lines being dominated by emission and absorption from gas that is further from the core centre – the gas therefore has lower infall velocity and correspondingly lower shifts in dip velocity. Coincident with an increase in the shift in dip velocities is the increase in asymmetry between the redshifted and blueshifted peak temperatures: this is most clearly seen in the collapse phase with the ratio of the blueshifted peak temperature to the redshifted peak temperature increasing from 1.3 for the $\text{HCO}^+(1-0)$ transition to 2.8 for the $\text{HCO}^+(4-3)$ transition. This compares with ratios of 1.64, 2.03 and 2.35 for $\text{HCO}^+(1-0)$, $\text{HCO}^+(3-2)$ and $\text{HCO}^+(4-3)$ line profiles respectively, as derived from the observations at the centre of B335 (Evans et al. 2005). The same general trend can also be seen when comparing the velocities of the emission peaks. For the blueshifted emission of the model HCO^+ line profiles, the velocities at the emission peaks decrease (i.e. become more negative) between $\text{HCO}^+(1-0)$ and $\text{HCO}^+(2-1)$ and increase between successively higher rotational transition lines. For the redshifted side of the model HCO^+ line profiles, the velocities at the emission peaks increase between $\text{HCO}^+(1-0)$ and $\text{HCO}^+(2-1)$ and decrease between successively higher rotational transition lines. The change in velocities at peak emission are significant: the blueshifted $(2-1)$ emission peaks at -207 ms^{-1} while the blueshifted $(4-3)$ emission peaks at -121 ms^{-1} . Observationally for B335, the velocity at the blueshifted $(1-0)$ emission peak is -250 ms^{-1} (relative to a LSR

velocity of 8.3 km s^{-1}), decreases to -300 ms^{-1} at the blueshifted (3-2) emission peak before increasing to -150 ms^{-1} at the (4-3) emission peak. However, the interpretation of the change in velocity at the emission peaks is not straightforward. The higher rotational transitions have higher critical densities and therefore probe denser, more central regions of the core. An examination of the change in HCO^+ excitation temperatures (T_{ex}) across the core, as calculated by SMMOL, shows the HCO^+ (1-0) line to have a peak T_{ex} at a radial distance of 6150 AU corresponding to an infall velocity of 70 ms^{-1} ; the HCO^+ (4-3) line has a T_{ex} that peaks at the central shell, at a radial distance of 1060 AU corresponding to an infall velocity of 69 ms^{-1} . Between these two peaks lie the (2-1) and (3-2) T_{ex} peaks – the (3-2) T_{ex} peak corresponding to the position of maximum ion infall velocity of 83 ms^{-1} . There is therefore little variation ($\sim 14 \text{ ms}^{-1}$) between the velocities at the T_{ex} peak for all the lines. The decrease in gas kinetic temperature between the radial positions of the (1-0) and the (4-3) T_{ex} peaks account for a decrease in the sound speed of around 10 ms^{-1} – this may result in a marginal decrease in the linewidth of the HCO^+ (4-3) emission. Ruling out differences in gas temperature and infall velocities as the reason for the shift in velocities at the emission peaks, and since the microturbulent velocity is kept constant throughout the core, absorption by gas between the position of the T_{ex} peak and the observer is left as the most probable cause for the changes in position of peak temperatures: the HCO^+ (4-3) line, having a T_{ex} that peaks in the central shell, suffers little absorption from gas in the blueshifted hemisphere of the core. On the other hand, the HCO^+ (1-0) line has a peak T_{ex} that is furthest away from the core centre compared with the other HCO^+ rotational transition lines – consequently there is greater absorption by gas with lower excitation temperature between the position of peak T_{ex} and the core centre. However, on the redshifted side of the line profiles, since the HCO^+ (4-3) has its peak T_{ex} furthest away from the observer, the redshifted line is subject to proportionally stronger absorption by gas at a lower excitation temperature between the core centre and the observer. This explanation also accounts for the increase in asymmetry between the redshifted and blueshifted peak temperatures with increasing rotational transition number. A caveat must be added to this analysis, since the model line profiles are primarily intended for comparison against pre-stellar cores, the inclusion of a temperature increase at the core centre has not been taken into account.

4.3.2 Synthetic HCO^+ line profiles in a protostellar core

A study of the dust temperature inside dense cores finds that for cores having embedded protostars, the dust temperature can be raised out to radii of about 5000 AU (Launhardt et al. 2013) and the dust temperature increases to around 18 K at a radial distance of 2000 AU. With the assumption that the gas kinetic temperature should be strongly coupled to the dust temperature at the centre of dense cores (Evans et al. 2001), the inclusion of an increase in the gas kinetic temperature at the core centre will affect the relative population densities of HCO^+ between the different rotational energy levels, and consequently the opacity of the rotational transition lines will change. Additionally, the gas will be denser compared to pre-stellar cores and the increase in temperature is likely to desorb some molecules from grain mantles back into the gas phase, thus altering the chemical composition at the core centre. As a crude test of how a temperature increase might affect the line profiles, the gas and dust temperature is modified to show an artificial increase in temperature between 5000 AU and 1060 AU, the radius of the inner core. A simple, constant temperature gradient with respect to the radial distance is applied, so that the temperature in the inner shell reaches around 20 K – this is slightly higher than the 18 K for the inner core temperature at a radial distance of 2000 AU as derived by Launhardt et al. (2013), but accounts for the inner shell being closer to the source of the protostellar radiation. The left hand side set of plots in Figure 4.6 show the line profiles using the modified temperature gradient in the inner core. Aside from the obvious increase in emission strength of all lines, the line profiles show a narrowing of the range of velocities at emission peaks: the blueshifted (3-2) emission peak is at -194 ms^{-1} while the blueshifted (4-3) emission peak is at -158 ms^{-1} . The ratio of the blueshifted peak temperature to the redshifted peak temperature also narrows in range: the ratio increases from 1.9 for the HCO^+ (1-0) transition to 2.7 for the HCO^+ (4-3) transition. A notable difference from the pre-stellar line profiles is that protostellar excitation temperatures now peak in the central shell for all lines, therefore narrowing the differentiation between the lines. However, there are still differences in excitation temperature profiles that account for the change in dip velocity: the excitation temperature for the (4-3) line is the most centrally concentrated of all the lines, therefore emission and absorption reflects faster moving gas. The dip velocities are also lower than for standard pre-stellar core model: 0 ms^{-1} for the (1-0) and (2-1) lines; 25 ms^{-1} for the (3-2) line and 58 ms^{-1} for the (4-

3) line. The plots on the right hand side of Figure 4.6 test the sensitivity of the line profiles to an enhanced level of HCO^+ depletion within the inner 5000 AU of the core: the HCO^+ abundance is reduced by a factor of 10. There is now a close similarity between this set of plots and the line profiles for the standard pre-stellar core model, indicating that absorption in both cases is dominated by gas outside the depletion zone and that the HCO^+ protostellar core line profiles are highly sensitive to the assumptions about depletion in the inner core. For both sets of plots in Figure 4.6, the trend of having increasing dip velocities with increasing rotational transition number is still present and the overall shape of the line profiles are consistent with the pre-stellar core line profiles. Since the higher transition lines have higher critical densities, a reasonable conclusion to be drawn from such observations is the existence of an ion infall velocity that increases towards the core centre. However, the use of the dip velocity in the HCO^+ (4-3) line profile does not appear to be sufficiently sensitive to probe the velocity structure in the inner core.

4.3.3 Synthetic line profiles using a beam size consistent with observations from ALMA

One possibility that might affect this conclusion is the impact of having different angular resolutions between the HCO^+ transitions: a 14 m diameter telescope gives an angular resolution of 49.5 arcsec for the HCO^+ (1-0) line while for the HCO^+ (4-3) line, the angular resolution is 12.4 arcsec. This means that line profiles for the lower transitions will be an aggregate of emission from gas that is further away from the core centre, possibly giving rise to a lower dip velocity due to the beam sampling, on average, lower velocity gas. This effect is tested by changing the diameter of the artificial beam to 300 m so that much smaller angular resolutions are obtained: 2.3 arcsec for the HCO^+ (1-0) line and 0.58 arcsec for the HCO^+ (4-3) line. An angular resolution of 0.58 arcsec for the HCO^+ (4-3) line is consistent with that obtained using interferometric measurements from ALMA, the Atacama Large Millimetre/submillimetre Array (García-Burillo et al. 2014). Figure 4.7 plots the line profiles for the protostellar core using the finer angular resolutions – this figure can be compared with the original plots in Figure 4.6. Although T_{mb} is seen to increase for all lines, particularly for the higher transitions HCO^+ (4-3) and HCO^+ (3-2), the dip velocities are left relatively unaffected. The large increase in T_{mb} for the higher transitions is due to the beam now sampling gas that is on average closer to the warmer

gas in the core centre compared to Figure 4.6. Since the higher rotational levels are more centrally concentrated, this effect is more noticeable in these line profiles. In conclusion, while higher main beam temperatures are expected with the improved resolution available with ALMA, the underlying trend of having increasing dip velocities with higher rotational transition is unaffected.

4.3.4 Alternative explanation for asymmetric line profiles

Another possibility exists that may give similar line profiles: if the transitions being observed are optically thin, and two separate, dense, volumes of gas are observed along the line of sight having different infall or outflow velocities, then similar line profiles could be observed. Specifically, observations of HC^{18}O^+ (1-0), taken at the centre of L1544, show a dominant blueshifted peak temperature and a significant redshifted dip velocity, yet the authors argue that due to the low abundance of this molecular species, the line must be optically thin (Caselli et al. 2002*b*). The study suggests that a depletion hole at the centre of L1544 could give rise to the asymmetric line profiles, when viewing an inclined disk structure, as suggested by ambipolar diffusion driven collapse models (Ciolek & Basu 2000). By removing any contribution to emission from a central depletion hole, a model is constructed that shows that synthetic line profiles, when calculated at the core centre, are double-peaked but symmetrical, while synthetic line profiles, when calculated above or below the core centre along the minor axis of the core, are asymmetrical. However, where observations are taken from multiple lines of the same molecular species, as in the case with the observations of HCO^+ in B335, this particular scenario can be ruled out, since for optically thin lines, the ratio of blueshifted to redshifted peak temperatures should all be similar. Moreover, when comparing the velocity of either the blueshifted or redshifted peak temperatures between optically thin lines, there should be little or no difference.

4.3.5 Synthetic CS line profiles

Figure 4.8 shows the CS line profiles for transitions (1-0) to (4-3). Deep self-absorption is seen in all lines. In collapse, there is a small offset of the dip velocity from the centre: the dip velocity is $+0.02 \text{ kms}^{-1}$ for CS (1-0) – this does not change appreciably for the CS (2-1) and CS (3-2) lines while an increase to 0.03 kms^{-1} is seen for CS (4-3). The offset in dip velocity for the lower transitions is attributed to the lower velocity gas in the outer region of the core dominating absorption. In expansion, the offset of the dip velocity from

the centre is greatly enhanced: for CS (1-0) the dip velocity is offset -0.05 km s^{-1} from the centre. The offset decreases to -0.07 km s^{-1} at CS(2-1) before increasing to -0.05 km s^{-1} at CS(3-2) and -0.02 km s^{-1} at CS(4-3). The change in dip velocity during the collapse phase compares to a study of the velocity profile of the Class 0 protostar, IRAM 04191, by Belloche et al. (2002). This study showed the dip velocity behaving in a similar way to the HCO^+ transitions in B335: the dip velocity is at $0.09 \pm 0.04 \text{ km s}^{-1}$ for CS (1-0), $0.15 \pm 0.05 \text{ km s}^{-1}$ for CS (3-2) and $0.2 \pm 0.06 \text{ km s}^{-1}$ for CS (5,4). The test core shows only a weak increase in the dip velocity for transition (4-3): the reason why the change in dip velocity is marginal compared to the change in dip velocity for HCO^+ is probably due to CS being strongly optically thick in the outer core, therefore absorption is dominated by the slower moving gas in the outer core.

4.3.6 Synthetic line profiles for optically thin lines

Figure 4.9 shows line profiles for optically thin transitions C^{18}O (1-0), HC^{18}O^+ (1-0), NH_3 (1,1) and N_2H^+ (1-0). The abundance fraction of C^{18}O and HC^{18}O^+ is derived by dividing the abundances of CO and HCO^+ by the terrestrial O^{18}O ratio (≈ 490). Collisional rate data files for C^{18}O , NH_3 and N_2H^+ are taken from Schöier et al. (2005). The molecular data file for HCO^+ is re-used for HC^{18}O^+ . It is noted that the slight shoulder on the redshifted side of the N_2H^+ (1-0) line profile during the expansion phase is atypical of observations made of dense cores. From a survey of 60 dense cores, Benson et al. (1998) find only a few cores that have non-Gaussian line profiles, and these are associated with cores showing highly asymmetric line profiles in C_3H_2 (2-1), indicating that these cores are strong infall candidates.

4.4 Summary

A self-consistent model with respect to the chemistry, ionization and ambipolar diffusion has been used to model the collapse of a pre-stellar core. It is found that expansion in the test core of mass, $M = 7.68M_\odot$, can occur when the magnetic flux density is above a critical value: $B > 6.1 \times 10^{-6} \text{ G}$ equivalent to when the mass to magnetic flux ratio, $M/\phi < 1.77$, in units of the critical mass to magnetic flux ratio, $1/2\pi G^{0.5}$. This is similar to the magnetic flux ratio found in collapsing pre-stellar cores (Crutcher et al. 2004). The chemistry and ionization fraction is modelled at low A_V . The model shows that

using a boundary condition in the outer core where the drift velocity is zero, is a valid approximation at low A_V .

Figure 4.10 is a schematic diagram showing the overall evolution of the radial profiles in gas density $n(\text{H})$, magnetic flux density B , and dust-gas ratio Dg . Figure 4.10a shows the starting configuration: the radial distribution in $n(\text{H})$, B and Dg are all flat. During the early stages of collapse or under conditions of a weak magnetic field (Figure 4.10b), charged particles are tightly coupled to the neutral gas and therefore ambipolar diffusion has little or no impact on the radial profiles. The radial profiles in $n(\text{H})$ and B collapse under conditions of ideal MHD whereby flux-freezing ensures that B and $n(\text{H})$ are tightly coupled: using the flux-freezing equation, $B \propto R^{-2}$ (§2.5), and combining with the expression for the mean $n(\text{H})$ as a function of radius, $n(\text{H}) \propto R^{-3}$, gives an expected relationship of the form $B \propto n(\text{H})^{2/3}$ (see also the results for model variation *b1* – a model having a weak magnetic field in §6.2.3). During the later stages of collapse (Figure 4.10c), the ionization level at the core centre drops due to increased attenuation of the external radiation field: charged particles and magnetic field lines can now drift outward relative to the inward motion of neutral gas. However, there is a limit to how far the charged particles and magnetic field lines can drift outwards: at a visual extinction of $A_V \sim 3$, ions no longer freeze out onto grains and the subsequent rise in ionization fraction acts as a barrier to any further ambipolar diffusion. The distribution of B inward of the ambipolar diffusion barrier is now compacted – the radial variation in B is now a weaker function of $n(\text{H})$: $B \propto n(\text{H})^{0.22}$; outwards from the ambipolar diffusion barrier there is now a much stronger fall-off in B : $B \propto n(\text{H})^{0.79}$. The distribution of B in the inner core, $B \propto n(\text{H})^{0.44}$, has a stronger dependence on $n(\text{H})$ compared to the middle core: due to the removal of B from the inner core, the impact that the magnetic pressure has in retarding collapse is reduced and allows B in the inner core to return to having a stronger dependence on $n(\text{H})$.

Moving outwards from the core centre, the steep rise in ionization fraction is coincident with a rise in the dust-gas ratio: dust moving out from the core centre supplies the build-up of dust at the ambipolar diffusion barrier. Specifically, this model predicts a drop in the dust-gas ratio to about 20% of its initial value at the core centre while at the ambipolar diffusion barrier, the dust-gas ratio increases to about 150% of its initial value. The changing dust-gas ratio has implications for freeze-out of species onto grains: molecular species freeze out at a slower rate in the centre of the core due to the reduced dust-gas ratio,

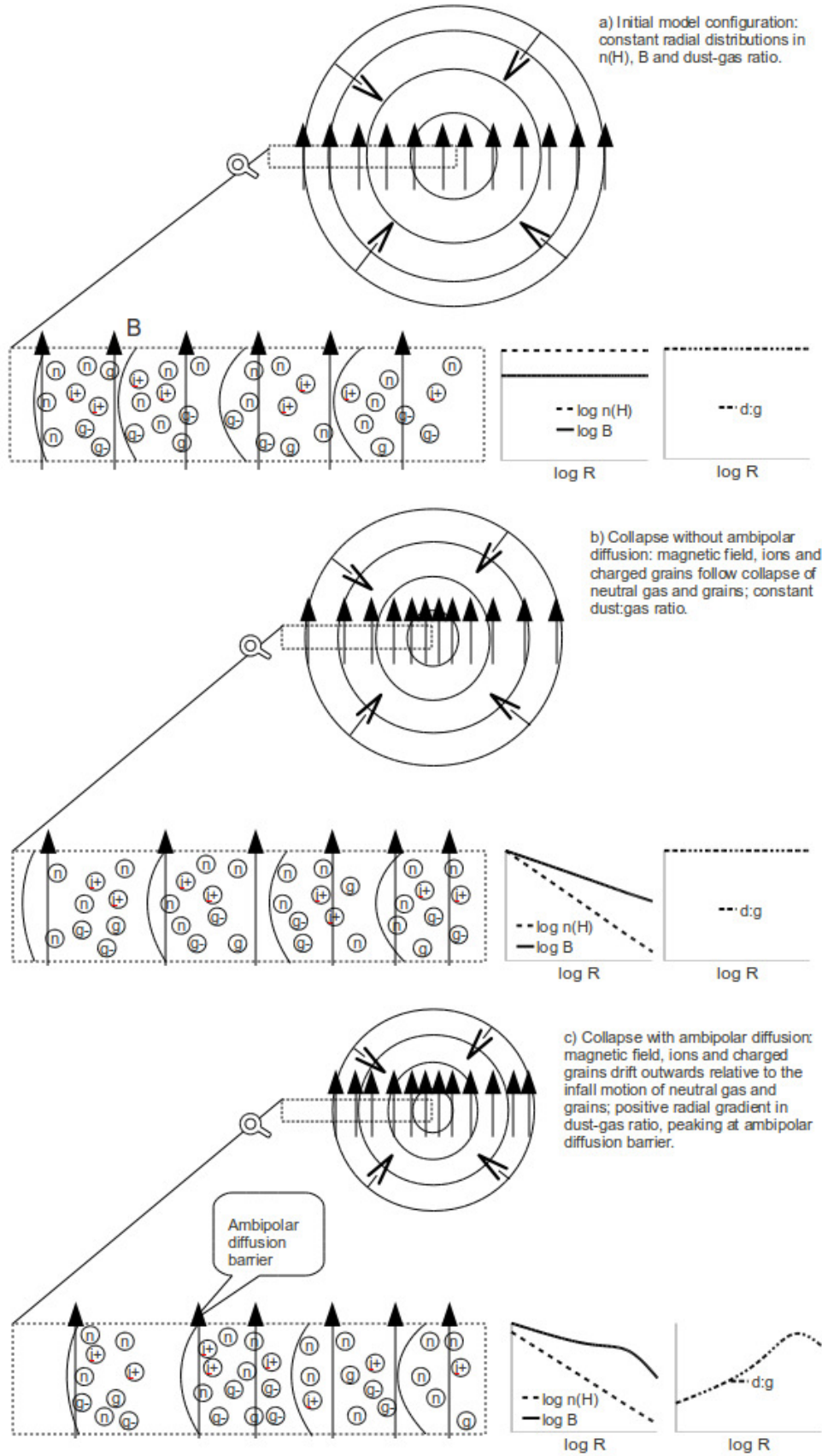


Figure 4.10. Schematic diagram of the ambipolar diffusion process.

leaving gas in a chemically younger state compared to models where the dust-gas ratio is kept constant. With regard to the ionization fraction, the situation is more complicated. On the one hand, the removal of ions via ambipolar diffusion decreases the ionization fraction. On the other hand, freeze-out onto grains is slower, resulting in an increase in the ionization fraction. Additionally, the removal of dust from the core centre reduces the visual extinction: UV radiation is therefore able to penetrate deeper into the core, giving rise to an increase in the ionization fraction. A changing dust-gas ratio at the centre of the core gains some support from Bergin et al. (2006) who find that in order to maintain a constant temperature throughout B68, observed through lines of NH_3 , the dust-gas coupling rate needs to be reduced by a factor of 10 such that the grain-gas cooling effect is reduced. The authors suggest that dust coagulation is the cause of the reduced dust-gas coupling; this analysis suggests that a reduction in the dust-gas ratio at the centre of the core could also be the cause of the reduced dust-gas coupling.

The radial gas density distribution is found to be similar between the inner, middle and outer core: in the inner and middle core, $n(\text{H}) \propto R^{-2.14}$, while in the outer core, $n(\text{H}) \propto R^{-2.19}$. A power law of the form $n(\text{H}) \propto R^{-2.14}$ is not inconsistent with centrally flattened dust continuum observations of L1544 when the dust temperature increases from the centre to the edge of the core (Evans et al. 2001). However, the gas density distribution is a closer fit to that derived from the dust continuum emission from Class 0/I sources by Shirley et al. (2000): $\rho \propto R^{-2.1 \pm 0.35}$.

The model predicts a broad velocity field with infall velocity increasing towards the centre. The line profiles of important tracers of star-forming regions are calculated. The spectral signature for optically thick lines that have an excitation temperature that increases towards the core centre is that of asymmetric line profiles with a dip velocity that is offset from the local standard of rest: in collapse the blueshifted peak dominates and the dip velocity increases with increasing rotational transition number for HCO^+ ; a marginal increase in dip velocity is seen at transition (4-3) for CS. This feature is observed for HCO^+ in the protostellar core B335 (Evans et al. 2005) and for CS in the protostellar core IIRAM 04191 (Belloche et al. 2002). In both cases the observed dip velocities are higher than the model predicts; it is possible that this feature of pre-stellar collapse may extend into the protostellar phase but with increased velocities. The diagnostic power of observations taken from multiple HCO^+ lines at the centre of pre-stellar and protostellar cores is analysed. It is found that observations of the dip velocity in the HCO^+ (4-3) line,

as observed in B335 by Evans et al. (2005), allows an estimate to be made of the infall velocity ($\sim 200 \text{ ms}^{-1}$). Additionally, the increase in dip velocity with higher rotational transition lines is a powerful diagnostic feature. It should be noted that the observed change in dip velocity is not evidence of ambipolar diffusion but of a broad velocity field with an infall velocity that increases towards the centre. However, this feature is likely to be a key differentiator between this model and Shu inside-out collapse models that require a mainly static outer core, and therefore cannot reproduce the observed shift in dip velocities (Evans et al. 2005).

Chapter 5

Modelling the linewidth – drift velocity relationship

The purpose of computing is insight, not numbers.

Richard Hamming

Optically thin transition lines are likely to be of particular relevance when determining whether ambipolar diffusion plays an important role in collapsing pre-stellar cores: by measuring the difference in linewidths between the spectral lines of ions and neutrals it should be possible to measure the ion-neutral drift velocity. In this section, linewidths are calculated for the optically thin synthetic line profiles over a range of epochs corresponding to when a significant difference in infall velocity exists between ions and neutrals, the purpose being to determine whether ion-neutral drift can be measured using the method of linewidth differencing. These results have been taken from Stace and Rawlings (2014a), in preparation.

5.1 Linewidths of optically thin lines

When using linewidths to determine the ion-neutral drift, it is important to choose lines that have low optical depths in order to minimise the effects of opacity broadening. In

Table 5.1. Central optical depths

Line	1.4 Myr	3.75 Myr
C ¹⁸ O (1-0)	3.32	2.69
HC ¹⁸ O ⁺ (1-0)	0.11	0.05
NH ₃ (1,1)	0.13	0.21
N ₂ H ⁺ (1-0)	0.58	0.65

Table 5.1, the optical depth, τ_0 , is calculated from the SMMOL code, at the centre of the core for those lines shown in Figure 4.9. It is clear from this table that the C¹⁸O (1-0) is not a suitable candidate for the test core ($\tau_0 \geq 2.69$). The HC¹⁸O⁺ (1-0) and NH₃ (1,1) lines are most suitable, having low optical depths ($\tau_0 \leq 0.21$) – but even here the NH₃ (1,1) line could suffer from opacity broadening that significantly skews an observation. This effect can be compensated for if an observer knows the optical depth of the line (Phillips et al. 1979; Kim & Hong 2002). However, it is not clear how effective linewidth differencing is when the position of maximum ion-neutral drift is not coincident with the maximum ion and neutral infall velocities (e.g. Figures 4.2 and 4.3). What may be measured by this method is the difference between the maximum ion and neutral infall velocities, hereafter termed V_{diff} – which is smaller than or equal to the maximum ion-neutral drift velocity, V_{drift} (Figure 5.1 shows the difference between V_{drift} and V_{diff}). In order to test out how effective this method is, line profile calculations are run for NH₃ (1,1) and HC¹⁸O⁺ (1-0) over epochs that have a central density, $n_c(\text{H}) \geq 4 \times 10^4 \text{ cm}^{-3}$, roughly corresponding to when drift velocities $\geq 10 \text{ ms}^{-1}$. Linewidths are calculated, correcting the NH₃ (1,1) linewidth according to Phillips et al. (1979):

$$\Delta V_{\text{cor}} = \sqrt{\ln 2} \Delta V_{\text{obs}} \left\{ \ln \left[\tau_0 / \ln \left(\frac{2}{1 + e^{-\tau_0}} \right) \right] \right\}^{-\frac{1}{2}} \quad (5.1)$$

where ΔV_{obs} is the observed value and ΔV_{cor} is the corrected value. It is noted that this equation is only applicable for conditions of LTE, but in the centre of the core, the excitation temperature for NH₃ ($\sim 7 \text{ K}$) is similar to the gas temperature ($8.5 \text{ K} \geq T \geq 7.5 \text{ K}$), implying near-LTE conditions. In Figures 5.2 and 5.4 the linewidth differences are plotted against: the difference between the maximum ion and neutral velocities; the drift velocity. An *ideal* line is also plotted, based on a simple model for how the linewidth

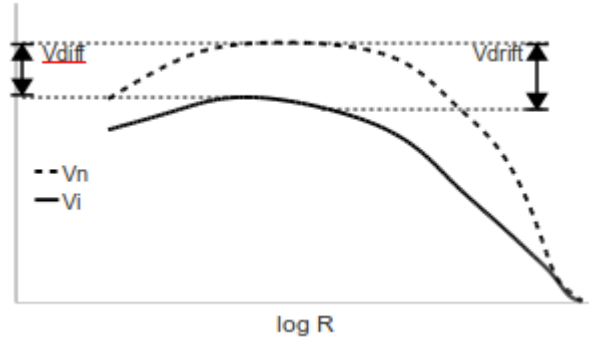


Figure 5.1. Schematic diagram showing how the maximum ion-neutral drift velocity, V_{drift} , differs from V_{diff} , the difference between the maximum ion and neutral infall velocities.

differences should behave if the core has the following properties: a constant temperature of $T = 10$ K; a constant microturbulent velocity component of $V_{TURB} = 0.065 \text{ kms}^{-1}$; a constant inward velocity for ions and neutrals of v_i and v_n respectively. The linewidths for ions, ΔV_i , and neutrals, ΔV_n , are then given by:

$$\Delta V_i = 2(\ln 2)^{0.5} [V_{TH}(i)^2 + V_{TURB}^2]^{0.5} + A_i v_i \quad (5.2)$$

$$\Delta V_n = 2(2\ln 2)^{0.5} [V_{TH}(n)^2 + V_{TURB}^2]^{0.5} + A_n v_n \quad (5.3)$$

where $V_{TH}(i) = (2kT/m_i)^{0.5}$ and $V_{TH}(n) = (2kT/m_n)^{0.5}$ are the thermal contributions to the linewidth for the ion and neutral lines respectively and m_i and m_n are the mass of the ion and neutral molecules respectively. The constants A_i and A_n are functions of the ion and neutral velocity profile functions respectively, which are dependent on the beamwidth, the beam offset and the density distribution in the core. For a very small beamwidth directed at the core centre, all the neutral gas within the beam has the same inward velocity. If the emission from the redshifted and blueshifted hemispheres are considered separately, the net effect is to shift the Gaussian emission profile by $+v_n$ in the redshifted hemisphere while shifting the emission in the blueshifted hemisphere by $-v_n$. In this limiting case, the combined neutral gas linewidth is increased by $2v_n$. Similarly, the linewidth for the ion is increased by $2v_i$ and therefore $A_n = A_i = 2$. The linewidth

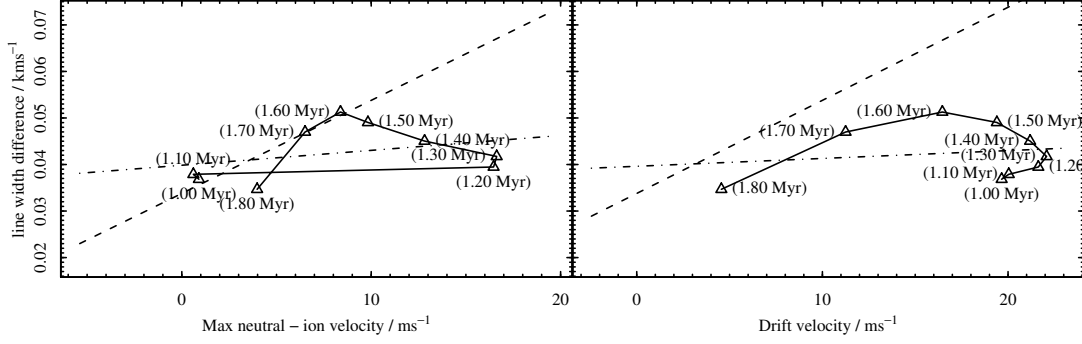


Figure 5.2. Linewidth differences between NH_3 (1,1) and HC^{18}O^+ (1-0) during the expansion phase ($1.0 \text{ Myr} \leq t \leq 1.8 \text{ Myr}$).

Left hand side plots linewidth differences against the difference between the maximum ion and neutral velocities; right hand side plots linewidth differences against the drift velocity. The dashed line represents an ideal line for a core with a constant temperature ($T = 10 \text{ K}$) throughout the core. The dot-dashed line is the linear least-squares fit to the data points.

difference is then given by:

$$\Delta V_n - \Delta V_i = \Delta V_{\text{constant}} + 2(v_n - v_i) \quad (5.4)$$

where $\Delta V_{\text{constant}} = 2(\ln 2)^{0.5}([V_{\text{TH}}(n)^2 + V_{\text{TURB}}^2]^{0.5} - [V_{\text{TH}}(i)^2 + V_{\text{TURB}}^2]^{0.5})$ is a constant. For the left hand side of the plots in Figures 5.2 and 5.4, $v_n - v_i$ is replaced by the difference between the maximum neutral and ion velocities while on the right hand side $v_n - v_i$ is replaced by the drift velocity.

Figure 5.2 plots the results during the expansion phase, $1.0 \text{ Myr} \leq t \leq 1.8 \text{ Myr}$. The ideal line is not representative of the plot of linewidth difference against V_{drift} : the maximum V_{drift} occurs at $t = 1.3 \text{ Myr}$ with a value of 22 ms^{-1} ; if the ideal line is used to infer a drift velocity, a value of 5 ms^{-1} is obtained. The linewidth difference is weakly correlated with V_{drift} , giving a correlation coefficient of 0.33 for the best fit linear model. Comparing the ideal line with the plot of linewidth difference against V_{diff} gives an excellent fit for periods 1.6 Myr and 1.7 Myr and a good fit for periods 1.0 Myr, 1.1 Myr, 1.5 Myr and 1.8 Myr while there is a poor fit for the remaining data points. Again the correlation coefficient, 0.30, between the linewidth difference and V_{diff} is low. During this phase it can be said that this method gives an underestimate of the actual drift velocity and has only partial success in following the difference between the maximum neutral and

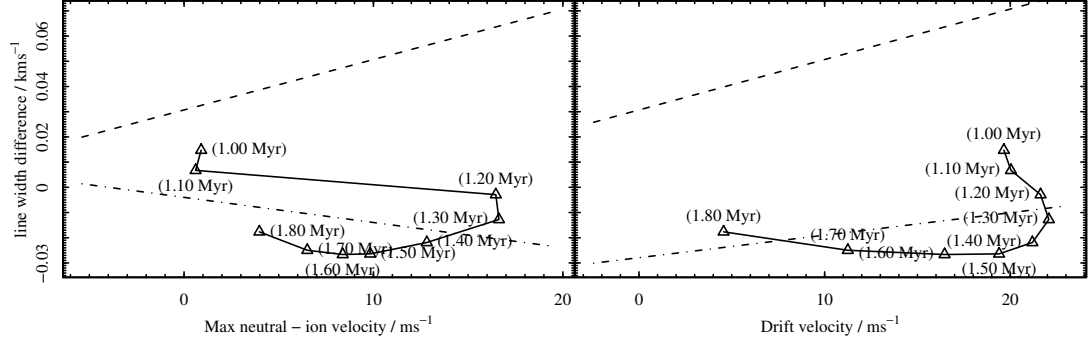


Figure 5.3. Linewidth differences between NH_3 (1,1) and N_2H^+ (1-0) during the expansion phase ($1.0 \text{ Myr} \leq t \leq 1.8 \text{ Myr}$).

Left hand side plots linewidth differences against the difference between the maximum ion and neutral velocities; right hand side plots linewidth differences against the drift velocity. The dashed line represents an ideal line for a core with a constant temperature ($T = 10 \text{ K}$) throughout the core. The dot-dashed line is the linear least-squares fit to the data points.

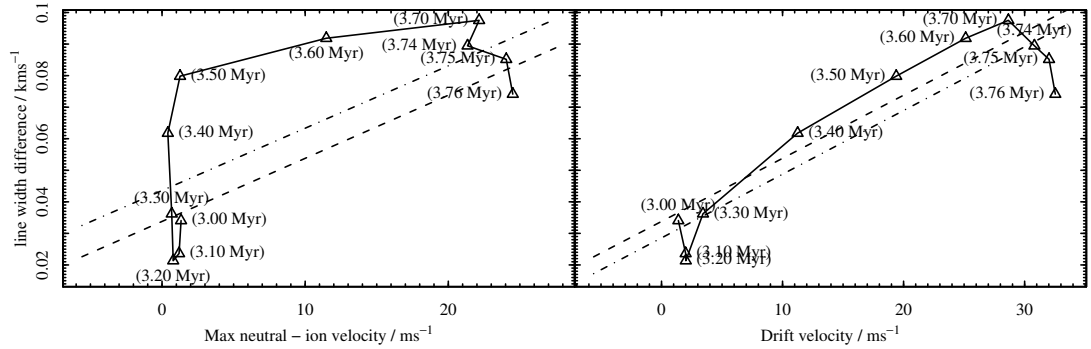


Figure 5.4. Linewidth differences between NH_3 (1,1) and HC^{18}O^+ (1-0) during the collapse phase ($3.0 \text{ Myr} \leq t \leq 3.76 \text{ Myr}$).

Left hand side plots linewidth differences against the difference between the maximum ion and neutral velocities; right hand side plots linewidth differences against the drift velocity. The dashed line represents an ideal line for a core with a constant temperature ($T = 10 \text{ K}$) throughout the core. The dot-dashed line is the linear least-squares fit to the data points.

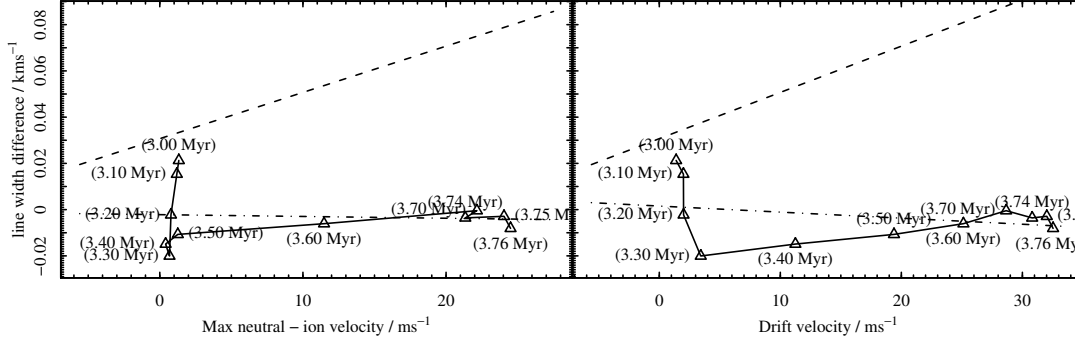


Figure 5.5. Linewidth differences between NH_3 (1,1) and N_2H^+ (1-0) during the collapse phase ($3.0 \text{ Myr} \leq t \leq 3.76 \text{ Myr}$).

Left hand side plots linewidth differences against the difference between the maximum ion and neutral velocities; right hand side plots linewidth differences against the drift velocity. The dashed line represents an ideal line for a core with a constant temperature ($T = 10$ K) throughout the core. The dot-dashed line is the linear least-squares fit to the data points.

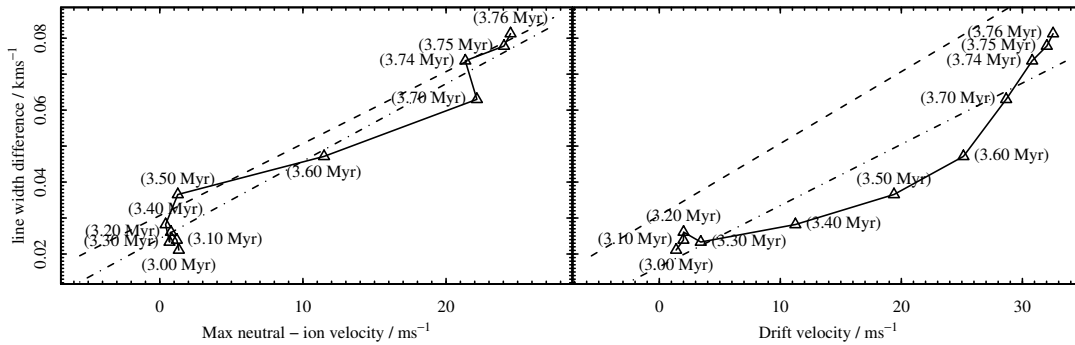


Figure 5.6. Linewidth differences between NH_3 (1,1) and N_2H^+ (1-0) during the collapse phase ($3.0 \text{ Myr} \leq t \leq 3.76 \text{ Myr}$) at a beam offset of 100 arcsec.

Left hand side plots linewidth differences against the difference between the maximum ion and neutral velocities; right hand side plots linewidth differences against the drift velocity. The dashed line represents an ideal line for a core with a constant temperature ($T = 10$ K) throughout the core. The dot-dashed line is the linear least-squares fit to the data points.

ion velocities. For comparison, the linewidth difference between NH_3 (1,1) and N_2H^+ (1-0) is calculated using equation 5.1 to correct for linewidth broadening in both NH_3 and N_2H^+ lines. Figure 5.3 plots the results for the linewidth difference between NH_3 (1,1) and N_2H^+ (1-0) during the expansion phase. The plot shows that there is an anti-correlation between linewidth difference and V_{diff} (correlation coefficient of -0.45) while a weak correlation exists between linewidth difference and V_{drift} (correlation coefficient of 0.22). The ideal line is not representative of either data set.

Figure 5.4 plots the results during the collapse phase, $3.0 \text{ Myr} \leq t \leq 3.75 \text{ Myr}$, for the $\text{NH}_3 - \text{HC}^{18}\text{O}^+$ linewidth difference. The ideal line is representative of the plot of linewidth difference against V_{drift} : the best-fit linear model for the data points shares the same slope to the ideal line. The linewidth difference peaks at $t = 3.7 \text{ Myr}$ with a value of 0.095 kms^{-1} ; this translates into a velocity difference of 32 ms^{-1} from the ideal line, a 14 % overestimate of the actual drift velocity of 28 ms^{-1} . There is a much stronger correlation between the linewidth difference and V_{drift} (0.90) than in the expansion phase (0.30). The ideal line is not representative of the plot of linewidth difference against V_{diff} . However, the correlation coefficient between linewidth difference and V_{diff} is higher (0.70) than in expansion case (0.33). Generally, the data points tend to follow the ideal line better using the drift velocity, although at late times ($3.74 \text{ Myr} \leq t \leq 3.76 \text{ Myr}$), the data points move away from the ideal line. Figure 5.5 plots the results for the linewidth difference between NH_3 (1,1) and N_2H^+ (1-0) during the collapse phase. In common with the expansion phase, the ideal line is not representative of either data set. The correlation coefficient between linewidth difference and V_{diff} is now weakly positive (0.62) while the correlation coefficient between linewidth differences and V_{drift} is marginally stronger, increasing from 0.30 to 0.40. In an attempt to understand the reason behind the weak correlation, $\text{NH}_3 - \text{N}_2\text{H}^+$ linewidth differences are calculated from synthetic line profiles that are generated using a beam offset of 100 arcsec, corresponding to a radial distance of $R = 2 \times 10^{17} \text{ cm}$: this is the position of maximum drift velocity at $t = 3.75 \text{ Myr}$. No correction for optical depth broadening has been used since optical depths for both species are lower at this radial position. The plots in Figure 5.6 show that the ideal line is a good fit to the plot of linewidth difference against V_{diff} while the ideal line consistently underestimates the actual drift velocity: for all data points an underestimate of the actual drift velocity is obtained if the ideal line is used to calculate drift velocities. Correlation coefficients are strong in both cases: a correlation coefficient of 0.98 is found between

linewidth difference and V_{diff} ; a correlation coefficient of 0.95 is found between linewidth difference and V_{drift} . Thus it appears that targeting observations at off-centre positions, corresponding to higher drift velocities, may be better at detecting differences between ion and neutral infall velocities but still underestimates the actual drift velocity. The reason why the linewidth difference (as measured at the core centre) is poorly correlated with either V_{diff} or V_{drift} is probably due to a combination of factors: the N_2H^+ (1-0) line samples only the central infall velocity from the dense gas in the core centre (that dominates N_2H^+ line emission) while the NH_3 line samples a wider range of densities and infall velocities; the angular resolution for both lines is poor and badly matched to the ideal line which was constructed around a thin beam. For a 14 m telescope, the beamwidth is ~ 230 arcsec for both NH_3 (1,1) and N_2H^+ (1-0) lines. In order to test the impact of using observations having finer angular resolution, NH_3 - N_2H^+ linewidth differences are recalculated using beam parameters that give an angular resolution consistent with ALMA. The diameter of the artificial beam is set to 300 m (see also §4.3.3) so that much smaller angular resolutions are obtained: ~ 11 arcsec for both NH_3 (1,1) and N_2H^+ (1-0) lines. Figure 5.7 plots the results from the recalculated linewidth differences. This figure shows the ideal line now having better correlation with both V_{diff} and V_{drift} : correlation coefficient for V_{diff} is now 0.92 compared to 0.62 in Figure 5.5; correlation coefficient for V_{drift} is now 0.76 compared to 0.40 in Figure 5.5. However, in common with Figure 5.5, the ideal line is still not representative of either data set.

It should be noted that this analysis is based on perfect simulated observations of synthetic line profiles and no consideration has been given to the technical problems of: a) deriving accurate linewidths for low-abundance species such as HC^{18}O^+ and b) having sensitive enough equipment to resolve velocity differences of $\leq 30 \text{ ms}^{-1}$ at the frequency of the observed lines. Although these technical problems may be limiting on the accuracy for individual data points, if applied to a sample of pre-stellar cores, a mean linewidth difference may still be representative of the mean velocity difference between ions and neutrals. The data points as calculated here, represent a sample of dense pre-stellar cores of the same mass for which the central densities are $n(\text{H}) \geq 4 \times 10^4 \text{ cm}^{-3}$. The mean and standard deviation of the ion-neutral velocity difference are calculated from the mean NH_3 – HC^{18}O^+ and NH_3 – N_2H^+ linewidth differences and compared with the actual mean V_{diff} or V_{drift} . This analysis is summarised in Table 5.2. The weightings (relative to a standard weighting of 1) of the last 3 data points (3.74 Myr, 3.75 Myr, 3.76 Myr) have been

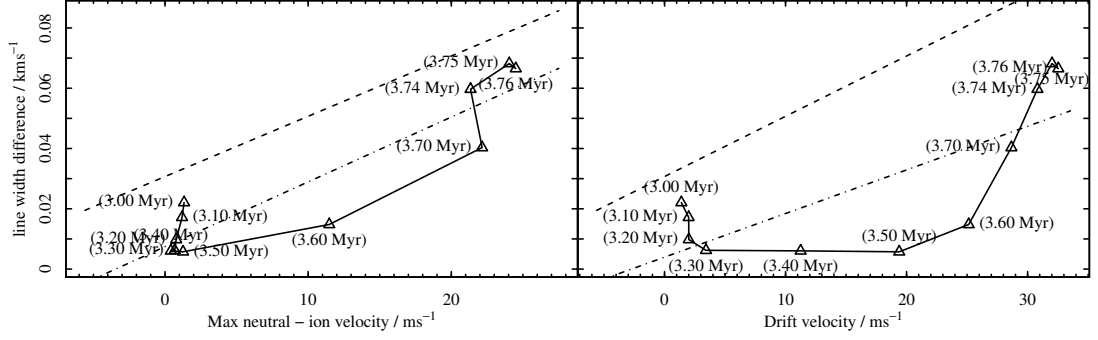


Figure 5.7. Linewidth differences between NH_3 (1,1) and N_2H^+ (1-0) during the collapse phase ($3.0 \text{ Myr} \leq t \leq 3.76 \text{ Myr}$) using a beam resolution consistent with ALMA.

Left hand side plots linewidth differences against the difference between the maximum ion and neutral velocities; right hand side plots linewidth differences against the drift velocity. The dashed line represents an ideal line for a core with a constant temperature ($T = 10 \text{ K}$) throughout the core. The dot-dashed line is the linear least-squares fit to the data points.

reduced to 0.4, 0.1 and 0.1 respectively, due to the shorter interval between the samples. For the expansion phase, the velocity difference as derived from the mean $\text{NH}_3 - \text{HC}^{18}\text{O}^+$ and $\text{NH}_3 - \text{N}_2\text{H}^+$ linewidth differences, do not reflect the mean V_{diff} or V_{drift} . In collapse, the velocity difference as derived from the mean $\text{NH}_3 - \text{HC}^{18}\text{O}^+$ linewidth difference gives a good match to the mean V_{drift} while the velocity difference derived from the mean $\text{NH}_3 - \text{N}_2\text{H}^+$ linewidth difference at the core centre is poor. However, observing $\text{NH}_3 - \text{N}_2\text{H}^+$ at an off-centre position results in a better estimate of the ion-neutral velocity difference than using observations taken at the core centre. These results indicate that only during the collapse phase are linewidth differences useful in deriving ion-neutral velocity differences.

5.2 Observations of linewidth differences

Benson et al. (1998), hereafter BCM98, observed with high resolution the linewidths for transitions of N_2H^+ and C_3H_2 for 60 dense cores for which $n(\text{H}_2) > 1 \times 10^4 \text{ cm}^{-3}$. The authors determined the mean difference in the local standard of rest velocity, V_{LSR} , between the lines of N_2H^+ (1-0) and C_3H_2 (2,1): $V_{\text{LSR}}(\text{N}_2\text{H}^+) - V_{\text{LSR}}(\text{C}_3\text{H}_2) = -0.024 \pm 0.010 \text{ kms}^{-1}$. Taking into account the noise of the observations and the uncertainty in the rest frequency of C_3H_2 , they conclude that an upper limit to bulk motions of ions

Table 5.2. Mean and standard deviation of ion-neutral velocity differences as derived from linewidths of simulated line profiles of NH_3 , HC^{18}O^+ and N_2H^+ .

Velocity difference	expansion μ /ms ⁻¹	σ /ms ⁻¹	collapse μ /ms ⁻¹	σ /ms ⁻¹
V_{drift}	17.4	5.9	13.0	11.3
V_{diff}	8.5	6.1	6.1	8.4
$\text{NH}_3 - \text{HC}^{18}\text{O}^+$	4.4	2.7	12.0	14.5
$\text{NH}_3 - \text{N}_2\text{H}^+$	-23.1	7.2	-16.75	6.5
$\text{NH}_3 - \text{N}_2\text{H}^+$ offset = 100''	-	-	2.9	8.5
$\text{NH}_3 - \text{N}_2\text{H}^+$ beamwidth $\sim 11''$	-	-	-6.1	8.0

The actual mean and standard deviation of the drift velocity, V_{drift} , and the difference between the maximum ion and neutral velocity, V_{diff} , are included for comparison. Results for $\text{NH}_3 - \text{N}_2\text{H}^+$ linewidth differences at an offset of 100 arcsec show a better match with actuals than for linewidth differences at the core centre.

Table 5.3. Mean and standard deviation of the difference between linewidths of C_3H_2 and N_2H^+ .

Population	μ / kms ⁻¹	σ / kms ⁻¹
no infrared source	0.061	0.099
no infrared source excluding B133 ^(a)	0.081	0.059

Sample data are taken from tables 1, 2 and 3 of Benson et al. (1998).

(a) B133 has been excluded from the population with no associated infrared source since it is a potential outlier having a large negative value of $\Delta V(\text{C}_3\text{H}_2) - \Delta V(\text{N}_2\text{H}^+) = -0.23 \text{ kms}^{-1}$

Table 5.4. Mean and standard deviation of the difference between linewidths of NH_3 and N_2H^+ .

Population	μ / kms ⁻¹	σ / kms ⁻¹
no infrared source	0.009	0.067
no infrared source excluding B133	0.019	0.058

Sample data are taken from table 2 of Benson et al. (1998), table 7 of Benson & Myers (1989) and table 3 of Ungerechts et al. (1982) for the NH_3 linewidth of B133.

and neutrals, i.e. the ion-neutral drift velocity, is $V_{drift} \leq 30 \text{ ms}^{-1}$. The authors stress the result is not a detection of ion-neutral drift, rather an upper limit to the ion-neutral drift velocity. Also of particular interest in this study is the correlation they find between the two linewidths: $\Delta V(\text{C}_3\text{H}_2) = (0.11 \pm 0.03) + (0.93 \pm 0.06)\Delta V(\text{N}_2\text{H}^+) \text{ kms}^{-1}$. The large constant component of this relation ($0.11 \pm 0.03 \text{ kms}^{-1}$) was not analysed further by the authors. Comparison with the simple model of linewidth differences (equation 5.4) implies a significant non-zero velocity difference between ions and neutrals: the constant component gives a value for the mean value of difference between neutral and ion velocities:

$$\langle v_n - v_i \rangle = \frac{(0.11 \pm 0.03) - \Delta V_{constant}}{2} \text{ kms}^{-1} \quad (5.5)$$

giving $\langle v_n - v_i \rangle = 61 \pm 15 \text{ ms}^{-1}$ although this result is weakly dependent on the assumed temperature and turbulence in the model. Using a value of $V_{TURB} = 0.15 \text{ kms}^{-1}$ gives $\langle v_n - v_i \rangle = 58 \pm 15 \text{ ms}^{-1}$; using a value of $T = 12.5 \text{ K}$ gives $\langle v_n - v_i \rangle = 62 \pm 15 \text{ ms}^{-1}$. The mean value is inconsistent at the 1σ level with the upper limit of 30 ms^{-1} derived by BCM98. Using the linewidth data from tables 1, 2 and 3 from BCM98, a direct calculation is made of the mean and standard deviation of $\Delta V(\text{C}_3\text{H}_2) - \Delta V(\text{N}_2\text{H}^+)$ for the population of cores without an infrared source. Where multiple observations are available for the same core, only one observation is taken in order to minimise any biasing effects. The results of this analysis are presented in Table 5.3. For the sub-population of cores with no associated infrared source and excluding B133, the mean value ($\mu = 0.081 \text{ kms}^{-1}$) is larger than the standard deviation ($\sigma = 0.059 \text{ kms}^{-1}$): B133 is the only core with no infrared source that shows a negative linewidth difference, $\Delta V(\text{C}_3\text{H}_2) - \Delta V(\text{N}_2\text{H}^+) = -0.23 \text{ kms}^{-1}$. The core also shows a large linewidth for N_2H^+ ($\Delta V(\text{N}_2\text{H}^+) = 0.62 \text{ kms}^{-1}$) that is significantly higher than the mean for the remainder of the sub-population ($\langle \Delta V(\text{N}_2\text{H}^+) \rangle = 0.25 \text{ kms}^{-1}$). Converting the mean and standard deviation of this sub-population into an equivalent velocity difference gives $\langle v_n - v_i \rangle = 46 \pm 30 \text{ ms}^{-1}$. The mean value is higher than the upper limit of 30 ms^{-1} derived by BCM98 but with the large scatter is still consistent with it. However, the assumption that these lines trace the same volume of gas may be incorrect, since N_2H^+ is mainly formed in the dense gas of the inner core (Turner 1995) while C_3H_2 is likely to trace the gas in the outer core (Lai et al. 2003). This view is supported by a study of the

TMC-1 molecular cloud by Hirahara et al. (1995) who find an anti-correlation between the distribution of N_2H^+ and carbon chain molecules. The linewidth difference could then be explained by differences in the gas properties between the inner and outer core: higher turbulent or dynamical velocities coupled with higher gas temperatures in the outer core could explain the linewidth difference without the need to include a drift velocity. On the other hand, NH_3 and N_2H^+ abundances are well correlated (Hirahara et al. 1995) and therefore more likely to trace the same volume of gas. Using the same population of cores with no associated infrared source from BCM98, the mean $\Delta V(\text{NH}_3) - \Delta V(\text{N}_2\text{H}^+)$ linewidth difference is calculated using data from Ungerechts et al. (1982), Myers & Benson (1983), Benson & Myers (1989) and BCM98. The results of this analysis are presented in Table 5.4. Using the mean and standard deviation of the sub-population of cores that exclude B133, an equivalent velocity difference is derived: $\langle v_n - v_i \rangle = -6 \pm 29 \text{ ms}^{-1}$. This result would indicate that no significant velocity difference exists between ions and neutrals. However, from the previous analysis of linewidth differences of simulated line profiles of NH_3 and N_2H^+ , observations taken at the core centre may not be indicative of the maximum velocity difference between ions and neutrals within the core: a negative mean velocity difference is derived at the core centre while the actual mean velocity difference is found to be positive.

5.3 Summary

The linewidths of the optically thin lines HC^{18}O^+ (1-0), N_2H^+ (1-0) and NH_3 (1,1) for a range of core densities are analysed and a simple model constructed of the linewidth difference between the lines of charged and neutral species. It is found that the method of ion-neutral linewidth differencing to be poor when used to determine velocity differences in expanding cores. For collapsing cores, $\text{NH}_3 - \text{HC}^{18}\text{O}^+$ linewidth differences are well correlated with the drift velocity. The $\text{NH}_3 - \text{N}_2\text{H}^+$ linewidth differences are poorly correlated with ion-neutral velocity differences. When observations are targeted at the region of maximum ion-neutral drift, a strong correlation is found between linewidth differences and ion-neutral velocity differences. The conclusion drawn from this analysis is: if careful observations are made of suitable pairs of ions and neutrals, and expanding cores are excluded from the sample, linewidth differences can be used to deduce the velocity difference between ions and neutrals.

A mean linewidth difference of 0.081 kms^{-1} is found between lines of C_3H_2 and N_2H^+ using observations from Benson et al. (1998) for 14 pre-stellar cores: a mean infall velocity difference between neutrals and ions of $46 \pm 30 \text{ ms}^{-1}$ is inferred – much higher than the model predicts. A possible explanation for the linewidth difference is that C_3H_2 and N_2H^+ sample gas in the outer and inner core respectively and that gas in the outer and inner core have different dynamical, thermal or turbulent properties. A mean linewidth difference of 0.019 kms^{-1} is found between lines of NH_3 and N_2H^+ using observations from Myers & Benson (1983), Benson & Myers (1989) and Benson et al. (1998) for the same population of pre-stellar cores: a mean infall velocity difference between neutrals and ions of $-6 \pm 29 \text{ ms}^{-1}$ is inferred. The model also predicts a negative infall velocity difference of $-16.5 \pm 6.5 \text{ ms}^{-1}$ when observations are taken at the core centre, in contrast to the actual mean drift velocity of $13 \pm 11 \text{ ms}^{-1}$.

Chapter 6

Results for model variations

What is the use of repeating all that stuff, if you don't explain it as you go on? It's by far the most confusing thing I ever heard!

Alice in Wonderland, Lewis Carroll

Chapter 4 presented results for a single run of the model for a set of parameters that define the standard model. The objective of this chapter is to present the results for all model variations and compare the results against the standard model and observational data. These results have been taken from Stace and Rawlings (2014b), in preparation.

6.1 Core dynamics over time

Table 6.1 summarises the analysis of the core dynamics over time for the standard model and model variations. Model runs are terminated when the central density reaches $n_c(\text{H}) \sim 10^7 \text{ cm}^{-3}$. Beyond a central density of $n_c(\text{H}) \sim 10^7 \text{ cm}^{-3}$, the evolution at the core centre is rapid and the chemical integration timestep needs to be reduced significantly, leading to long program run times. Moreover, the code would require shells at the core centre to be divided up into smaller sub-shells in order that results do not suffer from artificially-induced collapse due to shell sizes being larger than the Jeans length: Truelove et al. (1997) find in their simulations of isothermal, self-gravitational hydrodynamical collapse that the ratio of the cell size, Δx , to the Jeans length, λ_J , needs to satisfy $\Delta x/\lambda_J \leq 0.25$ in

order that artificial condensations are not created. Additional limitations with the current version of code would also support applying a central density limit of $n_c(\text{H}) \sim 10^7 \text{ cm}^{-3}$: at much higher densities, the creation of a hydrostatic core would need to be modelled and the resulting temperature increase would require desorption of molecules from grain surfaces to be included.

Apart from the model variations where the choice of initial magnetic flux density, B_0 , is used specifically to target models of magnetically subcritical cores, the approach to deciding what value of B_0 to use involves a number of re-runs of each model. Where a run of a model does not result in a magnetically supercritical core, B_0 is lowered until the core becomes marginally magnetically supercritical – i.e. the core goes through an expansion phase before re-collapsing. Where the model results in a magnetically subcritical core, the initial magnetic flux density is increased until the core becomes marginally magnetically supercritical. The reason for choosing an initial magnetic configuration where the core is just magnetically supercritical, is based on the assumption that cores condense out from core complexes that are themselves initially magnetically subcritical. Through a slow contraction of the core complex parallel to magnetic fields lines, the mass to magnetic flux ratio can be increased and cores can collapse under the initial conditions of marginally magnetic supercriticality.

The core dynamics over time are not plotted for all variations on the standard model, since in general they follow the same pattern of collapse, expansion followed by a second collapse phase. Where the change in parameters (such as lowering B_0) result in a core that is no longer marginally supercritical but supercritical, the core collapses in a manner similar to the second collapse phase: this is illustrated by Figure 6.1, which plots the core dynamics over time for $B_0 = 5.6 \mu\text{G}$. Where the change in parameters result in a subcritical core, the core repeats the collapse expansion cycle, with the central magnetic flux density gradually decreasing during each cycle along with an increase in the minimum central density: this is best illustrated in Figure 6.2, which plots the core dynamics over time for model *grainchem1* where B_0 has not been modified to achieve supercriticality.

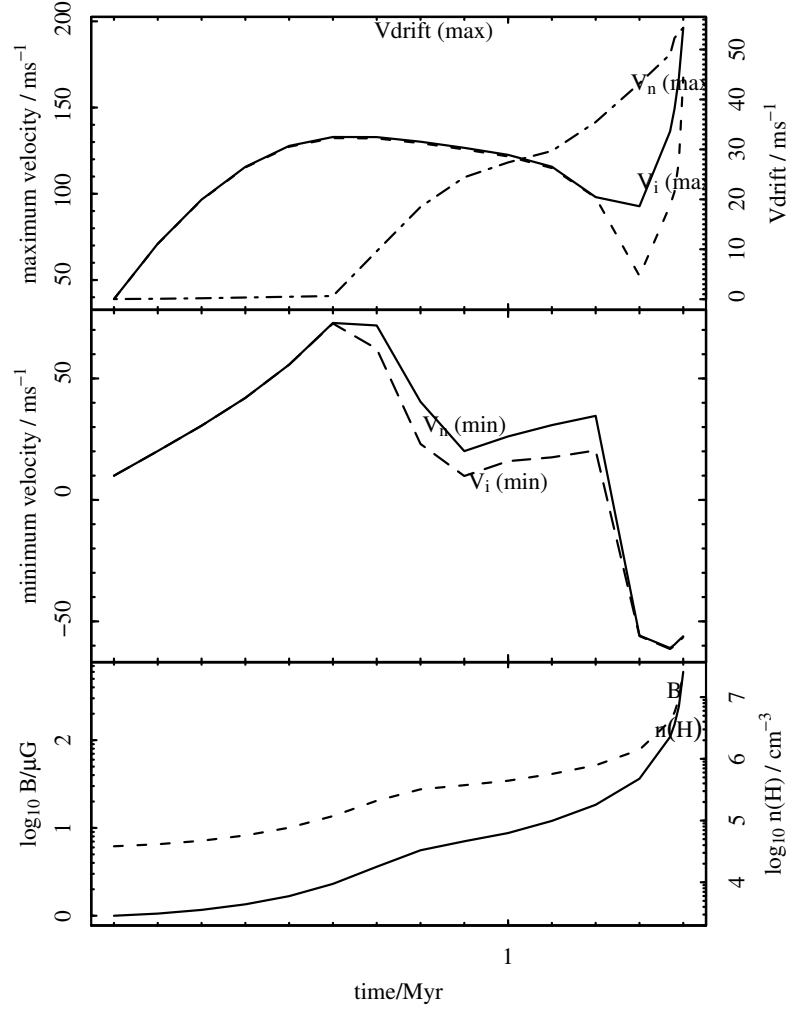


Figure 6.1. Core dynamics over time for the model variation b_4 .

Upper graph plots the maximum ion velocity, V_i (max), as the dashed line and the maximum neutral velocity, V_n (max), as the solid line against the y-axis on the left; the maximum drift velocity, V_{drift} (max), is plotted as the dash-dot line against the y-axis on the right. Middle graph plots the minimum ion velocity, V_i (min), as the dashed line and the minimum neutral velocity, V_n (min) as the solid line. For the central shell, the lower graph plots the magnetic flux density, B , as the dashed line and the hydrogen nuclei number density, $n(H)$, as the solid line.

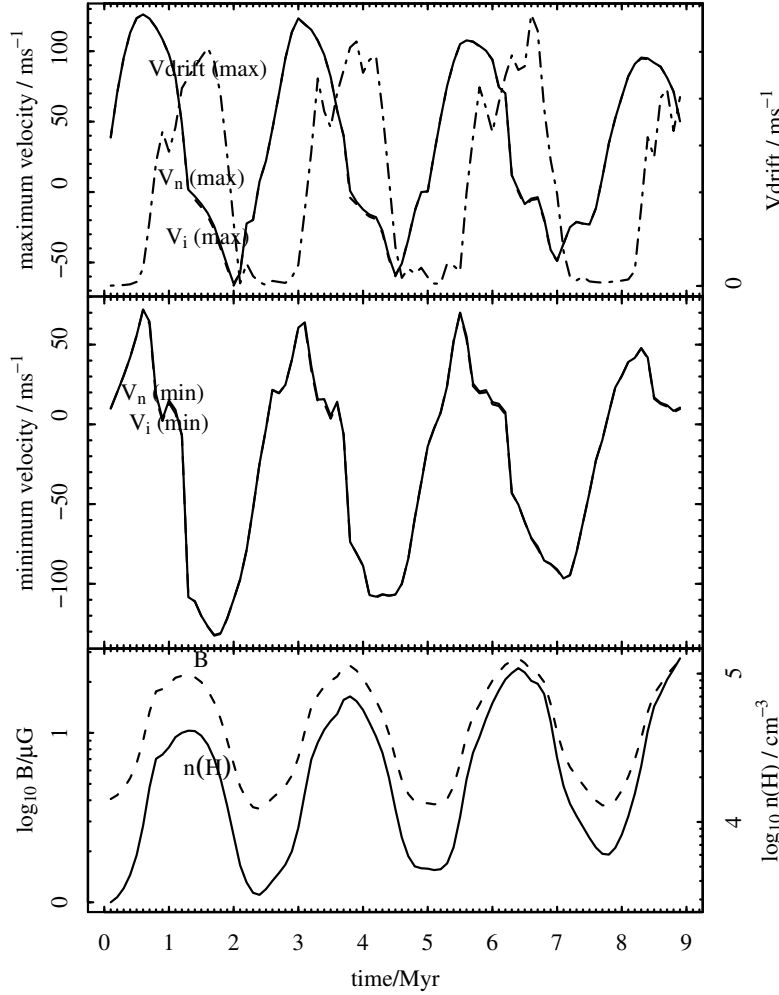


Figure 6.2. Core dynamics over time for a subcritical run for model variation *grainchem1*.

Upper graph plots the maximum ion velocity, V_i (max), as the dashed line and the maximum neutral velocity, V_n (max), as the solid line against the y-axis on the left; the maximum drift velocity, V_{drift} (max), is plotted as the dash-dot line against the y-axis on the right. Middle graph plots the minimum ion velocity, V_i (min), as the dashed line and the minimum neutral velocity, V_n (min) as the solid line. For the central shell, the lower graph plots the magnetic flux density, B , as the dashed line and the hydrogen nuclei number density, $n(\text{H})$, as the solid line.

Table 6.1. Model variations – core dynamics over time.

Model identifier	t_c /Myr	t_1 /Myr	$n_c(\text{H})$ / 10^6 cm^{-3}	$n_1(\text{H})$ / 10^3 cm^{-3}	B_0 / μG	B_c / μG	B_1 / μG	V_{Nmax} / ms^{-1}	V_{Nmin} / ms^{-1}	V_{Imax} / ms^{-1}	V_{Imin} / ms^{-1}	ΔV / ms^{-1}
standard	3.75	2.4	4.34	4.91	6.1	170.5	3.1	124.3	-110.7	123.62	-110.57	32.02
b1	0.87	0	3.51	2.80	1.4	138.4	1.4	352.8	10.0	348.13	9.97	23.90
b2	0.92	0	6.16	2.80	2.8	254.0	2.8	337.6	10.0	319.09	9.97	52.74
b3	1.04	0	6.32	2.80	4.2	289.9	4.2	277.7	10.0	277.08	9.98	63.83
b4	1.38	0	3.59	2.80	5.6	193.2	5.6	149.3	-61.0	132.29	-61.39	52.29
grainchem1	4.55	3.1	4.88	6.09	5.7	490.4	6.6	229.9	-103.0	223.80	-103.89	8.07
grainchem2	3.74	2.4	3.57	4.90	6.1	156.2	3.1	124.3	-110.5	123.62	-110.35	31.39
graindist1	4.00	2.3	3.68	4.03	6.1	165.2	3.7	124.3	-119.0	123.62	-120.45	26.11
graindist2	4.08	2.4	4.75	4.97	5.9	266.7	4.4	127.2	-113.9	126.45	-115.29	24.29
stick1	3.83	2.4	3.87	5.15	6.1	202.7	3.8	124.3	-110.8	123.62	-110.50	31.38
stick2	3.78	2.3	3.48	4.85	6.1	143.2	3.4	124.3	-111.4	123.62	-111.29	29.94
temp1	3.84	2.3	4.18	5.28	6.1	195.4	3.7	127.5	-110.4	126.81	-111.67	34.56
xnal	3.69	2.4	3.22	5.03	6.1	118.0	2.5	124.4	-109.2	123.58	-109.09	31.26
xsl	3.62	2.3	3.83	7.50	6.2	155.2	3.5	122.0	-94.5	119.58	-94.51	38.18
zeta1	4.24	2.4	4.75	5.57	5.8	311.5	5.1	128.3	-110.2	127.85	-111.23	20.45
zeta2	3.59	2.3	4.00	3.97	6.4	88.8	1.4	118.8	-135.1	118.01	-134.30	46.38
avcrit1	4.55	3.1	3.44	3.49	5.5	170.7	3.4	134.5	-139.4	133.76	-140.04	44.65
avcrit2	3.93	2.4	4.16	5.07	5.9	167.4	3.8	127.2	-113.6	126.45	-114.74	31.52

$n_c(\text{H})$ is the central hydrogen nuclei number density at the end of the run at time t_c ; t_1 is the time at the point of minimum central density, $n_1(\text{H})$, and magnetic flux density, B_1 , prior to the final collapse phase: $t_1 = 0$ indicates a single collapse phase; B_c is the central magnetic flux density; B_0 is the initial magnetic flux density; V_{Nmax} is the maximum neutral infall velocity; V_{Nmin} is the minimum neutral infall velocity; V_{Imax} is the maximum ion infall velocity; V_{Imin} is the minimum ion infall velocity; ΔV is the maximum drift velocity.

Table 6.1 shows little variation in B_0 for all runs of the model, indicating that the environment does not particularly affect the critical magnetic flux density. For those runs that are marginally supercritical, there is also little variation in maximum infall velocity and maximum drift velocity, although maximum velocities will tend to be higher for runs with a higher final central density. The largest change appears to be in the final magnetic flux density and the time cores take to collapse.

6.1.1 Comparing collapse times to the free-fall time

In Table 6.2 the time taken to collapse from the point of minimum density at time t_1 to the end of the model run at time t_c is compared with the modified free-fall time that takes into account a non-zero initial velocity, V_1 , at time t_1 and radius R_1 and a non-zero final radius R_c at time t_c (see Appendix B for a derivation of the following formula):

$$\Delta t_{ff} = \sqrt{\frac{3\pi}{32G\rho_1}} \frac{2\theta_c + \sin 2\theta_c - 2\theta_1 - \sin 2\theta_1}{\pi \cos^3 \theta_1} \quad (6.1)$$

with

$$\theta_1 = \arcsin \left(V_1 \sqrt{R_1 / 2GM_c} \right) \quad (6.2)$$

and

$$\theta_c = \arcsin \left(\sqrt{R_c / R_1} \cos \theta_1 \right) \quad (6.3)$$

where ρ_1 is the central mass density at time t_1 , G is the gravitational constant and $M_c = 0.0768M_\odot$ is the mass of the central shell. In this expression, an initially collapsing central shell has a positive V_1 , giving rise to a positive θ_1 ; an expanding central shell has a negative V_1 , giving rise to a negative θ_1 . In the limit that $R_c = 0$ and $V_1 = 0$, the equation reduces to the normal expression for free-fall time: $t_{ff} = \sqrt{3\pi/(32G\rho_1)}$. The table shows that for models that are marginally supercritical, the ratio of infall time to free-fall time, $(t_c - t_1)/\Delta t_{ff}$, varies between 1.55 for model *zeta2* (low cosmic ray ionization rate) to 3.11 for model *zeta1* (high cosmic ray ionization rate). This is in approximate

Table 6.2. Collapse time $t_c - t_1$ compared with free-fall time Δt_{ff} ; t_1 is the time at which the central density reaches $n_1(\text{H}) \simeq 3 \times 10^3 \text{ cm}^{-3}$.

Model identifier	$n_1(\text{H})$ / 10^3 cm^{-3}	V_1 / ms^{-1}	$t_c - t_1$ /Myr	Δt_{ff} /Myr	$\frac{t_c - t_1}{\Delta t_{ff}}$
standard	4.9	14.21	1.35	0.56	2.42
b1	2.8	0.00	0.87	0.86	1.01
b2	2.8	0.00	0.92	0.86	1.07
b3	2.8	0.00	1.04	0.86	1.21
b4	2.8	0.00	1.38	0.86	1.61
grainchem1	6.1	-2.85	1.45	0.60	2.42
grainchem2	4.9	12.90	1.34	0.56	2.38
graindist1	4.0	-11.81	1.7	0.83	2.06
graindist2	5.0	6.00	1.68	0.60	2.78
stick1	5.2	15.20	1.43	0.54	2.65
stick2	4.9	-12.91	1.48	0.76	1.95
temp1	5.3	-7.53	1.54	0.68	2.27
xna1	5.0	8.65	1.29	0.58	2.22
xs1	7.5	-6.85	1.32	0.56	2.35
zeta1	5.6	2.33	1.84	0.59	3.11
zeta2	4.0	-11.65	1.29	0.83	1.55
avcrit1	3.5	27.91	1.45	0.57	2.53
avcrit2	5.1	9.39	1.53	0.58	2.66

V_1 is the infall velocity of the central shell at time t_1 : positive values indicate infall; negative values indicate expansion.

agreement with the lifetimes of pre-stellar cores as estimated from counts of the number of starless cores compared with that of cores with embedded young stellar objects (Kirk et al. 2005; Beichman et al. 1986; Lee & Myers 1999). Kirk et al. (2005) find the lifetime of starless cores to be roughly 3 times the free-fall time for starless cores with central volume density, $n(\text{H}) \simeq 5 \times 10^4 \text{ cm}^{-3}$, and twice the free-fall time for starless cores with $n(\text{H}) \simeq 2 \times 10^5 \text{ cm}^{-3}$. However, these estimates are based on an approximate value of $\sim 2 \pm 1 \times 10^5 \text{ yr}$ for the lifetime of Class I protostars, implying uncertainties in the estimates pre-stellar core lifetimes of $\sim \pm 50$ percent.

The ratio of infall to free-fall times are calculated for all models. Tables 6.3 and 6.4 present the ratio of infall to free-fall times for initial central densities of $n(\text{H}) \simeq 5 \times 10^4 \text{ cm}^{-3}$ and $n(\text{H}) \simeq 2 \times 10^5 \text{ cm}^{-3}$ respectively. Table 6.2 shows that for models *b1*, *b2*, *b3* and *b4*, the ratio of infall time to free-fall time is lower than the average, varying from 1.01 (nearly free-fall time) for $B_0 = 1.4 \mu\text{G}$ to 1.61 for $B_0 = 5.6 \mu\text{G}$. Table 6.3 clearly shows the rate of infall slowing down relative to the overall rates for infall from Table

Table 6.3. Collapse time $t_c - t_2$ compared with free-fall time Δt_{ff} ; t_2 is the time at which the central density reaches $n_2(\text{H}) \simeq 5 \times 10^4 \text{ cm}^{-3}$.

Model identifier	$n_2(\text{H})$ / 10^4 cm^{-3}	V_2 / ms^{-1}	$t_c - t_2$ /Myr	Δt_{ff} /Myr	$\frac{t_c - t_2}{\Delta t_{ff}}$
standard	4.6	42.45	0.55	0.15	3.64
b1	10.0	149.77	0.07	0.06	1.17
b2	8.5	123.70	0.12	0.08	1.59
b3	5.7	81.75	0.24	0.11	2.17
b4	3.3	40.42	0.58	0.18	3.23
grainchem1	4.5	29.46	0.65	0.17	3.89
grainchem2	4.5	41.25	0.54	0.15	3.53
graindist1	3.4	44.22	0.9	0.17	5.18
graindist2	3.8	45.81	0.88	0.16	5.40
stick1	4.1	46.16	0.63	0.16	4.02
stick2	4.8	45.32	0.58	0.14	4.03
temp1	3.7	36.30	0.74	0.17	4.24
xna1	3.1	20.57	0.59	0.21	2.76
xs1	3.1	10.97	0.62	0.23	2.70
zeta1	4.4	43.83	0.94	0.15	6.09
zeta2	4.2	27.45	0.49	0.17	2.81
avcrit1	4.8	47.23	0.75	0.14	5.26
avcrit2	3.8	57.18	0.73	0.15	4.83

V_2 is the infall velocity of the central shell at time t_2 .

6.2. This is understandable, since in the initial phase of collapse, little or no magnetic or thermal pressure gradient exists at the centre of the core. Table 6.4 shows that the collapse rate increases for most cores relative to that in Table 6.3, and in a few instances is seen to decrease. This would indicate that for most models at this density, ambipolar diffusion has reduced the magnetic flux density to a sufficient level such that collapse rates can increase. In general, the ratio of infall to free-fall times are larger by a factor of 2 to those estimated by Kirk et al. (2005) for a central density of $n(\text{H}) \simeq 2 \times 10^5 \text{ cm}^{-3}$. Taking into account the uncertainties in the estimates of pre-stellar core lifetimes ($\sim \pm 50$ percent), 6 of the model cores are within the lower (~ 1) and upper (~ 3) limits: *b1*, *b2*, *b3*, *b4*, *xna1*, *xs1*. Model variation *b4* (having $B_0 = 5.6 \mu\text{G}$) gives the closest fit to observations with infall times at $n(\text{H}) \simeq 2 \times 10^5 \text{ cm}^{-3}$ larger than free-fall times by a factor of 1.96. For $n(\text{H}) \simeq 5 \times 10^4 \text{ cm}^{-3}$, the infall time for model *b4* is 3.23, in good agreement with the ratio of 3 derived from observations. However, the authors of this study calculate free-fall times without an initial velocity and therefore may underestimate the true ratio in comparison to a core already in collapse. In order to assess the impact of this assumption, the ratio

Table 6.4. Collapse time $t_c - t_3$ compared with free-fall time Δt_{ff} ; t_3 is the time at which the central density reaches $n_3(\text{H}) \simeq 2 \times 10^5 \text{ cm}^{-3}$.

Model identifier	$n_3(\text{H})$ / 10^5 cm^{-3}	V_3 / ms^{-1}	$t_c - t_3$ /Myr	Δt_{ff} /Myr	$\frac{t_c - t_3}{\Delta t_{ff}}$
standard	2.2	20.62	0.25	0.08	3.28
b1	2.6	169.00	0.04	0.03	1.17
b2	3.7	112.25	0.06	0.04	1.59
b3	8.1	85.74	0.04	0.03	1.48
b4	4.8	48.30	0.08	0.04	1.96
grainchem1	2.3	25.44	0.25	0.07	3.42
grainchem2	2.3	20.98	0.24	0.07	3.25
graindist1	2.5	20.60	0.3	0.07	4.24
graindist2	2.1	19.07	0.38	0.08	4.73
stick1	2.8	19.04	0.23	0.07	3.40
stick2	3.1	21.48	0.18	0.06	2.91
temp1	2.7	18.12	0.24	0.07	3.43
xna1	2.7	23.72	0.19	0.07	2.91
xs1	4.0	32.97	0.12	0.05	2.41
zeta1	2.1	14.08	0.44	0.08	5.28
zeta2	3.3	19.05	0.19	0.06	3.09
avcrit1	3.0	20.47	0.25	0.06	3.93
avcrit2	2.5	23.50	0.23	0.07	3.31

V_3 is the infall velocity of the central shell at time t_3 .

of infall to free-fall time is recalculated for model *b4*, assuming no initial velocities. For starting times of t_2 and t_3 , calculated ratios are 2.39 and 1.48 respectively; this compares with the original values of 3.23 and 1.96, indicating that there can be a significant decrease in calculated ratios. However, model *b4* is still collapsing in timescales that are consistent with observational data when the uncertainties in the estimates of pre-stellar core lifetimes are taken into account. For model *xs1*, ratios of 2.47 and 1.98 are calculated at starting times t_2 and t_3 and assuming no initial infall velocity. Again, the ratio of infall to free-fall times are consistent with observational data. This adjustment is sufficient to bring the ratio back to between 1 and 3 at an initial starting density of $n(\text{H}) \simeq 2 \times 10^5 \text{ cm}^{-3}$ for the following models: *standard*, *grainchem2*, *zeta2*, *avcrit2*. At an initial starting density of $n(\text{H}) \simeq 5 \times 10^4 \text{ cm}^{-3}$ all models are now consistent with observational data with the exception of the following: *b1*, *b2*, *b3*, *graindist2*, *zeta2*. In conclusion, the models generally show the correct trend in that collapse times are shorter relative to the free-fall time at higher densities. When taking the uncertainties in observational data into account and assuming that an adjustment is required to the observed ratios of core lifetimes to free-

fall times that takes into account a non-zero initial velocity, most marginally supercritical models are consistent with pre-stellar core lifetimes having an initial starting density of $n(\text{H}) \simeq 5 \times 10^4 \text{ cm}^{-3}$. However, less than half the marginally supercritical models are consistent with pre-stellar core lifetimes having $n(\text{H}) \simeq 2 \times 10^5 \text{ cm}^{-3}$. A summary of these results is provided in section 6.4.

6.2 Chemical and dynamical radial profiles

The chemical and dynamical radial profiles are summarised in six tables in order to aid comparison between the models: Table 6.5 gives the dynamical characteristics of the core when the central density reaches approximately, $n_c(\text{H}) \sim 3 \times 10^6 \text{ cm}^{-3}$; Table 6.6 describes the radial variation in $n(\text{H})$ and B by fitting power laws of the form: $n(\text{H}) \propto R^{-\alpha}$ and $B \propto n(\text{H})^\beta$ over three regions of the core; Table 6.7 summarises the variation in dust-gas ratio, visual extinction and temperature in the core; Tables 6.8 and 6.9 summarise the abundance variations of molecular species by comparing fractional abundances at the centre with the maximum fractional abundances in the core; Table 6.10 gives the maximum abundances of molecular species and the radial distance at which the maximum occurs. Plots of the radial profiles of specific examples are referenced in the text; for all other models, plots of the radial profiles are made available in Appendix C.

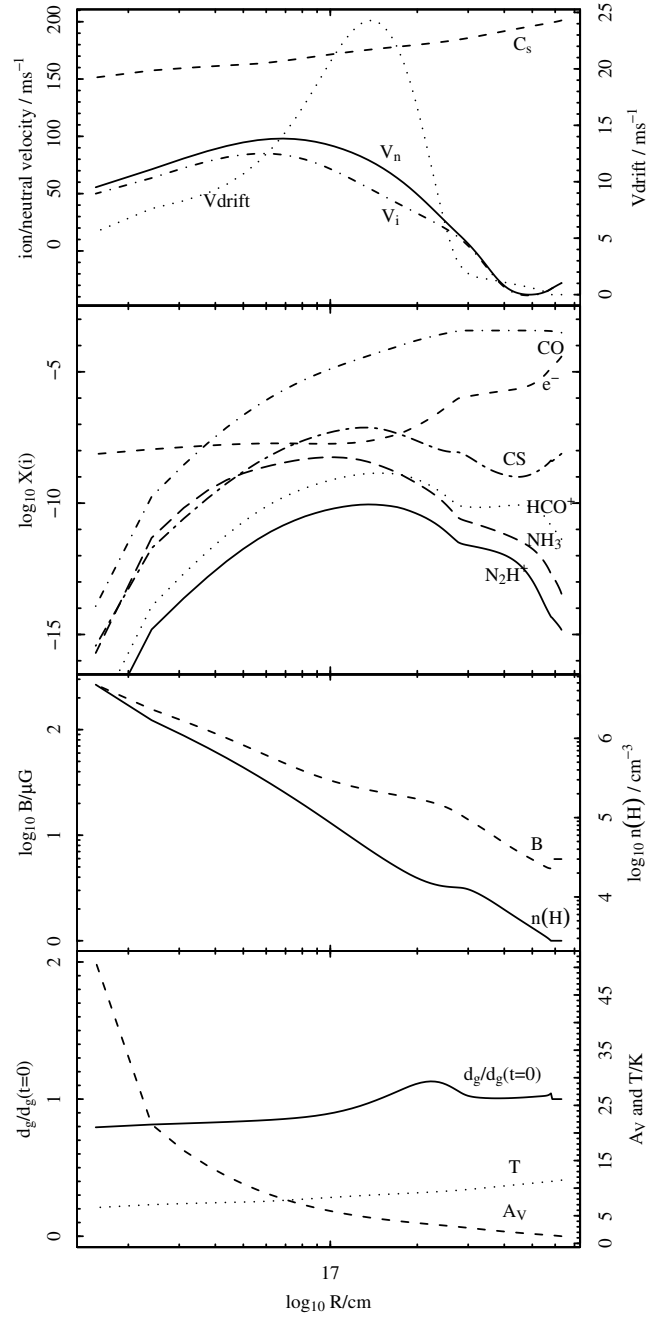


Figure 6.3. Chemical and dynamical radial profile for model *graindist2*.

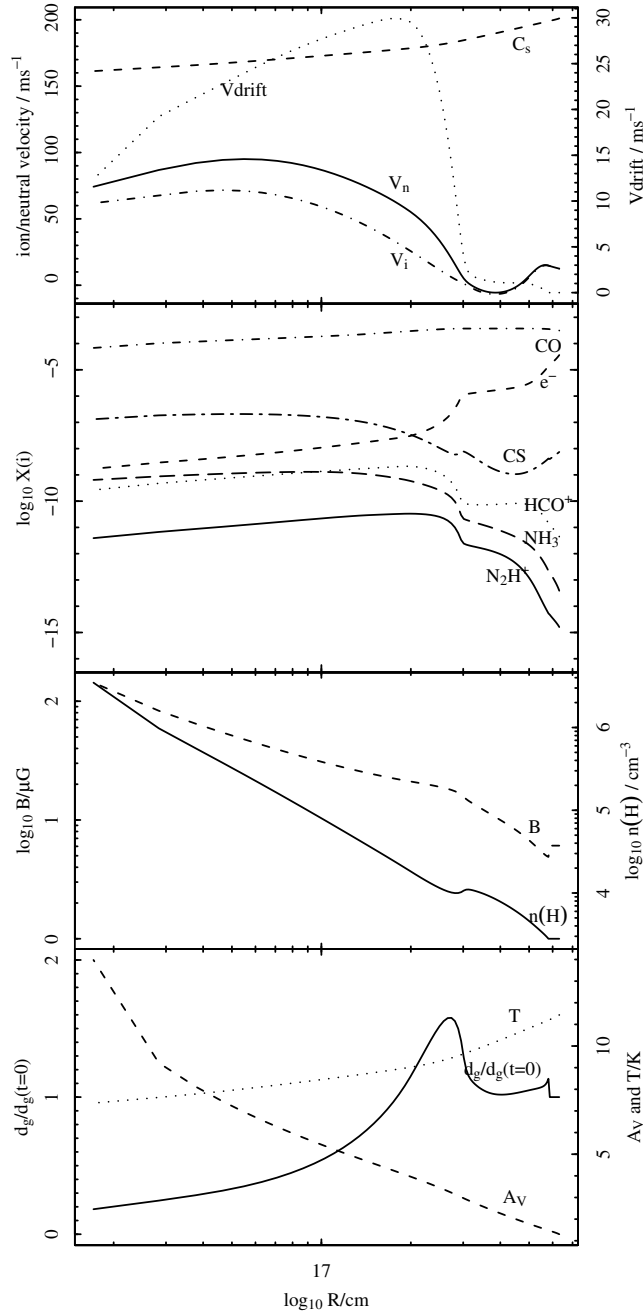


Figure 6.4. Chemical and dynamical radial profile for model *stick2*.

Table 6.5. Model variations – dynamical radial profiles when $n_c(\text{H}) \sim 3 \times 10^6 \text{ cm}^{-3}$.

Model identifier	$n_c(\text{H})$ / 10^6 cm^{-3}	t_c /Myr	B_c / μG	V_{Nmax} / ms^{-1}	V_{Nmin} / ms^{-1}	V_{Imax} / ms^{-1}	V_{Imin} / ms^{-1}	ΔV / ms^{-1}	$R(V_{Nmax})$ / 10^{16} cm	$R(V_{Imax})$ / 10^{16} cm	$R(\Delta V)$ / 10^{16} cm
standard	4.34	4.75	170.48	107.59	0.45	83.54	-0.79	32.02	5.21	4.39	14.97
b1	3.51	1.87	138.39	352.77	148.44	348.13	148.44	23.90	13.74	14.77	1.71
b2	6.16	1.92	253.97	337.65	139.83	319.09	130.46	52.74	14.20	22.42	5.08
b3	6.32	2.04	289.89	277.71	128.08	277.08	117.69	63.83	28.51	28.51	12.21
b4	3.59	2.38	193.20	149.26	-59.57	101.15	-60.05	52.29	7.58	6.43	12.73
grainchem1	4.88	5.55	490.39	229.95	60.75	223.80	59.36	6.66	10.36	9.96	15.62
grainchem2	3.57	4.74	156.15	103.04	3.67	83.06	2.41	31.39	6.12	4.51	15.89
graindist1	3.68	5.00	165.19	66.93	-63.63	52.45	-64.44	23.95	3.75	3.75	10.24
graindist2	4.75	5.08	266.72	98.05	-38.14	84.97	-38.79	24.29	6.86	5.61	13.53
stick1	3.87	4.83	202.67	102.76	5.38	88.88	4.31	31.28	7.45	6.78	19.61
stick2	3.48	4.78	143.20	95.06	-5.59	71.63	-6.75	29.94	5.48	4.65	17.44
temp1	4.18	4.84	195.38	114.38	-36.81	93.66	-37.41	34.56	6.19	4.95	14.69
xna1	3.22	4.69	118.02	95.63	12.98	71.53	12.98	31.26	5.78	3.96	11.78
xs1	3.83	4.62	155.24	114.90	19.00	89.96	19.00	38.18	6.04	5.26	18.54
zeta1	4.75	5.24	311.48	118.93	-17.10	108.23	-17.65	20.45	7.47	6.93	18.39
zeta2	4.00	4.59	88.76	92.33	-33.29	73.17	-33.98	46.38	1.63	1.63	18.13
avcrit1	3.44	5.55	170.68	86.40	15.01	54.73	12.10	44.65	4.60	37.16	7.09
avcrit2	4.16	4.93	167.44	90.77	-57.00	67.28	-57.39	31.52	4.51	3.63	8.78

$n_c(\text{H})$ is the central hydrogen nuclei number density; B_c is the central magnetic flux density; V_{Nmax} is the maximum neutral infall velocity; V_{Nmin} is the minimum neutral infall velocity; V_{Imax} is the maximum ion infall velocity; V_{Imin} is the minimum ion infall velocity; ΔV is the maximum drift velocity; $R(V_{Nmax})$ is the position of maximum neutral infall velocity; $R(V_{Imax})$ is the position of maximum ion infall velocity; $R(\Delta V)$ is the position of maximum drift velocity.

6.2.1 Dynamical radial profiles

Table 6.5 shows a notable distinction in dynamics between models that are substantially supercritical (models *b1*, *b2* and *b3*) and the remainder. Models *b1* to *b3* have: infall speeds that exceed the sound speed ($\simeq 188 \text{ ms}^{-1}$ at 10K); the position of peak drift velocity is closer to centre of the core than the positions of peak ion and neutral infall velocities. In general, for the remainder of the cores, the following properties hold: infall velocities are subthermal; the position of maximum ion infall velocity is closer than or equal to the position of maximum neutral infall velocity; the position of peak drift velocity is further from the centre of the core than the positions of peak ion and neutral infall velocities. Model *grainchem1* stands out as being atypical for the marginally supercritical cores in that its infall speed is also supersonic; a likely reason for this is the flattened magnetic field distribution in the core centre, resulting in weaker magnetic pressure. Observations of dense cores by Tafalla et al. (1998) show that the majority of starless cores have linewidths that are not substantially superthermal, indicating that models *b1*, *b2*, *b3* and *grainchem1* are inconsistent with these observations.

6.2.2 Radial profile of $n(\text{H})$

In Table 6.6, the radial distribution of $n(\text{H})$ and B are split into three regions of the core: the inner core is defined as the region within the innermost 10 shells; the middle core is defined as the region between the end of the inner core and the position of density dip; the outer core is defined as the region outward from the density dip to shell 90. The outer 10 shells are not modelled since both $n(\text{H})$ and B are held constant in this region. For most models, the following properties of $n(\text{H})$ hold: $n(\text{H})$ in the inner core is either flatter than or similar to the middle and outer cores; for all models $\alpha_i \leq 2.20$ (α_i is the exponent of the power law in the inner core). However, there are some notable exceptions to this general picture. Model *grainchem1* shows a much flatter distribution in the inner core: $\alpha_i = 1.28$. Model *graindist1* shows the distribution of $n(\text{H})$ getting flatter with increasing R . Model *avcrit1* shows the largest difference between gradients in the inner and outer core: $\alpha_o = 2.96$ in the outer core compares to $\alpha_i = 2.11$ in the inner core. Model *xs1* shows a very weak gradient in the outer core compared to the gradient in the inner core: $\alpha_o = 1.82$ in the outer core compares to $\alpha_i = 2.09$ in the inner core. Overall, for the marginally supercritical cores, the mean values are 2.04, 2.18 and 2.18 for α_i , α_m and

α_o respectively. These results compare with millimetre and submillimetre observations by Ward-Thompson et al. (1994), indicating that the density distribution in pre-stellar cores is given by $\rho \propto R^{-1.25}$ in the inner core and $\rho \propto R^{-2}$ outside the inner core. The inner core in this study, $R_{inner} \sim 4.6 \times 10^{16}$ cm, is smaller than the model inner core, $R_{10} \sim 1 \times 10^{17}$ cm, and comparable to R_4 , the radial distance of the fourth shell out from the centre. It is therefore difficult to make a direct comparison, other than to comment that there is flattening in the inner core for some models but only in model *grainchem1* is the flattening consistent with these observations. The observations are limited to a beam offset of around 65 arcsec, corresponding to 1.5×10^{17} cm at a distance of 160 pc – the mean distance for all pre-stellar cores in the sample. This limit is within the middle region of the model core. The observations of the density distribution outside the inner core are based on azimuthally averaged flux density profiles – as such they are subject to errors due to a core’s departure from spherical symmetry. For example, the observations of L1689A and L1689B would also be consistent with density profiles as steep as $\rho \propto R^{-3}$. Given the uncertainties in the observational data in the region outside the inner core, observations are consistent with the middle core of the model. A similar study of the radial profiles of the 1.2mm continuum emission of 5 pre-stellar cores by Tafalla et al. (2002) show excellent fits to density models of the form:

$$n(H) = \frac{n_0(H)}{1 + (R/R_0)^\alpha} \quad (6.4)$$

where $n_0(H)$ is the density at the core centre and R_0 is the radius of the flat inner region. The value of R_0 ranges from 4.5×10^{16} cm to 15×10^{16} cm; the value of α varies between 2 and 4. In conclusion, with respect to these observations, the gas density distribution is found to be too steep in the inner core but consistent with the middle core. However, the radial distribution of $n(H)$ is dependent on the epoch at which the radial profile is taken. For the standard model at $t = 3.5$ Myr, when $n_c(H) = 2.4 \times 10^5 \text{ cm}^{-3}$, the power law exponents are: $\alpha_i = 1.48$; $\alpha_m = 1.96$; $\alpha_o = 2.07$. For model *b4* at $t = 1.3$ Myr, when $n_c(H) = 4.8 \times 10^5 \text{ cm}^{-3}$, the power law exponents are: $\alpha_i = 1.38$; $\alpha_m = 1.88$; $\alpha_o = 2.36$. Overall, for the marginally supercritical cores, the mean values are 1.41, 1.92 and 2.32 for α_i , α_m and α_o respectively. This indicates that for earlier epochs, the density distribution in the inner core is consistent with Ward-Thompson et al. (1994). Another possibility is

that a reduction in the dust temperature in the core centre can account for the flattening of dust continuum emissions. Evans et al. (2001) find that a radial density distribution of the form $\rho \propto R^{-2}$ is consistent with the dust continuum emission from L1544 when the dust temperature increases from the core centre to the edge of the core. It is also possible that the density distribution is more representative of cores with embedded sources: Shirley et al. (2000) determined a single power law, $\rho \propto R^{-2.1 \pm 0.35}$, that can be used to fit the dust continuum observations of Class 0/I sources.

This model allows the dust-gas ratio to vary within the core, so while the gas density in the inner core is too steep to fit observations, the dust density distribution may still be consistent. The same exponents are calculated for a power law fit to the quantity $d_g n(\text{H})$ for the *standard* model: $\alpha_i = 1.59$; $\alpha_m = 1.01$; $\alpha_o = 2.25$. The strongest effect is in the middle core, reducing the exponent from 2.13 to 1.01. For models where the dust-gas ratio is not greatly reduced in the core centre, the change is less pronounced. For example, model *graindist2* gives $\alpha_i = 2.00$; $\alpha_m = 2.21$; $\alpha_o = 2.25$. Again the greatest change in power law exponent is in the middle core: α_m reduces from 2.37 to 2.21. Overall, for the marginally supercritical cores, the mean values are 1.55, 1.30 and 2.24 for α_i , α_m and α_o respectively. While this model suggests that the grain density distribution should be flatter in the inner and middle core than the gas distribution, the impact on the dust continuum emission is complicated due to the effect that grain-depletion would have on the temperature structure within the core: grain-depletion reduces the attenuation of the external radiation field leading to an increase in temperature and therefore intensity of emission for individual grains; the overall intensity of dust continuum emission will be reduced, owing to the reduction in the number density of grains. Without a detailed computation of the temperature structure, along the lines of Evans et al. (2001) or Zucconi et al. (2001), it is difficult to make a meaningful comparison with observations; the results from this type of analysis are presented in Chapter 7.

6.2.3 Dependence of B on $n(\text{H})$

For most models, the following properties of B as a function of $n(\text{H})$ hold: β_i (the exponent of the power law in the inner core) is between 0.27 and 0.69; β_m (the exponent of the power law in the middle region core) is either similar to or lower than β_i , consistent with drift of the magnetic field out of the core; β_o (the exponent of the power law in the outer core) is higher than β_m and is greater than 0.66 for all models, consistent with an increase of B

Table 6.6. Fits of $n(\text{H}) \propto R^{-\alpha}$ and $B \propto n(\text{H})^\beta$.

Model identifier	Inner α_i	β_i	Middle α_m	β_m	Outer α_o	β_o
standard	2.14	0.44	2.13	0.22	2.19	0.79
b1	1.87	0.69	1.93	0.70	2.37	0.72
b2	1.95	0.53	2.06	0.69	2.37	0.72
b3	1.85	0.47	2.06	0.50	2.65	0.82
b4	1.91	0.45	2.10	0.39	2.33	0.94
grainchem1	1.28	0.64	2.56	0.64	2.27	0.66
grainchem2	2.11	0.44	2.15	0.21	2.20	0.79
graindist1	2.20	0.46	1.99	0.22	1.96	0.73
graindist2	2.04	0.55	2.37	0.27	2.22	0.75
stick1	2.03	0.50	2.41	0.30	2.02	0.80
stick2	2.09	0.41	2.15	0.25	2.14	0.79
temp1	2.04	0.50	2.35	0.28	1.92	0.85
xna1	2.11	0.37	2.05	0.20	2.23	0.80
xs1	2.09	0.44	2.14	0.27	1.82	0.77
zeta1	1.92	0.56	2.47	0.43	1.91	0.82
zeta2	2.20	0.33	2.11	0.09	2.21	0.79
avcrit1	2.11	0.27	1.74	0.67	2.96	0.77
avcrit2	2.16	0.40	1.88	0.29	2.41	0.79

at the ambipolar diffusion barrier and a sharp decline of B at radii beyond the ambipolar diffusion barrier. For the inner core, β_i is consistent with observations of the scaling relation between the gas density, ρ , and B : $B \propto \rho^k$; $k = 0.47 \pm 0.08$ (Crutcher 1999); the distributions in the middle and outer core are inconsistent with this scaling relationship. It is noted however, that this scaling relationship applies to cores as a whole rather than the radial profile within a core and therefore it may not be a valid comparison. Overall, for the marginally supercritical cores, the mean values are 0.45, 0.31 and 0.78 for β_i , β_m and β_o respectively.

There are some notable deviations from this general description of the radial variation in B . For models where the cosmic ray ionization rate is reduced (*zeta2*) and where the initial sodium abundance is reduced (*xna1*), β_i is low compared to the average for all models; for the most supercritical model (*b1*) the value of β_i is high compared with the average. In the case of *b1*, the relation between B and $n(\text{H})$ in the inner core ($\beta_i = 0.69$) is close to that expected when there is no drift of the magnetic field out of the core: using the flux-freezing equation, $B \propto R^{-2}$ (section 2.5), and combining with the expression for gas density as a function of radius, $\rho \propto R^{-3}$, gives $B \propto \rho^{2/3}$.

Table 6.7. Model variations – radial variation in the dust-gas ratio, visual extinction and temperature.

Model identifier	$R/10^{16}$ cm centre	edge	A_V centre	edge	T/K centre	edge	$d_g/d_g(t=0)$ centre	max	$R(\text{max})$ $/10^{16}$ cm	$A_V(\text{max})$
standard	1.59	63.15	15.30	1.32	7.23	11.41	0.19	1.57	26.78	3.28
b1	1.71	58.89	45.73	1.30	6.48	11.43	0.80	1.01	14.26	5.33
b2	1.41	58.33	46.03	1.30	6.48	11.44	0.45	1.08	13.18	5.80
b3	1.40	56.48	37.93	1.30	6.54	11.44	0.33	1.27	18.98	4.32
b4	1.69	58.04	20.18	1.31	7.01	11.43	0.24	1.62	26.14	3.43
grainchem1	1.53	56.33	53.17	1.31	6.48	11.43	0.52	1.23	29.15	2.63
grainchem2	1.70	63.31	14.39	1.32	7.35	11.41	0.19	1.57	26.90	3.27
graindist1	1.68	65.77	25.43	1.32	6.91	11.41	0.46	1.29	26.66	3.09
graindist2	1.54	62.59	50.98	1.31	6.48	11.42	0.79	1.13	22.24	3.46
stick1	1.65	62.84	17.74	1.32	7.20	11.40	0.22	1.78	27.27	3.19
stick2	1.71	62.63	13.98	1.33	7.36	11.40	0.18	1.58	27.39	3.22
temp1	1.61	61.97	17.54	1.33	10.00	10.00	0.21	1.80	27.79	3.21
xna1	1.76	63.93	12.30	1.32	7.45	11.41	0.17	1.49	26.16	3.34
xsl	1.66	65.32	14.07	1.33	7.29	11.40	0.18	1.25	27.22	3.10
zeta1	1.54	62.10	27.57	1.32	6.85	11.42	0.31	1.65	24.37	3.39
zeta2	1.63	66.48	10.33	1.32	7.49	11.40	0.13	1.65	27.66	3.15
avcrit1	1.72	55.50	20.16	1.31	7.07	11.43	0.22	1.29	10.23	8.00
avcrit2	1.61	60.81	15.70	1.32	7.29	11.40	0.19	1.33	23.81	3.66

For each model the radial distance of the central and outermost shell (edge) of the core are tabulated; the values of visual extinction, A_V , and temperature, T , are given at the centre and edge of the core. The dust-gas ratio, d_g , as a fraction of the initial dust-gas ratio, $d_g(t=0)$ are given at the centre and at the $d_g/d_g(t=0)$ maximum; $R(\text{max})$ and $A_v(\text{max})$ are the corresponding radial distance and visual extinction to the point of maximum dust-gas ratio respectively.

Table 6.8. Model variations – radial profiles for fractional abundances of CO, HCO⁺ and CS.

Model identifier	Model class	$X(\text{CO})$ centre	max	$R(\text{CO})$ / 10^{16} cm	$X(\text{HCO}^+)$ centre	max	$R(\text{HCO}^+)$ / 10^{16} cm	$X(\text{CS})$ centre	max	$R(\text{CS})$ / 10^{16} cm
standard	A	-6.05	-3.43	46.53	-10.05	-8.61	19.20	-8.68	-7.06	11.66
b1	C	-4.57	-3.43	39.94	-9.52	-8.80	17.32	-7.67	-7.14	6.78
b2	C	-5.11	-3.43	39.46	-9.71	-8.78	16.24	-7.88	-7.13	7.13
b3	C	-5.05	-3.43	37.38	-9.74	-8.73	18.52	-7.65	-7.06	7.44
b4	C	-5.01	-3.43	43.60	-9.65	-8.61	21.70	-7.50	-6.90	8.72
grainchem1	B	-11.30	-3.43	25.70	-17.03	-9.53	25.70	-13.46	-7.08	11.64
grainchem2	A	-6.12	-3.43	46.67	-10.04	-8.60	19.31	-8.80	-7.19	12.55
graindist1	A	-7.90	-3.43	49.08	-11.75	-8.75	14.14	-10.52	-7.04	11.20
graindist2	B	-13.92	-3.43	45.71	-18.20	-8.86	14.38	-15.43	-7.12	13.53
stick1	B	-14.92	-3.43	46.80	-18.75	-8.56	19.61	-17.72	-7.71	17.82
stick2	C	-4.17	-3.43	46.68	-9.58	-8.67	19.91	-6.88	-6.68	5.48
temp1	A	-6.79	-3.43	47.24	-10.54	-8.55	19.68	-9.51	-7.17	12.38
xna1	A	-5.69	-3.43	47.30	-9.44	-8.59	18.62	-8.65	-7.15	10.93
xs1	A	-5.67	-3.43	45.39	-9.83	-8.56	17.73	-10.25	-9.14	8.35
zeta1	B	-14.14	-3.43	43.26	-17.96	-8.14	19.22	-16.70	-6.90	19.22
zeta2	C	-5.28	-3.43	49.53	-10.35	-9.18	15.99	-8.14	-7.97	2.97
avcrit1	A	-5.70	-3.43	20.67	-9.77	-9.02	7.90	-8.13	-6.10	9.50
avcrit2	A	-5.82	-3.43	46.06	-9.86	-8.83	12.14	-8.36	-6.76	9.62

For each molecule the log of the abundance relative to hydrogen nuclei is given: at the centre and maximum (max). $R(x)$ gives the radial distance from the centre of the core to the maximum for species x .

Table 6.9. Model variations – radial profiles for fractional abundances of NH_3 , N_2H^+ and e^- .

Model identifier	Model class	$X(\text{NH}_3)$ centre	max	$R(\text{NH}_3)$ / 10^{16} cm	$X(\text{N}_2\text{H}^+)$ centre	max	$R(\text{N}_2\text{H}^+)$ / 10^{16} cm	$X(\text{e}^-)$ centre	max	$R(\text{e}^-)$ / 10^{16} cm
standard	A	-8.97	-8.31	7.62	-11.04	-10.06	12.48	-8.75	-4.49	63.15
b1	C	-10.45	-9.23	12.71	-11.54	-11.11	18.85	-9.08	-4.47	58.89
b2	C	-10.16	-9.22	13.18	-11.25	-11.09	18.80	-9.14	-4.46	58.33
b3	C	-9.89	-9.20	14.42	-11.20	-11.04	17.13	-9.10	-4.45	56.48
b4	C	-9.19	-8.90	12.73	-10.98	-10.47	18.62	-8.91	-4.47	58.04
grainchem1	B	-13.19	-8.37	9.57	-18.43	-11.01	14.03	-7.37	-4.50	56.33
grainchem2	A	-8.89	-8.21	7.71	-11.03	-9.94	12.55	-8.51	-4.49	63.31
graindist1	A	-9.94	-8.24	8.36	-12.69	-9.99	13.15	-8.40	-4.49	65.77
graindist2	B	-15.71	-8.25	10.32	-18.96	-10.05	13.53	-8.13	-4.47	62.59
stick1	B	-16.25	-8.27	13.80	-20.13	-9.83	17.82	-8.40	-4.49	62.84
stick2	C	-9.19	-8.88	9.46	-11.41	-10.48	19.91	-8.77	-4.49	62.63
templ	A	-9.32	-8.02	8.80	-11.55	-9.98	12.38	-8.39	-4.51	61.97
xna1	A	-8.78	-8.36	6.65	-10.51	-10.01	10.93	-8.85	-4.50	63.93
xs1	A	-8.79	-8.36	6.04	-10.86	-10.22	10.64	-8.79	-4.53	65.32
zeta1	B	-11.08	-7.58	10.42	-16.84	-9.23	17.57	-7.94	-4.41	62.10
zeta2	C	-9.79	-9.78	2.97	-12.19	-12.08	10.98	-9.43	-4.52	66.48
avcrit1	A	-8.90	-8.90	1.72	-10.77	-10.77	1.72	-8.69	-4.46	55.50
avcrit2	A	-8.85	-8.60	4.51	-10.86	-10.38	7.93	-8.64	-4.49	60.81

For each molecule the log of the abundance relative to hydrogen nuclei is given: at the centre and maximum (max). $R(x)$ gives the radial distance from the centre of the core to the maximum for species x .

Table 6.10. Model variations – maximum abundances for molecular species.

Model identifier	$n(\text{CO})$ /cm ⁻³	$R(\text{CO})$ /10 ¹⁶ cm	$n(\text{HCO}^+)$ /cm ⁻³	$R(\text{HCO}^+)$ /10 ¹⁶ cm	$n(\text{CS})$ /cm ⁻³	$R(\text{CS})$ /10 ¹⁶ cm	$n(\text{NH}_3)$ /cm ⁻³	$R(\text{NH}_3)$ /10 ¹⁶ cm	$n(\text{N}_2\text{H}^+)$ /cm ⁻³	$R(\text{N}_2\text{H}^+)$ /10 ¹⁶ cm
standard	0.77	2.64	-3.41	1.59	-1.79	2.64	-2.34	1.59	-4.41	1.59
b1	1.97	1.71	-2.98	1.71	-1.13	1.71	-3.90	1.71	-4.99	1.71
b2	1.80	2.89	-2.92	1.41	-1.09	1.41	-3.37	1.41	-4.46	1.41
b3	1.75	1.40	-2.94	1.40	-0.85	1.40	-3.09	1.40	-4.40	1.40
b4	1.54	1.69	-3.09	1.69	-0.95	1.69	-2.64	1.69	-4.43	1.69
grainchem1	0.91	18.52	-5.02	12.09	-2.01	10.36	-2.89	6.58	-6.06	11.20
grainchem2	0.62	30.77	-3.47	2.76	-2.04	2.76	-2.33	1.70	-4.48	1.70
graindist1	0.54	32.32	-3.77	4.68	-2.11	6.51	-2.75	2.79	-4.82	3.75
graindist2	0.68	28.29	-4.19	11.09	-2.37	10.32	-3.13	6.86	-5.30	9.59
stick1	0.59	30.85	-4.26	16.97	-3.28	16.14	-3.50	10.89	-5.42	16.14
stick2	2.37	1.71	-3.04	1.71	-0.34	1.71	-2.65	1.71	-4.87	1.71
templ	0.59	32.52	-3.48	3.09	-2.09	4.95	-2.43	3.09	-4.53	3.09
xna1	0.84	2.95	-2.93	1.76	-1.95	2.95	-2.27	1.76	-4.00	1.76
xs1	1.00	2.73	-3.25	1.66	-3.58	2.73	-2.21	1.66	-4.28	1.66
zeta1	0.64	28.68	-3.70	13.77	-2.52	16.77	-2.18	4.86	-4.68	13.07
zeta2	1.32	1.63	-3.75	1.63	-1.54	1.63	-3.19	1.63	-5.59	1.63
avcrit1	1.79	4.60	-3.23	1.72	-0.86	3.72	-2.36	1.72	-4.23	1.72
avcrit2	1.07	2.69	-3.24	1.61	-1.43	2.69	-2.23	1.61	-4.24	1.61

For each molecule the log of the absolute abundance in cm⁻³ is given: at the centre and maximum (max); $R(\text{max})$ gives the radial distance from the centre of the core to the maximum for the species.

6.2.4 Radial variation in visual extinction, temperature and dust-gas ratio

Table 6.7 shows the differences in visual extinction and temperature between the centre and edge of the core; the dust-gas ratio d_g , normalised relative to the initial dust-gas ratio, $d_g(t = 0)$, is presented for the core centre and the point of maximum dust-gas ratio. The table shows a wide variation in central A_V which correlates with the dust-gas ratio at the centre of the core: models with high visual extinction are correlated with low depletion of grains in the core centre. Observations of the pre-stellar core B68 by Alves et al. (2001b) give $A_V \sim 30$ at the centre of the core and an estimated central density of $n_c(\text{H}) \sim 6 \times 10^5 \text{ cm}^{-3}$. For models where $d_g/d_g(t = 0) \leq 0.24$, $A_V \leq 20.2$ indicating that B68 is not subject to strong central depletion of grains. Models with central $d_g/d_g(t = 0) \geq 0.33$ are required in order to obtain the A_V observed in B68.

6.2.5 Chemical radial profiles

Tables 6.8 and 6.9 present the fractional abundances of molecular species at the core centre and at the point of maximum fractional abundance. The table shows that large differences in central molecular abundances exist between models – this is in contrast to the dynamical behaviour which showed little difference between models that are marginally supercritical. Comparison with observations of the chemical properties of cores is therefore likely to be crucial in differentiating between models. There are in general, three classifications of models. Models that show comparable chemical properties to the standard model (hereafter termed class A); models falling into this category are *grainchem2*, *graindist1*, *temp1*, *xna1*, *xs1*, *avcrit1* and *avcrit2*. Models that show much stronger molecular depletion in the core centre than the standard model (hereafter termed class B); models falling into this category are *grainchem1*, *graindist2*, *stick1* and *zeta1*. Models that show weaker molecular depletion in the core centre than the standard model (hereafter termed class C); models falling into this category are *b1*, *b2*, *b3*, *b4*, *stick2* and *zeta2*.

Within classes A and B the peak fractional abundances show a tendency for $X(\text{NH}_3)$ to peak closest to the centre of the core; $X(\text{HCO}^+)$, $X(\text{CS})$ and $X(\text{N}_2\text{H}^+)$ peak in approximately the same region; $X(\text{CO})$ peaks furthest from the core centre. Model *avcrit1* stands out from other class A models since peak fractional abundances occur much closer to the core centre: this is due to the high value of $A_{V_{\text{crit}}}$ preventing freeze-out of molecules

for $R \gtrsim 1 \times 10^{17}$ cm.

Models in class C show non-standard behaviour. For models *b1*, *b2* and *b3*, the peaks of $X(\text{CS})$ and $X(\text{HCO}^+)$ are closest to the core centre; $X(\text{N}_2\text{H}^+)$ is next closest followed by $X(\text{NH}_3)$; $X(\text{CO})$ remains furthest from the core centre. Model *zeta2* shows that the peak $X(\text{CS})$ is furthest from the core centre while for model *stick2* the peak in $X(\text{CS})$ is nearly as close as the peak in $X(\text{NH}_3)$ to the core centre. Model *b4* follows the trend in position of fractional abundance peaks with classes A and B.

Models where $X(\text{NH}_3)$ and $X(\text{N}_2\text{H}^+)$ are more centrally peaked than either $X(\text{CO})$ or $X(\text{CS})$ are consistent with observations of 5 pre-stellar cores by Tafalla et al. (2002). In this study, fits to the radial change in integrated emission from rotational transition lines of CS, C^{18}O , C^{17}O , NH_3 and N_2H^+ are used to constrain the fractional abundances. They find the best fits when $X(\text{NH}_3)$ and $X(\text{N}_2\text{H}^+)$ are kept constant throughout the core and $X(\text{CS})$ and $X(\text{CO})$ fall off exponentially for densities greater than a critical density for each species: the critical density is found to be higher for CS than CO in 4 out of the 5 cores.

For most models, the ionization fraction in the core centre is between 10^{-8} and 10^{-9} . Notable exceptions to this are for models *grainchem1*, *zeta1* and *zeta2*. For model *grainchem1*, ions recombine with electrons on the surface of grains and return to the gas phase, leading to an increase in the ionization fraction. For model *zeta1*, the cosmic ray ionization rate is increased, leading to a higher than average ionization level in the core centre. Model *zeta2* shows the opposite behaviour for a decreasing cosmic ray ionization rate. The ionization fraction compares well with estimates of $X(\text{e}^-)$ in dense clouds with $n(\text{H}) \sim 2 \times 10^6 \text{ cm}^{-3}$ by de Boisanger et al. (1996). This study finds $X(\text{e}^-)$ to be in the range: $2 \times 10^{-9} < X(\text{e}^-) < 4 \times 10^{-8}$. A study of the ionization fraction in L1544 by Caselli et al. (2002c) gives $X(\text{e}^-) \sim 1 \times 10^{-9}$ at the core centre – this is at the low end of ionization fraction predicted by these models.

The absolute abundances of molecular species at the core centre are compared with the maximum in the core in Table 6.10. This table shows that for class A and C models, absolute molecular abundances tend to peak close to the core centre. For most class B models, the peak abundance of carbon species is far from the core centre; this is the result of the strong depletion of carbon species in the core centre for these models.

The dynamical and chemical profiles for examples of class B and C are plotted in Figures 6.3 and 6.4 respectively.

6.3 Synthetic line profiles

For each class of model, the line profiles of C^{18}O (1-0), HCO^+ (1-0), CS (1-0), NH_3 (1,1) and N_2H^+ (1-0) are plotted at six radial positions within the core, corresponding to beam offsets of 0 arcsec to 125 arcsec at a distance of 140 pc. The radial chemical profiles are converted into line profiles that could be observed with typical existing single dish telescopes (such as JCMT or FCRAO), using spherical radiative transfer code, SMMOL (Rawlings & Yates 2001), and the collisional rate data files therein for HCO^+ and CS (Monteiro 1985; Green & Chapman 1978). Collisional rate data files for C^{18}O , NH_3 and N_2H^+ are taken from Schöier et al. (2005). The abundance fraction of C^{18}O is derived by dividing the abundance of CO by the terrestrial O^{18}O ratio (≈ 490). The dust temperature is assumed to be the same as the gas temperature and a constant turbulent velocity of 0.065 km s^{-1} applies throughout the core. The background radiation field uses that defined by Mathis et al. (1983) with the addition of a black body of 2.7 K to simulate the cosmic background radiation. Beam parameters for an artificial beam are chosen: the beam efficiency is set to 1.0 in order to generate beam temperatures on the T_{mb} scale. A Gaussian beam profile is assumed with beam sizes derived from a 14m telescope (such as the FCRAO 14m telescope).

6.3.1 Radial line profiles

Figure 6.5 shows line profiles for the standard model. The C^{18}O (1-0) line profiles show a small increase in maximum T_{mb} out to $\theta = 125$ arcsec. The total integrated flux density decreases by about 10 % from the centre to the outer core. The decrease in integrated flux density is consistent with a decrease in linewidth: since the turbulent velocity is constant throughout the core and the temperature increases from the centre to the core edge, the decrease in linewidth is due to a combination of a reduction in optical depth broadening and a reduction in infall velocity. The HCO^+ (1-0) line profiles show a strong self-absorbed line with the blueshifted peak T_{mb} significantly higher than for the redshifted peak; the peak T_{mb} and integrated flux density decrease rapidly over the core. The CS (1-0) line profiles show a self-absorbed line with the blueshifted peak T_{mb} higher than the redshifted peak; the peak T_{mb} and integrated flux density gradually decrease over the core. The NH_3 (1,1) and N_2H^+ (1-0) lines show a decrease in peak T_{mb} and integrated flux density over the core, with the N_2H^+ (1-0) line decreasing more rapidly than the NH_3 (1,1) line.

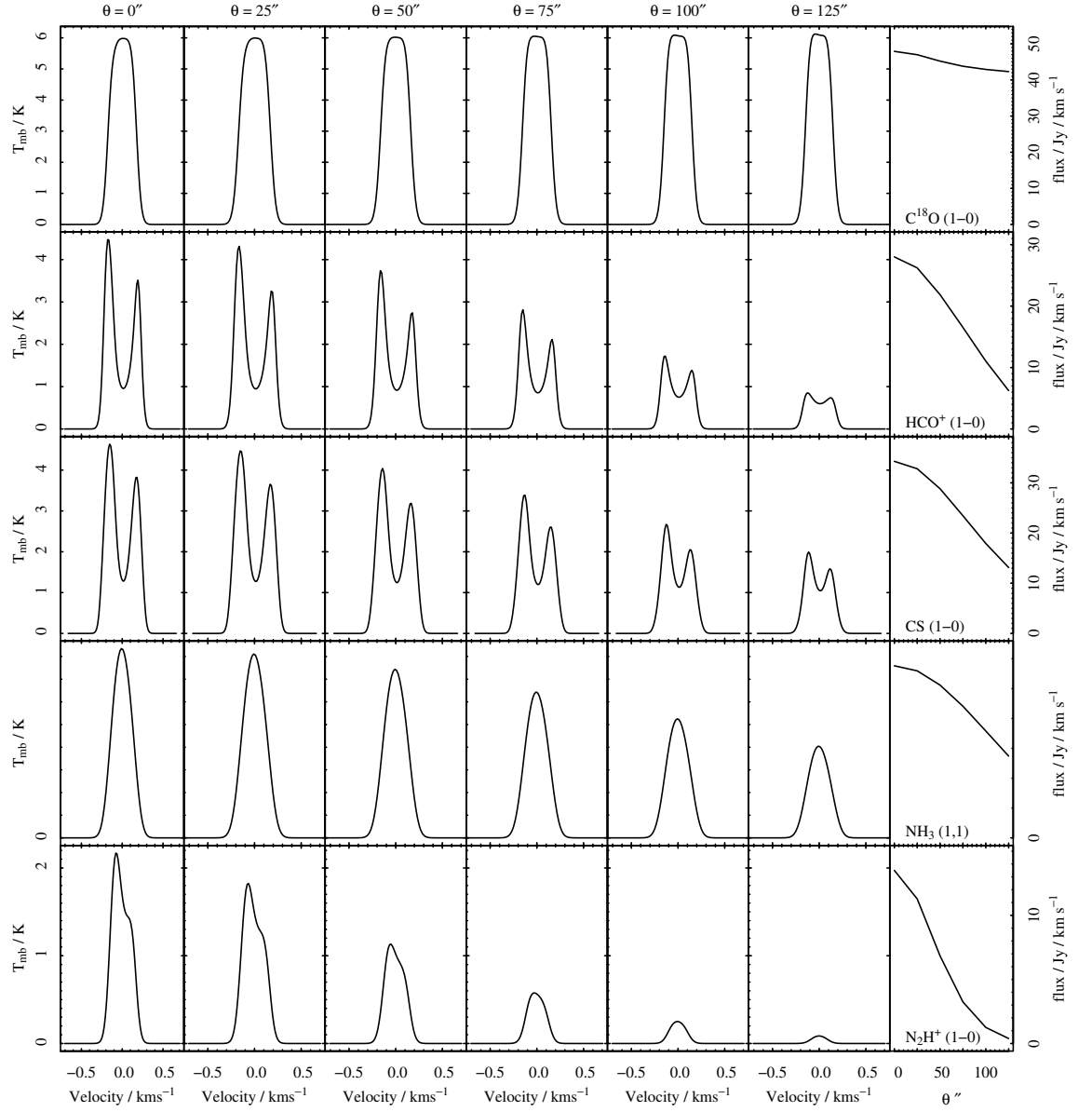


Figure 6.5. Radial line profiles for the *standard* model.

Line profiles for beam offsets between $0''$ and $125''$ are plotted together with the integrated flux in the right-most column of the grid.

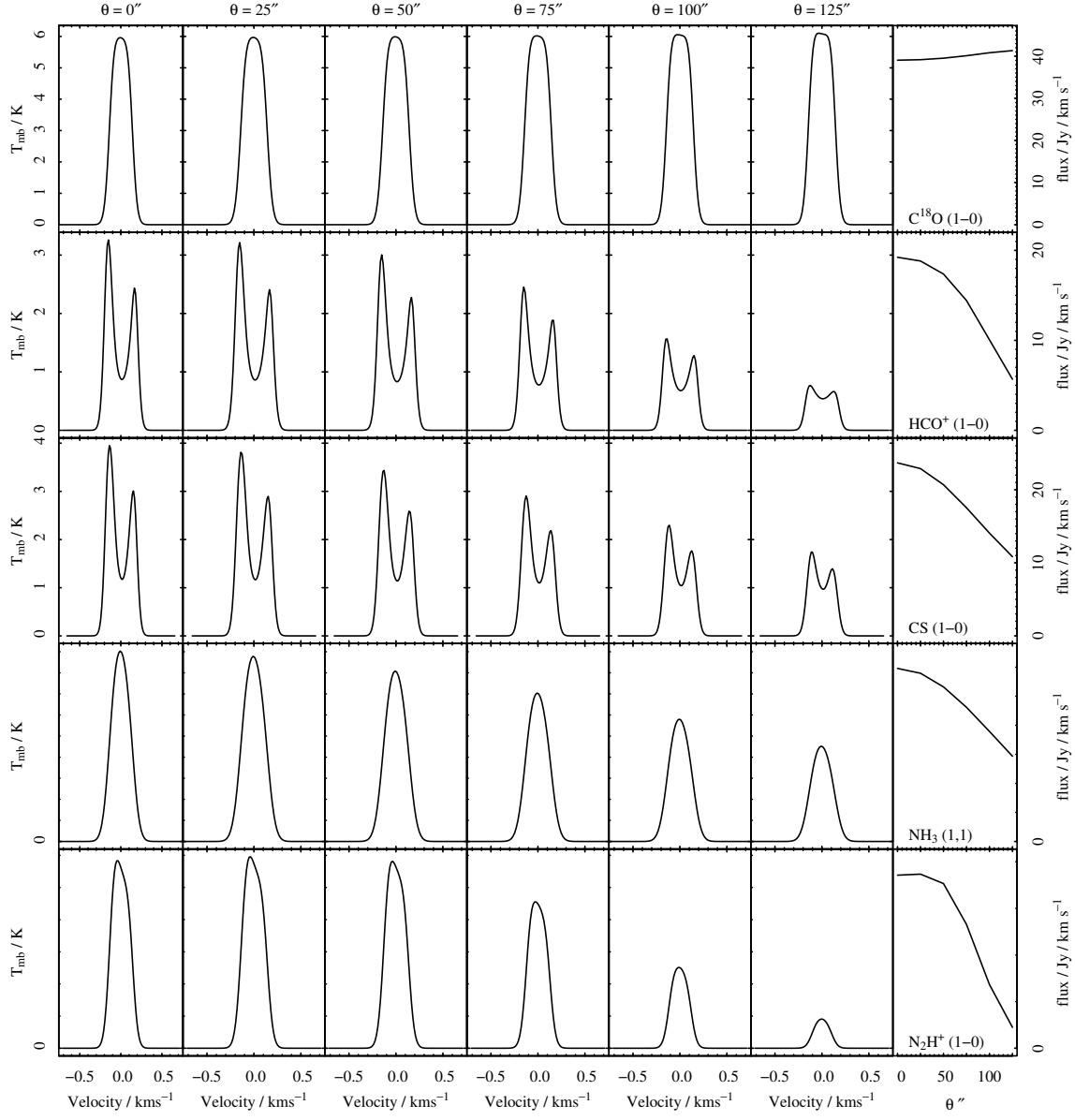


Figure 6.6. Radial line profiles for an example of a class B model, *stick1* (neutral-grain sticking coefficient increased to 1.0).

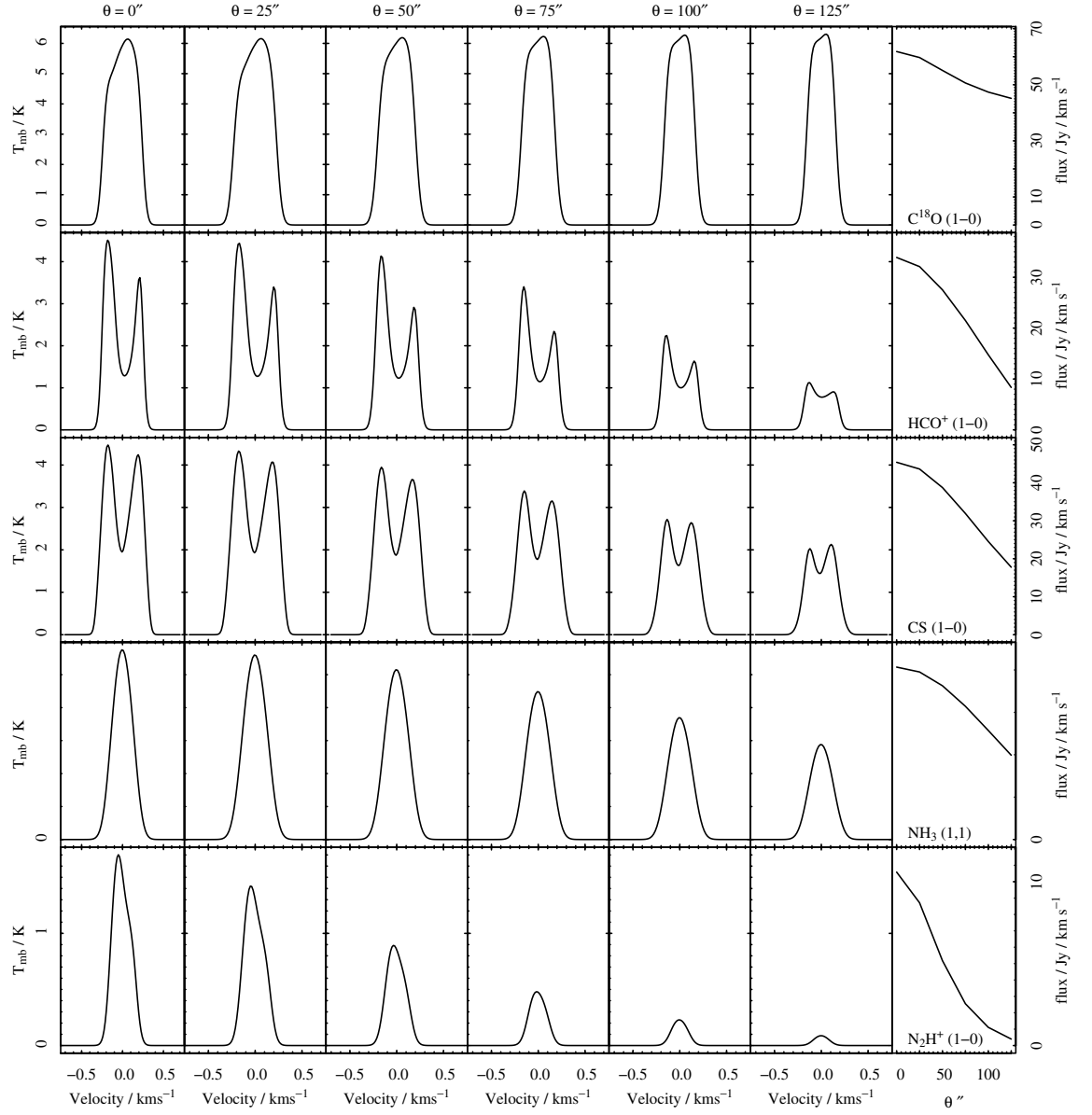


Figure 6.7. Radial line profiles for an example of a class C model, b_4 (magnetic flux density reduced to $5.6 \mu\text{G}$).

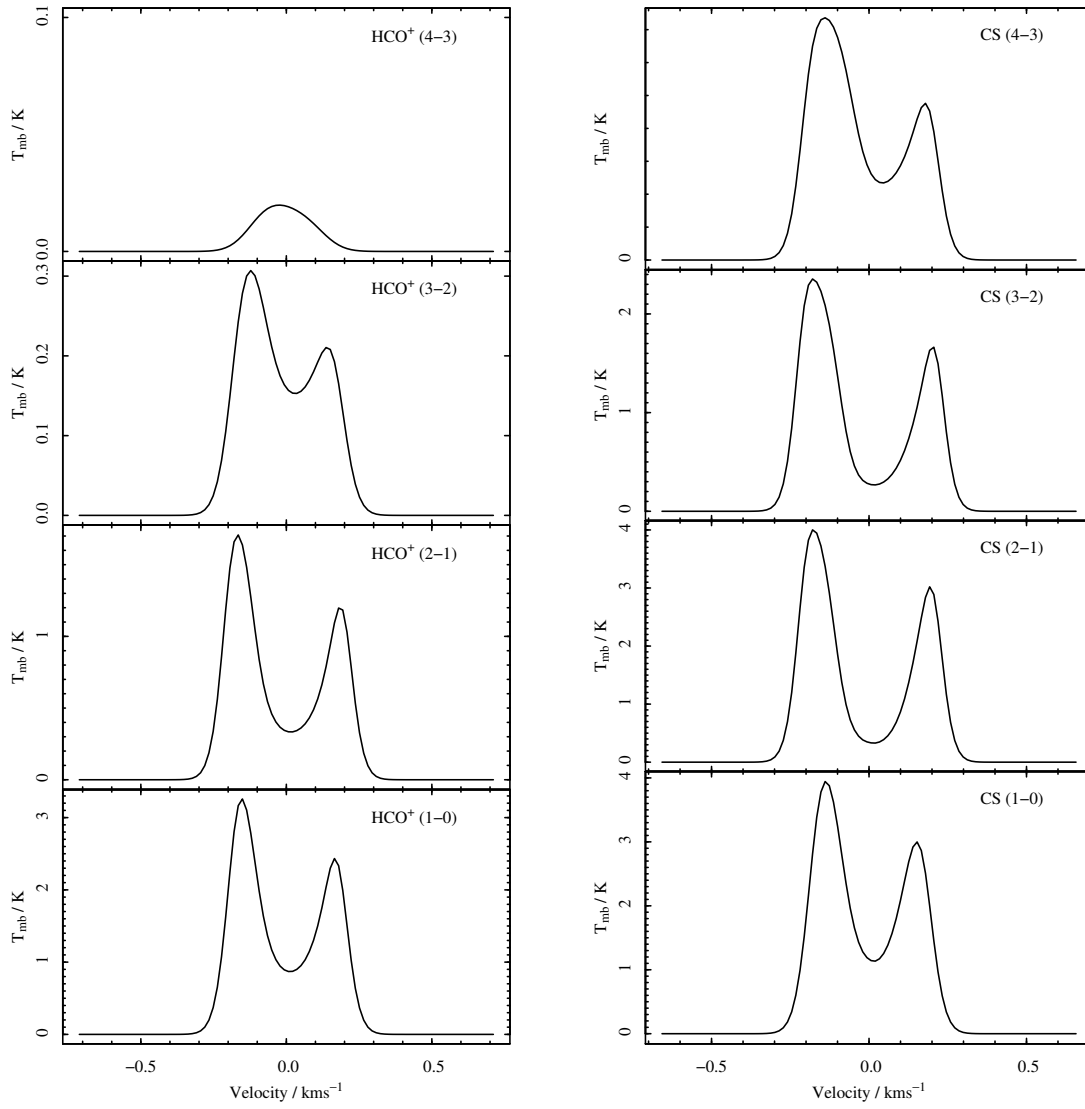


Figure 6.8. Line profiles at the core centre for a class B model, *stick1* (neutral-grain sticking coefficient increased to 1.0).

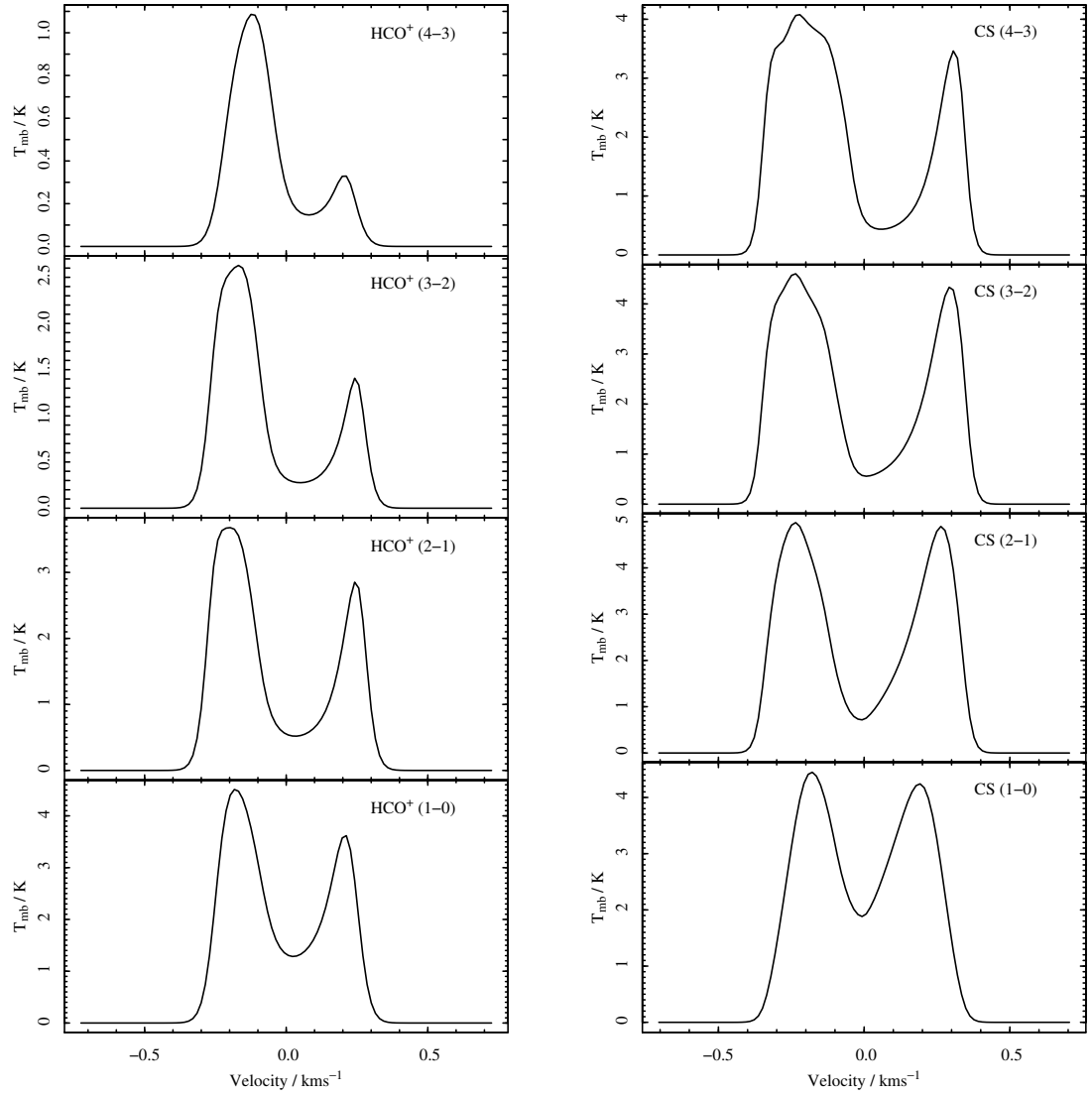


Figure 6.9. Line profiles at the core centre for a class C model, b_4 (magnetic flux density reduced to $5.6 \mu\text{G}$).

Figure 6.6 shows line profiles for model *stick1* – an example of a class B model as defined in section 6.2. The C^{18}O (1-0) line profiles show a steeper increase in maximum T_{mb} out to $\theta = 125$ arcsec accompanied by a marginal increase in integrated flux density. The HCO^+ (1-0) line profiles are similar to the standard model although for $\theta \leq 50$ arcsec the gradient in maximum T_{mb} and integrated flux density is much flatter. The CS (1-0) line profiles are similar to the standard model but have a weaker gradient in maximum T_{mb} and integrated flux-density. The NH_3 (1,1) line shows little change from the standard model. The N_2H^+ (1-0) lines show a marginal increase in peak T_{mb} and integrated flux density out to $\theta = 25$ arcsec before decreasing rapidly to the outer core. For all lines, there is an overall reduction in the integrated flux density, consistent with stronger depletion of molecules.

Figure 6.7 shows line profiles for model *b4* – an example of a class C model as defined in section 6.2. The C^{18}O (1-0), HCO^+ (1-0), NH_3 (1,1) and N_2H^+ (1-0) line profiles show little difference over the standard model other than the overall integrated flux density being higher, consistent with weaker depletion of molecules. The CS (1-0) line profiles have a blueshifted peak T_{mb} marginally higher than for the redshifted peak out to $\theta = 100$ arcsec; at $\theta = 125$ arcsec the redshifted peak dominates over the blueshifted peak. For this model the maximum outflow velocity in the outer core is high ($\sim 60 \text{ ms}^{-1}$), consequently observations in the outer core have a dominant redshifted peak, despite the collapse in the central and middle regions of the core.

6.3.2 Comparing radial synthetic line profiles with observations

The models are compared with observations of the starless cores L1498, L1495, L1517B, L1400K and L1544 by Tafalla et al. (2002). All these cores with the exception of L1400K lie in the Taurus complex with an estimated distance of 140 pc (Elias 1978). L1400K lies at an estimated distance of 170pc (Snell 1981). This study finds a similar pattern in emission maps for all 5 cores. The N_2H^+ and NH_3 emission maps are centrally concentrated and have approximately the same peak position as the peak dust continuum emission and share similar shapes; the C^{18}O , C^{17}O and CS emission maps are more diffuse and fragmented and have peak emissions that do not coincide with the peak dust continuum emission. The authors argue that strong depletion in the central core is required in order to reproduce the flat emission profile for CS in the inner core. For C^{18}O and C^{17}O , the integrated emission is seen to decrease towards the centre of the core. These observations tend to

favour the class B models over either of class A or C, although the emission maxima of N_2H^+ in the sample class B model is shown to have a maxima that is not coincident with the centre. Another possibility is that since these cores were selected based on the emission maps of N_2H^+ and NH_3 being nearly circular, there is a bias towards flattened cores that are being observed face-on. If cores are oblate as suggested by Jones et al. (2001) and the magnetic field lines run parallel to the short axis, then the models and line profiles presented here more accurately reflect the core when viewed edge-on rather than face-on. An investigation into this effect is not within scope of this thesis, but it seems reasonable to expect that any emission peaks that are off-centre would appear stronger in emission maps when viewed face on (since the column density at the centre would not pass through the abundance peak). So while class B models appear to be favoured over class C and A, the gradients in integrated flux density may be too steep when viewed face-on.

Chapter 4 presented line profiles of higher rotational transition lines for the standard model; a trend in HCO^+ and CS was identified that shows the velocity at which the self-absorption dip occurs, the *dip velocity*, increases with increasing transition number for a collapsing core. The results from the standard model are compared with line profiles for class B and C cores. In Figures 6.8 and 6.9 the profiles for rotational transitions (4-3), (3-2), (2-1) and (1-0) are plotted for models *stick1* and *b4* respectively. Figure 6.8 shows much weaker HCO^+ lines than the standard model with transition (4-3) showing no self-absorption; for the self-absorbed lines there is little variation in dip velocity ($\sim 20 \text{ ms}^{-1}$). The CS lines show the blueshifted peak dominating over the red and also little variation in the dip velocity ($\sim 20 \text{ ms}^{-1}$); only for transition (4-3) is the dip velocity seen to increase to $\sim 50 \text{ ms}^{-1}$. Figure 6.9 shows HCO^+ lines similar to those for the standard model; the dip velocity increases from 20 ms^{-1} for transition (1-0) to 80 ms^{-1} for transition (4-3). The CS lines shows the dip velocity to be close to 0 ms^{-1} for transitions (1-0), (2-1) and (3-2); only for transition (4-3) does the dip velocity increase significantly ($\sim 60 \text{ ms}^{-1}$).

6.4 Summary

The sensitivity of the standard model to changes to the parameter set and model assumptions is investigated. It is found that dynamically, the model is sensitive to a change in the initial magnetic flux density, B_0 , but for models that are marginally supercritical, B_0 is only weakly dependent on the environment.

The ratio of the collapse time to the free-fall time is calculated for all models. The range of ratios for an initial density of $n(\text{H}) \sim 3 \times 10^3 \text{ cm}^{-3}$ is between 1 and 3, in reasonable agreement with estimates of core collapse times based on the lifetime of pre-stellar cores (Kirk et al. 2005). When taking the uncertainties in observational data into account and assuming that an adjustment is required to the observed ratios of core lifetimes to free-fall times that takes into account a non-zero initial velocity, most marginally supercritical models are consistent with pre-stellar core lifetimes having an initial starting density of $n(\text{H}) \simeq 5 \times 10^4 \text{ cm}^{-3}$. However, comparison of collapse times from an initial starting density of $n(\text{H}) \sim 2 \times 10^5 \text{ cm}^{-3}$ shows that about half of the marginally supercritical models have longer collapse times than that inferred from observations. Model *b4* best fits the collapse times having an initial magnetic flux density of $B = 5.6 \mu\text{G}$, just below the value at which the core becomes marginally supercritical.

The chemical and dynamical radial profiles are presented at a point in time when the central density is $n_c(\text{H}) \sim 3 \times 10^6 \text{ cm}^{-3}$. Wide variation in abundance fractions of all molecular species exist between the models. For example, in Table 6.8, model *graindist2* gives a core centre HCO^+ abundance fraction, $\log[X(\text{HCO}^+)] = -18.20$, while model *avcrit1* gives $\log[X(\text{HCO}^+)] = -9.77$. Similarly for nitrogen-based chemistry, Table 6.9 gives core centre N_2H^+ abundance fractions of $\log[X(\text{N}_2\text{H}^+)] = -20.13$ and $\log[X(\text{N}_2\text{H}^+)] = -10.77$ for models *stick1* and *avcrit1* respectively. The ionization fraction is fairly consistent between the models, ranging from 10^{-8} and 10^{-9} . Models are classified by whether they are similar in abundance fraction to the standard model (class A), show stronger depletion in the centre (class B) or show weaker depletion in the centre (class C). The line profiles and integrated flux densities are calculated at 6 beam offsets from the centre of the core for all classes of model. It is found that models in class B fit the observational evidence from Tafalla et al. (2002) better than classes A and C: class B models show flatter emission gradient in CS (1-0) while the C^{18}O (1-0) emission is weakest at the core centre. There is a possibility that observing a flattened core face-on increases the contrast between an off-centre emission peak and emission at the core centre, and therefore cannot be directly compared with synthetic line profiles that more accurately reflect observations from an edge-on perspective.

The radial gas density distribution across the core is analysed by fitting power-laws of the form $\rho \propto R^{-\alpha}$ to inner (α_i), middle (α_m) and outer (α_o) regions of the core. The mean values for α_i , α_m and α_o indicate that the density distribution is marginally flatter in the

inner core than in the middle and outer core: $\langle \alpha_i \rangle \sim 2.04$; $\langle \alpha_m \rangle \sim 2.18$; $\langle \alpha_o \rangle \sim 2.18$. There are some notable exceptions to these average values. Model *grainchem1* shows a much flatter distribution than the average in the inner core: $\alpha_i = 1.28$. Model *avcrit1* shows the largest difference between gradients in the inner and outer core: $\alpha_o = 2.96$ in the outer core compares to $\alpha_i = 2.11$ in the inner core. Model *xs1* shows a very weak gradient in the outer core compared to the gradient in the inner core: $\alpha_o = 1.82$ in the outer core compares to $\alpha_i = 2.09$ in the inner core. The gas distribution is found to be too steep in the inner core to match the inferred density distribution ($0 \leq \alpha_i \leq 1.5$) from observations of the dust continuum emission from several pre-stellar cores. It is found that the gas density distribution at earlier epochs are better at fitting the observed gas density distribution: only one core, L1544, is comparable to the central density of the standard model and this core may be consistent with $\rho \propto R^{-2}$ when a radial increase in the dust temperature is taken into account (Evans et al. 2001). Overall, the gas density distribution is a better fit to that derived from the dust continuum emission from Class 0/I sources by Shirley et al. (2000): $\rho \propto R^{-2.1 \pm 0.35}$. Taking the dust density distribution as proportional to the product of the gas density and the varying dust-gas ratio results in a better fit in the inner core but the resulting dust density gradient is too weak in the middle core.

The magnetic flux density as a function of the density is analysed by fitting power laws of the form $B \propto \rho^\beta$ to the inner (β_i), middle (β_m) and outer (β_o) regions of the core. Values for β averaged over all marginally supercritical models indicate that B is a weak function of $n(\text{H})$ in the middle core, $\beta_m \sim 0.31$, while in the outer core, a strong dependence exists, $\beta_o \sim 0.78$ and in the inner core an intermediate dependence exists, $\beta_i \sim 0.45$. Mean values of β are consistent with the trend found for the standard model. The increase in β in the outer core occurs at the ambipolar diffusion barrier: inward from this point, neutrals are able to drift through the ions and charged grains, allowing greater decoupling between the neutral gas and magnetic field; outward from the ambipolar diffusion barrier, neutrals, ions and charged grains are tightly coupled so that strong coupling between the neutral gas and magnetic field is expected. The power law exponent in the inner core, β_i , is higher relative to β_m : due to the removal of B from the inner core, the impact that the magnetic pressure has in retarding collapse is reduced and allows B in the inner core to return to having a stronger dependence on $n(\text{H})$.


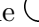




















The observed visual extinction in pre-stellar cores provides additional constraints on

the model. The visual extinction, A_V , at the core centre is strongly correlated with the values for the core centre dust-gas ratio. A wide variation in dust-gas ratio is found between some of the models: model *graindist2* is an example of a model where the dust-gas ratio does not change significantly from its initial value, $\frac{d_g}{d_g(t=0)} = 0.79$ while model *zeta2* shows a strong depletion of dust from the core centre with $\frac{d_g}{d_g(t=0)} = 0.13$. The wide range in dust-gas ratio between the models translates into a wide range in A_V at the core centre. Taking B68 as an example core with well determined measurements of A_V , it is found that models with a central $\frac{d_g}{d_g(t=0)} > 0.33$ are required.

Table 6.11 provides a summary of results from the observational tests performed on the models. It is noticeable that no single model satisfies all observational criteria. However, the sampling strategy from the outset is not to provide a best-fit model; the strategy tests the sensitivity to changes in parameters so that an understanding can be obtained of the different effects that each parameter has on the model. It is noted that the sampling strategy leaves much of the parameter space still to be explored. It is useful however, to consider which models have attributes that provide the closest fit to all observational data. In order to satisfy the observational constraint that carbon-bearing molecular species are heavily depleted at the centre of pre-stellar cores, the selection of a class B model would seem an obvious choice. However, examination of Table 6.11 shows that all class B models have collapse times from an initial central density of $n_c(\text{H}) \sim 2 \times 10^5 \text{ cm}^{-3}$ that are too long when compared to observational data. Yet in order for models to be consistent with the heavily depleted inner core, reasonably long collapse timescales are required in order for freeze-out to significantly reduce the gas-phase abundances. For models where grains are tightly coupled to the magnetic field, this is a more significant problem since the reduction in grains at the core centre will tend to increase the timescales for freeze-out, therefore keeping the core chemically young. It remains an outstanding problem to resolve these conflicting observational constraints with the current parameter set.

The trend observed for the standard model, that for HCO^+ and CS lines the *dip velocity* increases with increasing transition number, is strongly affected by freeze-out of molecules in the core centre. Where strong freeze-out occurs in the core centre, the dip velocity remains very nearly constant for lower transitions, indicating that absorption is dominated by the slower moving gas in the outer core.

Table 6.11. Model summary – comparing models against observational constraints.

Observational test	standard	b1	b2	b3	b4	grainchem1	grainchem2	graindist1	graindist2	stick1	stick2	templ	xna1	xs1	zeta1	zeta2	avcrit1	avcrit2	mean ¹
a) Ratio of infall to free-fall times at $n(\text{H}) \simeq 5 \times 10^4 \text{ cm}^{-3}$ (Table 6.3)	●	○	○	○	●	●	●	●	○	●	●	●	●	●	●	○	●	●	
b) Ratio of infall to free-fall times at $n(\text{H}) \simeq 2 \times 10^5 \text{ cm}^{-3}$ (Table 6.4)	●	●	●	●	●	○	●	○	○	○	○	○	●	●	○	●	○	●	
c) Subsonic infall speed (§6.2.1)	●	○	○	○	●	○	●	●	●	●	●	●	●	●	●	●	●	●	
d) Radial profile in $n(\text{H})$: inner  /middle  core (§6.2.2)						●													
e) As d) but at an earlier epoch	●				●														●
f) As d) but compared with class 0/I sources	●	●	●		●	○	●	●	●	●	●	●	●	●	●	●		●	●
g) A_V at centre compared with B68 (§6.2.4)	○	●	●	●	○	●	○	●	●	○	○	○	○	○	○	○	○	○	
h) Chemical radial profiles (§6.2.5 and §6.3.2)	○	○	○	○	○	●	○	○	●	●	○	○	○	○	●	○	○	○	

Filled circles ● indicate consistency with observations; unfilled circles ○ indicate inconsistency with observations.

¹ mean here indicates the mean for all marginally supercritical cores.

Chapter 7

Modelling the dust continuum emission

So many worlds. But connecting them all is Dust.

The Golden Compass, Philip Pullman

Chapter 6 analysed the sensitivity of the radial change in density and dust-gas ratio to various model parameters. For most models, the density distribution is found to be too steep in the inner core to be consistent with observational data. When the dust-gas ratio is taken into account, the dust distribution is found to be significantly flatter in the inner and middle core compared with the gas distribution. In this chapter, the effect on the core temperature and dust continuum emission is examined when a reduction in the dust-gas ratio is taken into account. These results have been taken from Stace and Rawlings (2014c), in preparation.

This chapter is organised as follows: Section 7.1 describes the method of calculating the core temperature and dust continuum emission; Sections 7.3 and 7.4 present the results for the standard model and model variations respectively with supplementary material given in Appendix D. Section 7.5 provides a summary of the results.

7.1 Dust model

The dust model calculations follow closely the method described by Zucconi et al. (2001), hereafter ZWG. ZWG made a number of simplifying assumptions in order to model a pre-stellar core with properties similar to that of L1544. These assumptions are carried forward into this model. ZWG assume that for visual extinctions typical of dense cores ($A_V \geq 10$), infrared interstellar radiation dominates; for infrared radiation the Rayleigh limit holds and scattering becomes negligible. A further assumption is that grains are only heated by the incident radiation field; this assumption is supported by a more detailed discussion of the relative importance of other heating effects by Evans et al. (2001). A further assumption that allows ZWG to model non-spherically symmetric geometries makes the cores optically thin to their own radiation such that only the external radiation field need be considered. Although the ability to model non-spherically symmetric geometries is not needed, this method is chosen in preference to other models (that do include re-absorption and scattering within the core) since the method is relatively simple to implement. For conditions similar to L1544, ZWG find their results compare well with those of Evans et al. (2001), predicting low central temperatures of around 5-6K that increase to 12-13K at the core edge.

For the test core, the physical parameters at the end of a simulation of the collapse of the standard model are used: the properties of the core are chosen to be close to that for L1544 (see Chapter 3). Table 7.1 lists the main parameters at the end of the run for the standard model. Included is a contribution to the visual extinction within the core due to the core being embedded in a more diffuse cloud; the external visual extinction is assumed to be 0.9; the external visual extinction is converted into an envelope depth R_{env} for an outer core hydrogen nuclei number density $n(\text{H}) = 2.8 \times 10^3 \text{ cm}^{-3}$ using the relation: $A_V \approx 4$ when $n(\text{H}) R_{\text{env}} = 8 \times 10^{21} \text{ cm}^{-2}$ (Spitzer 1998) gives $R_{\text{env}} = 6.43 \times 10^{17} \text{ cm}$.

The core is subdivided into 100 concentric shells of mass $0.0768 M_\odot$. Following ZGW and Spitzer (1998), the grain temperature at each shell is calculated by applying the equilibrium condition between grain cooling and heating:

$$\int_0^\infty Q_\nu B_\nu [T_d(r)] d\nu = \int_0^\infty Q_\nu I_\nu(r) d\nu \quad (7.1)$$

where Q_ν is the absorption efficiency of grains at frequency ν , $T_d(r)$ is the grain tempera-

Table 7.1. Parameters of the standard model at the end of the model run.

Parameter	Value
Mass	$M_{core} = 7.68 M_{\odot}$
Final Radius	$R = 0.203 \text{ pc } (6.26 \times 10^{17} \text{ cm})$
Final central number density of hydrogen nuclei	$n(\text{H}) = 4.3 \times 10^6 \text{ cm}^{-3}$
Final central visual extinction	$A_{V_{centre}} = 15.0$
External visual extinction	$A_{V_{ext}} = 0.9$

ture at radius r , B_{ν} is the Planck function and $I_{\nu}(r)$ is the average intensity at frequency ν of the incident radiation field at radial position r . The calculation of $I_{\nu}(r)$ is derived from the background interstellar radiation field I_{ν}^0 at frequency ν attenuated by absorption due to grains and averaged over all solid angles. In this model, the calculation of $I_{\nu}(r)$ takes into account the variable dust-gas ratio. A schematic diagram for a single ray of radiation is shown in Figure 2.2. The specific intensity I_{ν} at any point P due to radiation travelling along AP is given by equations 2.22 and 2.23. To arrive at an expression for the average specific intensity, equation 2.22 is integrated over all solid angles and divided by 4π :

$$I_{\nu}(r) = \frac{I_{\nu}^0}{4\pi} \int_0^{2\pi} \int_0^{\pi} e^{-\tau_{\nu}} \sin\phi \, d\phi \, d\theta \quad (7.2)$$

$$I_{\nu}(r) = \frac{I_{\nu}^0}{2} \int_0^{\pi} e^{-\tau_{\nu}} \sin\phi \, d\phi \quad (7.3)$$

Note that to arrive at 7.3, the outer integral in equation 7.2 reduces to 2π due to symmetry around the OP axis.

A convenient way to express equation 2.23 in terms of the initial dust-gas gas ratio, $d_g(t=0)$, appropriate at all r is to make the substitution:

$$n^*(\text{H}) = \frac{d_g}{d_g(t=0)} n(\text{H}) \quad (7.4)$$

giving

$$\tau_\nu(\phi, \theta) = Q_\nu \sigma_d d_g(t=0) \int_0^S n^*(H) ds \quad (7.5)$$

where $n^*(H)$ can be thought of as an equivalent hydrogen nuclei number density if the gas-dust ratio is held constant and S is the distance along a single ray of radiation (AP in Figure 2.2).

For the external radiation field, the analytical expressions derived in ZWG are used, which in turn are derived from the work of R. M. Cutri & W. B. Latter (1994) and Mathis et al. (1983). The interstellar radiation field at wavelengths above 0.1 mm is represented by the sum of three modified blackbody intensity profiles representing the near-infrared, far-infrared and cosmic background radiation fields and a power-law profile representing the mid-infrared radiation field. The modified blackbody profiles are given by:

$$I_\nu^0 = \frac{2h\nu^3}{c^2} \left(\frac{\lambda_p}{\lambda} \right) \sum_i \frac{W_i}{e^{h\nu/kT_i} - 1} \quad (7.6)$$

where h is the Plank constant, k is the Boltzmann constant, T_i is a representative blackbody temperature for component i , λ_p is a peak wavelength for component i and W_i is a dilution factor for component i . The mid-infrared component is given by:

$$I_\nu^0 = W_{\text{MIR}} \frac{2h\nu^3}{c^2} \left(\frac{\lambda_p}{\lambda} \right)^p \quad (7.7)$$

where W_{MIR} is the dilution factor for the mid-infrared component. The values of W_i , λ_p and T_i are taken from Table B.1 of ZWG.

The analytic expression for opacities from ZWG are used: ZWG fit piece-wise power-laws of the form $Q_\nu = Q_{\nu_p} (\lambda_p/\lambda)^\alpha$ to the thin ice, $n(H) \sim 10^6 \text{ cm}^{-3}$ model of Ossenkopf & Henning (1994). The analytic expression gives an accuracy to within 20 % of the tabulated values from Ossenkopf & Henning (1994). The parameters α and Q_{ν_p} for wavelengths below $10\mu\text{m}$, between $10\mu\text{m}$ and $400\mu\text{m}$, and above $400\mu\text{m}$ are taken from Table B.2 of ZWG. However, the following caveats apply to the use of this dust opacity model, given the extended period of time ($\sim 4 \text{ Myr}$) that core collapse models run for and the final

central densities of model cores ($n_c(\text{H}) \sim 3 \times 10^6 \text{ cm}^{-3}$). Grain agglomeration is likely to have an impact on the values of Q_ν : grain agglomeration will result in fewer but larger grains. The freeze-out of ice onto grain surfaces in the central, densest region of the core is also likely to alter the values of Q_ν .

7.2 Model Solution

For dust temperatures, T , in the range 5K to 20K at 0.1K intervals, a grid is populated with T and the total output intensity, I_{out} , calculated by numerical integration of the left-hand side of equation 7.1. A third order spline is then used to fit the grid of I_{out} versus T values. For all shells in the core, the total input intensity, I_{in} , is calculated by numerical integration of the right-hand side of equation 7.1. Using the values of I_{in} at each shell, the spline coefficients are used to determine T at each shell.

The specific intensity at wavelengths $1300\mu\text{m}$, $850\mu\text{m}$ and $450\mu\text{m}$ is calculated by integrating the left-hand side of equation 7.1 using the values of T calculated for each shell through lines of sight with impact parameters spaced at fixed radial intervals. The contribution from the background, more diffuse gas of the embedding cloud is excluded from the emission in order to more accurately reflect observations where *chopping* is used to remove the background emission from an extended source such as L1544 (Evans et al. 2001, Kirk et al. 2005). The resulting specific intensity profiles are convolved using Gaussian beams with half-power beamwidths of 11, 15.2 and 7.9 arcsec respectively; the half-power beamwidths are taken from the IRAM 30m telescope for $1300\mu\text{m}$ (Andre et al. 1996) and SCUBA at the James Clerk Maxwell Telescope for $850\mu\text{m}$ and $450\mu\text{m}$ (Shirley et al. 2000). The core is assumed to be at a distance of 140 pc.

7.2.1 Code validation

In their analysis of the dust temperature structure inside pre-stellar cores, ZWG provide both an analytic approximation for the dust temperature at the centre of spherical pre-stellar cores, and numerical solutions giving the dust temperature as a function of radius for spherical cores having dust density distributions defined by a singular isothermal sphere and a Bonner-Ebbert sphere. Figure 3 of ZWG shows that the analytic model gives a good fit to the radial distribution in dust temperature as calculated for Bonner-Ebbert spheres. This figure is used to check the radial distribution in temperature as calculated for the

standard model in Figure 7.2. Dust temperatures are compared to the analytic model by comparing temperatures at the same A_V . Dust temperatures are also compared to the results from the numerical solutions for Bonner-Ebbert spheres: Bonner-Ebbert spheres are chosen for comparison purposes in preference to singular isothermal spheres since the flattening of density profile in the inner core of Bonner-Ebbert spheres is likely to be better match to the radial distribution of dust as calculated for the standard model.

The visual extinction, A_V , and dust temperature, T , at the centre of the standard model are $A_V = 15$ and $T = 8.2$ K respectively. This compares to dust temperatures, at the same A_V , from the analytic model and the numerical solution for a Bonner-Ebbert sphere (having a central $A_V = 30$) of $T = 8.1$ K and $T = 7.9$ K respectively. When $A_V = 10$, the standard model gives $T = 8.7$ K while ZWG gives $T = 8.5$ K and $T = 8.3$ K for the analytic model and numerical solution respectively. When $A_V = 5$, the standard model gives $T = 9.3$ K while ZWG gives $T = 9.2$ K for the numerical solution (no analytic value is available at this value of A_V). Overall, these results indicate that values derived for the standard model are within 0.2 K of the analytic values derived by ZWG. A further check is carried out on the standard model for the case where the dust-gas ratio is set to 1.0 throughout the core: this case tests the accuracy for models having much higher central visual extinctions. In this case, $T = 6.9$ K and $A_V = 52$ in the central shell of the standard model. This compares to dust temperatures from the analytic model and the numerical solution for a Bonner-Ebbert sphere (having a central $A_V = 60$) of $T = 6.6$ K and $T = 6.5$ K respectively. This indicates a slight worsening in the accuracy of the calculated values of T for high visual extinctions and is likely due to the poor resolution in the innermost shell of the standard model where the visual extinction is highest. However, inaccuracies in the dust temperature of the innermost shell are unlikely to have a significant impact on the calculation of convolved dust continuum emission since the beamwidths used in this calculation require a weighted aggregate (according to a Gaussian profile) of dust emission over several shells, thus reducing the impact of errors in any single shell.

As a check on the code written to generate the convolved dust continuum emission, the radial distributions for the dust density and dust temperature for the standard model are used with the LIME package (Brinch & Hogerheijde 2010) to generate unconvolved dust continuum images at a frequency of 450, 850 and 1300 μm . The LIME code can be used to generate millimetre and submillimetre emission images from arbitrary 3D geometries; in this case the simple, spherically symmetric geometry of the standard model is used to

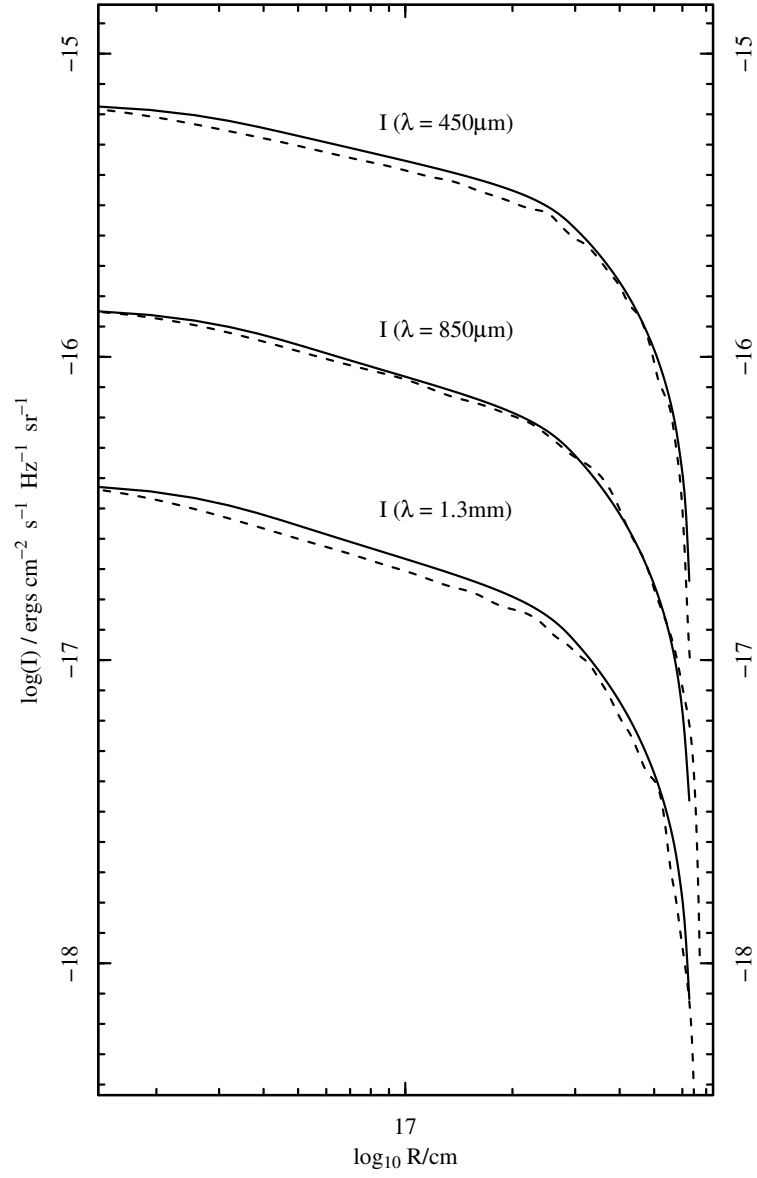


Figure 7.1. Comparing the dust continuum radial profiles from the standard model with output from LIME/MIRIAD.

Solid line plots the emission profiles for wavelengths $450\mu\text{m}$, $850\mu\text{m}$ and 1.3mm from the standard model; dashed lines show the equivalent profiles as output by LIME/MIRIAD.

generate the dust continuum images. The MIRIAD package (Sault et al. 1995) is then used to convolve the 450, 850 and 1300 μm images with a Gaussian beam with half-power beamwidths of 7.9, 15.2 and 11 arcsec respectively – consistent with beamwidths used for the standard model. From the 2-dimensional images output by MIRIAD, a slice along one axis of the image is taken in order to create a 1-dimensional intensity profile. The intensity profile output by the standard model and the equivalent output from the LIME/MIRIAD packages are shown in Figure 7.1. In this Figure, the intensity of the output from LIME/MIRIAD has been normalised so that for the data point closest to the origin, the intensities match: for all other LIME/MIRIAD data points the intensities have been scaled by the same amount. In this manner, the closeness in fit between the slopes of the two sets of radial profiles can be visually inspected. The LIME code uses different opacity tables to those used by the standard model and therefore the absolute values for the intensity calculations are not expected to match. For the analysis that follows, it is the slope of the intensity profiles that is important. Figure 7.1 shows a good fit between all intensity profiles. It is noted that the intensity profiles from LIME/MIRIAD are less *smooth* than the standard model in the outer region of the core – this is due to the LIME package using larger ray-tracing cells in the outer region of the core while cells in the dense, inner region of the core have smaller cell sizes.

7.3 Results for the standard model – dust emission

The temperature profile and dust continuum radial profiles for the standard model are plotted in Figure 7.2. The model is compared with the equivalent profile if a constant gas-dust ratio is assumed and also where a constant temperature is assumed. Comparison with a constant temperature model is important since there is strong evidence to suggest that the gas temperature may be constant throughout the inner and middle core (Tafalla et al. 2002, Caselli et al. 2002*c*); if there is strong thermal coupling between dust and gas as might be expected in the densest region of the core, a constant dust temperature cannot be ruled out. The figure shows that the strong depletion of grains at the core centre increases the temperature from 6.9 K to 8.2 K while the increase in dust-gas ratio with radial distance flattens the emission gradient out to a radial distance of $R \simeq 2 \times 10^{17}$ cm. For $R > 3 \times 10^{17}$ cm, charged grains and neutral gas are strongly coupled, therefore there is little difference between the variable and constant dust-gas ratio models. Comparison

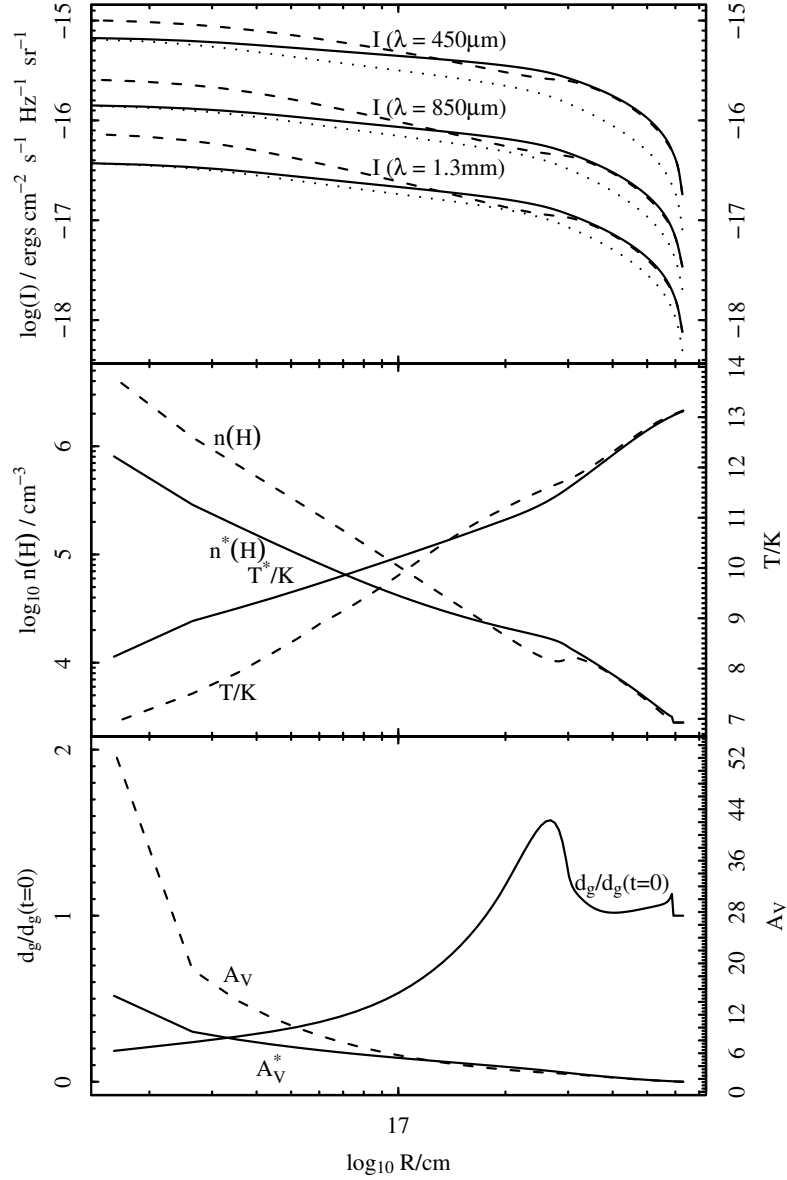


Figure 7.2. Core temperature and dust continuum radial profiles for the standard model.

Upper graph plots the emission profiles for wavelengths $450 \mu\text{m}$, $850 \mu\text{m}$ and 1.3mm . Solid lines show the model profile where the dust-gas ratio varies throughout the core; dashed lines show the profiles assuming a constant dust-gas ratio; dotted lines show the profiles assuming a constant temperature, $T = 10 \text{K}$. Middle graph plots the density and temperature gradient in the core. Lower graph plots the variation in visual extinction and dust-gas ratio. Solid lines and descriptors marked with * show the model profile where the dust-gas ratio varies throughout the core. Dashed lines and unmarked descriptors show the profiles assuming a constant dust-gas ratio.

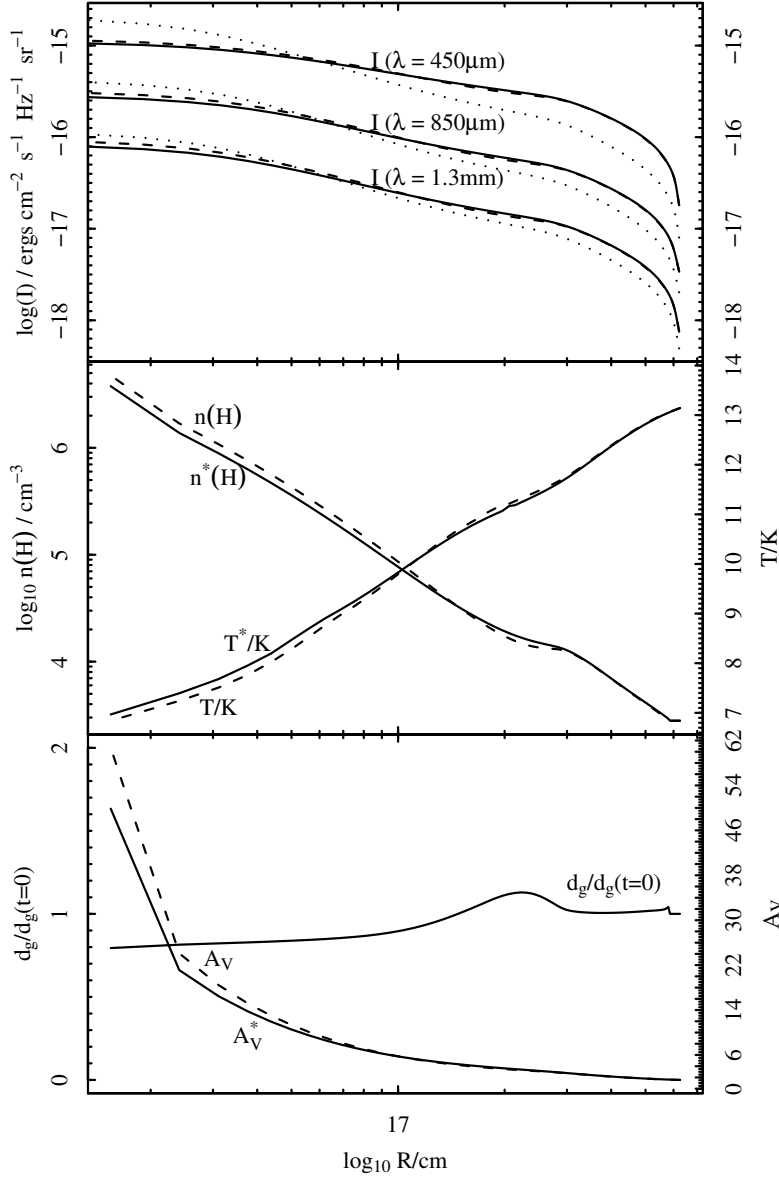


Figure 7.3. Core temperature and dust continuum radial profiles for the model *graindist2*.

Upper graph plots the emission profiles for wavelengths $450 \mu\text{m}$, $850 \mu\text{m}$ and 1.3mm . Solid lines show the model profile where the dust-gas ratio varies throughout the core; dashed lines show the profiles assuming a constant dust-gas ratio; dotted lines show the profiles assuming a constant temperature, $T = 10 \text{K}$. Middle graph plots the density and temperature gradient in the core. Lower graph plots the variation in visual extinction and dust-gas ratio. Solid lines and descriptors marked with * show the model profile where the dust-gas ratio varies throughout the core. Dashed lines and unmarked descriptors show the profiles assuming a constant dust-gas ratio.

with the profiles that use a constant, $T = 10\text{K}$, dust temperature show the peak central intensity to be approximately equal but the constant temperature profile falling off more sharply than for the variable temperature profile.

The flattening of the emission gradient in the inner core is a well-established observational feature of pre-stellar cores (Ward-Thompson et al. 1994, Tafalla et al. 2002, Kirk et al. 2005, Evans et al. 2001). Observations by Ward-Thompson et al. (1994) indicate that the isothermal density distribution in pre-stellar cores can be described by $\rho \propto R^{-1.25}$ in the inner core and $\rho \propto R^{-2}$ outside the inner core. The inner core in this study, $R_{inner} \sim 4.6 \times 10^{16}$ cm, is significantly smaller than the radial distance, $R \simeq 2 \times 10^{17}$ cm, inside which the emission gradient is seen to flatten for the standard model. A similar study of the radial profiles of the 1.2mm continuum emission of 5 pre-stellar cores by Tafalla et al. (2002) show excellent fits to isothermal density models of the form:

$$n(\text{H}) = \frac{n_0(\text{H})}{1 + (R/R_0)^\alpha} \quad (7.8)$$

where $n_0(\text{H})$ is a constant inner density for the region with $R \leq R_0$. The value of R_0 ranges from 4.5×10^{16} cm for L1544 to 1.5×10^{17} cm for L1498. The flattening in the standard model appears to be too broad to fit L1544, while being marginally too broad to fit the low-density core L1498. Kirk et al. (2005) compared the dust emission of several pre-stellar cores including L1544 with density models based on isothermal Bonnor-Ebert spheres (Bonnor 1956, Ebert 1955); the flat region of the Bonnor-Ebert spheres for L1544 in this study is approximately 7×10^{16} cm, confirming that the flattening of emission gradient in the standard model is too broad to fit L1544. However, it is possible that the model overestimates the mass of cores such as L1544; a lower mass decreases the radial distance of the ambipolar diffusion barrier (and therefore the extent of the flattening of the emission profiles) since ionizing photons would penetrate deeper into the core. A lower mass also implies a smaller radial distance to the edge of the core, allowing edge effects on the emission profile to become more significant closer in to the core centre. At least for the pre-stellar core L1544, this possibility is ruled out since Kirk et al. (2005) estimate the total mass of L1544 within a 150 arcsec aperture to be $3.1 M_\odot$ based on the total flux; the mass within 150 arcsec for the standard model is $2.7 M_\odot$, slightly less than that derived from observations.

7.4 Results for model variations – dust emission

The core temperatures and dust emission profiles are calculated for all other model variations listed in Table 3.7. Table 7.2 summarises the central temperature, visual extinction and radial density distributions for all models. The radial distribution of $n^*(\text{H})$ and $n(\text{H})$ are described by splitting the core into three regions: the inner core is defined as the region within the innermost 10 shells; the middle core is defined as the region between the end of the inner core and the position of density dip (at shell number 25 for most models); the outer core is defined as the region outward from the density dip to shell 90. The outer 10 shells are not modelled since $n(\text{H})$ is held constant in this region. The power law indices for the inner, middle and outer regions of the core are denoted by α_i^* , α_m^* and α_o^* for $n^*(\text{H})$ and by α_i , α_m and α_o for $n(\text{H})$. Table 7.3 summarises the resulting intensity profiles for emission of each model for $n^*(\text{H})$ at $450\mu\text{m}$, $850\mu\text{m}$ and 1.3mm . The intensity profile is described by power laws of the form $I \propto R^{-m}$; the profile is split into an inner, middle and outer core with m_i , m_m and m_o denoting the power law indices for the three regions. Table 7.4 summarises the resulting intensity profiles where the dust temperature is kept constant throughout the core.

Table 7.2 shows that for most models, the flattening of density profile in the middle core is similar to that for the standard model: these models show the flattening of the density profile to be too extended to fit the dust continuum observations. Models *b1*, *b2* and *graindist2* show marginal flattening in the middle core and therefore are more consistent with observations. For these models, the dust-gas ratio is not strongly depleted so that the dust distribution follows closely that for the gas. Table 7.3 shows that the intensity profile is directly affected by the flat density profiles; emission gradients for most models are too weak in the middle core to match observations by Andre et al. (1996) of the radial change in intensity at 1.3 mm for the pre-stellar core L1689B. This analysis concluded that the intensity profile falls off as $I \propto \theta^{-m}$ inside an angular radius $\theta \lesssim 25\text{ arcsec}$ (a radial distance of $5.8 \times 10^{16}\text{ cm}$ at an assumed distance of 160 pc) where $m = 0.3 \pm 0.2$ assuming an axisymmetric source and $m = 0.2 \pm 0.2$ assuming an elliptical source; outside this region up to $\theta \lesssim 90\text{ arcsec}$ (a radial distance of $2.1 \times 10^{17}\text{ cm}$) $m = 1.0 \pm 0.3$ regardless of the assumed symmetry of the source. The authors note however, that for the circularly averaged profile, the gradient steepens such that $m > 1.0$ beyond $\theta = 70\text{ arcsec}$ (a radial distance of $1.6 \times 10^{17}\text{ cm}$). For models *b1*, *b2*, *grainchem1* and *graindist2*, the power law

indices of the 1.3 mm profile for the inner and middle core are within the range derived by these observations, although the gradient in the middle core for model *graindist2* is at the low end of the range of permissible values. The results from Table 7.4 for intensity profiles using a constant temperature indicate that models *b1*, *b2* and *graindist2* are again consistent with observations while *grainchem1* is marginally too steep in the middle core; additionally models *b3*, *b4*, *zeta1* and *avcrit1* now also fit the data.

The gradient in the outer core is found to be strongly affected by edge effects; no single power law is able to accurately model the combination of fall-off in density and the steep fall-off in column length as the beam offset approaches the edge of the core. There is some difficulty in making a direct comparison between model emission profiles and observations at large impact parameters due to the effect that the observational technique of *chopping* has on the intensity profile (Kirk et al. 2005, Evans et al. 2001). Evans et al. (2001) restrict comparison between model emission profiles and observations of L1544 out to impact parameter $b = 1.5 \times 10^{17}$ cm, corresponding approximately to the outer limit of the middle core in this model; for larger impact parameters the emission profile is sensitive to the particular model of chopping used. However, Bacmann et al. (2000) studied 24 starless cores in the mid-infrared ($\lambda \simeq 7\mu\text{m}$) and used the absorption profile to determine the variation in column density out to larger impact parameters and with better sensitivity and angular resolution than the sub-millimetre emission studies. Moreover, the column density of the absorbing dust is independent of the temperature structure in the core. The column density of a subset of the 24 cores with the strongest absorption profiles were derived from the absorption maps. This study confirmed the flattening in the inner core that is observed in the sub-millimetre emission studies. The cores were then sub-divided into 2 categories: those cores where the column density outside the flat region can be described by a single power law, $N(\text{H}_2) \propto R^{-m_1}$; those cores that require a second power law to describe a steeper fall-off in column density at larger radial distances, $N(\text{H}_2) \propto R^{-m_2}$. For all cores, $0.8 \leq m_1 \leq 1.6$. For the latter category, $1.7 \leq m_2 \leq 4.4$. The latter category is consistent with intensity profiles in the outer core for most models from tables 7.3 and 7.4; all models show a steepening in the fall-off of intensity with radial distance in the outer core compared with the middle core. In particular, for source L1689B (South), the radius at which the $7\mu\text{m}$ absorption profile steepens is $R_{\text{mid}} \sim 3 \times 10^{17}$ cm, consistent with the model core.

Figure 7.3 plots the radial temperature and emission profiles for model *graindist2*; this

is a good example of a model where the dust is only weakly depleted from the core centre. For this model, the emission profiles for $n^*(\text{H})$ are not significantly different from those for $n(\text{H})$ and have a flat emission region that is closer to the core centre than for the standard model. The flattening of the emission profile in this case is due to the radial change in temperature rather than the re-distribution of dust out from the core centre. For the remaining models, the temperature and emission profiles are given in Appendix D.

Table 7.2. Central temperature T , visual extinction A_V and least-squares fits to the density distribution of the form $n(\text{H}) \propto R^{-\alpha}$ for the inner (α_i), middle (α_m) and outer (α_o) core.

Model identifier	T / K	T^* / K	A_V	A_V^*	Inner α_i	α_i^*	Middle α_m	α_m^*	Outer α_o	α_o^*
standard	6.93	8.24	53.29	14.96	2.14	1.59	2.14	1.01	2.19	2.25
b1	6.95	7.03	50.94	44.73	1.87	1.75	1.91	1.89	2.37	2.37
b2	6.71	7.03	73.60	45.01	1.95	1.45	2.05	1.93	2.37	2.38
b3	6.67	7.15	77.66	37.09	1.85	1.32	2.04	1.48	2.65	2.86
b4	6.93	7.79	53.13	19.73	1.91	1.36	2.08	1.34	2.33	2.87
grainchem1	6.60	6.94	86.03	52.00	1.28	1.09	2.45	2.09	2.27	2.19
grainchem2	6.99	8.35	48.08	14.07	2.11	1.56	2.16	1.00	2.20	2.26
graindist1	7.00	7.50	47.30	24.87	2.20	1.99	2.12	1.36	1.96	1.93
graindist2	6.84	6.97	60.70	49.85	2.04	2.00	2.47	2.21	2.22	2.23
stick1	6.93	7.98	52.95	17.35	2.03	1.57	2.31	1.46	2.02	2.15
stick2	7.00	8.40	46.93	13.66	2.09	1.49	2.13	1.06	2.14	2.21
temp1	6.87	8.00	57.75	17.15	2.04	1.61	2.35	1.35	1.92	2.28
xna1	7.04	8.65	44.01	12.02	2.11	1.48	2.08	0.87	2.23	2.29
xsl	6.96	8.39	50.05	13.76	2.09	1.57	2.15	1.14	1.82	1.85
zeta1	6.78	7.42	65.94	26.95	1.92	1.55	2.44	1.78	1.91	2.20
zeta2	7.00	8.98	47.25	10.10	2.20	1.58	2.26	0.60	2.21	2.20
avcrit1	6.98	7.79	48.73	19.71	2.11	1.08	0.91	1.35	2.96	2.87
avcrit2	6.95	8.19	51.69	15.35	2.16	1.51	1.96	0.97	2.41	2.42

Column names annotated with * indicate the equivalent radial profiles adjusted for the varying dust-gas ratio.

Table 7.3. Fits to the intensity profiles of the form $I \propto R^{-m}$ for the inner (m_i), middle (m_m) and outer (m_o) core.

Model identifier	450 μ m			850 μ m			1.3mm		
	m_i	m_m	m_o	m_i	m_m	m_o	m_i	m_m	m_o
standard	0.15	0.31	1.70	0.17	0.38	1.82	0.19	0.40	1.86
b1	0.15	0.64	1.87	0.20	0.83	1.99	0.24	0.89	2.03
b2	0.16	0.69	1.87	0.22	0.89	1.99	0.26	0.96	2.03
b3	0.13	0.57	2.03	0.17	0.77	2.16	0.20	0.83	2.21
b4	0.11	0.38	2.14	0.14	0.50	2.29	0.17	0.53	2.35
grainchem1	0.19	0.76	1.83	0.25	0.99	1.95	0.30	1.06	1.99
grainchem2	0.14	0.31	1.71	0.16	0.38	1.82	0.18	0.40	1.86
graindist1	0.21	0.43	1.51	0.26	0.51	1.60	0.29	0.53	1.63
graindist2	0.23	0.60	1.69	0.31	0.74	1.80	0.37	0.77	1.83
stick1	0.16	0.39	1.67	0.19	0.47	1.78	0.22	0.49	1.81
stick2	0.12	0.33	1.69	0.14	0.40	1.80	0.16	0.42	1.84
temp1	0.17	0.35	1.71	0.20	0.43	1.83	0.23	0.45	1.87
xna1	0.11	0.29	1.70	0.13	0.35	1.82	0.15	0.37	1.85
xs1	0.15	0.36	1.52	0.17	0.43	1.61	0.19	0.45	1.64
zeta1	0.19	0.48	1.72	0.24	0.60	1.83	0.28	0.63	1.87
zeta2	0.12	0.23	1.60	0.13	0.27	1.70	0.15	0.28	1.73
avcrit1	0.07	0.42	2.23	0.09	0.56	2.39	0.10	0.61	2.45
avcrit2	0.13	0.31	1.81	0.15	0.39	1.94	0.17	0.41	1.98

Table 7.4. Fits to the constant temperature intensity profiles of the form $I \propto R^{-m}$ for the inner (m_i), middle (m_m) and outer (m_o) core.

Model identifier	450 μ m			850 μ m			1.3mm		
	m_i	m_m	m_o	m_i	m_m	m_o	m_i	m_m	m_o
standard	0.26	0.50	2.04	0.23	0.51	2.04	0.25	0.50	2.04
b1	0.36	1.16	2.22	0.32	1.18	2.22	0.34	1.17	2.22
b2	0.38	1.26	2.21	0.34	1.28	2.22	0.37	1.27	2.22
b3	0.30	1.12	2.42	0.27	1.13	2.42	0.29	1.13	2.42
b4	0.23	0.70	2.59	0.21	0.71	2.59	0.22	0.70	2.59
grainchem1	0.43	1.39	2.18	0.38	1.43	2.18	0.41	1.41	2.18
grainchem2	0.24	0.50	2.04	0.22	0.50	2.04	0.24	0.50	2.04
graindist1	0.41	0.64	1.78	0.37	0.66	1.78	0.39	0.65	1.78
graindist2	0.54	0.97	2.00	0.48	0.99	2.00	0.52	0.98	2.00
stick1	0.30	0.61	1.99	0.28	0.62	1.99	0.29	0.62	1.99
stick2	0.22	0.52	2.03	0.20	0.53	2.03	0.21	0.52	2.03
temp1	0.32	0.57	2.06	0.29	0.58	2.06	0.31	0.57	2.06
xna1	0.20	0.46	2.04	0.18	0.46	2.04	0.19	0.46	2.04
xs1	0.26	0.55	1.80	0.24	0.55	1.80	0.25	0.55	1.80
zeta1	0.41	0.81	2.05	0.37	0.83	2.05	0.39	0.81	2.05
zeta2	0.19	0.33	1.89	0.17	0.34	1.89	0.18	0.33	1.89
avcrit1	0.14	0.82	2.71	0.13	0.82	2.71	0.14	0.82	2.71
avcrit2	0.23	0.52	2.19	0.20	0.53	2.18	0.22	0.52	2.19

7.5 Summary

The temperature structure for all model variations are calculated. The resulting dust continuum emission profiles are determined at $450\mu\text{m}$, $850\mu\text{m}$, and 1.3mm and compared with models where the dust-gas ratio is held constant and where a constant temperature in the core is assumed. It is found that for all models, the emission gradient at 1.3 mm for the inner region of the core is consistent with observations of the pre-stellar core L1689B by Andre et al. (1996). The flattening of the emission profile in the inner core is most apparent in models having a strong radial gradient in the dust-gas ratio: the dust-gas ratio increasing with increasing radial distance from the core centre. The gradient in the dust-gas ratio has two effects on the emission profile. 1) A reduction in the dust-gas ratio increases the core temperature over models that assume a constant dust-gas ratio. The increase in temperature is most significant at the core centre. For example, the central temperature in the standard model increases by 1.3 K over the same model that assumes a constant dust-gas ratio. This has the effect of increasing emission from individual grains: the increase in emission is greatest at the core centre. 2) The increase in emission due to a temperature increase is more than offset by the decrease in emission due to the reduction in the number density of grains over a model that uses a constant dust-gas ratio. Overall, the gradient in the emission profile is reduced, as illustrated by the standard model in Figure 7.2. For models where the dust-gas ratio does not vary significantly over the core, there is a reduction in inner core emission gradient over a constant temperature model due to the decrease in temperature towards the core centre. The most significant change in the inner core emission gradient is illustrated in Figure 7.3 for model *graindist2*. Here, the decrease in emission gradient accounts for a reduction in the $450\mu\text{m}$ intensity profile from $I \propto R^{-0.54}$ to $I \propto R^{-0.23}$. For most models, the emission gradient in the middle core is too weak to match observations. However, for models that have a dust-gas ratio that does not vary significantly over the core, the emission gradient is consistent with observations. Specifically, models *b1*, *b2* and *graindist2* are consistent with the 1.3mm dust continuum emission and $7\mu\text{m}$ absorption features of the pre-stellar core L1689B, regardless of whether a variable or constant temperature is assumed. For models where a constant temperature is assumed throughout the core, models *b3*, *grainchem1* and *zeta1* are also consistent with observations. Thus it is possible to constrain the types of model to those where:

1. the magnetic field is too weak to have a strong effect on the dust-gas ratio;

-
2. only a small fraction of grains move with the magnetic field: this could be due to the majority of grains having no charge or grain sizes being too large to be strongly coupled to the magnetic field;
 3. ionization remains strong in the core centre resulting in stronger coupling between neutral and charged grains resulting in weaker ambipolar diffusion effects on the dust-gas ratio: this could be the result of high cosmic ray ionization levels or a grain chemistry returning products of electron-ion recombination at the grain surface to the gas phase;
 4. freeze-out occurs at a higher critical visual extinction so that only emission in the inner core is affected by the reduction in the dust-gas ratio.

Chapter 8

Modelling the collapse of a cloud

HAL, you have an enormous responsibility on this mission, in many ways perhaps the greatest responsibility of any single mission element. You're the brain, and central nervous system of the ship, and your responsibilities include watching over the men in hibernation. Does this ever cause you any lack of confidence? HAL: Let me put it this way, Mr. Amor. The 9000 series is the most reliable computer ever made. No 9000 computer has ever made a mistake or distorted information. We are all, by any practical definition of the words, foolproof and incapable of error.

2001: A Space Odyssey, Arthur C. Clarke & Stanley Kubrick

In this chapter the collapse of a cloud is modelled: here the term *cloud* refers to a core and extended envelope. A cloud mass of $M_{cloud} = 28M_{\odot}$ is used – this is the mass of L1544 cloud as estimated by Tafalla et al. (1998). The purpose of this chapter is to test how consistent the cloud model is when compared to the core model. Note that the code used to simulate the collapse of cloud is no different to the code used to model the collapse of a core, other than a change of physical parameters to reflect the larger mass of the cloud and a lower initial gas density and magnetic flux density.

8.1 Model parameters

Two models are chosen in order to compare with the results from earlier chapters: the standard model and model *graindist2*; model *graindist2* is an example of a Class B model, defined in section 6.2 as having a chemical abundance at the core centre that is strongly depleted in comparison to the standard model. Class B models are of particular interest since they are a better fit to the observed radial chemical abundances than the standard model. An initial density of $n(\text{H}) = 1 \times 10^3 \text{ cm}^{-3}$ is used to simulate the collapse from a more diffuse state compared to the collapse of the pre-stellar core. A mass of $M_{\text{cloud}} = 28M_{\odot}$ implies an initial radius of $R = 1.808 \times 10^{18} \text{ cm}$; an external visual extinction of $A_{V_{\text{ext}}} = 0$ is used. The remaining parameters are then taken for the standard model while for model *graindist2*, the sulphur abundance is reduced by a factor of 10.

8.2 Results

The models are run until the central density reaches $n_c(\text{H}) \approx 3 \times 10^6 \text{ cm}^{-3}$ – this density being consistent with estimates for L1544 (e.g. Ward-Thompson et al. 1999; Evans et al. 2001; Tafalla et al. 2002; Crapsi et al. 2007).

8.2.1 Chemical and dynamical radial profiles

In Figure 8.1, the chemical and dynamical radial profiles of the standard cloud model at time $t = 6.36 \text{ Myr}$ are plotted. The upper graph shows the radial profile of the ion and neutral gas velocities – the maximum ion and neutral gas infall velocities of 139 ms^{-1} and 151 ms^{-1} occur at the core centre; this is in contrast to the standard core model having lower infall velocity and maxima that are away from the centre. The maximum drift velocity of 31 ms^{-1} and the position of maximum drift velocity is similar to the standard core model.

The upper middle graph plots the abundance of molecular species as a fraction of the hydrogen nuclei number density, $n(\text{H})$. A rapid fall in ionization (labelled e^-) at the edge of the cloud, between $R = 9 \times 10^{17} \text{ cm}$ and $R = 7 \times 10^{17} \text{ cm}$ occurs at a visual extinction between $0.8 \leq A_V \leq 1.5$: in common with the standard core model, this is attributed to the steep drop in the rate of photodissociation of CO by UV photons. A second rapid decrease in the ionization fraction between $R = 4 \times 10^{17} \text{ cm}$ and $R = 3 \times 10^{17} \text{ cm}$ occurs at a visual extinction between $3 \leq A_V \leq 4$: in common with the standard core model, the

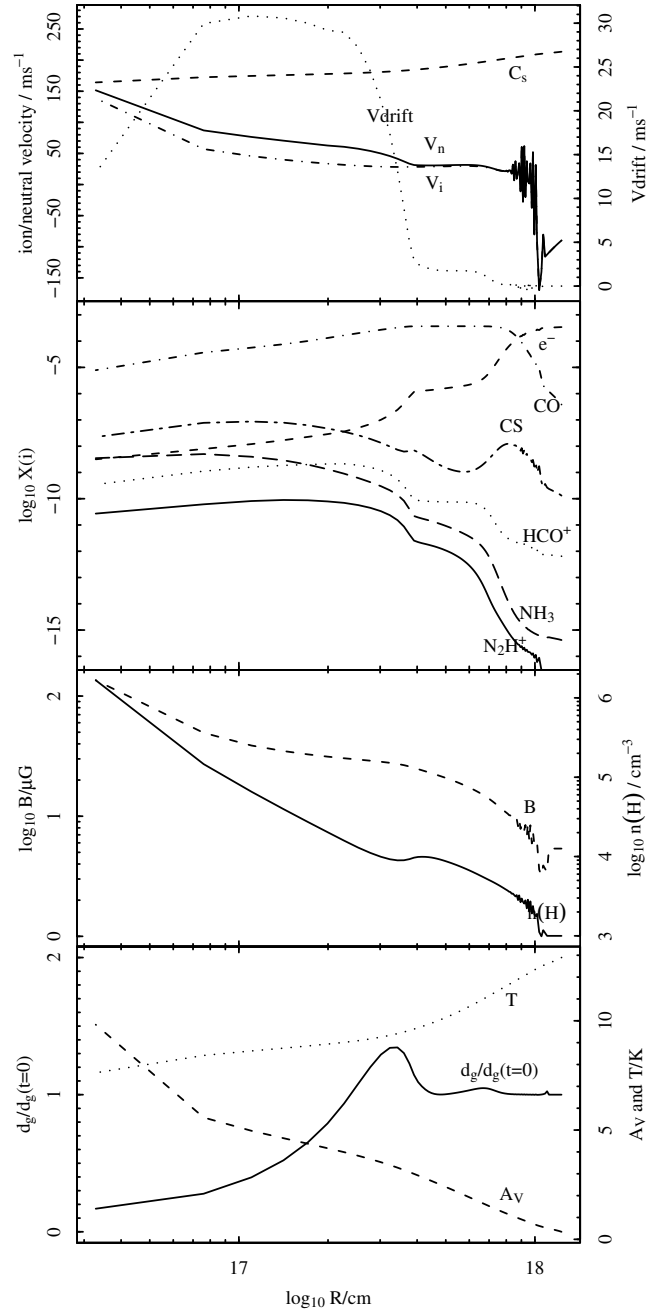


Figure 8.1. Chemical and dynamical radial profile for the standard cloud model using 100 shells.

rapid decrease is attributed to the freeze-out of molecules onto the surface of dust grains for $A_V \geq 3$. The abundance fractions are similar to those for the standard core model, although the radial change in abundance fraction is marginally flatter in the inner region of the cloud compared to the inner region of the core.

The lower middle graph plots B – the magnetic flux density; B is held constant at $5.4 \mu\text{G}$ in the outer 10 shells and increases toward the centre, peaking at $135 \mu\text{G}$ in the central shell. The critical magnetic flux density, $B_{\text{cloud}} = 5.4 \mu\text{G}$, is the magnetic flux density at which the cloud is found to be supercritical; this is found to be marginally lower than in the standard core model, $B_{\text{core}} = 6.1 \mu\text{G}$. This is expected due to the lower initial density in the cloud. The mass-to-flux ratio, $M_{\text{cloud}}/\phi = 1.64$ (in units of the critical mass-to-flux ratio $M_\phi/\phi = 1/(2\pi G^{0.5})$), is found to be marginally lower than for the standard core model, $M_{\text{core}}/\phi = 1.77$. The hydrogen nuclei number density, $n(\text{H})$, is plotted against the second y -axis; $n(\text{H})$ is held constant at $1.0 \times 10^3 \text{ cm}^{-3}$ in the outer 10 shells and increases toward the centre, peaking at $1.67 \times 10^6 \text{ cm}^{-3}$ in the central shell.

The lower graph plots the dust-gas ratio, d_g , normalised relative to the initial dust-gas ratio, $d_g(t=0)$; d_g is lowest in the centre of the cloud and increases with increasing radial distance, peaking at a visual extinction, $A_V \sim 4$. This peak coincides with the rapid decrease in ionization fraction. This is consistent with the results for the standard core model. The visual extinction, A_V , and temperature, T , are plotted against the second y -axis; note that the temperature at the edge of the cloud (13 K) is higher than the temperature at the edge of the standard core model (11.5 K), due to the lower external visual extinction in the cloud model.

The significant increase in the infall velocity of the central shell when compared to the core model could be the result of the increased size of the central shell: Truelove et al. (1997) find in their simulations of isothermal, self-gravitational hydrodynamical collapse that the ratio of the cell size to the Jeans length needs to satisfy $\Delta x/\lambda_J \leq 0.25$ in order that artificial condensations are not created. Since there has been no change in the number of shells between the core and cloud model, $\Delta x/\lambda_J$ for the inner shell in the cloud model is greater by a factor of 1.6 at the same density. For the cloud model at a central density of $n(\text{H}) = 1.67 \times 10^6 \text{ cm}^{-3}$, $\Delta x/\lambda_J = 1.12$ while for the core model, $\Delta x/\lambda_J = 0.7$ at the same density. Since the shell size in the cloud model is greater than the Jeans length, it is possible that the inner shell in the cloud model is subject to an artificial increase in infall velocity. Note however, that the Jeans length does not take into

account the contribution from magnetic pressure. The modified Jeans length, $\lambda_{J(g+B)}$, as derived by Zengin et al. (2004), takes into account both gas and magnetic pressure terms: $\lambda_{J(g+B)} = \pi \sqrt{(C_s^2 + V_A^2)/G\rho}$ where $V_A = B/(4\pi\rho)^{0.5}$ is the Alfvén velocity. The effect of including the magnetic pressure term in the Jeans length is to allow larger shell sizes before models are subject to an artificial increase in infall velocity. Using $V_A = 280 \text{ ms}^{-1}$, the Alfvén velocity in the central shell at $t = 6.36 \text{ Myr}$ for the standard cloud model, gives $\Delta x/\lambda_J = 0.62$ for the cloud model while $\Delta x/\lambda_J = 0.39$ for the core model. Note that both the cloud and core models are outside the limit as determined by Truelove et al. (1997), but this limit is almost certainly model dependent.

8.2.2 Oscillations at the edge of the cloud

Note also, the large-amplitude oscillations in the ion and neutral infall velocities at the cloud edge. The reason for these oscillations deserve a detailed analysis since it is important to determine whether they are the result of an algorithmic instability or whether there is an underlying physical reason for the oscillations. Various physical possibilities can be ruled out: since the infall velocity is below the sound speed in the gas, these oscillations are not initiated by sonic or magnetosonic shocks. Numerical instabilities may arise if the distance travelled by the gas over an integration time step, Δt , is comparable to the distance between shells, Δx . The dynamical time step is 10 yr which is equivalent to $5 \times 10^{12} \text{ cm}$ for an infall/outflow velocity of 150 ms^{-1} ; this is much smaller than the distance between shells in the outer cloud, $\Delta x \sim 1.8 \times 10^{16} \text{ cm}$. The code also includes a consistency check to ensure that local velocities do not result in the boundaries of a shell advancing beyond the boundaries of a neighbouring shell. A more restrictive limit is set by the Courant-Freidrichs-Lewy (CFL) stability condition (Courant et al. 1928), that $\Delta t \leq \Delta x/C_s$. The stability condition prohibits the sending of information across a shell faster than the integration time step. In the case of magnetohydrodynamic equations, the stability condition needs to be corrected by substituting the sound speed with the fast-mode Alfvén wave velocity: $\Delta t \leq \Delta x/\sqrt{(C_s^2 + V_A^2)}$. However, even here $\Delta t = 10 \text{ y}$ is sufficiently small enough to prevent information crossing a shell within a single time step at the maximum Alfvén velocity observed in the model: $V_A(\text{max}) \sim 400 \text{ ms}^{-1}$. A further possibility is that information regarding the ionization in the shell (which affects the dynamics of the cloud) violates the CFL condition. The chemical time step is 10000 yr which is equivalent to $5 \times 10^{15} \text{ cm}$ for an infall/outflow velocity of 150 ms^{-1} ; this is

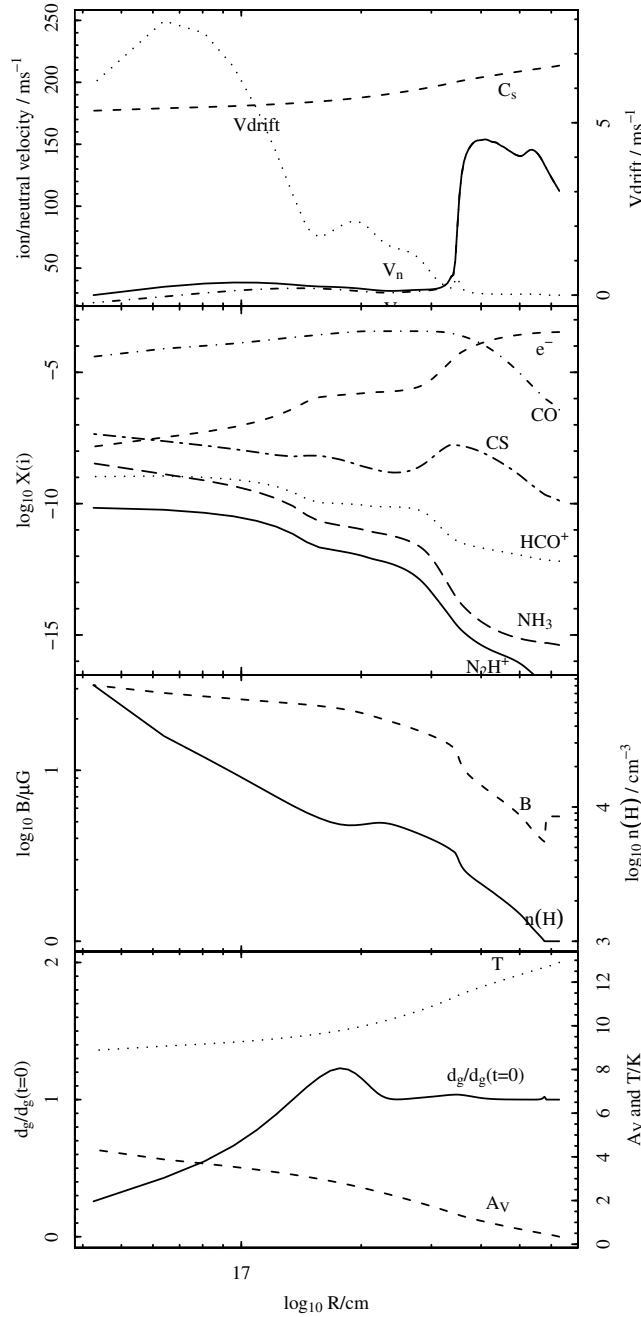


Figure 8.2. Chemical and dynamical radial profile for the standard cloud model at $t = 5.9$ Myr, the epoch just prior to the onset of oscillations in the velocity profile.

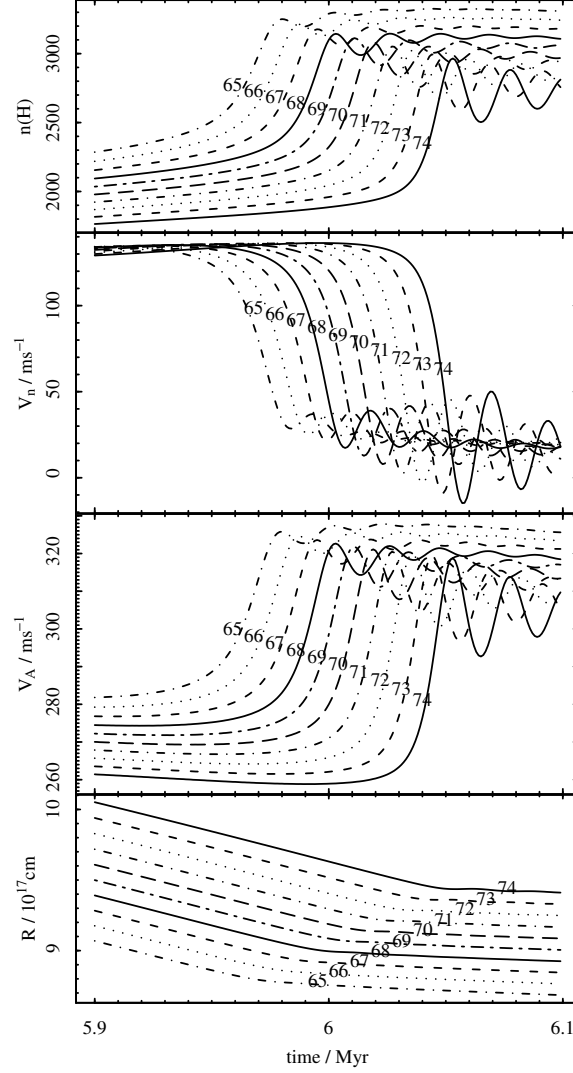


Figure 8.3. Dynamical evolution of 10 shells near the source of cloud oscillations.

Upper graph plots $n(H)$, the number density of hydrogen atoms, at each shell over time – shell numbers annotate each line. Upper middle graph plots V_n , the infall velocity of neutral gas, at each shell over time – in this region of the cloud, ion infall velocities are strongly coupled to the neutral infall velocities. Lower middle graph plots V_A , the Alfvén velocity, at each shell over time. Lower graph plots R , the radial distance of each shell from the cloud centre, at each shell over time. Line points where the gradient in R changes are used to identify the radial distances at the point where the compression wave encounters a shell.

about a third of the size of Δx , so it might be possible that instabilities arise due to the chemical time step being too long. In order to test this hypothesis, the chemical time step is reduced to 1000 yr from the epoch at which the oscillations start. This results in no significant damping of the oscillations, indicating that the chemical time step is not the source of the instabilities. The oscillations are likely to be linked to the transition from collapse to expansion in the outer cloud. The start of the oscillations can be traced back to a point at $t = 5.9$ Myr: the outer cloud is collapsing with an infall velocity of 150 ms^{-1} while the inner and middle cloud is at a nearly constant infall velocity of 30 ms^{-1} (see Figure 8.2). A steep drop in infall velocity occurs at a point coinciding with a rapid drop in ionization; this is accompanied by a steep increase in both $n(\text{H})$ and B (in the direction of the cloud centre). As the cloud collapses and becomes denser, the position at which the rapid change in ionization fraction occurs moves outwards. An increasingly steep change in velocity is accompanied by larger amplitude oscillations. Eventually, the sign of the oscillations switch from being positive to negative and the outer cloud expands at about 150 ms^{-1} . This sequence of events is easier to show using a JPEG movie: when the electronic version of this document is viewed through Adobe Reader, a movie of the collapsing cloud can be viewed by clicking on Figure 8.1. Note that under a Unix environment, the movie will need to be saved as an attachment. The steep gradient in both $n(\text{H})$ and B is similar to that found across a shock; the modelling of shocks using algorithms based on the finite difference method are known to be problematic, giving rise to large amplitude oscillations (Anderson 1987). In reality, modellers often introduce an artificial viscosity component into the material being modelled in order to dampen the amplitude of these oscillations (Anderson 1987).

A further, detailed examination of the dynamical behaviour of the closest 10 shells to the position at which the oscillations start, indicates that a compression wave is moving out from the core centre. Figure 8.3 plots the dynamical behaviour of shells 65 to 74 between $t = 5.9$ Myr and $t = 6.1$ Myr. The lower graph plots the radial position of each of the shells over time: this plot can be used to estimate the progression of the wave over time, using the point where there is a change-over of the overall infall velocity from high ($\sim 130 \text{ ms}^{-1}$) to low ($\sim 30 \text{ ms}^{-1}$). As a shell encounters the compression wave, passage through the wave forces oscillations in $n(\text{H})$ (which is strongly coupled to B) and V_n , the neutral gas infall velocity (which is strongly coupled to the ion infall velocity). The amplitude of these oscillations increase with each successive shell that the wave encounters.

The suggested reason for this behaviour is a significant error component in the calculated gas density and magnetic pressure gradients, due to the steep radial gradients in $n(\text{H})$ and B : when the number of shells spanning the steep gradients drops to a few (~ 5), these errors become significant enough to trigger the oscillations observed in the model. The steepness of the radial gradients increase as the wave propagates through the cloud, giving rise to increasingly large errors which translate into increasingly large amplitudes of oscillation. In order to test how a reduction in shell size might alter this behaviour, the standard model is re-run using 400 shells. It is found that the period of oscillations is affected by the shell size but there is only a marginal effect on the radial position at which the oscillations start: the oscillations start at a slightly lower density. Thus the period of oscillations are an artificial artefact of the choice of shell size while the position of the onset of the oscillations is nearly independent of the shell size: this is due to the physical process of the rapid steepening of radial gradients in $n(\text{H})$ and B , giving rise to a physical discontinuity, i.e. a shock. The impact these errors have on the radial distribution of dust, B and molecular species is likely to be small since ions and neutrals are strongly coupled in the outer region of the cloud, and the oscillations are transient in nature: Figure 8.3 indicates that for any shell, the amplitude of oscillations have decayed away to about half their initial value after approximately 40000 yr. It is noticeable however, that these oscillations are not observed when the code is run for the lower mass core. The reason for this is that the oscillations only occur at a density $n(\text{H}) \lesssim 3 \times 10^3 \text{ cm}^{-3}$ – only slightly higher than the value of $n(\text{H})$ that is fixed in the outer 10 shells of the core models.

8.2.3 Improving the resolution of cloud models with additional shells

In order to test the hypothesis that the increase in size of the central shell is responsible for an artificially induced increase in infall velocity at the cloud centre, the standard and *graindist2* cloud models are run with 400 shells in order to reduce the inner shell radius to a value similar to that used in the core model. Figure 8.4 plots the same series of graphs as in Figure 8.1 but for the standard cloud model using 400 shells at time $t = 6.66 \text{ Myr}$, corresponding to a central $n(\text{H}) = 2.66 \times 10^6 \text{ cm}^{-3}$ and $B = 163 \mu\text{G}$. The ion and neutral gas infall velocities are not centrally peaked in this model, consistent with the profiles for the standard core model. The maximum ion and neutral infall velocities of 71 ms^{-1} and 105 ms^{-1} respectively are similar to the maxima for the core model. The minimum infall velocity of -120 ms^{-1} occurs at the cloud edge, indicating expansion.

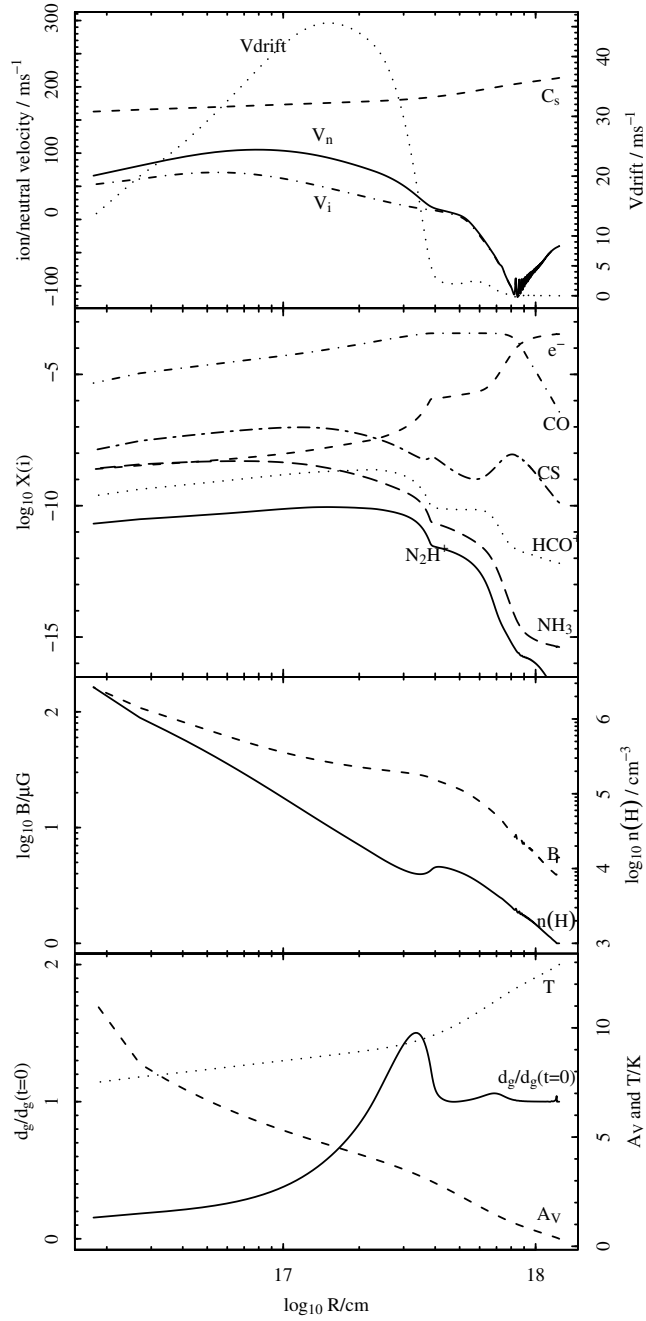


Figure 8.4. Chemical and dynamical radial profile for the standard cloud model, increasing the number of shells from 100 to 400.

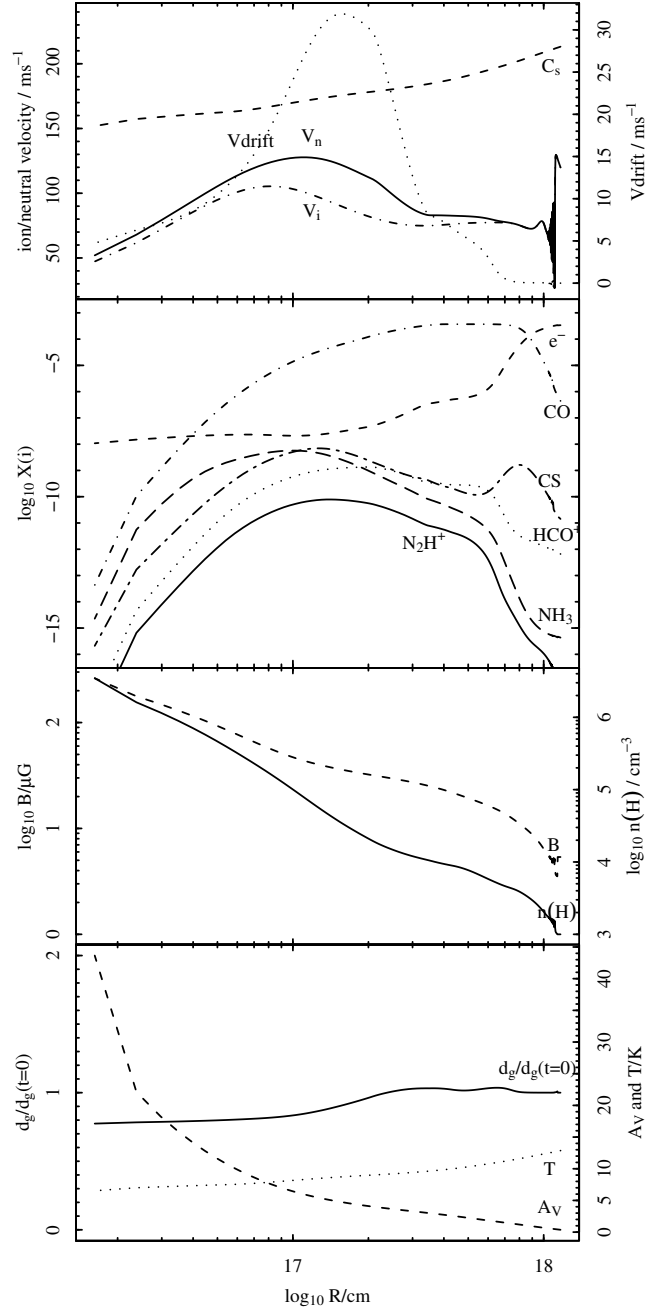


Figure 8.5. Chemical and dynamical radial profile for the cloud model *graindist2* using 400 shells.

Large amplitude oscillations still exist in the ion and neutral infall velocities at the cloud edge. The maximum drift velocity of 46 ms^{-1} is higher than for the core model (32 ms^{-1}). The chemical radial profile, and the radial change in T and A_V are similar to that from the previous run of the standard cloud model.

For the standard cloud model, the co-existence of expansion in the outer cloud and collapse in the inner and middle cloud is similar to that inferred from observations of L1506C (Pagani et al. 2010a). L1506C is not gravitationally bound and therefore not classified as a pre-stellar core. However, it is thought that L1506C is at stage just prior to becoming pre-stellar. L1506C shows, through lines of C^{17}O and C^{18}O , an infall velocity of about 100 ms^{-1} at the core edge while observations of ^{13}CO show the extended envelope to be expanding at about 90 ms^{-1} . The collapsing core has a mass of about $4M_{\odot}$ within a radius of $4.5 \times 10^{17} \text{ cm}$ while the expanding envelope has a mass of $20M_{\odot}$ within a radius of $1.9 \times 10^{18} \text{ cm}$. This compares to a mass of $6.2M_{\odot}$ within a radius of $4.5 \times 10^{17} \text{ cm}$ for the standard cloud model and an envelope mass of $21.8M_{\odot}$ within an outer cloud radius of $1.1 \times 10^{18} \text{ cm}$. So while core infall and envelope expansion speeds of L1506C are similar to the standard cloud model, the average density within the core and envelope is less dense than the standard cloud model.

Figure 8.5 plots the same series of graphs as in Figure 8.1 but for cloud model *graindist2* using 400 shells at time $t = 6.5 \text{ Myr}$, corresponding to a central $n(\text{H}) = 3.47 \times 10^6 \text{ cm}^{-3}$ and $B = 262 \mu\text{G}$. Again, the ion and neutral gas infall velocities are not centrally peaked, consistent with the core model *graindist2*. The maximum ion and neutral infall velocities in the middle cloud of 129 ms^{-1} and 102 ms^{-1} respectively are higher than the maxima for the core model (98 ms^{-1} and 85 ms^{-1}). The maximum ion and neutral infall velocity over the entire cloud is 130 ms^{-1} and occurs at the cloud edge. Here, large amplitude oscillations exist in both the ion and neutral infall velocities. In contrast to the standard cloud model, the cloud is collapsing at the cloud edge. The maximum drift velocity of 32 ms^{-1} is higher than for the core model (24 ms^{-1}). The results for all radial profiles, including the results from core models, are summarised in Table 8.1.

Table 8.1. Cloud dynamical radial profiles when $n_c(\text{H}) \sim 3 \times 10^6 \text{ cm}^{-3}$.

Model identifier	Shells	$n_c(\text{H})$ / 10^6 cm^{-3}	t_c /Myr	B_c / μG	V_{Nmax} / ms^{-1}	V_{Nmin} / ms^{-1}	V_{Imax} / ms^{-1}	V_{Imin} / ms^{-1}	ΔV / ms^{-1}	$R(V_{Nmax})$ / 10^{16} cm	$R(V_{Imax})$ / 10^{16} cm	$R(\Delta V)$ / 10^{16} cm
standard core	100	4.34	4.75	170.48	107.59	0.45	83.54	-0.79	32.02	5.21	4.39	14.97
standard cloud	100	1.67	6.36	135.45	151.47	-169.83	138.56	-169.90	30.82	3.28	3.28	11.03
standard cloud	400	2.66	6.66	163.06	105.23	-117.24	71.00	-117.30	45.62	7.75	5.38	14.93
graindist2 core	100	4.75	5.08	266.72	98.05	-38.14	84.97	-38.79	24.29	6.86	5.61	13.53
graindist2 cloud	100	3.24	6.54	293.46	124.16	-108.47	113.49	-108.51	37.97	9.73	2.62	16.96
graindist2 cloud	400	3.47	6.50	262.21	129.65	26.63	129.62	26.94	31.89	111.80	111.80	15.41

$n_c(\text{H})$ is the central hydrogen nuclei number density; B_c is the central magnetic flux density; V_{Nmax} is the maximum neutral infall velocity; V_{Nmin} is the minimum neutral infall velocity; V_{Imax} is the maximum ion infall velocity; V_{Imin} is the minimum ion infall velocity; ΔV is the maximum drift velocity; $R(V_{Nmax})$ is the position of maximum neutral infall velocity; $R(V_{Imax})$ is the position of maximum ion infall velocity; $R(\Delta V)$ is the position of maximum drift velocity.

Table 8.2. Fits of $n(\text{H}) \propto R^{-\alpha}$ for the inner (α_i), middle (α_m) and outer (α_o) regions of the cloud and core models.

Model identifier	Shells	Inner α_i	Middle α_m	Outer α_o
standard core	100	2.14	2.13	2.19
standard cloud	100	2.58	2.05	2.72
standard cloud	400	1.96	2.08	2.99
graindist2 core	100	2.04	2.37	2.22
graindist2 cloud	100	2.55	2.30	2.82
graindist2 cloud	400	1.77	2.27	4.71

8.2.4 Radial profile of $n(\text{H})$

The radial gas density distribution is analysed for all cloud models by fitting power-laws of the form $n(\text{H}) \propto R^{-\alpha}$ to inner (α_i), middle (α_m) and outer (α_o) regions of the cloud. In common with the core models, the outer 10 shells are not modelled since both $n(\text{H})$ and B are held constant in this region. The regions of the cloud are defined as follows: the inner cloud is defined as the region within the innermost 10 shells; the middle cloud is defined as the region between the end of the inner cloud and the position of density dip; the outer cloud is defined as the region outward from the density dip to the shell just inward of the region of constant $n(\text{H})$ and B . Table 8.2 summarises the results for all cloud models, including previous results for the core models and a run of cloud model *graindist2* using 100 shells.

For cloud models that use 100 shells, hereafter termed *Low Resolution* cloud models, the radial distribution of $n(\text{H})$ is found to be much steeper in the inner core, consistent with the idea that using a shell size in the inner core that is larger than the Jeans length could be the cause of artificially induced, runaway collapse in the inner cloud. For cloud models that use 400 shells, hereafter termed *High Resolution* cloud models, the density distribution is marginally flatter in the inner cloud, indicating that artificial, runaway collapse is not a problem for these models. For all cloud models, the density gradient in the middle region of the cloud is marginally flatter than for the core models while the density gradient in the outer cloud is steeper for all cloud models.

Table 8.3. Collapse time compared with free-fall time for a starting central density of $n_1(\text{H}) \sim 3 \times 10^3 \text{ cm}^{-3}$ at time t_1 .

Model identifier	Shells	$n_1(\text{H})$ / 10^3 cm^{-3}	V_1 / ms^{-1}	$t_c - t_1$ /Myr	Δt_{ff} /Myr	$\frac{t_c - t_1}{\Delta t_{ff}}$
standard core	100	4.9	14.21	1.35	0.56	2.42
standard cloud	100	2.3	19.97	1.66	1.31	1.27
standard cloud	400	2.1	0.43	1.96	0.90	2.17
graindist2 core	100	5.0	6.00	1.68	0.60	2.78
graindist2 cloud	100	2.5	-0.23	1.94	1.69	1.15
graindist2 cloud	400	3.5	-1.50	1.7	0.72	2.36

V_1 is the infall velocity of the central shell at time t_1 : positive values indicate infall; negative values indicate expansion.

Table 8.4. Collapse time compared with free-fall time for a starting central density of $n_2(\text{H}) \sim 5 \times 10^4 \text{ cm}^{-3}$ at time t_2 .

Model identifier	Shells	$n_2(\text{H})$ / 10^4 cm^{-3}	V_2 / ms^{-1}	$t_c - t_2$ /Myr	Δt_{ff} /Myr	$\frac{t_c - t_2}{\Delta t_{ff}}$
standard core	100	4.6	42.45	0.55	0.15	3.64
standard cloud	100	3.4	88.63	1.06	0.21	5.02
standard cloud	400	3.4	25.06	1.36	0.18	7.58
graindist2 core	3.8	45.81	100	0.88	0.16	5.40
graindist2 cloud	100	4.1	21.63	1.14	0.32	3.51
graindist2 cloud	400	3.0	22.53	1	0.20	5.11

V_2 is the infall velocity of the central shell at time t_2 .

Table 8.5. Collapse time compared with free-fall time for a starting central density of $n_3(\text{H}) \sim 2 \times 10^5 \text{ cm}^{-3}$ at time t_3 .

Model identifier	Shells	$n_3(\text{H})$ / 10^5 cm^{-3}	V_3 / ms^{-1}	$t_c - t_3$ /Myr	Δt_{ff} /Myr	$\frac{t_c - t_3}{\Delta t_{ff}}$
standard core	100	2.2	20.62	0.25	0.08	3.28
standard cloud	100	2.3	32.74	0.16	0.11	1.48
standard cloud	400	2.9	25.64	0.16	0.06	2.88
graindist2 core	100	2.1	19.07	0.38	0.08	4.73
graindist2 cloud	100	2.3	29.03	0.24	0.12	1.93
graindist2 cloud	400	3.2	21.08	0.2	0.06	3.59

V_3 is the infall velocity of the central shell at time t_3 .

8.2.5 Comparing collapse times to the free-fall time

The dynamics over time are not plotted for the cloud models, since in general they follow the same pattern of collapse, expansion followed by a second collapse phase as illustrated in Figure 4.1 for the core models. Of particular interest however, is the ratio of collapse times relative to the modified free-fall time as defined in equation 6.1. In Table 8.3 the time taken to collapse from the point of minimum density during the second collapse phase at time t_1 to the end of the model run at time t_c is compared with the modified free-fall time that takes into account a non-zero initial velocity, V_1 , at time t_1 and radius R_1 and a non-zero final radius R_c at time t_c according to equation 6.1; the core collapse times are also included in order to highlight the difference between core and cloud collapse times. For the Low Resolution cloud models, the ratio of infall to free-fall time, $\frac{t_c - t_1}{\Delta t_{ff}}$, is significantly lower compared to the core models while for the High Resolution cloud models, $\frac{t_c - t_1}{\Delta t_{ff}}$ is marginally lower compared to the core models. This would indicate that overall, the cloud models collapse at a faster rate relative to their free-fall times compared to the core models. Tables 8.4 and 8.5 present the ratio of infall to free-fall times for initial cloud central densities of $n(\text{H}) \simeq 5 \times 10^4 \text{ cm}^{-3}$ and $n(\text{H}) \simeq 2 \times 10^5 \text{ cm}^{-3}$ respectively. Table 8.4 clearly shows the rate of infall decreasing relative to the overall rates of infall from Table 8.3. This is understandable since in the initial phase of collapse, little or no magnetic or thermal pressure gradient exists at the centre of the core. There is however, no pattern with regard to the class of model with the highest ratio: this could be due to the wide range of initial infall velocities (V_2). Table 8.5 shows that the collapse rate increases relative to that in Table 8.4. For Low Resolution cloud models, the ratio of infall to free-fall times is significantly lower than the core models while for the High Resolution cloud models, the ratio is marginally lower compared to the core models.

8.2.6 Consistency between cloud and core models

Taking into account the steep density gradient in the inner region of Low Resolution cloud models and the significant increase in the rate of collapse when $n(\text{H}) \geq 2 \times 10^5 \text{ cm}^{-3}$, the conclusion drawn is that Low Resolution cloud models are inconsistent with respect to the dynamical timescales of the core models. However, High Resolution cloud models are reasonably consistent with the core models: the density gradient in the inner region of the cloud is marginally flatter than the core models; collapse times are marginally faster in the

later stages of collapse compared with core models. For this reason, no further detailed analysis on the Low Resolution cloud models is performed; hereafter, any reference to cloud models refers to High Resolution cloud models only.

8.2.7 Synthetic line profiles

For each of the cloud models, the line profiles of C^{18}O (1-0), HCO^+ (1-0), CS (1-0), NH_3 (1,1) and N_2H^+ (1-0) are plotted at six radial positions within the cloud corresponding to beam offsets of 0 arcsec to 125 arcsec at a distance of 140 pc. The radial chemical profiles are converted into line profiles that could be observed with typical existing single dish telescopes (such as JCMT or FCRAO), using spherical radiative transfer code, SMMOL (Rawlings & Yates 2001), and the collisional rate data files therein for HCO^+ and CS (Monteiro 1985; Green & Chapman 1978). Collisional rate data files for C^{18}O , NH_3 and N_2H^+ are taken from Schöier et al. (2005). The abundance fraction of C^{18}O is derived by dividing the abundance of CO by the terrestrial O^{18}O ratio (≈ 490). In common with the core models, the dust temperature is assumed to be the same as the gas temperature and a constant turbulent velocity of 0.065 km s^{-1} applies throughout the core. The background radiation field uses that defined by Mathis et al. (1983) with the addition of a black body of 2.7 K to simulate the cosmic background radiation. Beam parameters for an artificial beam are chosen: the beam efficiency is set to 1.0 in order to generate beam temperatures on the T_{mb} scale. A Gaussian beam profile is assumed with beam sizes derived from a 14m telescope (such as the FCRAO 14m telescope).

8.2.8 Radial line profiles

Figure 8.6 presents the results for the standard cloud model: this figure shows that line profiles and plots of integrated flux for HCO^+ (1-0), C^{18}O (1-0), NH_3 (1,1) and N_2H^+ (1-0) are similar in shape and intensity to those for the standard core model from Figure 6.5, indicating that there is close agreement between the standard core and cloud models for these molecular species. The CS (1-0) line profile is different from the core model: the line shows a redshifted peak at all radii, indicating that emission is dominated by the expanding gas at the edge of the cloud.

Figure 8.7 shows line profiles and plots of integrated flux for the cloud model *graindist2*. The line profiles have higher intensity and are more centrally peaked in C^{18}O (1-0) and CS (1-0) than for core model *stick1* given in Figure 6.6 – an example of a Class B core model:

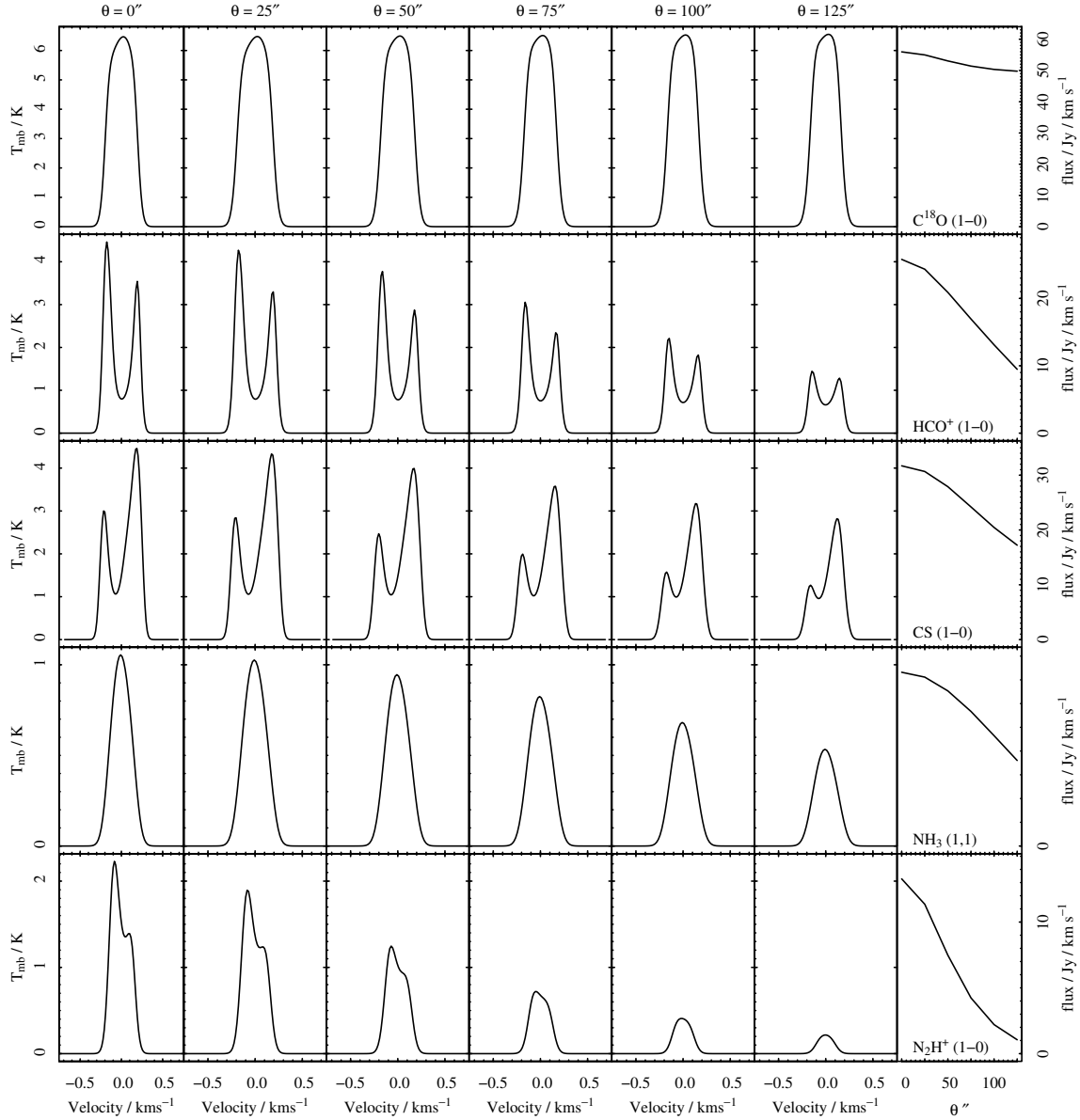


Figure 8.6. Radial line profiles for the *standard* cloud model.

Line profiles for beam offsets between $0''$ and $125''$ are plotted together with the integrated flux in the right-most column of the grid.

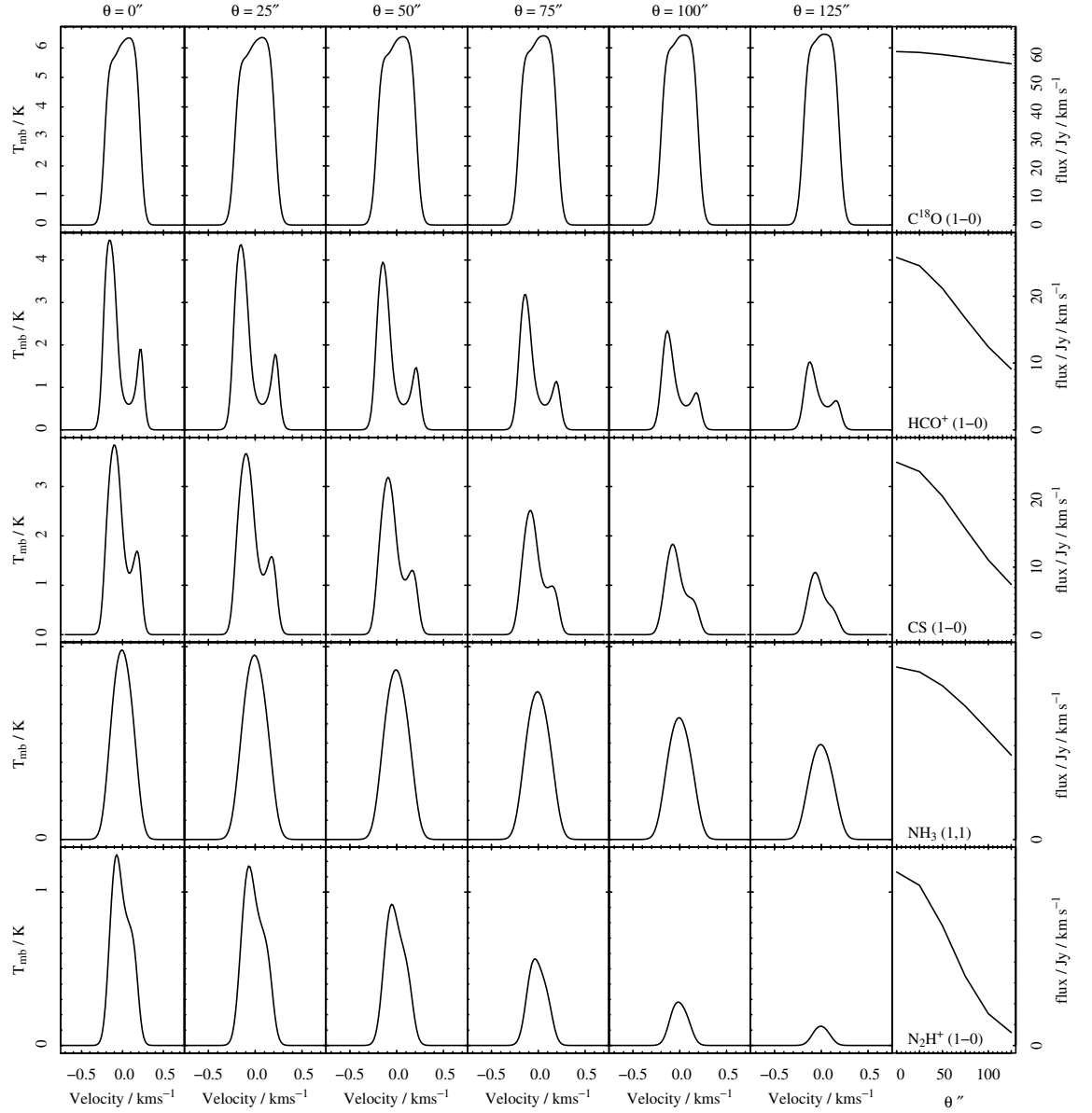


Figure 8.7. Radial line profiles for cloud model *graindist2*.

the plots are closer to those for the standard core model rather than core model *stick1*. The increased neutral-grain sticking coefficient of 1.0 and slower collapse times at higher density both contribute to increased freeze-out of molecules in core model *stick1*. Both the HCO^+ (1-0) and CS (1-0) lines show strong asymmetric profiles with the dominant blueshifted peak significantly higher than the redshifted peak.

8.2.9 Line profiles for higher rotational transition lines

Chapters 4 and 6 presented line profiles of higher rotational transition lines for the standard, *stick1* and *b4* models. For the standard model and model *b4*, a trend in HCO^+ was identified that showed the velocity at which the self-absorption dip occurs, the *dip velocity*, increases with increasing transition number for a collapsing core. In the CS line, only the (4-3) line shows a significant shift from the lower transition lines. In Figures 8.8 and 8.9, the profiles for rotational transitions (4-3), (3-2), (2-1) and (1-0) are plotted for the standard and *graindist2* cloud models respectively. Figure 8.8 shows similar line profiles to the standard core model: the dip velocity increases with increasing transition number. The CS transitions show asymmetric line profiles with the redshifted peak dominating over the blue for transitions (1-0) and (2-1) while for the (4-3) transition, the blueshifted peak dominates; the CS (3-2) redshifted peak temperature is marginally higher than the blueshifted peak temperature. The dip velocity changes from being blueshifted to redshifted with increasing line transition number. The CS line profiles are consistent with expanding gas in the outer core dominating line emission and absorption for the lower transitions while the collapsing gas in the inner core dominates the line profiles for the higher transitions. Figure 8.9 shows much weaker HCO^+ lines compared to the standard model. In particular, the peak temperature of the (4-3) line is now around 0.05 K – this compares with a peak temperature of 1.1 K for the standard cloud model. The decrease in emission is due to the depletion of HCO^+ at the core centre. In chapter 4, it was suggested that the dip velocity in the (4-3) line could provide an estimate of the infall velocity outside the inner core. For models where strong freeze-out is present, such as model *graindist2*, the reduction in emission coupled with a decrease in dip velocity clearly shows that the diagnostic power of the HCO^+ (4-3) line in determining infall velocities is now weakened, since there is now less self-absorption and the dip velocity ($\sim 10\text{ms}^{-1}$) is now much less than for the lower transitions; for transitions (1-0), (2-1) and (3-2) there is little variation in dip velocity ($\sim 80\text{ms}^{-1}$). The CS lines show the blueshifted peak

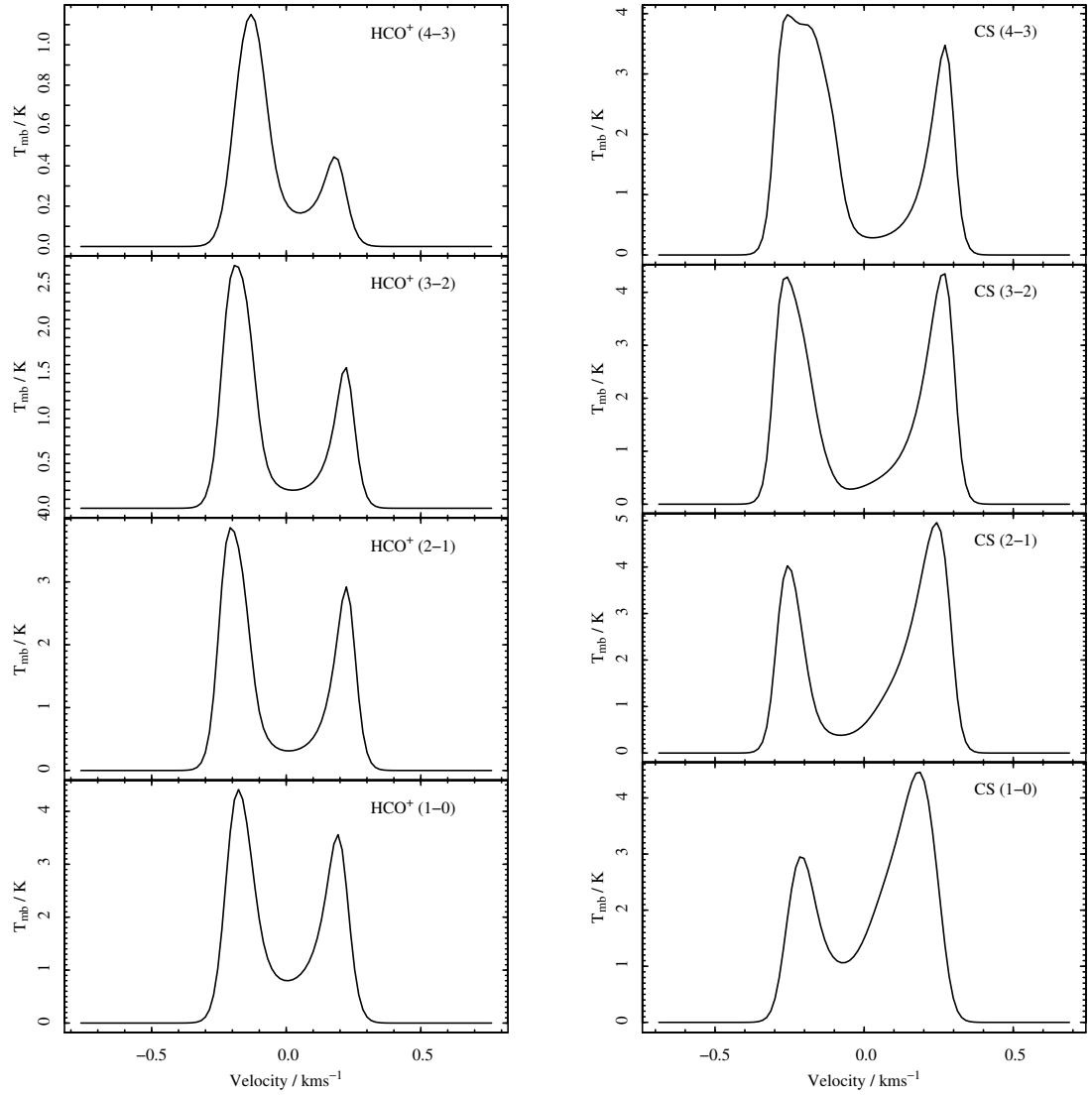


Figure 8.8. Line profiles at the cloud centre for the standard cloud model

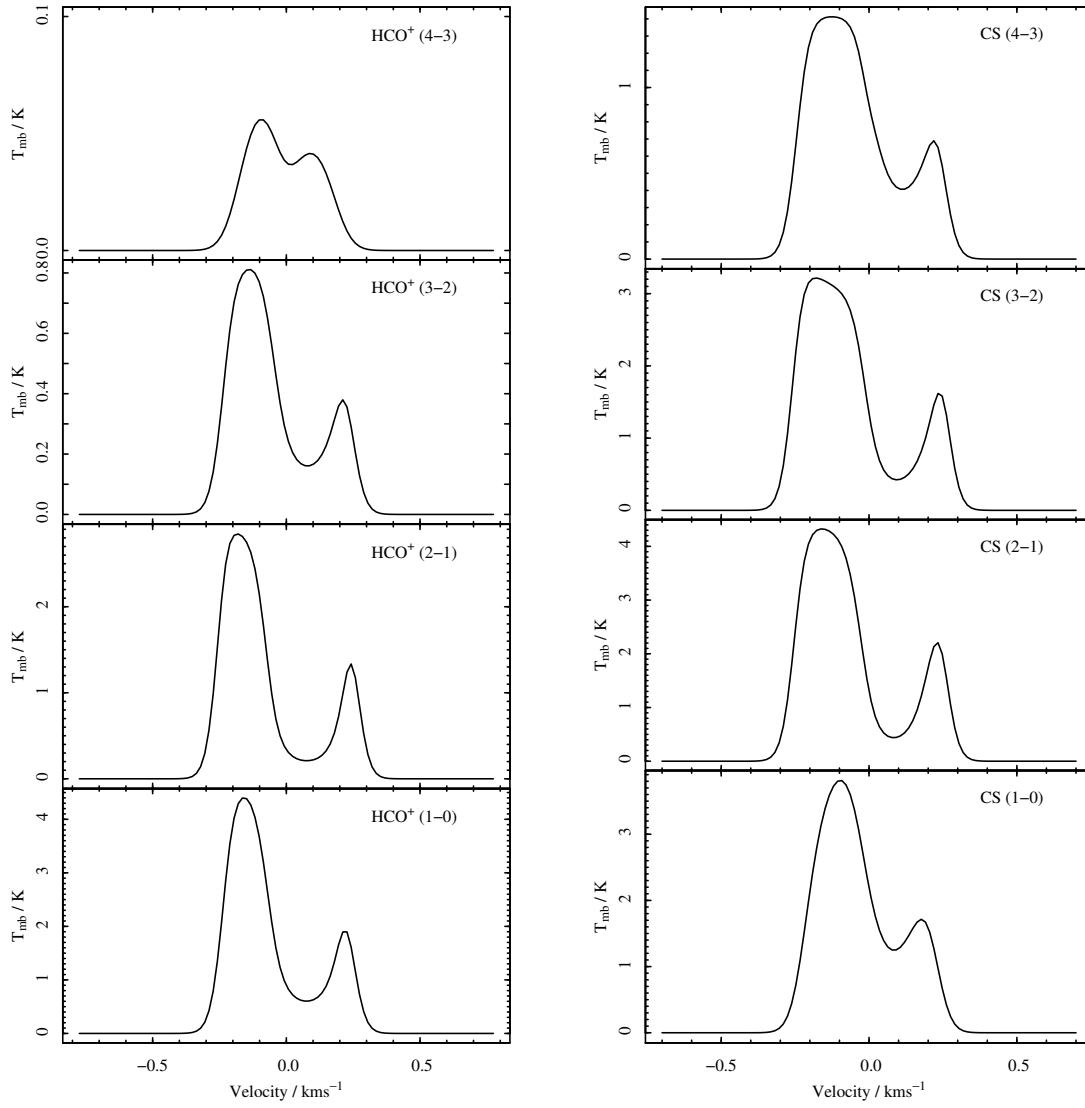


Figure 8.9. Line at the cloud centre for cloud model *graindist2*.

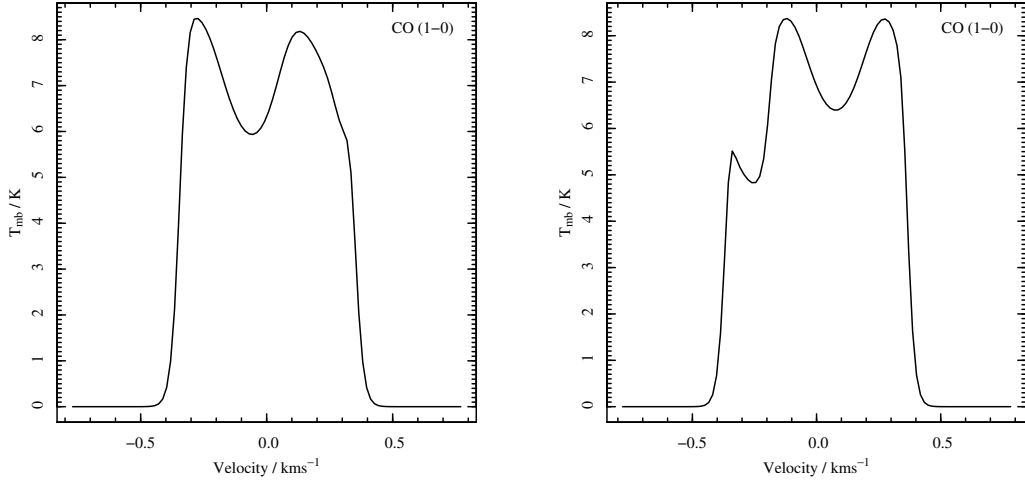


Figure 8.10. CO (1-0) line profiles at the cloud centre for the standard (left-hand plot) and *graindist2* (right-hand plot) cloud models.

temperature dominating over the redshifted peak temperature and a small variation in the dip velocity between transition (1-0) ($\sim 80 \text{ ms}^{-1}$) and transition (4-3) ($\sim 120 \text{ ms}^{-1}$). The line profiles are similar to those found for core model *stick1* but the ratio of the dominant blueshifted peak over the weaker redshifted peak is much higher.

8.2.10 Line profiles and excitation temperature for CO (1-0)

In Figure 8.10, the CO (1-0) line profiles are plotted for the standard and *graindist2* cloud models. The purpose of these plots are to show the emission profile for lines where the line excitation temperature decreases towards the centre. For the standard cloud model, the blueshifted peak has a higher main beam temperature than the redshifted peak while the emission minimum is also blueshifted. This is in contrast to emission lines of HCO^+ and CS for which the excitation temperature generally increases towards the centre: here the velocity at which the dominant emission peak occurs has the opposite sign to the velocity at which the emission minimum occurs. A simple interpretation of this property of the CO line is that peak emission is dominated by the blueshifted collapsing inner region of the far-side of the cloud while absorption is dominated by the expanding, blueshifted outer region of the near-side of the cloud. The line differs to the C^{13}O line observed in L1506C (Pagani et al. 2010a). The authors argue that strong depletion of CO in the core results in a C^{13}O line profile with a dominant redshifted peak indicating expansion in the envelope

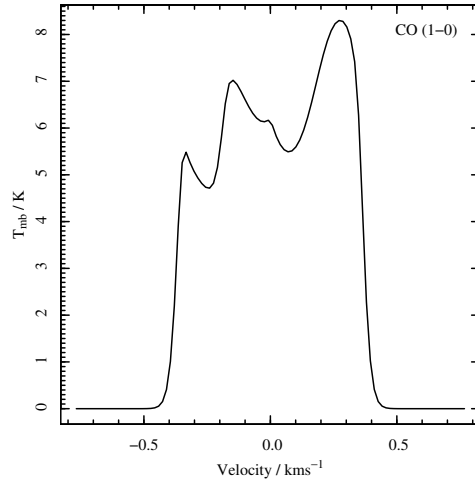


Figure 8.11. CO (1-0) line profiles at the cloud centre, excluding the contribution from the outer 25% of the cloud mass for cloud model *graindist2*. Although the cloud is collapsing at all radii the redshifted emission peak dominates line emission.

while dominant blueshifted emission peaks in lines of C¹⁷O and C¹⁸O indicate collapse in the core. A possible reason for the difference between the standard cloud model and L1506C is that CO depletion is not strong enough in the standard cloud model to allow emission from the envelope to dominate.

For cloud model *graindist2*, there is hardly any difference between the peak temperatures in the redshifted and blueshifted hemispheres: the redshifted peak has a marginally higher peak temperature, despite the cloud collapsing at all radii. Due to the stronger depletion of CO in the inner region of the cloud, emission and absorption are dominated by gas in the middle and outer regions of the cloud. The large infall velocities at the cloud edge, coupled with CO (1-0) lines being optically thick implies that emission between the redshifted and blueshifted hemispheres is radiatively decoupled. This results in a redshifted and blueshifted emission component (rather than a single emission component with a self absorption dip) with the peak temperature from both hemispheres being approximately equal. There is however, a weak self-absorption dip in the blueshifted hemisphere. The line profile is in contrast to the single-peaked line profile of CO (1-0) observed in L1544 by Tafalla et al. (1998). However, there does appear to be a significant shoulder on the blueshifted side of the line which could be due to weak self-absorption in the blueshifted hemisphere. In an attempt to understand the source of the weak self absorption dip in the

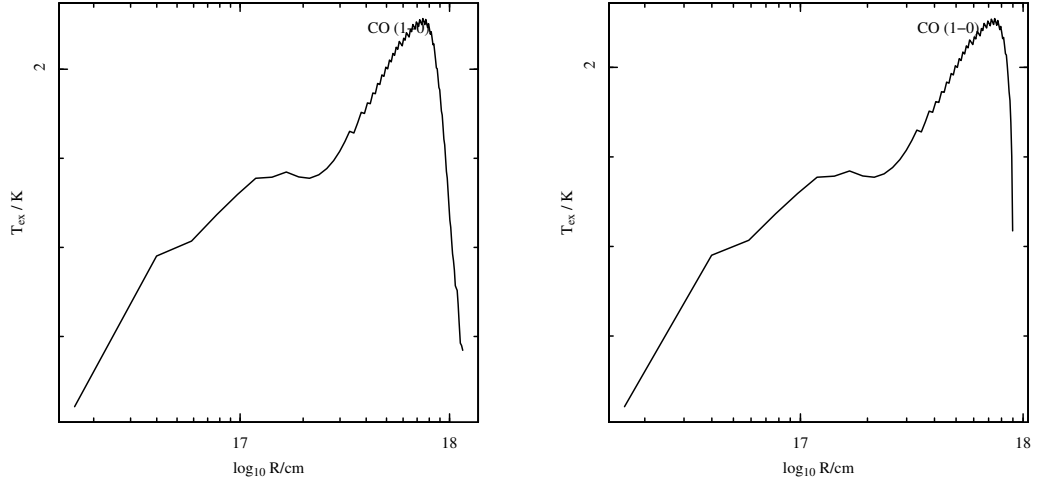


Figure 8.12. Excitation temperature for CO (1-0) for cloud model *graindist2*. Left hand plot includes the contribution from the entire cloud; right-hand plot excludes the contribution from the outer 25% of the cloud mass. The reduction in outer region of the cloud where the excitation temperature increases towards the cloud is responsible for the removal of the blueshifted emission peak in the CO (1-0) line profile.

blueshifted hemisphere, the CO (1-0) line profile is recalculated ignoring the contribution from the outer 25% of the cloud mass. The reasons for excluding the outer 25% of the cloud mass are as follows: the velocity profile shows strong oscillations in this region of the cloud; in this region, the infall velocity increases to the maximum infall velocity of 130 ms^{-1} at the cloud edge. Figure 8.11 shows the resulting CO (1-0) line profile to have a strongly dominant redshifted emission peak despite the cloud collapsing at all radii. The emission from the blueshifted hemisphere is highly irregular and indicates that strong self-absorption has reduced the blueshifted peak temperature from about 8 K to 5.5 K. Figure 8.12 shows the difference in the excitation temperature between the two models. By removing the outer 25% of the cloud mass, the section of the outer cloud where the excitation temperature is increasing towards the centre is reduced significantly; it is this region that is responsible for the blueshifted emission peak in the original, untruncated cloud model. This result has implications for the interpretation of CO line profiles, since although the line profile was derived by artificially excluding the outer 25% of the cloud, a velocity and density profile exists such that the normal interpretation of this line could be misleading: the normal interpretation of an optically thick line is to assume the dominant

redshifted peak indicates expansion (e.g. the dominant redshifted peak in the C^{13}O line observed in L1506C by Pagani et al. (2010a)), but in this case, the cloud is collapsing at all radii.

8.2.11 Dust continuum emission

Chapter 7 calculated the dust temperature and dust continuum emission for all core models. A similar analysis is performed here for the cloud models. The method of calculating the dust continuum emission is taken from chapter 7, but with a modification: the dust model assumes that the inner $7 M_{\odot}$ of the cloud is spherical while the outer envelope is modelled by assuming a constant background emission. The modification is used to better model structures such as the centrally condensed L1544 core embedded in a more diffuse cloud envelope. Assuming spherical symmetry over the entire cloud results in a flat emission profile at the position of the core boundary which is not matched by observations of the L1544 core. This approach also allows a better comparison with the emission profiles calculated from the core models.

The temperature profile and dust-continuum radial profiles for both cloud models are plotted in Figure 8.13. The radial intensity profiles are consistent with the results for the equivalent core models: the standard model is much flatter in the middle region compared to cloud model *graindist2*. The models are compared with the equivalent profile if a constant gas-dust ratio is assumed and also where a constant temperature is assumed. The figure shows that for the standard model, the strong depletion of grains at the core centre increases the temperature from 7.1 K to 8.6 K while the increase in dust-gas ratio with radial distance flattens the emission gradient out to a radial distance $R \simeq 3 \times 10^{17}$ cm. For model *graindist2*, there is little difference between the variable and constant dust-gas ratio models, therefore the central temperatures are nearly identical. There is little difference in emission profile when comparing the standard model with the dust model that uses a constant, $T = 10\text{K}$ temperature profile. For model *graindist2*, the emission profile is marginally steeper for a constant temperature profile. Table 8.6 summarises the resulting intensity profiles for emission of each model at $450\mu\text{m}$, $850\mu\text{m}$ and 1.3mm . The intensity profile is described by power laws of the form $I \propto R^{-m}$; the profile is split into an inner and middle region of the cloud with m_i and m_m denoting the power law indices for the two regions. The inner cloud is defined as the region within $R \leq 2 \times 10^{16}$ cm; the middle cloud is defined as the region between the end of the inner cloud and $R \leq 3 \times 10^{17}$ cm.

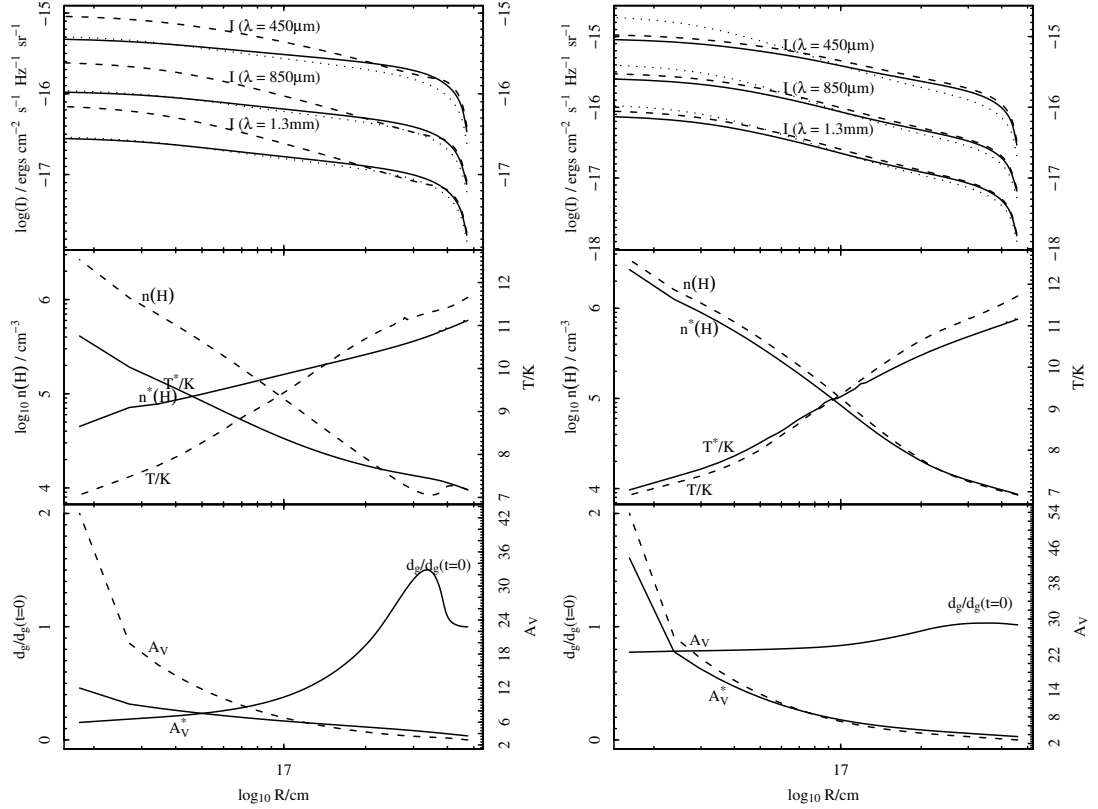


Figure 8.13. Temperature and dust continuum radial profiles for the standard (left-hand plot) and *graindist2* (right-hand plot) cloud models.

Upper graph plots the emission profiles for wavelengths $450 \mu\text{m}$, $850 \mu\text{m}$ and 1.3 mm . Solid lines show the model profile where the dust-gas ratio varies throughout the cloud; dashed lines show the profiles assuming a constant dust-gas ratio; dotted lines show the profiles assuming a constant temperature, $T = 10\text{K}$. Middle graph plots the density and temperature gradient in the cloud. Lower graph plots the variation in visual extinction and dust-gas ratio. Solid lines and descriptors marked with * show the model profile where the dust-gas ratio varies throughout the cloud. Dashed lines and unmarked descriptors show the profiles assuming a constant dust-gas ratio.

Table 8.6. Fits to the intensity profiles of the form $I \propto R^{-m}$ for the inner (m_i) and middle (m_m) regions of the core/cloud.

Model identifier	450 μ m m_i	m_m	850 μ m m_i	m_m	1.3mm m_i	m_m
standard core	0.15	0.31	0.17	0.38	0.19	0.40
standard cloud	0.02	0.37	0.02	0.36	0.02	0.37
graindist2 core	0.23	0.60	0.31	0.74	0.37	0.77
graindist2 cloud	0.04	0.93	0.04	0.91	0.04	0.92

The outer region is not analysed in this way since it is subject to strong edge effects so that a power law model is not a good fit to the data points. The power law indices for the core models are also included in order to aid the comparison between cloud and core models. The table shows that: the dust continuum emission in the inner region of the cloud is found to be shallower when compare with the core models; the dust continuum emission in the middle region of the cloud is found to be similar or steeper when compared with the core models.

8.3 Summary

A self-consistent model with respect to the chemistry, ionization and ambipolar diffusion has been used to model a collapsing cloud of mass $28 M_{\odot}$. The resulting dynamical timescales, dynamical and chemical radial profiles and radial dust continuum emission are compared with core models.

It is found that the collapse rate in the central shell of the cloud model is sensitive to the size of the shell: a central shell radius that exceeds the Jeans length results in an artificially increased infall velocity at the centre of the cloud. Using cloud models with shell sizes similar to the core model produces reasonably consistent dynamical and chemical results between cloud and core models. A notable difference in the velocity field is the tendency for large amplitude oscillations to exist at the cloud edge: this is attributed to the transition between collapse and expansion at the edge of the cloud. A compression wave moves out from the cloud centre and as the radial gradient in $n(\text{H})$ and B steepens at the head of the wave, a discontinuity or shock forms. The passage of the compression wave through the cloud triggers oscillations in the model. The oscillations themselves are the result of the inability of the finite difference algorithm to accurately model shock

conditions. However, the shock is a physical artefact of the model and appears in both low and high resolution cloud models.

For the standard cloud model, the co-existence of expansion in the outer cloud and collapse in the inner and middle cloud is found to be similar to that inferred from observations of CO emission in L1506C (Pagani et al. 2010a). Synthetic line profiles of HCO^+ , calculated for the standard cloud model, have a dominant blueshifted peak temperature, indicating collapse; for the CS (1-0) and (2-1) line profiles, the redshifted peak temperature dominates, indicating expansion. The co-existence of both dominant blueshifted and redshifted peak temperatures in line profiles, offers a strong diagnostic of this type of dynamical behaviour: the dominant redshifted peak temperature must be for an optically thick line that probes the less dense gas in the outer cloud; the dominant blueshifted peak temperature must be for an optically thick line that probes the dense gas in the inner cloud or core. Cloud or core rotation may impact the interpretation of such lines, but where observations are directed towards the centre of a core, since the direction of rotation should be perpendicular to the line of sight, the effect on the line profiles should be negligible (Pagani et al. 2010a).

For the *graindist2* cloud model, molecular depletion of HCO^+ is found to weaken the line profiles, especially for the HCO^+ (4-3) line. While the standard cloud model is consistent with the trend found for the standard core model, with dip velocities increasing with increasing rotational transition number, the HCO^+ (4-3) line profile for the *graindist2* cloud model shows only marginal self-absorption and a dip-velocity that is much less than dip velocities found for the lower rotational transition lines. In conclusion, using the dip velocity in the HCO^+ (4-3) line as a diagnostic tool to probe the velocity in the central region of the core must be treated with caution: only when the dip velocity increases over the lower transition lines and where the ratio of the blueshifted to redshifted peak temperatures are seen to increase over the lower transition lines, can the line be used to give a reasonable estimate of the infall velocity close to the core centre.

Synthetic line profiles of CO (1-0) are calculated for the standard and *graindist2* cloud models. For the standard cloud model, the CO (1-0) line profile has a dominant blueshifted peak, despite the expansion in the outer core. For model *graindist2*, the cloud is collapsing at all radii. In this case the CO (1-0) line profile shows a small self-absorption dip in the blueshifted hemisphere. The CO(1-0) line profile for cloud model *graindist2* is recalculated ignoring the contribution from the outer 25% of the cloud mass. The line profile shows a

dominant redshifted emission peak, despite the cloud collapsing at all radii.

The dust continuum emission in the inner region of the cloud is found to be shallower when compared with the core models; the dust continuum emission in the middle region of the cloud is found to be similar or steeper when compared with the core models.

In Chapter 6, Table 6.11 gave a summary of results from the observational tests performed on core models. Table 8.7 gives an equivalent analysis for the cloud models which also take into account the analysis of dust continuum intensity profiles. Entries for the related core models are also included in order to help determine whether cloud models are more consistent with observational data compared to core models. This table shows an improvement in the consistency with observational data for cloud model *graindist2* compared to core model *graindist2*. As noted already in Chapter 6, core model *graindist2* is at the lower end of the range of permissible values for the 1.3 mm dust continuum intensity profile in the middle core: $I \propto \theta^{-m}$ with $m = 1.0 \pm 0.3$ as the observed value and $m_{core} = 0.77$ as the model core value. On the other hand, cloud model *graindist2* is well within the range of permissible values: $m_{cloud} = 0.92$. It is also noted that cloud model *graindist2* is now marginally outside the upper limit for the ratio of infall to free-fall time (as opposed to the core model being well outside the upper limit), when a non-zero initial velocity is taken into account, at an initial density of $n(\text{H}) \simeq 2 \times 10^5 \text{ cm}^{-3}$: the ratio of infall to free-fall time is 3.16 while the upper limit is 3.

Table 8.7. Model summary – comparing cloud and core models against observational constraints.

Observational test	standard core	standard cloud	grandist2 core	grandist2 cloud
a) Ratio of infall to free-fall times at $n(\text{H}) \simeq 5 \times 10^4 \text{ cm}^{-3}$ (§6.1.1 and Table 8.4)	●	○	○	●
b) Ratio of infall to free-fall times at $n(\text{H}) \simeq 2 \times 10^5 \text{ cm}^{-3}$ (§6.1.1 and Table 8.5)	●	●	○	○
c) Subsonic infall speed (§6.2.1 and Table 8.1)	●	●	●	●
d) Radial profile in $n(\text{H})$: inner ●/middle ○ core (§6.2.2 and Table 8.2)	◐	◐	◐	◐
e) As d) but compared with class 0/I sources	●	●	●	●
f) A_V at centre compared with B68 (§6.2.4)	○	○	●	●
g) Chemical radial profiles (§6.2.5, §6.3.2 and §8.2.8)	○	○	●	●
h) Dust continuum intensity profile at 1.3 mm: inner ●/middle ○ core (§7.4 and Table 8.6)	◐	◐	●	●
i) Dust continuum intensity profile at 7 μm in the outer core (§7.4 and Table 8.6)	●	●	●	●

Filled circles ● indicate consistency with observations; unfilled circles ○ indicate inconsistency with observations.

Chapter 9

Discussion and conclusion

*There are more things in heaven and earth, Horatio,
Than are dreamt of in your philosophy.*

Hamlet, William Shakespeare

In this chapter a comparison is made between the overall results of the model with other models of pre-stellar and protostellar collapse. A section is included that discusses the limitations of the current model with suggestions for future improvements. The final section provides a summary of the main results and the conclusions.

9.1 Comparison with other collapse models

This is not the first multi-point model to use a consistent approach to calculating the ionization fraction and subsequently the retarding force on the neutral gas due to ambipolar diffusion in a collapsing pre-stellar core. However, this model is possibly the first self-consistent multi-point model to include the effects of a changing dust-to-gas ratio and to model the ionization fraction out to regions of low visual extinction ($A_V \lesssim 1$).

The model of Li et al. (2002) and Shematovich et al. (2003), hereafter LSWS, follows the chemistry at multiple points in a collapsing core and uses the ionization fraction to determine a coupling factor between neutral and charged particles. The chemistry is based on the chemical model of Shematovich et al. (1997, 1999): a network of 2000 reactions

between 59 neutral and 83 ion species is used. Accretion of species onto grains and desorption of species from grains has been taken into account; 53 grain surface reactions are included – these reactions are mainly through the addition of hydrogen. In common with model variation *grainchem1*, the authors assume that the products of dissociative recombination from reactions between ions and grains return to the gas phase. The initial starting conditions assume $n(\text{H}) = 2 \times 10^3 \text{ cm}^{-3}$ and a core mass of $M_{\text{core}} = 20 M_{\odot}$; a gas temperature of 10K is assumed throughout the collapse of the core. The dynamical results of this model indicate an infall velocity of between 200 ms^{-1} and 350 ms^{-1} at a final density of $n(\text{H}) = 2 \times 10^6 \text{ cm}^{-3}$, higher than the maximum infall velocity observed in L1544 ($\sim 100 \text{ ms}^{-1}$) by Tafalla et al. (1998) and higher than the infall velocity of the standard model ($\sim 108 \text{ ms}^{-1}$) at a final density of $n(\text{H}) = 4 \times 10^6 \text{ cm}^{-3}$. The reason for the higher infall velocity could be due to the higher core mass or possibly the different assumptions about the mass-to-magnetic flux ratio, M_{core}/ϕ : while $M_{\text{core}}/\phi \sim 1.77$ (in units of the critical mass-to-magnetic flux ratio) is chosen to be just supercritical in the standard model, LSWS uses a ratio of magnetic to thermal pressures of unity, consistent with observations of magnetic fields in molecular cores (Crutcher 1999). The implied $M_{\text{core}}/\phi \sim 2.0$ indicates that the core has a marginally weaker magnetic field relative to the core mass, which could result in a higher infall velocity. The standard cloud model (as studied in Chapter 8) shows a marginally higher infall velocity when compared to the standard core model, indicating that the difference in infall velocities is not due to the difference in mass, while the core models that are substantially supercritical (models *b1*, *b2* and *b3*) all show infall velocities that are much higher than the standard model, with maximum infall velocities between 275 ms^{-1} and 355 ms^{-1} that are closer to the maximum velocities found in the LSWS model. The conclusion drawn from this analysis, is that the LSWS model is behaving more like the substantially supercritical core models. Due to the use of a semi-analytic coupling factor between the flow of the neutral gas and the magnetic field, LSWS makes no distinction between the ion or neutral infall velocities, so it is not possible to compare predictions about the drift velocity. Chemically, LSWS predicts strong depletion of CO and CS at the core centre and to a lesser extent HCO^+ while NH_3 and N_2H^+ are hardly depleted at all. These results are similar to the Class B models defined in Chapter 6. In order that the model of LSWS can be compared with line profile observations, Pavlyuchenkov et al. (2003) simulated line profiles using the standard model of LSWS and varied the assumptions about the microturbulent velocity field and

the temperature distribution in the core. Using a constant microturbulent velocity of $V_T = 0.15 \text{ km s}^{-1}$ and a constant kinetic temperature of $T_k = 8.75 \text{ K}$, the authors find their standard model gives deep asymmetric line profiles for CS (2-1) and HCO^+ (3-2) with linewidths and adsorption dips much wider than the observed line profiles. Variations on the assumed V_T and T_k distributions do not improve the fit between the synthetic and observed line profiles. There is agreement with the standard model of this thesis in that the dip velocity is redshifted for both the CS (2-1) and HCO^+ (3-2) lines, although the dip velocity is much higher, $V_{dip} \sim 200 \text{ ms}^{-1}$, due to the increased infall velocity of the LSWS model. Pavlyuchenkov et al. (2003) conclude that in order to reproduce the line profiles, the velocity profile needs to be reduced by a factor of 4 to simulate the expected apparent infall velocity when the core is tilted by 75° from an edge-on perspective; an adjustment to the abundance of HCO^+ is also required, no change to $n(\text{HCO}^+)$ at the core centre but decreasing by a factor that rises linearly to 30 at the core edge.

The model of Ciolek & Basu (2000) used input parameters specifically for L1544 in order to reproduce the infall velocity of L1544. The authors assume the core axis of symmetry in cylindrical coordinates is inclined at an angle of 16° to the plane of the sky, reducing the observed infall velocity by $\cos(16^\circ) = 0.96$. At a radial distance of 0.14 pc ($R = 4.2 \times 10^{17} \text{ cm}$) the neutral infall velocity is 110 ms^{-1} while the ion infall velocity is 70 ms^{-1} ; at a radial distance of 0.02 pc ($R = 6 \times 10^{16} \text{ cm}$), the neutral infall velocity is 140 ms^{-1} while the ion infall velocity is 110 ms^{-1} . The neutral and ion infall velocities at $R = 6 \times 10^{16} \text{ cm}$ are higher than the maximum neutral and ion infall velocities of the standard model (108 ms^{-1} and 84 ms^{-1} respectively) but the maximum drift velocity (40 ms^{-1}) is in reasonable agreement with that for the standard model (32 ms^{-1}). However, the infall velocities at $R = 4.2 \times 10^{17} \text{ cm}$ are significantly higher than those for the standard model ($\sim 0 \text{ ms}^{-1}$).

The model of Aikawa et al. (2001), hereafter A01, used a Larson-Penston collapse model (Larson 1969; Penston 1969) coupled with a chemical model applied to multiple shells to investigate the radial chemical profile in L1544. A01 assumes an initial density of $n(\text{H}) = 2 \times 10^4 \text{ cm}^{-3}$ and a final central density of $n(\text{H}) = 3 \times 10^6 \text{ cm}^{-3}$ that is constant inside a radial distance of 3000 AU ($R = 4.5 \times 10^{16} \text{ cm}$); beyond the central core the density falls off as $n(\text{H}) \propto R^{-2}$. The gas-phase chemical model is taken from Aikawa & Herbst (1999) and Terzieva & Herbst (1998). Freeze-out and desorption of molecules from grains is taken into account; the probability of molecules sticking to the

surface when they collide with grains is assumed to be $S = 1.0$. The recombination of ions and electrons are assumed to occur on the surface of grains. The rate of desorption of molecules from grains is sensitively dependent on the adsorption energies adopted by the model: this is a much more sophisticated approach to the freeze-out rates than is assumed by the standard model in which most molecular species are assumed to freeze-out above a critical visual extinction with no return to the gas phase. A01 tests the chemical evolution for an unmodified Larson-Penston collapse and for a series of modified models where the infall velocity is lowered by dividing the infall velocity by a factor $3 \leq f \leq 10$ in order to investigate the effects of a retarding force due to a magnetic field, rotation or turbulence. The model predicts a centrally peaked abundance of N_2H^+ , consistent with observations of L1544 and with the standard model. Comparing the predicted model abundances of CO and CCS with observational data, the authors conclude that a modified Larson-Penston collapse with $f = 1$ (i.e. an unmodified Larson-Penston collapse) is most successful at reproducing the CO and CCS abundance *holes* observed within a radius of 6000 - 8000 AU from the core centre ($0.9 \times 10^{17} \text{ cm} \leq R \leq 1.2 \times 10^{17} \text{ cm}$). This compares with an abundance of CO that is centrally peaked as predicted by the standard model while for class B models the CO abundance peak is co-located at the position of peak dust-gas ratio, $R \sim 3 \times 10^{17} \text{ cm}$. However, model *avcrit1* shows that the radial distance of the CO abundance peak is sensitive to the assumed critical visual extinction; in the case of model *avcrit1*, this has been increased to $8 \leq A_{Vcrit} \leq 12$. The change in A_{Vcrit} can be thought of as modelling (in a simplified manner) an increased rate of desorption over freeze-out; thus it should be possible to reproduce the observed abundance hole in CO by changing the value of A_{Vcrit} or by using of a more sophisticated approach to modelling the desorption of individual molecular species. Dynamically, A01 note that the Larson-Penston collapse model predicts an infall velocity ($\sim 500 \text{ ms}^{-1}$) in the outer core that is much higher than that observed (Tafalla et al. 1998), although this problem can be mitigated if an outer boundary condition fixing the infall velocity to 0 ms^{-1} is used in simulated collapse models; the infall velocity also decreases towards the core centre in contrast to all models of pre-stellar collapse presented here.

The line profiles of CS and HCO^+ resulting from a Shu inside-out collapse model (Shu 1977) have been compared with a chemical model that uses the dynamical output from a version of the ambipolar diffusion code created as part of this thesis (Roberts et al. 2010). Although the code was initially developed to model the pre-stellar phase of core collapse,

this paper follows the evolution of the core to a central density comparable to protostellar cores, $n(\text{H}) \sim 2 \times 10^7 \text{ cm}^{-3}$. An important feature in this study, is that both models use the same chemical model, although the core masses and initial densities are different. This study finds the Shu inside-out collapse model has difficulty in reproducing the strong asymmetric line profiles associated with infall when molecules are depleted at the core centre. In contrast, the ambipolar diffusion model, due to the extended non-zero infall velocity profile, has strong asymmetric line profiles even when molecules are depleted at the core centre. In order for the Shu collapse model to exhibit strong asymmetric line profiles, freeze-out needs to be suppressed and a kinetic temperature gradient is required: the kinetic temperature increases towards the core centre. The authors argue that this is a major inconsistency for the Shu model since CS depletion has been detected in several dense cores (Bergin et al. 2001; Pagani et al. 2005) while strong blueshifted asymmetric line profiles are observed in many class-0 protostars (Mardones et al. 1997). The Shu collapse model was also used by Evans et al. (2005) to model the HCO^+ line profiles in the Bok globule, B335. The study finds that although the antenna temperature and relative strength between the blueshifted and redshifted peaks of the HCO^+ line profiles are a good fit to observations, the Shu model cannot reproduce the increasing shift in dip-velocity with increasing line transition number. However, this feature is in qualitative agreement with the HCO^+ line profiles generated using the standard model, due to the extended inward motions.

The chemical-dynamical model of Tassis et al. (2012), hereafter T12, is based on the MHD dynamical model of Basu & Mouschovias (1994) which follows the collapse of pre-stellar cores that condense out from self-gravitating, magnetic, rotating clouds. Core temperatures are assumed to be isothermal. Both ambipolar diffusion and magnetic breaking are taken into account in the model. An axially symmetric thin disk approximation is used to model the cloud morphology. Added to the MHD equations governing the core collapse are separate continuity equations for neutral and charged particles: charged particles also include all grains which are assumed to have a single negative charge. The continuity equations include source and sink terms in order to model the change in number density of particles due to chemical reactions. The model of Mathis et al. (1977) is used to model the size distribution of grains. Freeze-out of atoms and molecules follows R92; the probability of molecules and atoms sticking to the surface of grains is assumed to be $S = 0.3$. A total of 33 grain mantle and 78 gas phase atomic or molecular species are included in the

chemical model; the chemical network comprises 1553 reactions. Gas phase reaction rates are taken from Woodall et al. (2007). Desorption of grain mantle species back into the gas phase is included; grain surface reactions and binding energies of molecules to grain surfaces are taken from Hasegawa & Herbst (1993). A major difference affecting the rate of freeze-out of molecules between T12 and the standard model, is the assumption about the dust-gas ratio: T12 assumes the dust-gas ratio to be constant over the core (despite allowing all negatively charged grains to move with the ions) while the standard model allows the dust-gas ratio to vary over the core. For some models (such as the standard model) where the dust is strongly coupled to the magnetic field, ambipolar diffusion will result in grains being depleted at the core centre with the consequence that freeze-out rates are reduced and the cores appear chemically *young*. The initial number density of hydrogen atoms is $n(H) \sim 2 \times 10^3 \text{ cm}^{-3}$ – marginally lower than for the standard model $n(H) = 2.8 \times 10^3 \text{ cm}^{-3}$. The time it takes for the T12 reference model to collapse to a central number density $n(H) \sim 2 \times 10^6 \text{ cm}^{-3}$ is around 4.6 Myr, significantly longer than the 1.35 Myr required for standard model to collapse from a central number density of $n_c(H) = 4.9 \times 10^3 \text{ cm}^{-3}$ (the number density at the start of the second collapse phase) to a central density of $n_c(H) = 4.3 \times 10^6 \text{ cm}^{-3}$. On the other hand, there is reasonably good agreement between the upper limits on neutral infall speeds between the models: all T12 magnetic models have infall speeds that are subsonic while all but one of the marginally magnetically supercritical models have subsonic infall speeds. The maximum infall speed of the T12 reference model is $0.8C_s = 150 \text{ ms}^{-1}$ where $C_s = 188 \text{ ms}^{-1}$ is the sound speed at a gas temperature of 10 K. This compares to a maximum subsonic infall speed for all marginally magnetically supercritical cores of 120 ms^{-1} . No published values for the drift velocity are available with which to make comparisons. Chemically, there is strong depletion for both carbon and nitrogen bearing molecular species: at a central density of $n(H) \sim 2 \times 10^6 \text{ cm}^{-3}$, the T12 reference model gives $X(\text{CO}) \sim 10^{-10}$ and $X(\text{NH}_3) \sim 5 \times 10^{-11}$. This level of depletion is only matched by the class B models: the class of models showing strong depletion compared to the standard model, as defined in Chapter 6. Despite the much longer collapse times of the T12 models, all class B models have stronger CO and NH₃ depletion. A difference in the assumed grain size distribution may in part account for the apparent increased rates of freeze-out in the class B models. The model of Weingartner & Draine (2001) is used for the grain distribution which includes a much higher percentage of grains with smaller radii; the calculated freeze-out

rates for charged particles is found to be approximately 7 times as fast as that used in R92 (section 3.3).

9.2 Model limitations and future direction

9.2.1 Testing updated chemical reaction rate data files

The chemical model uses a version of the UMIST Database for Astrochemistry (Millar et al. 1997) that has been the subject of three major revisions. The last two revisions are studied in order to assess their impact on this model. The revision of Woodall et al. (2007), hereafter RATE06, results in approximately 200 reaction rates that have either changed or been dropped from the network of reactions that define the chemistry in this model. The revision of McElroy et al. (2013), hereafter RATE12, results in a further 530 reaction rates that have either changed or been dropped since the RATE06 revision. Recently, the chemical reaction rate file has been modified to reflect the updates from both RATE06 and RATE12 and the standard core model has been re-run in order to test the impact the new chemistry has on the chemical and dynamical radial profiles. When the model is run using the RATE06 updates, the new chemistry is found to have minimal impact on the dynamics of the core, while the chemical radial profile shows that N_2H^+ is marginally more abundant at the centre while abundances of other species show little or no difference over the old chemistry. The magnetic flux density, $B_{\text{core}} = 6.1 \mu\text{G}$, at which the core is found to be just magnetically subcritical, is identical to that found using the old chemistry. Figure 9.1 shows the results of running the standard core model, using the RATE12 updates, at the end of the collapse phase, when the central density is $n(\text{H}) = 4.3 \times 10^6 \text{ cm}^{-3}$. This figure can be compared with Figure 4.3 in order to test the impact the RATE12 chemistry has on the chemical and dynamical radial profiles. For this run of the model, the initial magnetic flux density is increased by 2.5 per cent in order for the core to remain in a state of marginal magnetic supercriticality. The resulting dynamical profile shows a small shift in the drift velocity profile but otherwise remains remarkably similar to the plot using the old chemistry. It is the ionization fraction which determines the strength of interaction between charged and neutral species and therefore strongly affects the dynamics of the collapsing core. The nearly identical dynamical profiles implies that the ionization structure within the core does not change significantly when using the RATE12 updates. This conclusion is born out by the plot of the radial change in

ionization fraction, which, along with the other chemical radial profiles, shows little change over the old chemistry. The conclusion from this analysis is that the new chemistry does not strongly affect the overall results of this thesis and the differences are certainly less significant than the differences found when running the model variations in Chapter 6.

9.2.2 Desorption processes

The model does not directly include the effects of desorption of molecules from grains. Indirectly, a crude model of desorption is used that assumes that freeze-out does not occur below a critical visual extinction: the critical visual extinction can be thought of as the point where the rates of desorption and freeze-out are equal. A more sophisticated approach, as used by several authors (Willacy et al. 1994; Aikawa & Herbst 1999; Roberts et al. 2007), is to model desorption by taking into account the binding energy between molecules and grains; the binding energies are specific to individual molecular species. A natural extension to the model is to follow the pre-stellar collapse phase into the proto-stellar phase. This will require that the chemical model is able to respond to increases in temperature at the core centre; modelling desorption correctly then becomes critical to understanding the release of molecules back into the gas phase, and the subsequent slowing-down or reversal of the rate of increase in average grain size, as the temperature rises. Recent observations from the Herschel Space Observatory (Caselli et al. 2012) detected water vapour in the densest, central few thousand AU of L1544. The authors argue that the high abundance of water vapour is due to the desorption process whereby cosmic rays excite electronic states of H_2 , the decays from the excited electronic states of H_2 produce a FUV flux that irradiate icy mantles, releasing water back into the gas phase. This result would indicate that in this case, even without a temperature increase, desorption plays a significant role in the chemical evolution at the core centre.

9.2.3 Modelling the effects of grain growth during core collapse

The model assumes the grain population remains constant during core collapse; this assumption is unlikely to be correct over the several million years that the models run for. It is likely that significant grain growth will occur in the densest region of the core, resulting in fewer but larger grains. A survey of 110 cores by Pagani et al. (2010b) shows that about half the cores, including L1544, reflected scattered light in the mid-infrared – an observational phenomenon known as *coreshine*. For those cores where coreshine is

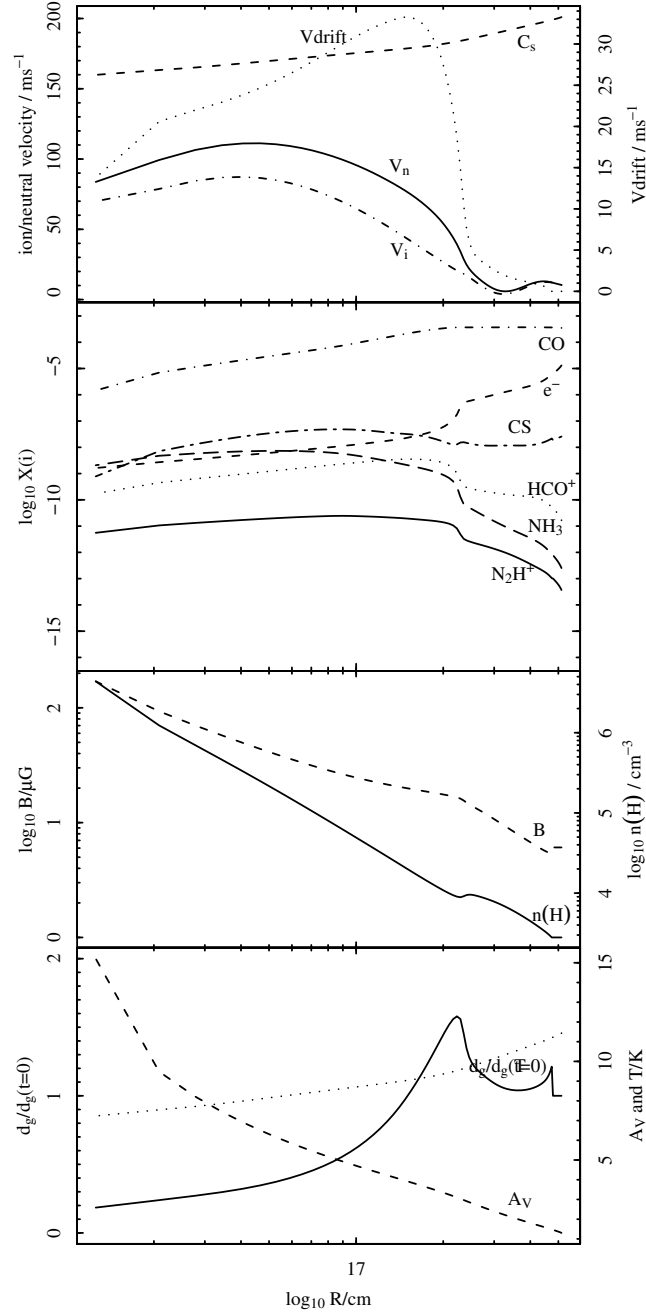


Figure 9.1. Chemical and dynamical radial profile at $t = 3.67$ Myr using the RATE12 version of the UMIST Database for Astrochemistry (McElroy et al. 2013).

observable, dust absorbs the external radiation field at $8\ \mu\text{m}$ and scatters the external radiation field at $3.6\ \mu\text{m}$; the region of absorption and flux of scattered light is spatially correlated with the central, dense region of the cores. The inference from these observations is that large grains with size $\sim 1\ \mu\text{m}$ must be responsible for the mid-infrared scattered light. A significant population of large grains will affect the overall grain size distribution and therefore the freeze-out rates as determined in section 3.3. As previously mentioned in section 7.1, grain agglomeration is expected to impact the grain opacity so that calculated dust continuum emission profiles will change. Additionally, if the average grain size exceeds a critical value, charged grains will no longer be strongly coupled to the magnetic field. This could eventually lead to a bimodal distribution of grains: large grains retained by the densest region of the core while the small, charged grains are pushed to the outer region due to ambipolar diffusion. Alternatively, the opposite effect could be true: small grains are without charge and so are retained by the inner core; as grains grow above a threshold radius, the mean charge becomes $-e$. As long as the grain growth rate is not too rapid, grains will be subject to ambipolar diffusion and can drift outwards relative to the neutral gas, leaving behind a population of small grains with no charge. By combining a model of grain growth with the ambipolar diffusion model, these effects could be investigated.

9.2.4 Modelling the effects of a changing ion-neutral collision cross-section

With respect to the calculation of the ion-neutral drag, the model assumes that a constant ion mass and collision cross-section (for $\text{HCO}^+ - \text{H}_2$) applies throughout the collapse. This assumption is approximately correct for most models, with Na^+ or HCO^+ typically being the dominant ion in the core centre during the later stages of collapse. However, for the low metal model *zna1*, H_3^+ is left as the dominant ion. At the core centre, H_2^+ is formed from the ionization of H_2 by cosmic rays; H_3^+ rapidly forms according to the ion-molecule reaction (Hartquist et al. 1993):



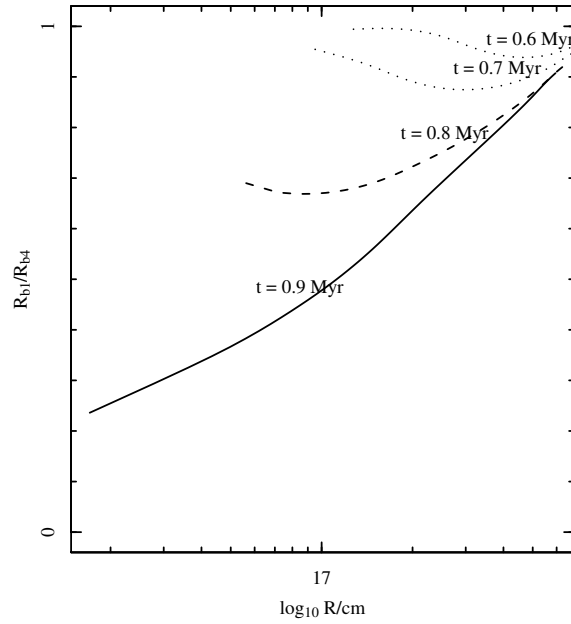


Figure 9.2. Ratio of shell radii between models *b1* and *b4*.

Proton transfer reactions such as:



remove H_3^+ . During the later stages of collapse, freeze-out decreases the abundance of the neutral reactant, leaving a relatively high abundance of H_3^+ . The ion-neutral drag is therefore likely to change significantly from its initial value. An improvement to this model would require the calculation of a mean ion mass and collision cross-section that is consistent with the chemical model.

9.2.5 Modelling the collapse of non-spherical cores

Perhaps the most significant limitation on the model is the assumption of spherical symmetry. The reasons for choosing a spherically symmetric geometry are twofold: the dynamical model is simplified to a 1-dimensional problem; existing, reliable 1-dimensional radiative transfer code (Rawlings & Yates 2001) can be used to generate the line profiles. However, pre-stellar cores are, in general, not spherically symmetric (Jones et al. 2001; Kauffmann

et al. 2008). A future enhancement to the model is to investigate the chemistry and core collapse using a 2-dimensional dynamical model. A relatively simple case might be to test a 2-dimensional version of the code that assumes: collapse perpendicular to the magnetic field is strongly affected by ambipolar diffusion; collapse parallel to the magnetic field is weakly affected or not affected at all by ambipolar diffusion. Insight into the structures that might be expected by such a model can be gained by comparing the radii of shells between models *b1* (a weak magnetic field) and *b4* (a strong magnetic field). Figure 9.2 plots the ratio of the shell radii between models *b1* and *b4* at 4 snapshots in time. The figure shows that up to 0.8 Myr into the collapse, the ratio of the shell radii is higher than about 0.7, indicating that up to this point, the assumption of spherical symmetry is quite good. Only at 0.9 Myr does the figure show a dramatic decrease in the ratio of shell radii, particularly in the inner core. This figure suggests that the core flattens preferentially in the centre while the outer core is barely flattened at all. With the availability of code that performs radiative transfer calculations in 2 and 3 dimensions (Hogerheijde & van der Tak 2000; Brinch & Hogerheijde 2010), the output of the 2-dimensional model could then be used to generate line profiles at varying observation angles.

9.2.6 The unexplained CO line profile in L1544

The model cannot explain the single-peaked line profile of CO (1-0) observed in L1544 by Tafalla et al. (1998). The right-hand plot in Figure 8.10 shows the CO (1-0) line profiles for cloud model *graindist2* at time $t = 6.5$ Myr. Clearly the double-peaked CO (1-0) line in the cloud model is inconsistent with the single-peaked line observed in L1544 by Tafalla et al. (1998). The difference could be due to a number of factors: the viewing angle of a flattened core may be important when modelling line profiles that are dominated by gas at the core edge; alternatively, the assumption of a constant turbulent velocity component may be incorrect. Tafalla et al. (1998) suggest that a three-component velocity field in the core is required in order to reproduce the central, single-peak: a constant infall velocity of 0.01 kms^{-1} applies throughout the core; a broad turbulent field, $\text{FWHM} = 0.25 \text{ kms}^{-1}$, plus thermal width applies to the inner one-third of the core; a narrow turbulent field, $\text{FWHM} = 0.125 \text{ kms}^{-1}$, plus thermal width applies to the outer two-thirds of the core. Using these assumptions, their model is able to recreate a single-peaked line profile. However, recent observations of L1544 (Caselli et al. 2010) indicate that there are two emission peaks in the CO (1-0) line profile: a broad peak with antenna temperature $T_{mb} = 12 \text{ K}$ is centred

on the core velocity, 7.2 km s^{-1} ; a narrow peak with antenna temperature $T_{mb} = 8 \text{ K}$ is at 9.3 km s^{-1} . Such a large difference in velocity is hard to explain using the model proposed by Tafalla et al. (1998). Core rotation could be a factor: Tafalla et al. (1998) found a velocity gradient of about 1 km s^{-1} over the L1544 cloud – this is still too small to account for the 2 km s^{-1} velocity difference between the two peaks.

9.2.7 Changing the initial conditions prior to the onset of gravitational collapse

In Chapters 6 and 8, it was found that no single model could satisfy the observational constraints of having heavily depleted molecular species at the core centre while at the same time, having collapse times that are fast enough to satisfy estimates of the lifetimes of pre-stellar cores based on statistical counts of populations of pre-stellar and protostellar cores. One change to the model that could potentially solve this problem is to allow freeze-out of molecular species prior to the start of gravitational collapse. In the standard model, freeze-out occurs above a critical visual extinction, $A_{Vcrit} = 3$: since the initial density distribution is constant throughout the core, and the initial A_V at the core centre is less than A_{Vcrit} , freeze-out at the core centre only starts after $t \sim 0.6 \text{ Myr}$ – the time at which $A_V \sim A_{Vcrit}$. If the initial density distribution is changed to the configuration of an unstable Bonner-Ebbert sphere and prevented from collapse during a *delay* period, this configuration might better reflect the conditions prior to collapse whereby a core gradually loses its turbulent support against gravitational collapse. The delay period reflects the time it takes for turbulence to decay to levels where gravitational collapse can begin. Since A_V at the core centre is expected to be greater than A_{Vcrit} (see Figure 1.9 showing the plot of A_V in B68), then freeze-out of molecular species will occur prior to the main phase of gravitational collapse. This extra gas-phase depletion time may be enough to allow model cores with sufficiently depleted molecular species while at the same time, allowing cores to collapse at a rate consistent with observations.

9.3 Conclusion

This thesis has attempted to bridge a gap between models of collapsing pre-stellar cores that: a) use an analytical model of collapse and a complex chemical model; b) use an analytical model of the ionization fraction and a simulated model of dynamical collapse.

Here, a self-consistent model with respect to the chemistry, ionization and ambipolar diffusion is used to follow the collapse of a pre-stellar core. The resulting dynamical and chemical radial profiles are used to derive line profiles for molecular species that are typically used to trace the gas distribution in pre-stellar cores. A distinctive feature of this model is a velocity profile that may include both infall and outflow velocities at the same time, with the implication that spectral line observations of gas having both blueshifted and redshifted asymmetric line profiles, would be an important observational difference between this model and other models that result in infall only. Indeed, line profiles calculated in Chapter 8 for the standard cloud model, confirm the possibility of observing both dominant blueshifted HCO^+ asymmetric line profiles and dominant redshifted asymmetric CS line profiles. Spectral observations of a gravitationally unbound core, L1506C, suggests that cores exhibiting this type of dynamical behaviour do exist: Pagani et al. (2010a) shows, through lines of C^{17}O and C^{18}O , an infall velocity of about 100 ms^{-1} at the core edge while observations of ^{13}CO show the extended envelope to be expanding at about 90 ms^{-1} .

A key assumption about the boundary conditions in the collapsing core, is the condition of zero drift velocity between neutral and charged gas. By following the chemistry and ionization fraction out to regions of low visual extinction, the results in Chapter 4 confirm the validity of this assumption, due to small drift velocities in the outer region of the core in both expanding and collapsing core models.

Chapter 4 also shows that for the standard model, the spectral signature for HCO^+ is that of an asymmetric line profile with a dip velocity that is offset from the local standard of rest velocity: in collapse the blueshifted peak dominates and the dip velocity increases with increasing rotational transition number. This feature is observed in the protostellar core B335 and a similar feature is found for CS in the protostellar core IRAM 04191. This does not in itself present evidence for ambipolar diffusion but presents evidence for a class of model that predicts a broad, non-zero velocity field with an infall velocity increasing towards the centre. It is found that the dip velocity in the HCO^+ (4-3) line profile of the standard model gives an estimate of the infall velocity outside the inner core, and this is also likely to apply to protostellar cores such as B335. However in Chapter 8, the diagnostic power of the line is shown to be weakened when the HCO^+ abundance has been significantly reduced due to freeze-out of molecular species.

In Chapter 5, it was shown that when observations are taken at the core centre, the

linewidth difference between spectra of ions and neutrals is not representative of the maximum ion-neutral drift velocity. When observations are targeted at off-centre positions, linewidth differences are more accurate at deriving the true ion-neutral drift in the core. The conclusion drawn from this chapter is: where careful observations are made of suitable pairs of ions and neutrals, and expanding cores are excluded from the sample, linewidth differences can be used to deduce the velocity difference between ions and neutrals.

In Chapter 6, several variations on the standard model are run in order to test the sensitivity of the dynamical and chemical characteristics of the core when model parameters are changed. Given the intentionally wide parameter space with which to test the model, it is somewhat unsurprising that a wide variation in collapse timescales, density distribution and abundance fractions of molecular species are found. However, the critical magnetic flux density at which the models are found to be marginally magnetically supercritical, is found not to change significantly for different model variations. Molecular depletion is found to be extremely sensitive to the choice of model parameters, and this is reflected in the choice of classification system used. Models are classified according to whether the degree of molecular depletion at the core centre is: similar to the standard model (class A); stronger than the standard model (class B); weaker than the standard model (class C). Strong depletion of molecular species due to freeze-out affects the radial profile of integrated flux density. For an example of a class B model (model *stick1*), it is shown that the radial profile of the integrated flux density for C¹⁸O (1-0) emission has a minimum at the core centre, in contrast to class A and C models having maxima at the core centre. For calculations of synthetic HCO⁺ and CS line profiles for artificial beams directed at the centre of model cores, it is found that depletion affects the position of the dip velocity: class B models show a decrease in the dip velocity relative to the standard model due to emission and absorption being dominated by slower-moving gas in the middle and outer regions of the core. At least one class C model (model *b4*) is found to have both blueshifted and redshifted asymmetric CS (1-0) line profiles in the inner/middle and outer regions of the core respectively. This change in dominance between the blueshifted and redshifted peak in the CS line profile is due to the coexistence of expansion in the outer core and collapse in the inner and middle regions of the core.

Despite the wide range of parameter values investigated by the different model variations, it is still possible to put constraints on the parameter set and identify the most successful models by comparing model results to observational data:

1. Dynamically, it is found that models having a weak magnetic field (models *b1*, *b2* and *b3*) result in supersonic infall speeds: this is inconsistent with linewidth observations of pre-stellar cores, indicating that infall speeds are in general subsonic during the pre-stellar phase. Model *grainchem1* stands out as being atypical for the marginally magnetically supercritical cores in that its infall speed is also supersonic; a likely reason for this is the flattened magnetic field distribution in the core centre resulting in weaker magnetic pressure.
2. For all models, the ratio of the collapse time to free-fall time is calculated and compared with ratios derived from estimated densities and lifetimes of pre-stellar cores: model *b4* (a supercritical core) is the closest fit to observations while about half the marginally magnetically supercritical cores have collapse timescales that are too long when compared to collapse timescales inferred from observations.
3. Chemically, it is found that models having strong freeze-out at the core centre are better at modelling the radial change in integrated flux density of molecular line profiles. Models falling into this category are: *grainchem1*, *graindist2*, *stick1* and *zeta1*. Models *grainchem1* and *zeta1* give rise to models with high ionization levels at the core centre. Since there is a higher probability of ions sticking to grains when compared to neutrals, these models result in a faster overall freeze-out rate when compared with models where the ionization level is low. Model *stick1* uses a sticking probability of 1.0 for collisions between neutrals and grains, resulting in a faster overall freeze-out rate. Model *graindist2* assumes that 75% of grains have no charge and therefore do not move with the magnetic field; this means a higher dust-gas ratio at the core centre, resulting in a faster freeze-out rate when compared to the standard model.
4. A specific feature of this model is the distribution of dust: as a result of ambipolar diffusion, the dust distribution does not exactly follow the gas distribution. Typically, the dust-gas ratio peaks at a visual extinction $A_V \sim 3 - 4$: this is the visual extinction above which molecules freeze-out onto grains. In Chapter 7, the distribution of dust is compared with observational data by first calculating the temperature in the core and then calculating the radial distribution in dust continuum emission at three wavelengths: 450 μm , 850 μm , and 1.3 mm. Subsequently, the radial distribution in the 1.3mm emission profile is compared with observations. For all models,

the emission gradient in the inner core is found to be consistent with observations. However, for most models the emission gradient in the middle core is found to be too weak to match observations. For models that have a dust-gas ratio that does not vary significantly over the core, the emission gradient is consistent with observations. Specifically, models *b1*, *b2* and *graindist2* are consistent with 1.3mm dust continuum emission of the pre-stellar core L1689B.

In Chapter 8, the model is used to follow the collapse of a core and extended envelope (cloud), starting from a lower initial density. The results show that cloud and core models are reasonably consistent with respect to predictions of chemical and dynamical properties. However, the following differences are found:

1. Cloud models tend to have marginally higher infall speeds. However, infall speeds still remain subsonic. For cloud model *graindist2*, the higher infall speed provides a better fit (when compared to core model *graindist2*) with estimates of the lifetime of pre-stellar cores,
2. With regard to the radial change in dust continuum emission, cloud models have a flatter profile in the inner region and either a similar or steeper profile in the middle region when compared to core models. For cloud model *graindist2*, the steepening of emission gradient in the middle region provides a better fit (when compared to core model *graindist2*) to observations of the the intensity profile at 1.3 mm.
3. Strong oscillations in the velocity field are found at the edge of the cloud; these oscillations are not found in the core models. It is suggested that core oscillations may be due to the change from inflow to outflow in the outer region of the cloud. The passage of a compression wave through the cloud triggers oscillations in the low density, outer region of the cloud: as the radial gradient in $n(\text{H})$ and B steepens at the head of the wave, a discontinuity or shock forms; the onset of oscillations is the result of the inability of the finite difference algorithm to accurately model shock conditions.

Appendix A

Finite difference method for the solution of ambipolar diffusion equations

The multi-point model follows the collapse of a set of N concentric shells or elements centred around $r = 0$ - the centre of the collapsing cloud (see Figure A.1). A constant gas density and magnetic flux density region is defined for the outermost M shells, $s \in \{N - M + 1..N\} : \rho_s(t) = \rho_s = \text{constant}; B_s(t) = B_s = \text{constant}$. The boundary points $s \in \{1, N - M\}$ have special computations applied to them to achieve better accuracy. The special computations take the form of fitting the radial variations in density and magnetic flux density using 3rd order splines and using the spline coefficients to calculate attributes ρ , $\frac{1}{\rho} \frac{d\rho}{dr}$ and $\frac{dB^2}{dr}$. These computations have not been applied to the remaining shells since in general they are more unstable when attempting to model conditions where rapid changes in density can occur.

Each element in the grid has the following attributes:

1. Each shell s has mass m_s interior to radius $r_s(t)$; m_s is fixed throughout the collapse with $m_0 = 0$ and $m_N = M_{\text{core}}$ - the total mass of the core at outer shell N . The temperature at each shell is denoted by T_s - the sound speed at each shell is denoted by $C_s = (kT_s/\mu m_H)^{0.5}$. The magnetic flux density at each shell is denoted by B_s .

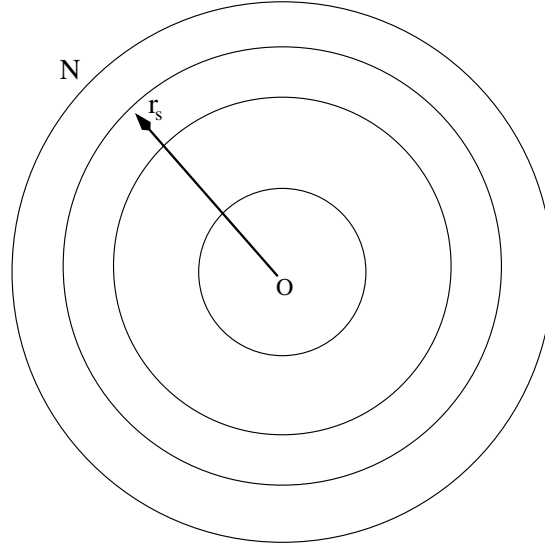


Figure A.1. Grid layout for solution by the finite difference method

The mean collision time between a neutral particle and a charged particle at each shell is denoted by τ_s . Each shell s is enclosed between radial distances r_s and r_{s-1} .

2. For $s > 1$ the mass density at the midpoint of each shell is given by:

$$\overline{\rho}_s = \frac{3(m_s - m_{s-1})}{4\pi(r_s^3 - r_{s-1}^3)} \quad (\text{A.1})$$

3. For $1 < s < N$ the mass density at r_s - the boundary of shell s is given by linear interpolation between the midpoint values of enclosing shells:

$$\rho_s(t) = \overline{\rho}_s + (r_s - r_{s-1}) \left(\frac{\overline{\rho}_{s+1} - \overline{\rho}_s}{r_{s+1} - r_{s-1}} \right) \quad (\text{A.2})$$

4. For $1 < s < N - M - 1$ the neutral gas pressure gradient term $\frac{1}{\rho} \frac{dP}{dr}$ at r_s - is given by the difference between the midpoint pressures of enclosing shells divided by the distance between the midpoints:

$$\frac{1}{\rho_s} \frac{dP}{dr}_s = \frac{2}{\rho_s} \left(\frac{\overline{\rho}_{s+1} C_{s+1}^2 - \overline{\rho}_s C_s^2}{r_{s+1} - r_{s-1}} \right) \quad (\text{A.3})$$

5. The magnetic pressure component $\frac{dB^2}{dr}$ for $1 < s < N - M - 1$ is given by

$$\frac{dB^2}{dr}_s = 2 \left(\frac{B_{s+1}^2 - B_s^2}{r_{s+1} - r_{s-1}} \right) \quad (\text{A.4})$$

The numerical solution proceeds as follows; note that in the following section the notation (t) refers to variables at time t while $(t + \Delta t)$ refers to variables after a time-step Δt .

1. First calculate the 3rd order spline coefficients for $s \in \{-N - 1, \dots, N + 1\}$ for both $\rho_s(t)$ and $B_s^2(t)$ - these coefficients will be used to calculate values at $s \in \{1, N - M\}$.

For $s \in \{1..N\}$ do

2. Start with the radius of the boundaries of the charged and neutral particles being equal ($r_{is}(t) = r_s(t)$). Divide equation (2.8) by ρ_n to obtain an expression for the acceleration of the neutral gas, $\frac{dv_s}{dt}$. Assuming $\frac{dv_s}{dt}$ is constant over a small integration time-step, calculate the velocity of neutral particles at shell s , $v_s(t + \Delta t)$, after integration time-step Δt according to:

$$v_s(t + \Delta t) = v_s(t) + \frac{dv_s}{dt} \Delta t \quad (\text{A.5})$$

3. The change in radial position of neutral particles is given by:

$$r_s(t + \Delta t) = r_s(t) + \frac{\Delta t}{2} (v_s(t) + v_s(t + \Delta t)) \quad (\text{A.6})$$

4. Use equation (2.18) to calculate the initial velocity of charged particles $v_{is}(t)$.
5. Assuming that over the integration time-step the variables on the right hand side of equation (2.18) are constant, then the quasi-static approximation holds, i.e. $\frac{dv_{is}}{dt} = \frac{dv_s}{dt}$. Calculate the velocity of charged particles at shell s , $v_{is}(t + \Delta t)$, after integration time-step Δt according to:

$$v_{is}(t + \Delta t) = v_{is}(t) + \frac{dv_{is}}{dt} \Delta t \quad (\text{A.7})$$

6. Get the change in radial position of the charged particles using:

$$r_{is}(t + \Delta t) = r_{is}(t) + \frac{\Delta t}{2}(v_{is}(t) + v_{is}(t + \Delta t)) \quad (\text{A.8})$$

7. Using the change in area crossed by the magnetic field in each shell, get the revised magnetic field strengths using the flux-freezing equation and map the magnetic flux density values onto the new position for each shell.
8. Using the spatial drift between r_{is} and r_s to calculate new values for the number densities of charged particles in each shell and derive τ_s at each shell.

The above sequence is then repeated for the next time-step. Note that since the temperature is only expected to change slowly, the temperature at each shell is only recalculated after a chemical time-step, $\Delta t_C \gg \Delta t$.

Appendix B

Spherical collapse of a uniform sphere

The following section derives the time t_1 it takes for a sphere of mass M with uniform initial density ρ_0 , initial infall velocity V_0 and initial radius R_0 to collapse to a final density ρ_1 . The equation of motion is (Spitzer 1998):

$$\frac{d^2r}{dt^2} = -\frac{GM}{r^2} \quad (\text{B.1})$$

where G is the gravitational constant. Multiplying equation B.1 by dr/dt and integrating gives the energy equation:

$$\frac{1}{2} \left(\frac{dr}{dt} \right)^2 = \frac{GM}{r} - C \quad (\text{B.2})$$

with boundary conditions $\frac{dr}{dt} = -V_0$ at $r = R_0$ giving $C = GM/R_0 - V_0^2/2$. Re-arranging the energy equation gives:

$$\left(\frac{\frac{r}{2GM}}{1 - \frac{Cr}{GM}} \right)^{1/2} dr = dt \quad (\text{B.3})$$

Making the substitution $\cos^2 \theta = Cr/GM$ and integrating gives:

$$\frac{-GM}{2^{1/2}C^{3/2}} \left[\theta + \frac{1}{2} \sin 2\theta \right]_{\theta_0}^{\theta_1} = t_1 \quad (\text{B.4})$$

$$\theta_0 = \arccos \left(1 - \frac{V_0^2 R_0}{2GM} \right)^{1/2} = \arcsin V_0 \left(\frac{R_0}{2GM} \right) \quad (\text{B.5})$$

$$\theta_1 = \arccos \left(\sqrt{R_1/R_0} \cos \theta_0 \right) \quad (\text{B.6})$$

where $R_1 = (4\pi\rho_1/3M)^{-1/3}$ is the radius of the sphere at time t_1 . Evaluating the integral in equation B.4 gives:

$$t_1 = \sqrt{\frac{3\pi}{32G\rho_0}} \frac{2\theta_1 + \sin 2\theta_1 - 2\theta_0 - \sin 2\theta_0}{\pi \cos^3 \theta_0} \quad (\text{B.7})$$

Appendix C

Chemical and dynamical radial profiles

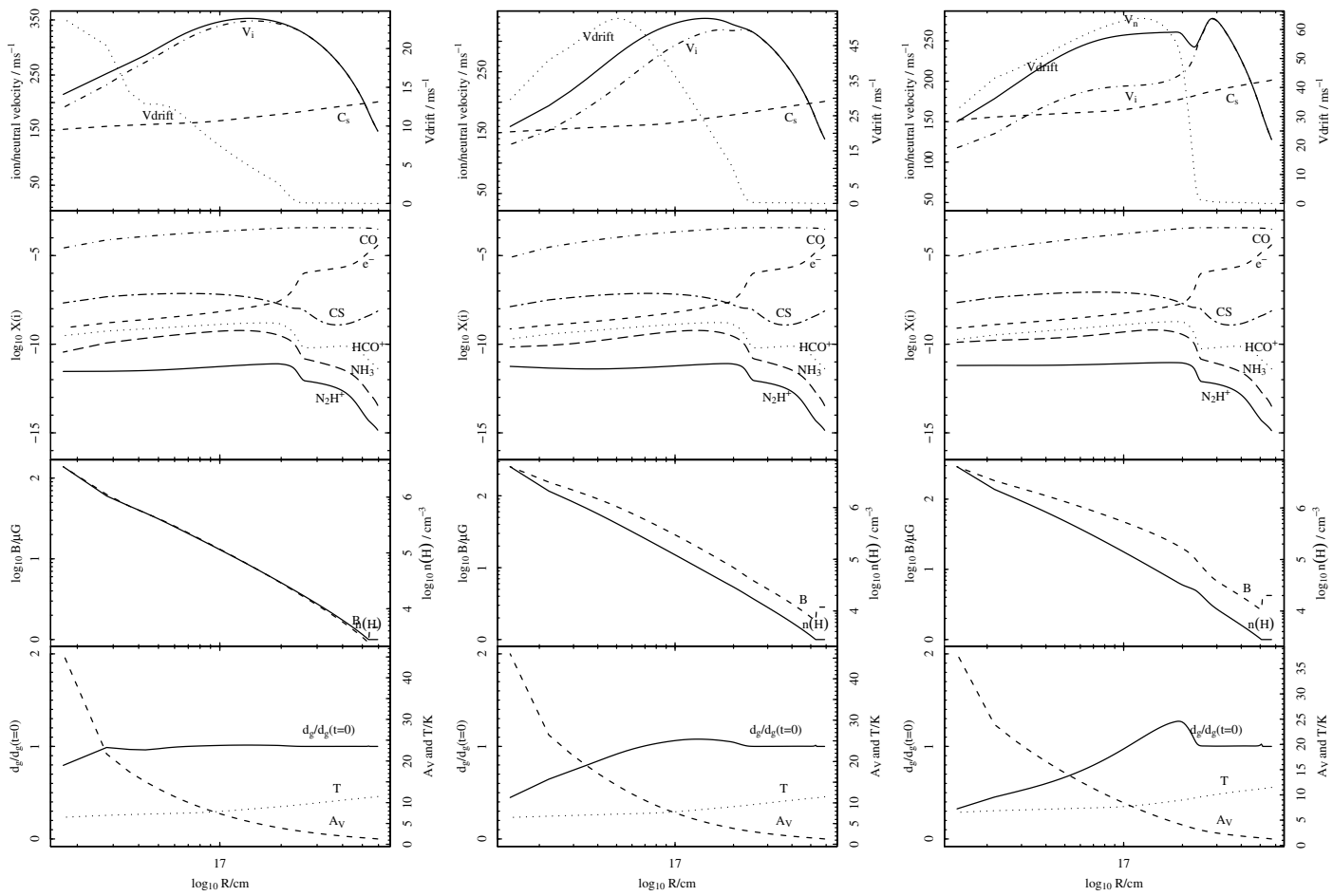


Figure C.1. Chemical and dynamical radial profiles for models *b1*, *b2* and *b3*.

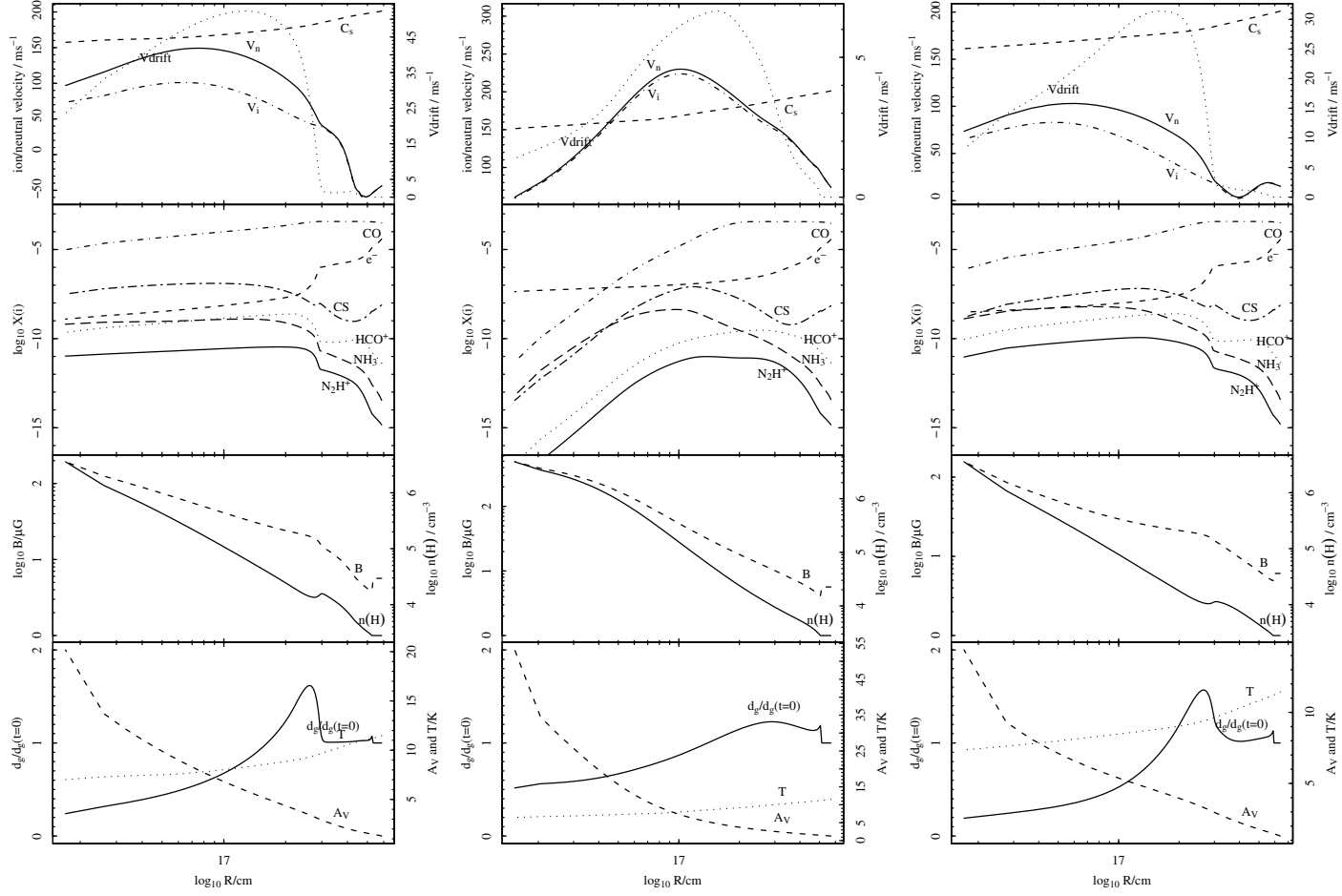


Figure C.2. Chemical and dynamical radial profiles for models *b4*, *grainchem1* and *grainchem2*.

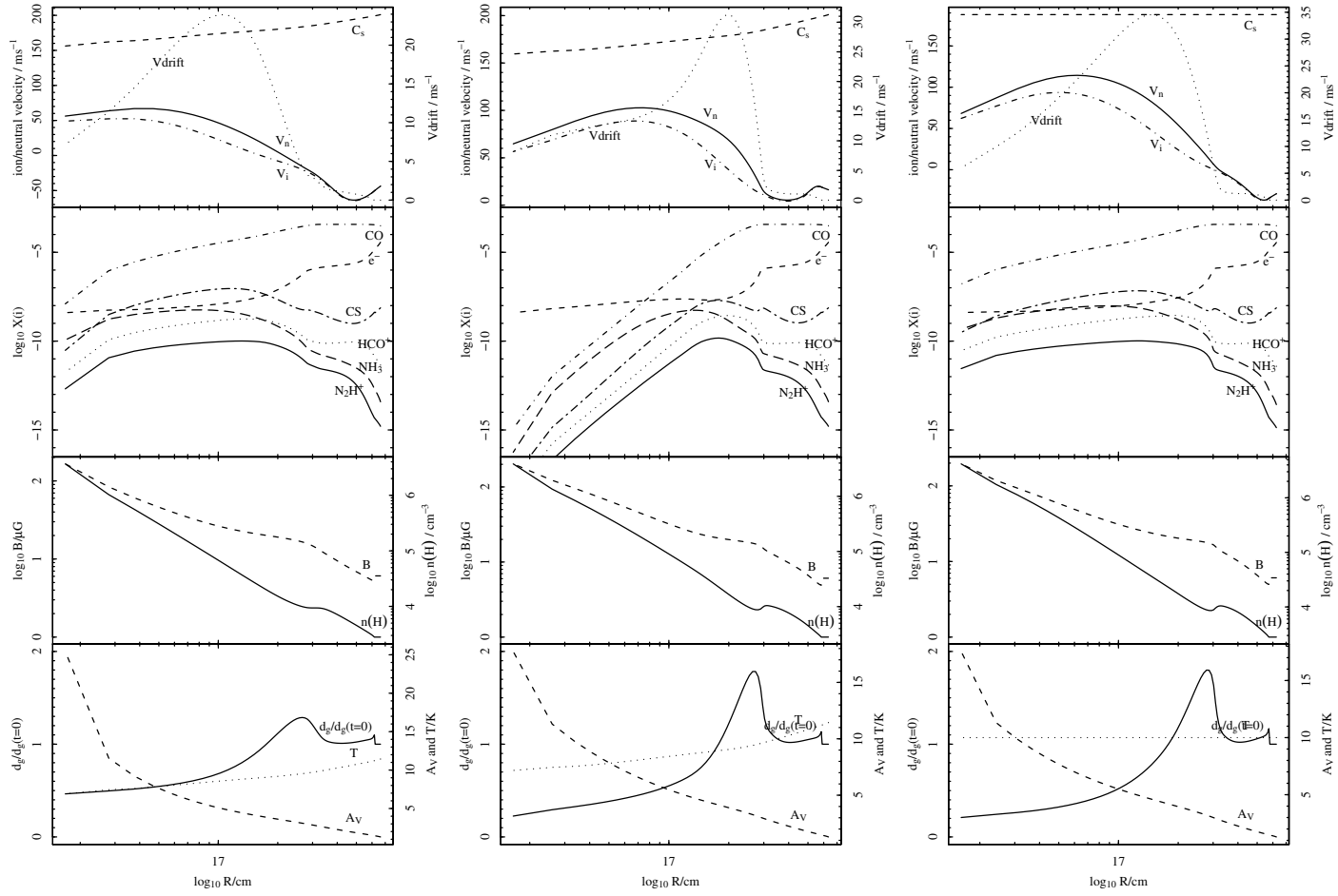


Figure C.3. Chemical and dynamical radial profiles for models *graindist1*, *stick1* and *temp1*.

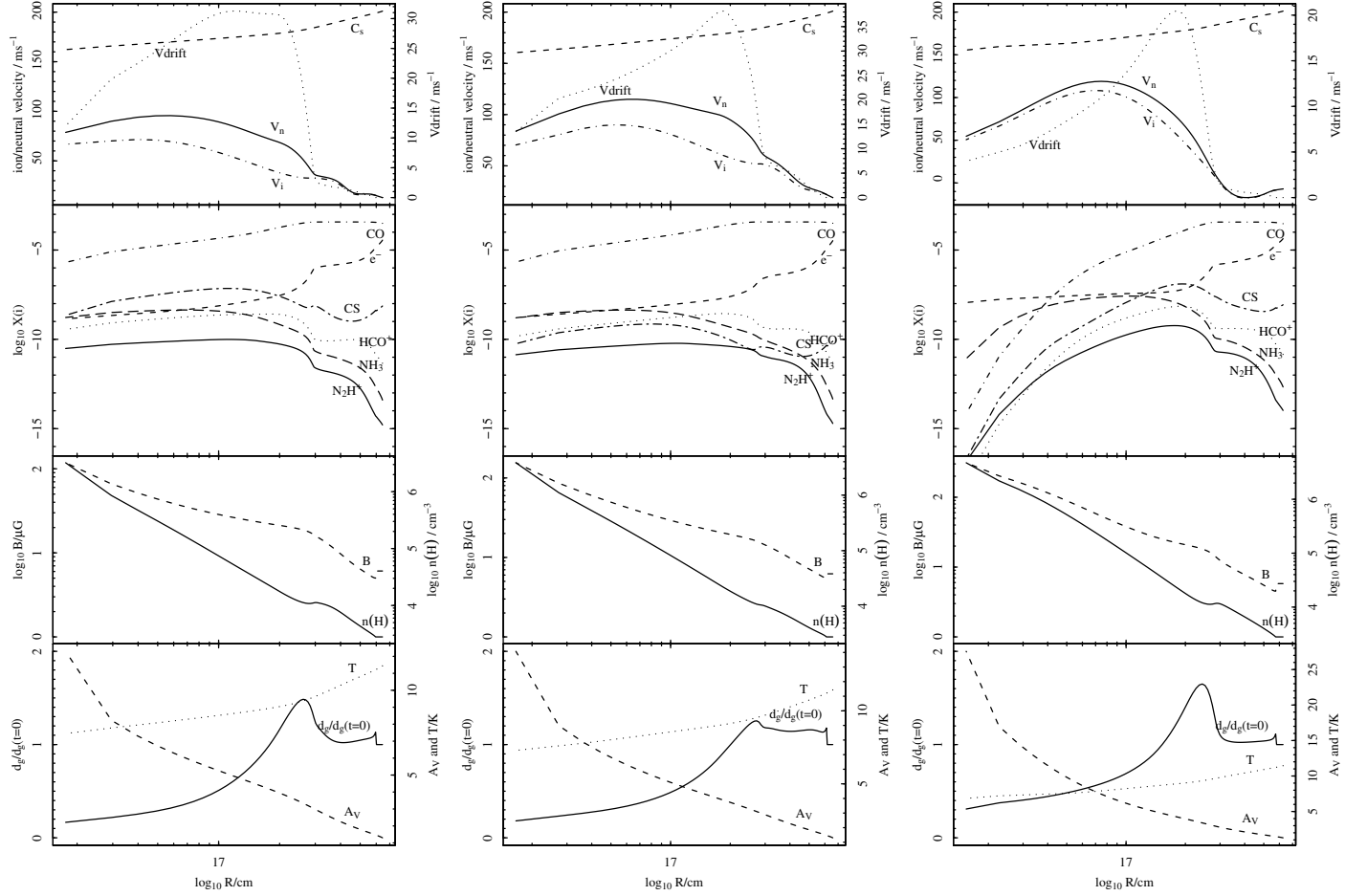


Figure C.4. Chemical and dynamical radial profiles for models *xna1*, *xs1* and *zeta1*.

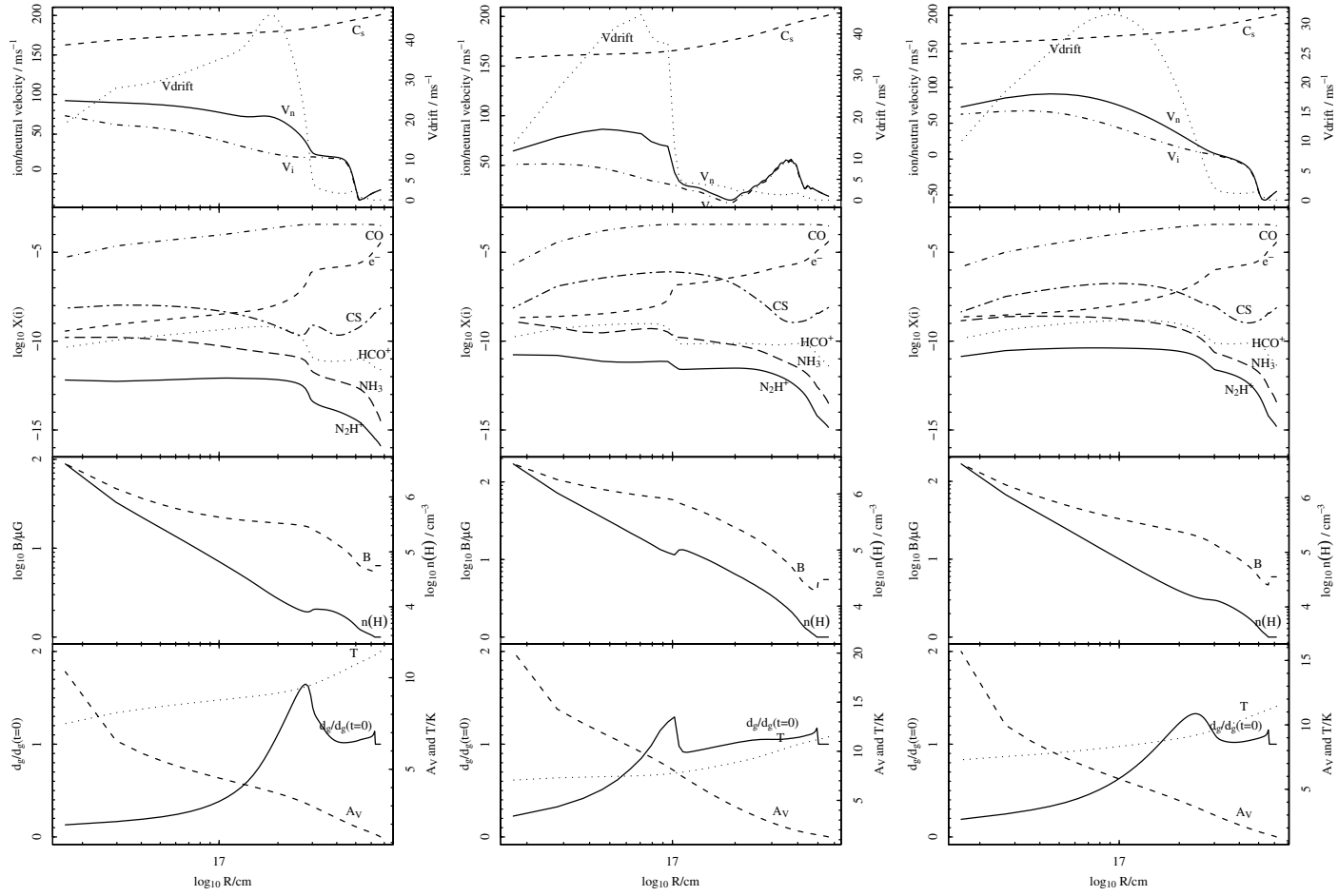


Figure C.5. Chemical and dynamical radial profiles for model *zeta2*, *avcrit1* and *avcrit2*.

Appendix D

Core temperature and dust continuum radial profiles

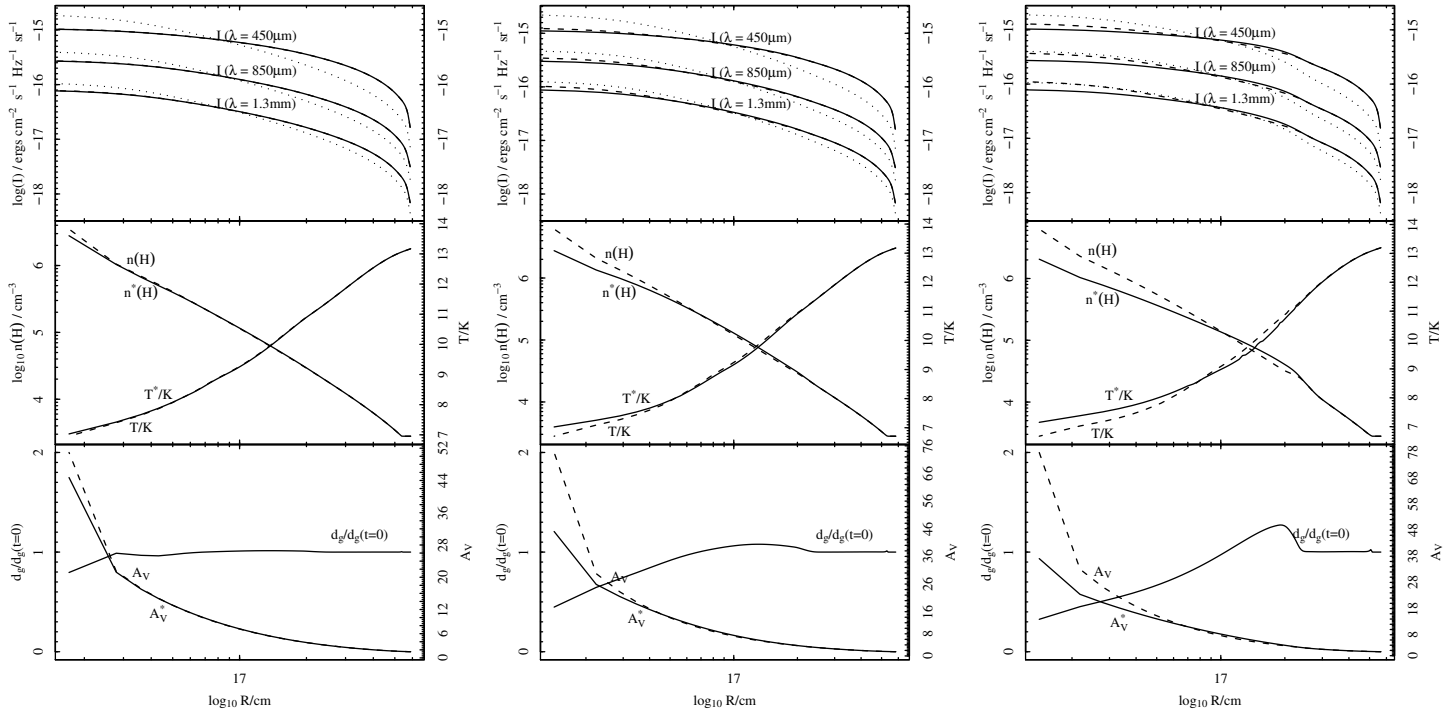


Figure D.1. Core temperature and dust continuum radial profiles for models *b1*, *b2* and *b3*.

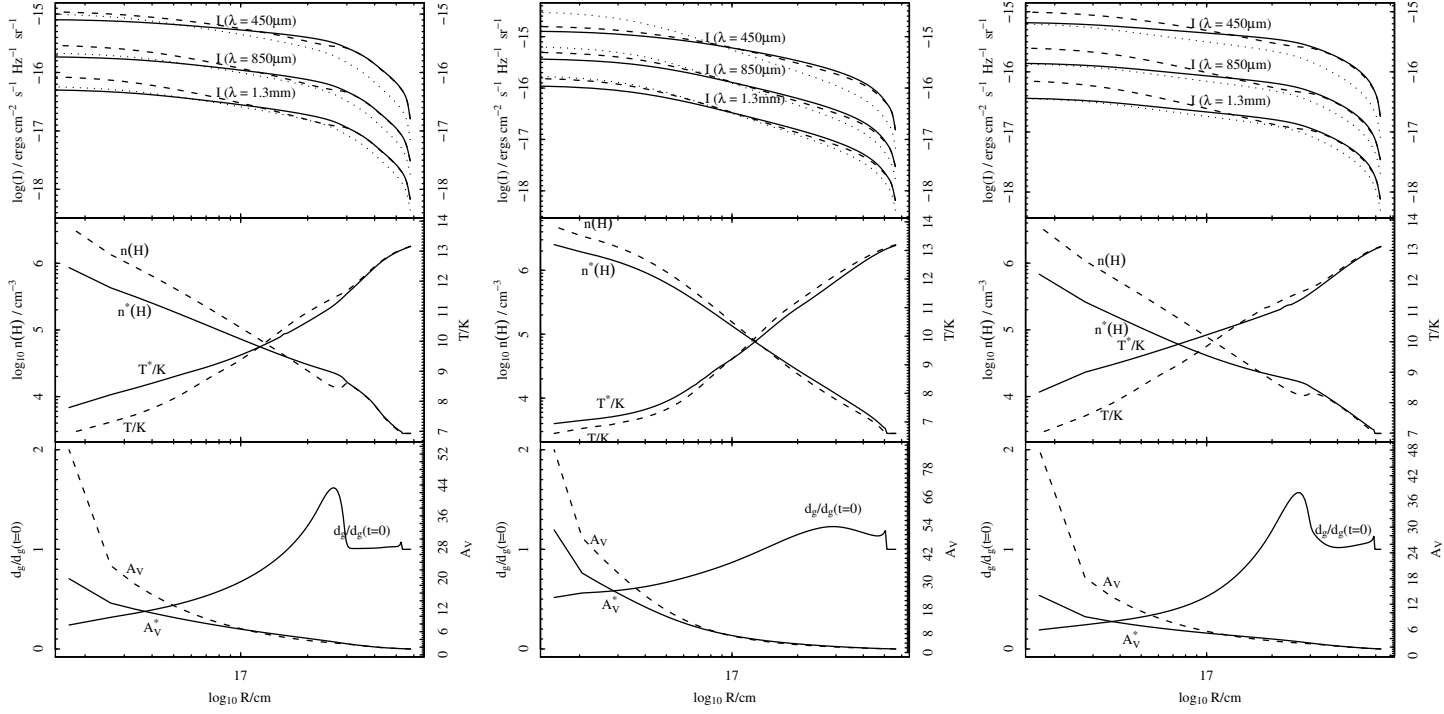


Figure D.2. Core temperature and dust continuum radial profiles for models *b4*, *grainchem1* and *grainchem2*.

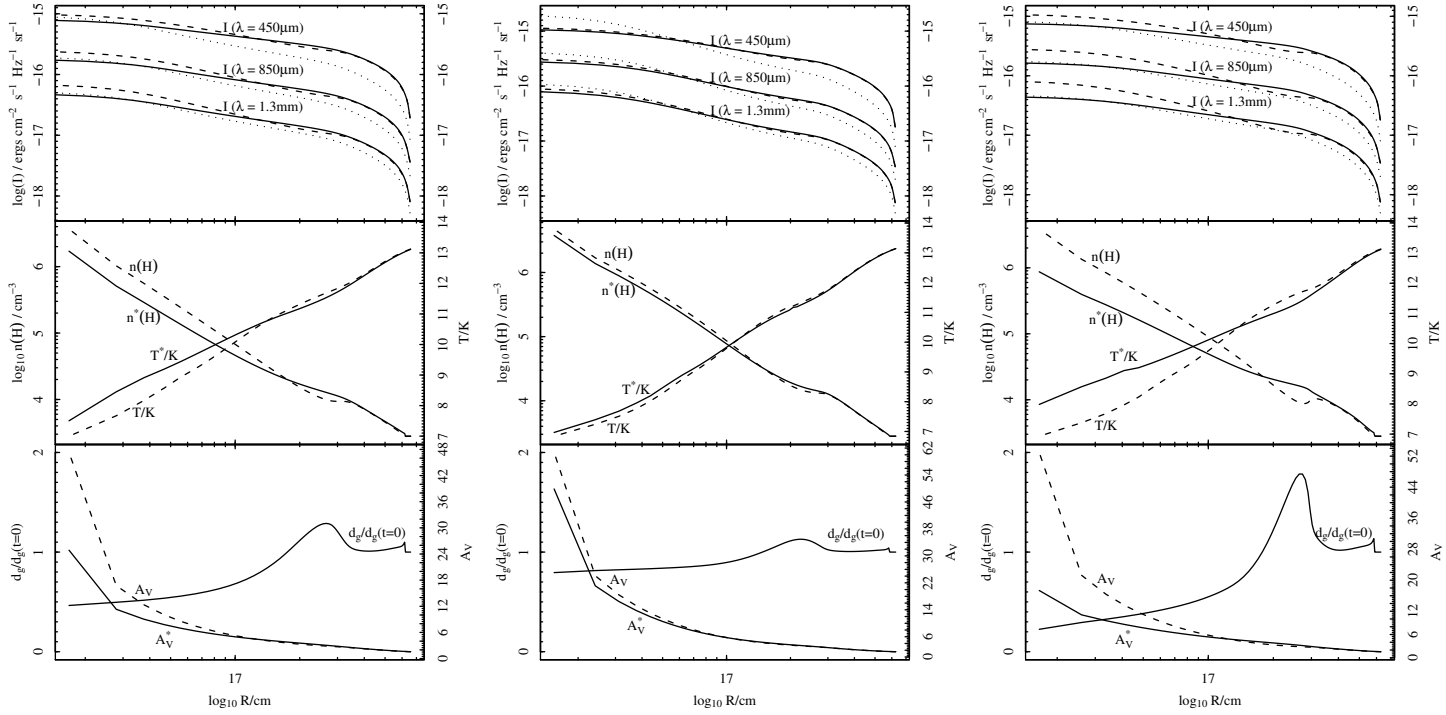


Figure D.3. Core temperature and dust continuum radial profiles for models *graindist1*, *graindist2* and *stick1*.

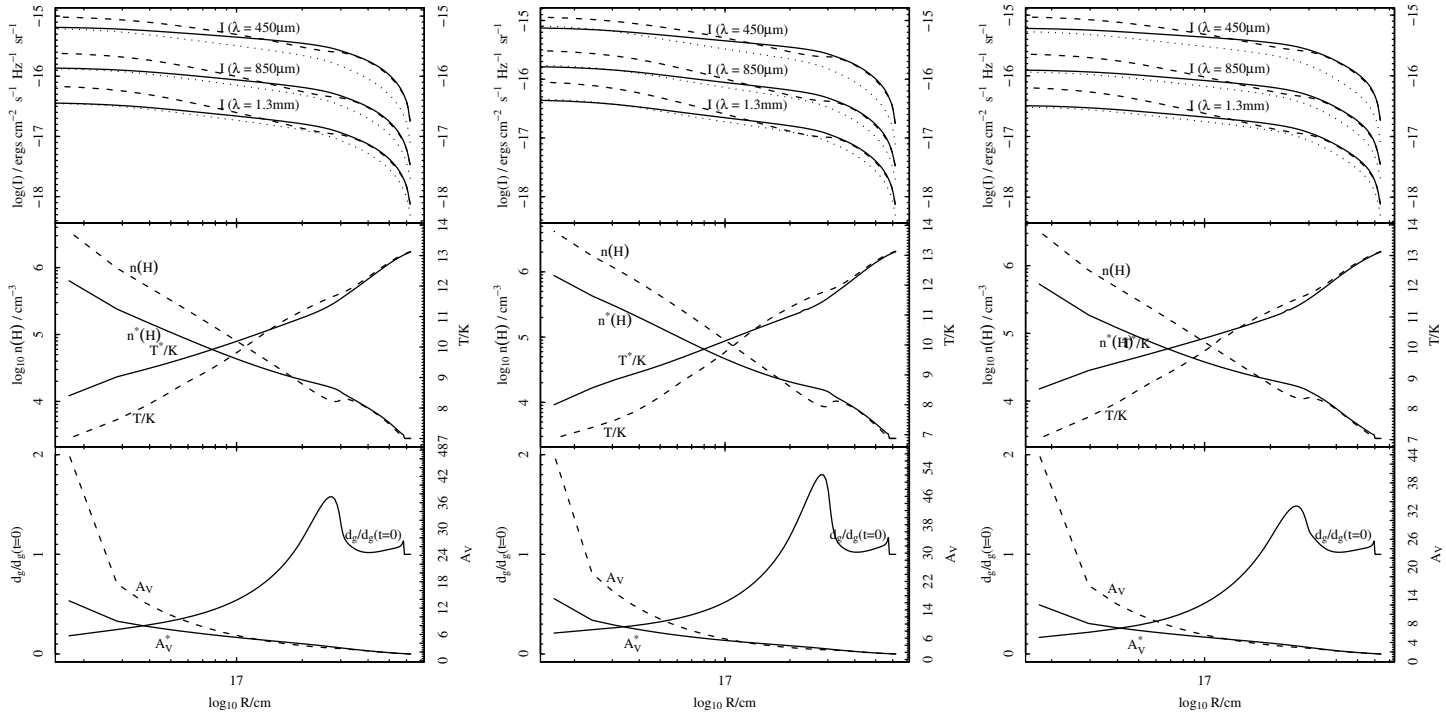


Figure D.4. Core temperature and dust continuum radial profiles for models *stick2*, *temp1* and *xna1*.

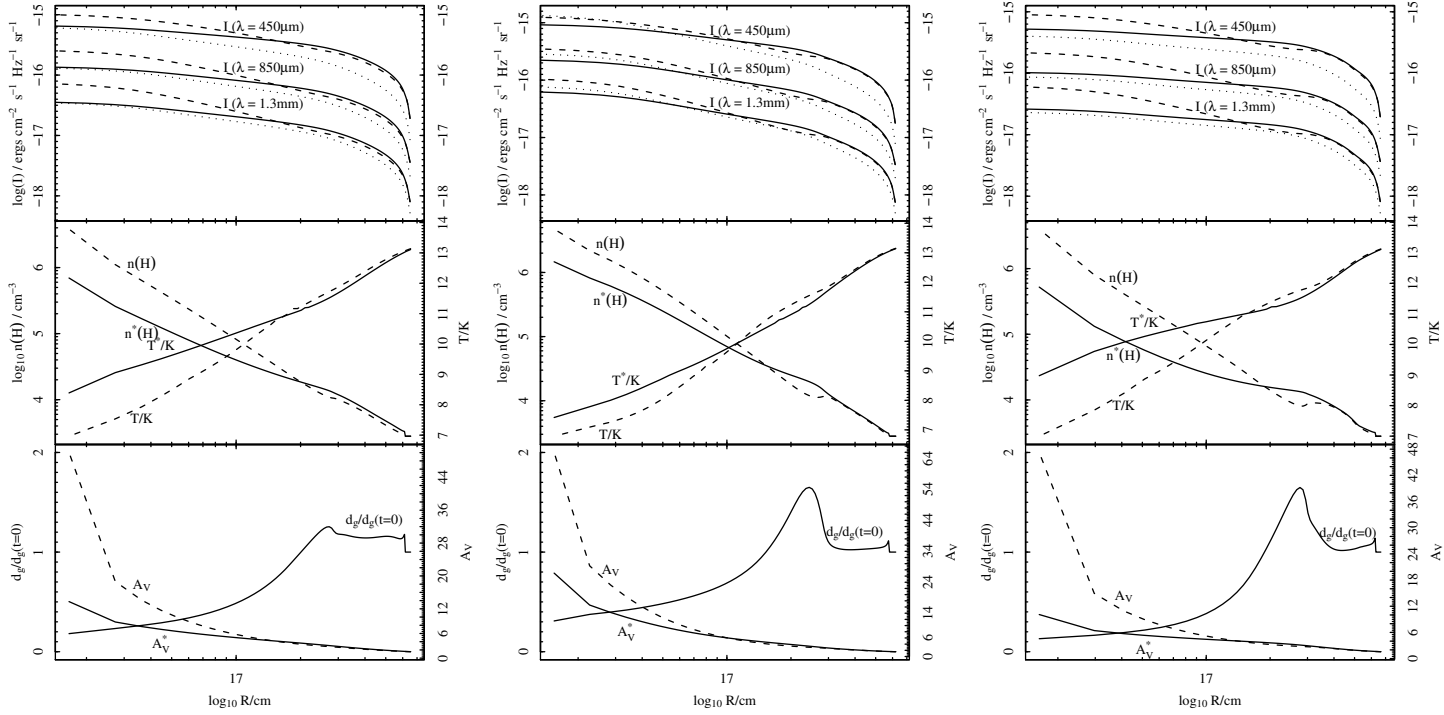


Figure D.5. Core temperature and dust continuum radial profiles for models *xs1*, *zeta1* and *zeta2*.

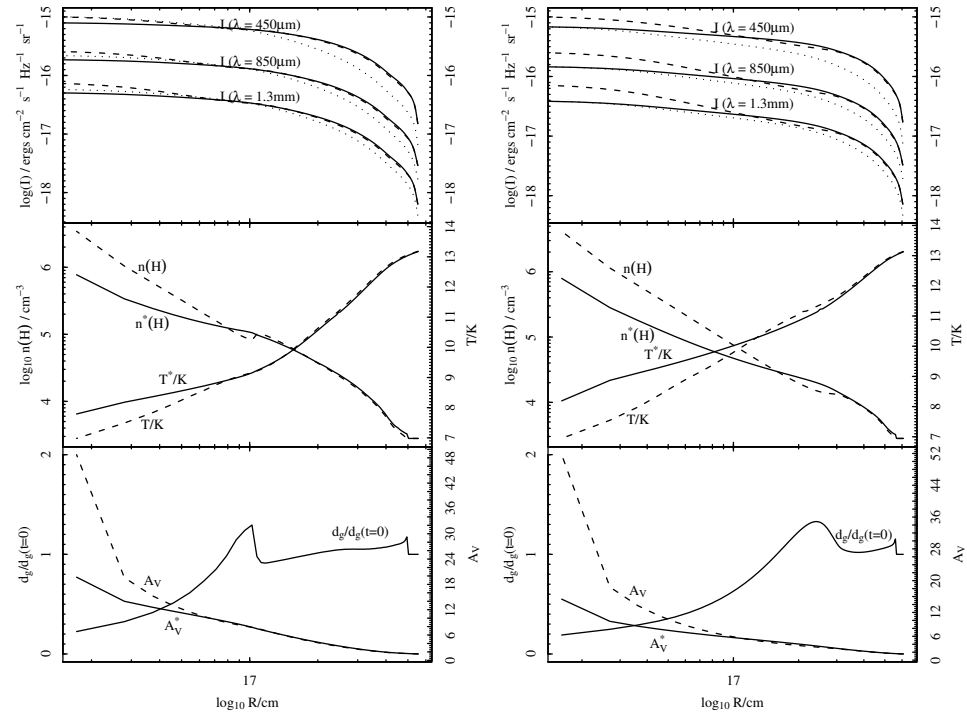


Figure D.6. Core temperature and dust continuum radial profiles for models *avcrit1* and *avcrit2*.

Bibliography

- Aannestad, P. A. & Kenyon, S. J., 1979, *ApJ*, **230**, 771
- Aannestad, P. A. & Purcell, E. M., 1973, *Ann. Rev. Astr. Astrophys.*, **11**, 309
- Adams, F. C., Lada, C. J. & Shu, F. H., 1987, *ApJ*, **312**, 788
- Aikawa, Y. & Herbst, E., 1999, *ApJ*, **526**, 314
- Aikawa, Y., Herbst, E. & Dzegilenko, F. N., 1999, *ApJ*, **527**, 262
- Aikawa, Y., Ohashi, N., Inutsuka, S., Herbst, E. & Takakuwa, S., 2001, *ApJ*, **552**, 639
- Alves, J., Lada, C. & Lada, E., 2001*a*, *The Messenger*, **103**, 1
- Alves, J. F., Lada, C. J. & Lada, E. A., 2001*b*, *Nature*, **409**, 159
- Anderson, C. E. J., 1987, *International Journal of Impact Engineering*, **5**(1-4), 33 ,
Hypervelocity Impact Proceedings of the 1986 Symposium
- André, P., 1994, in T. Montmerle, C. J. Lada, I. F. Mirabel & J. Tran Thanh Van (eds.),
The Cold Universe, p. 179
- André, P., Men'shchikov, A., Bontemps, S., Könyves, V., Motte, F., Schneider, N., Dide-
lon, P., Minier, V., Saraceno, P., Ward-Thompson, D., di Francesco, J., White, G., Moli-
nari, S., Testi, L., Abergel, A., Griffin, M., Henning, T., Royer, P., Merín, B., Vavrek,
R., Attard, M., Arzoumanian, D., Wilson, C. D., Ade, P., Aussel, H., Baluteau, J.-P.,
Benedettini, M., Bernard, J.-P., Blommaert, J. A. D. L., Cambrésy, L., Cox, P., di Gior-
gio, A., Hargrave, P., Hennemann, M., Huang, M., Kirk, J., Krause, O., Launhardt, R.,
Leeks, S., Le Penneec, J., Li, J. Z., Martin, P. G., Maury, A., Olofsson, G., Omont, A.,
Peretto, N., Pezzuto, S., Prusti, T., Roussel, H., Russeil, D., Sauvage, M., Sibthorpe,

- B., Sicilia-Aguilar, A., Spinoglio, L., Waelkens, C., Woodcraft, A. & Zavagno, A., 2010, *A&A*, **518**, L102
- Andre, P., Ward-Thompson, D. & Barsony, M., 1993, *ApJ*, **406**, 122
- Andre, P., Ward-Thompson, D. & Motte, F., 1996, *A&A*, **314**, 625
- Arons, J. & Max, C. E., 1975, *ApJL*, **196**, L77
- Bacmann, A., André, P., Puget, J., Abergel, A., Bontemps, S. & Ward-Thompson, D., 2000, *A&A*, **361**, 555
- Basu, S. & Mouschovias, T. C., 1994, *ApJ*, **432**, 720
- Beichman, C. A., Jennings, R. E., Emerson, J. P., Baud, B., Harris, S., Rowan-Robinson, M., Aumann, H. H., Gautier, T. N., Gillett, F. C., Habing, H. J., Marsden, P. L., Neugebauer, G. & Young, E., 1984, *ApJL*, **278**, L45
- Beichman, C. A., Myers, P. C., Emerson, J. P., Harris, S., Mathieu, R., Benson, P. J. & Jennings, R. E., 1986, *ApJ*, **307**, 337
- Belloche, A., André, P., Despois, D. & Blinder, S., 2002, *A&A*, **393**, 927
- Benson, P. J., Caselli, P. & Myers, P. C., 1998, *ApJ*, **506**, 743
- Benson, P. J. & Myers, P. C., 1989, *ApJSS*, **71**, 89
- Bergin, E. A., Ciardi, D. R., Lada, C. J., Alves, J. & Lada, E. A., 2001, *ApJ*, **557**, 209
- Bergin, E. A., Maret, S., van der Tak, F. F. S., Alves, J., Carmody, S. M. & Lada, C. J., 2006, *ApJ*, **645**, 369
- Binney, J. & Tremaine, S., 1987, *Galactic dynamics*
- Bok, B. J. & Reilly, E. F., 1947, *ApJ*, **105**, 255
- Bonnor, W. B., 1956, *MNRAS*, **116**, 351
- Brinch, C. & Hogerheijde, M. R., 2010, *A&A*, **523**, A25
- Cabrit, S., Goldsmith, P. F. & Snell, R. L., 1988, *ApJ*, **334**, 196
- Caselli, P., Benson, P. J., Myers, P. C. & Tafalla, M., 2002*a*, *ApJ*, **572**, 238

Caselli, P., Keto, E., Bergin, E. A., Tafalla, M., Aikawa, Y., Douglas, T., Pagani, L., Yıldız, U. A., van der Tak, F. F. S., Walmsley, C. M., Codella, C., Nisini, B., Kristensen, L. E. & van Dishoeck, E. F., 2012, *ApJL*, **759**, L37

Caselli, P., Keto, E., Pagani, L., Aikawa, Y., Yıldız, U. A., van der Tak, F. F. S., Tafalla, M., Bergin, E. A., Nisini, B., Codella, C., van Dishoeck, E. F., Bachiller, R., Baudry, A., Benedettini, M., Benz, A. O., Bjerkeli, P., Blake, G. A., Bontemps, S., Braine, J., Bruderer, S., Cernicharo, J., Daniel, F., di Giorgio, A. M., Dominik, C., Doty, S. D., Encrenaz, P., Fich, M., Fuente, A., Gaier, T., Giannini, T., Goicoechea, J. R., de Graauw, T., Helmich, F., Herczeg, G. J., Herpin, F., Hogerheijde, M. R., Jackson, B., Jacq, T., Javadi, H., Johnstone, D., Jørgensen, J. K., Kester, D., Kristensen, L. E., Laauwen, W., Larsson, B., Lis, D., Liseau, R., Luinge, W., Marseille, M., McCoey, C., Megej, A., Melnick, G., Neufeld, D., Olberg, M., Parise, B., Pearson, J. C., Plume, R., Risacher, C., Santiago-García, J., Saraceno, P., Shipman, R., Siegel, P., van Kempen, T. A., Visser, R., Wampfler, S. F. & Wyrowski, F., 2010, *A&A*, **521**, L29

Caselli, P., Walmsley, C. M., Zucconi, A., Tafalla, M., Dore, L. & Myers, P. C., 2002*b*, *ApJ*, **565**, 331

Caselli, P., Walmsley, C. M., Zucconi, A., Tafalla, M., Dore, L. & Myers, P. C., 2002*c*, *ApJ*, **565**, 344

Cazzoli, G., Cludi, L., Buffa, G. & Puzzarini, C., 2012, *ApJSS*, **203**, 11

Chapman, N. L., Goldsmith, P. F., Pineda, J. L., Clemens, D. P., Li, D. & Krčo, M., 2011, *ApJ*, **741**, 21

Ciolek, G. E. & Basu, S., 2000, *ApJ*, **529**, 925

Ciolek, G. E. & Koenigl, A., 1998, *ApJ*, **504**, 257

Ciolek, G. E. & Mouschovias, T. C., 1993, *ApJ*, **418**, 774

Ciolek, G. E. & Mouschovias, T. C., 1994, *ApJ*, **425**, 142

Ciolek, G. E. & Mouschovias, T. C., 1996, *ApJ*, **468**, 749

Coker, R. F., Rae, J. G. L. & Hartquist, T. W., 2000, *A&A*, **360**, 290

Courant, R., Friedrichs, K. & Lewy, H., 1928, *Mathematische Annalen*, **111**, 32

- Crapsi, A., Caselli, P., Walmsley, C. M., Myers, P. C., Tafalla, M., Lee, C. W. & Bourke, T. L., 2005, *ApJ*, **619**, 379
- Crapsi, A., Caselli, P., Walmsley, M. C. & Tafalla, M., 2007, *A&A*, **470**, 221
- Crutcher, R. M., 1999, *ApJ*, **520**, 706
- Crutcher, R. M., Nutter, D. J., Ward-Thompson, D. & Kirk, J. M., 2004, *ApJ*, **600**, 279
- Crutcher, R. M. & Troland, T. H., 2000, *ApJL*, **537**, L139
- Dame, T. M., Elmegreen, B. G., Cohen, R. S. & Thaddeus, P., 1986, *ApJ*, **305**, 892
- Davidson, P. A., 2004, *Turbulence : an introduction for scientists and engineers*
- de Boisanger, C., Helmich, F. P. & van Dishoeck, E. F., 1996, *A&A*, **310**, 315
- Doty, S. D. & Neufeld, D. A., 1997, *ApJ*, **489**, 122
- Dyson, J. E. & Williams, D. A., 1997, *The physics of the interstellar medium*
- Ebert, R., 1955, *Zeitschrift fur Astrophysik*, **37**, 217
- Elias, J. H., 1978, *ApJ*, **224**, 857
- Enoch, M. L., Evans, II, N. J., Sargent, A. I., Glenn, J., Rosolowsky, E. & Myers, P., 2008, *ApJ*, **684**, 1240
- Evans, II, N. J., Lee, J., Rawlings, J. M. C. & Choi, M., 2005, *ApJ*, **626**, 919
- Evans, II, N. J., Rawlings, J. M. C., Shirley, Y. L. & Mundy, L. G., 2001, *ApJ*, **557**, 193
- Fatuzzo, M. & Adams, F. C., 1993, *ApJ*, **412**, 146
- Ferguson, E. E., 1975, *Annual Review of Physical Chemistry*, **26**, 17
- Flower, D. R., Pineau des Forets, G. & Hartquist, T. W., 1985, *MNRAS*, **216**, 775
- Foster, P. N. & Chevalier, R. A., 1993, *ApJ*, **416**, 303
- Franco, G. A. P., Alves, F. O. & Girart, J. M., 2010, *ApJ*, **723**, 146
- Fuller, G. A., Williams, S. J. & Sridharan, T. K., 2005, *A&A*, **442**, 949

- García-Burillo, S., Combes, F., Usero, A., Aalto, S., Krips, M., Viti, S., Alonso-Herrero, A., Hunt, L. K., Schinnerer, E., Baker, A. J., Boone, F., Casasola, V., Colina, L., Costagliola, F., Eckart, A., Fuente, A., Henkel, C., Labiano, A., Martín, S., Márquez, I., Muller, S., Planesas, P., Ramos Almeida, C., Spaans, M., Tacconi, L. J. & van der Werf, P. P., 2014, *A&A*, **567**, A125
- Gear, C. W., 1971, *Numerical initial value problems in ordinary differential equations*
- Gillis, J., Mestel, L. & Paris, R. B., 1974, *Ap&SS*, **27**, 167
- Gioumousis, G. & Stevenson, D. P., 1958, *J. Chem. Phys.*, **29**, 294
- Goldsmith, P. F., Langer, W. D. & Wilson, R. W., 1986, *ApJL*, **303**, L11
- Goodman, A. A., Benson, P. J., Fuller, G. A. & Myers, P. C., 1993, *ApJ*, **406**, 528
- Green, S. & Chapman, S., 1978, *ApJSS*, **37**, 169
- Hartquist, T. W., Rawlings, J. M. C., Williams, D. A. & Dalgarno, A., 1993, *QJRAS*, **34**, 213
- Harvey, D. W. A., Wilner, D. J., Myers, P. C. & Tafalla, M., 2003, *ApJ*, **596**, 383
- Hasegawa, T. I. & Herbst, E., 1993, *MNRAS*, **261**, 83
- Herbst, E., 2001, *Chem. Soc. Rev.*, **30**, 168
- Hirahara, Y., Masuda, A., Kawaguchi, K., Ohishi, M., Ishikawa, S., Yamamoto, S., Takano, S. & Kaifu, N., 1995, *Astron. Soc. of Japan*, **47**, 845
- Ho, P. T. P. & Townes, C. H., 1983, *Ann. Rev. Astr. Astrophys.*, **21**, 239
- Hogerheijde, M. R. & van der Tak, F. F. S., 2000, *A&A*, **362**, 697
- Hollenbach, D., Kaufman, M. J., Bergin, E. A. & Melnick, G. J., 2009, *ApJ*, **690**, 1497
- Hollenbach, D. J. & Tielens, A. G. G. M., 1997, *Ann. Rev. Astr. Astrophys.*, **35**, 179
- Hotzel, S., Harju, J. & Juvela, M., 2002, *A&A*, **395**, L5
- Hunter, C., 1977, *ApJ*, **218**, 834
- Inutsuka, S.-I. & Miyama, S. M., 1997, *ApJ*, **480**, 681

- Jones, A. P., Tielens, A. G. G. M. & Hollenbach, D. J., 1996, *ApJ*, **469**, 740
- Jones, C. E., Basu, S. & Dubinski, J., 2001, *ApJ*, **551**, 387
- Kauffmann, J., Bertoldi, F., Bourke, T. L., Evans, II, N. J. & Lee, C. W., 2008, *A&A*, **487**, 993
- Keene, J., Davidson, J. A., Harper, D. A., Hildebrand, R. H., Jaffe, D. T., Loewenstein, R. F., Low, F. J. & Pernic, R., 1983, *ApJL*, **274**, L43
- Keto, E. & Caselli, P., 2010, *MNRAS*, **402**, 1625
- Kim, H. G. & Hong, S. S., 2002, *ApJ*, **567**, 376
- Kirk, J. M., Ward-Thompson, D. & André, P., 2005, *MNRAS*, **360**, 1506
- Könyves, V., André, P., Men'shchikov, A., Schneider, N., Arzoumanian, D., Bontemps, S., Attard, M., Motte, F., Didelon, P., Maury, A., Abergel, A., Ali, B., Baluteau, J.-P., Bernard, J.-P., Cambrésy, L., Cox, P., di Francesco, J., di Giorgio, A. M., Griffin, M. J., Hargrave, P., Huang, M., Kirk, J., Li, J. Z., Martin, P., Minier, V., Molinari, S., Olofsson, G., Pezzuto, S., Russeil, D., Roussel, H., Saraceno, P., Sauvage, M., Sibthorpe, B., Spinoglio, L., Testi, L., Ward-Thompson, D., White, G., Wilson, C. D., Woodcraft, A. & Zavagno, A., 2010, *A&A*, **518**, L106
- Kroupa, P., 2001, *MNRAS*, **322**, 231
- Kroupa, P., 2002, *Science*, **295**, 82
- Kulsrud, R. & Pearce, W. P., 1969, *ApJ*, **156**, 445
- Lada, C. J., Bergin, E. A., Alves, J. F. & Huard, T. L., 2003, *ApJ*, **586**, 286
- Lai, S., Velusamy, T., Langer, W. D. & Kuiper, T. B. H., 2003, *AJ*, **126**, 311
- Larson, R. B., 1969, *MNRAS*, **145**, 271
- Larson, R. B., 2003, *Reports on Progress in Physics*, **66**, 1651
- Launhardt, R., Stutz, A. M., Schmiedeke, A., Henning, T., Krause, O., Balog, Z., Beuther, H., Birkmann, S., Hennemann, M., Kainulainen, J., Khanzadyan, T., Linz, H., Lippok, N., Nielbock, M., Pitann, J., Ragan, S., Risacher, C., Schmalzl, M., Shirley, Y. L., Stecklum, B., Steinacker, J. & Tackenberg, J., 2013, *A&A*, **551**, A98

- Lee, C. W. & Myers, P. C., 1999, *ApJSS*, **123**, 233
- Lee, C. W., Myers, P. C. & Tafalla, M., 2001, *ApJSS*, **136**, 703
- Leger, A., Jura, M. & Omont, A., 1985, *A&A*, **144**, 147
- Li, H., Dowell, C. D., Goodman, A., Hildebrand, R. & Novak, G., 2009, *ApJ*, **704**, 891
- Li, Z. & McKee, C. F., 1996, *ApJ*, **464**, 373
- Li, Z., Shematovich, V. I., Wiebe, D. S. & Shustov, B. M., 2002, *ApJ*, **569**, 792
- Liu, F. K., 1996, *MNRAS*, **281**, 1197
- Longair, M. S., 1992, *High energy astrophysics. Vol.1: Particles, photons and their detection*
- Mardones, D., Myers, P. C., Tafalla, M., Wilner, D. J., Bachiller, R. & Garay, G., 1997, *ApJ*, **489**, 719
- Maret, S., Bergin, E. A. & Lada, C. J., 2007, *ApJL*, **670**, L25
- Mathis, J. S., Mezger, P. G. & Panagia, N., 1983, *A&A*, **128**, 212
- Mathis, J. S., Rumpl, W. & Nordsieck, K. H., 1977, *ApJ*, **217**, 425
- McElroy, D., Walsh, C., Markwick, A. J., Cordiner, M. A., Smith, K. & Millar, T. J., 2013, *A&A*, **550**, A36
- McKee, C. F. & Ostriker, E. C., 2007, *Ann. Rev. Astr. Astrophys.*, **45**, 565
- Ménard, F. & Duchêne, G., 2004, *A&A*, **425**, 973
- Men'shchikov, A., André, P., Didelon, P., Könyves, V., Schneider, N., Motte, F., Bon-temps, S., Arzoumanian, D., Attard, M., Abergel, A., Baluteau, J.-P., Bernard, J.-P., Cambrésy, L., Cox, P., di Francesco, J., di Giorgio, A. M., Griffin, M., Hargrave, P., Huang, M., Kirk, J., Li, J. Z., Martin, P., Minier, V., Miville-Deschênes, M.-A., Molinari, S., Olofsson, G., Pezzuto, S., Roussel, H., Russeil, D., Saraceno, P., Sauvage, M., Sibthorpe, B., Spinoglio, L., Testi, L., Ward-Thompson, D., White, G., Wilson, C. D., Woodcraft, A. & Zavagno, A., 2010, *A&A*, **518**, L103
- Meyerdierks, H., Berry, D., Draper, P. W., Privett, G. & Currie, M., 2005, *Starlink User Note 194.3*, Technical report, Rutherford Appleton Laboratory

- Millar, T. J., Bennett, A., Rawlings, J. M. C., Brown, P. D. & Charnley, S. B., 1991, *A&AS*, **87**, 585
- Millar, T. J., Farquhar, P. R. A. & Willacy, K., 1997, *A&AS*, **121**, 139
- Millar, T. J. & Williams, D. A., 1993, *Dust and chemistry in astronomy*
- Moneti, A., Pipher, J. L., Helfer, H. L., McMillan, R. S. & Perry, M. L., 1984, *ApJ*, **282**, 508
- Monteiro, T. S., 1985, *MNRAS*, **214**, 419
- Mouschovias, T. C., 1975, *Static equilibria of the interstellar gas in the presence of magnetic and gravitational fields*, Ph.D. thesis, California Univ., Berkeley.
- Mouschovias, T. C. & Paleologou, E. V., 1979, *ApJ*, **230**, 204
- Mouschovias, T. C. & Psaltis, D., 1995, *ApJL*, **444**, L105
- Mouschovias, T. C., Tassis, K. & Kunz, M. W., 2006, *ApJ*, **646**, 1043
- Myers, P. C., 1983, *ApJ*, **270**, 105
- Myers, P. C. & Benson, P. J., 1983, *ApJ*, **266**, 309
- Myers, P. C., Fuller, G. A., Goodman, A. A. & Benson, P. J., 1991, *ApJ*, **376**, 561
- Nakano, T. & Nakamura, T., 1978, *Publ. Astron. Soc. Jpn.*, **30**, 671
- Ossenkopf, V. & Henning, T., 1994, *A&A*, **291**, 943
- Pagani, L., Pardo, J., Apponi, A. J., Bacmann, A. & Cabrit, S., 2005, *A&A*, **429**, 181
- Pagani, L., Ristorcelli, I., Boudet, N., Giard, M., Abergel, A. & Bernard, J., 2010a, *A&A*, **512**, A3+
- Pagani, L., Steinacker, J., Bacmann, A., Stutz, A. & Henning, T., 2010b, *Science*, **329**, 1622
- Pavlyuchenkov, Y. N., Shustov, B. M., Shematovich, V. I., Wiebe, D. S. & Li, Z., 2003, *Astronomy Reports*, **47**, 176
- Penston, M. V., 1969, *MNRAS*, **144**, 425

- Phillips, T. G., Huggins, P. J., Wannier, P. G. & Scoville, N. Z., 1979, *ApJ*, **231**, 720
- Prasad, S. S., Heere, K. R. & Tarafdar, S. P., 1991, *ApJ*, **373**, 123
- Prasad, S. S. & Tarafdar, S. P., 1983, *ApJ*, **267**, 603
- R. M. Cutri & W. B. Latter (ed.), 1994, *The First Symposium on the Infrared Cirrus and Diffuse Interstellar Clouds*, volume 58 of *Astronomical Society of the Pacific Conference Series*
- Rawlings, J. M. C., 1996*a*, *Ap&SS*, **237**, 299
- Rawlings, J. M. C., 1996*b*, *QJRAS*, **37**, 503
- Rawlings, J. M. C., 2000, in Y. C. Minh & E. F. van Dishoeck (ed.), *From Molecular Clouds to Planetary*, volume 197 of *IAU Symposium*, pp. 15–+
- Rawlings, J. M. C., Hartquist, T. W., Menten, K. M. & Williams, D. A., 1992, *MNRAS*, **255**, 471
- Rawlings, J. M. C. & Yates, J. A., 2001, *MNRAS*, **326**, 1423
- Redman, M. P., Keto, E. & Rawlings, J. M. C., 2006, *MNRAS*, **370**, L1
- Redman, M. P., Keto, E., Rawlings, J. M. C. & Williams, D. A., 2004, *MNRAS*, **352**, 1365
- Roberts, J. F., Rawlings, J. M. C. & Stace, H. A., 2010, *MNRAS*, **408**, 2426
- Roberts, J. F., Rawlings, J. M. C., Viti, S. & Williams, D. A., 2007, *MNRAS*, **382**, 733
- Rosolowsky, E. W., Pineda, J. E., Foster, J. B., Borkin, M. A., Kauffmann, J., Caselli, P., Myers, P. C. & Goodman, A. A., 2008, *ApJSS*, **175**, 509
- Ruffle, D. P., Hartquist, T. W., Caselli, P. & Williams, D. A., 1999, *MNRAS*, **306**, 691
- Ruffle, D. P., Hartquist, T. W., Rawlings, J. M. C. & Williams, D. A., 1998, *A&A*, **334**, 678
- Safier, P. N., McKee, C. F. & Stahler, S. W., 1997, *ApJ*, **485**, 660
- Saito, M., Sunada, K., Kawabe, R., Kitamura, Y. & Hirano, N., 1999, *ApJ*, **518**, 334

- Sault, R. J., Teuben, P. J. & Wright, M. C. H., 1995, in R. A. Shaw, H. E. Payne & J. J. E. Hayes (eds.), *Astronomical Data Analysis Software and Systems IV*, volume 77 of *Astronomical Society of the Pacific Conference Series*, p. 433
- Schöier, F. L., van der Tak, F. F. S., van Dishoeck, E. F. & Black, J. H., 2005, *A&A*, **432**, 369
- Shematovich, V. I., Shustov, B. M. & Wiebe, D. S., 1997, *MNRAS*, **292**, 601
- Shematovich, V. I., Wiebe, D. S. & Shustov, B. M., 1999, *Astronomy Reports*, **43**, 645
- Shematovich, V. I., Wiebe, D. S., Shustov, B. M. & Li, Z., 2003, *ApJ*, **588**, 894
- Shirley, Y. L., Evans, II, N. J. & Rawlings, J. M. C., 2002, *ApJ*, **575**, 337
- Shirley, Y. L., Evans, II, N. J., Rawlings, J. M. C. & Gregersen, E. M., 2000, *ApJSS*, **131**, 249
- Shu, F. H., 1977, *ApJ*, **214**, 488
- Shu, F. H., Adams, F. C. & Lizano, S., 1987, *Ann. Rev. Astr. Astrophys.*, **25**, 23
- Snell, R. L., 1981, *ApJSS*, **45**, 121
- Snow, T. P. & Bierbaum, V. M., 2008, *Annual Review of Analytical Chemistry*, **1**, 229
- Snow, T. P. & McCall, B. J., 2006, *Ann. Rev. Astr. Astrophys.*, **44**, 367
- Spitzer, L., 1998, *Physical Processes in the Interstellar Medium*
- Stutz, A., Launhardt, R., Linz, H., Krause, O., Henning, T., Kainulainen, J., Nielbock, M., Steinacker, J. & André, P., 2010, *A&A*, **518**, L87
- Tafalla, M., Mardones, D., Myers, P. C., Caselli, P., Bachiller, R. & Benson, P. J., 1998, *ApJ*, **504**, 900
- Tafalla, M., Myers, P. C., Caselli, P., Walmsley, C. M. & Comito, C., 2002, *ApJ*, **569**, 815
- Takahashi, T., Silk, J. & Hollenbach, D. J., 1983, *ApJ*, **275**, 145
- Tassis, K., Willacy, K., Yorke, H. W. & Turner, N. J., 2012, *ApJ*, **753**, 29

- Teixeira, T. C. & Emerson, J. P., 1999, *A&A*, **351**, 292
- Terzieva, R. & Herbst, E., 1998, *ApJ*, **501**, 207
- Tomisaka, K., Ikeuchi, S. & Nakamura, T., 1988, *ApJ*, **335**, 239
- Truelove, J. K., Klein, R. I., McKee, C. F., Holliman, II, J. H., Howell, L. H. & Greenough, J. A., 1997, *ApJL*, **489**, L179+
- Tsamis, Y. G., Rawlings, J. M. C., Yates, J. A. & Viti, S., 2008, *MNRAS*, **388**, 898
- Turner, B. E., 1995, *ApJ*, **449**, 635
- Umebayashi, T. & Nakano, T., 1980, *Astron. Soc. of Japan*, **32**, 405
- Ungerechts, H., Winnewisser, G. & Walmsley, C. M., 1982, *A&A*, **111**, 339
- van der Tak, F. F. S. & van Dishoeck, E. F., 2000, *A&A*, **358**, L79
- van Dishoeck, E. F. & Black, J. H., 1988, *ApJ*, **334**, 771
- Vrba, F. J., Strom, S. E. & Strom, K. M., 1976, *AJ*, **81**, 958
- Ward-Thompson, D., Kirk, J. M., Crutcher, R. M., Greaves, J. S., Holland, W. S. & André, P., 2000, *ApJL*, **537**, L135
- Ward-Thompson, D., Motte, F. & Andre, P., 1999, *MNRAS*, **305**, 143
- Ward-Thompson, D., Scott, P. F., Hills, R. E. & Andre, P., 1994, *MNRAS*, **268**, 276
- Ward-Thompson, D., Sen, A. K., Kirk, J. M. & Nutter, D., 2009, *MNRAS*, **398**, 394
- Weingartner, J. C. & Draine, B. T., 2001, *ApJ*, **548**, 296
- Willacy, K., Rawlings, J. M. C. & Williams, D. A., 1994, *MNRAS*, **269**, 921
- Williams, J. P., Myers, P. C., Wilner, D. J. & di Francesco, J., 1999, *ApJL*, **513**, L61
- Woodall, J., Agúndez, M., Markwick-Kemper, A. J. & Millar, T. J., 2007, *A&A*, **466**, 1197
- Zengin, D., Pekünlü, E. R. & Tigrak, E., 2004, in B. Uyaniker, W. Reich, & R. Wielebinski (ed.), *The Magnetized Interstellar Medium*, pp. 133–136

Zhou, S. & Evans, II, N. J., 1994, in D. P. Clemens & R. Barvainis (ed.), *Clouds, Cores, and Low Mass Stars*, volume 65 of *Astronomical Society of the Pacific Conference Series*, pp. 183–+

Zhou, S., Evans, II, N. J., Koempe, C. & Walmsley, C. M., 1993, *ApJ*, **404**, 232

Zucconi, A., Walmsley, C. M. & Galli, D., 2001, *A&A*, **376**, 650

We have to abandon the idea that schooling is something restricted to youth. How can it be, in a world where half the things a man knows at 20 are no longer true at 40 - and half the things he knows at 40 hadn't been discovered when he was 20?

Arthur C. Clarke

